

© 2016

Yiğit Muzaffer Arısoy

ALL RIGHTS RESERVED

PHYSICS-BASED SIMULATION MODELING AND OPTIMIZATION OF
MICROSTRUCTURAL CHANGES INDUCED BY MACHINING AND SELECTIVE
LASER MELTING PROCESSES IN TITANIUM AND NICKEL BASED ALLOYS

By

YİĞİT MUZAFFER ARISOY

A dissertation submitted to the

Graduate School-New Brunswick

Rutgers, The State University of New Jersey

In partial fulfillment of the requirements

For the degree of

Doctor of Philosophy

Graduate Program in Industrial and Systems Engineering

Written under the direction of

Tuğrul Özel

And approved by

New Brunswick, New Jersey

JANUARY 2016

ABSTRACT OF THE DISSERTATION

Physics-Based Simulation Modeling and Optimization of Microstructural Changes
Induced by Machining and Selective Laser Melting Processes in Titanium and Nickel
Based Alloys

by YİĞİT MUZAFFER ARISOY

Dissertation Director:

Assoc. Prof. Tuğrul Özel

Manufacturing processes may significantly affect the quality of resultant surfaces and structural integrity of the metal end products. Controlling manufacturing process induced changes to the product's surface integrity may improve the fatigue life and overall reliability of the end product. The goal of this study is to model the phenomena that result in microstructural alterations and improve the surface integrity of the manufactured parts by utilizing physics-based process simulations and other computational methods. Two different (both conventional and advanced) manufacturing processes; i.e. machining of Titanium and Nickel-based alloys and selective laser melting of Nickel-based powder alloys are studied. 3D Finite Element (FE) process simulations are developed and

experimental data that validates these process simulation models are generated to compare against predictions.

Computational process modeling and optimization have been performed for machining induced microstructure that includes; i) predicting recrystallization and grain size using FE simulations and the Johnson-Mehl-Avrami-Kolmogorov (JMAK) model, ii) predicting microhardness using non-linear regression models and the Random Forests method, and iii) multi-objective machining optimization for minimizing microstructural changes. Experimental analysis and computational process modeling of selective laser melting have been also conducted including; i) microstructural analysis of grain sizes and growth directions using SEM imaging and machine learning algorithms, ii) analysis of thermal imaging for spattering, heating/cooling rates and meltpool size, iii) predicting thermal field, meltpool size, and growth directions via thermal gradients using 3D FE simulations, iv) predicting localized solidification using the Phase Field method.

These computational process models and predictive models, once utilized by industry to optimize process parameters, have the ultimate potential to improve performance of products in their service life.

ACKNOWLEDGEMENTS

I would like to use this opportunity to thank some of the great people who have had a significant impact on my life and education. First and foremost, I would like to thank my family for having faith in me and for their continued support. I express my gratitude to my dear friends from all around the globe whose friendship has been truly invaluable to me. I respectfully acknowledge my PhD advisor, Dr. Tuğrul Özel, whom I have received a vast amount of knowledge and advice from. I greatly appreciate the suggestions of my committee members: Dr. David W. Coit, Dr. Myong K. Jeong, Dr. George W. Scherer and Dr. Changsheng Guo. I further extend my gratitude to all my teachers and mentors starting from primary school, to my undergraduate and Master's advisors, Dr. Melike Nikbay and Dr. Kurt Maute for contributing in my education. I am also very grateful to Dr. M. Alkan Dönmez, Dr. Brandon Lane and Dr. Shawn Moylan from National Institute of Standards and Technology, for their support. I am thankful for the administrative and technical help I have received from Ms. Cindy Ielmini, Ms. Helen Pirello, and Mr. Joe Lippencott during my PhD education. Lastly, I gratefully acknowledge the support for this research by the United States National Science Foundation with Grant No. CMMI-1130780 for "Predictive Modeling and Optimization of Machining Induced Surface Integrity with Applications in Titanium and Nickel-Based Alloyed End Products" and by the Department of Commerce National Institute of Standards and Technology with Grant No. 70NANB14H227 for "Predictive Modeling for Laser Based Powder Metal Additive Manufacturing of Nickel-Based Alloyed Parts".

TABLE OF CONTENTS

ABSTRACT OF THE DISSERTATION	ii
ACKNOWLEDGEMENTS	iv
TABLE OF CONTENTS.....	v
LIST OF TABLES	xi
LIST OF FIGURES	xiv
CHAPTER 1: INTRODUCTION	1
1.1 Background.....	1
1.1.1 Conventional and Advanced Manufacturing of Titanium & Nickel Based Alloyed Parts.....	3
1.2 Microstructure of Ti-6Al-4V and IN100 Alloys	6
1.2.1 Microstructure of the Ti-6Al-4V alloy	6
1.2.2 Microstructure of the IN100 alloy	7
1.2.3 Process Induced Microstructural Changes.....	10
1.3 Microstructure Modeling.....	15
1.3.1 Johnson-Mehl-Avrami-Kolmogorov (JMAK).....	16
1.3.2 Kocks-Mecking (KM).....	19
1.3.3 Zener-Hollomon (ZH).....	21
1.3.4 Solidification Microstructure in SLM of IN625	22
1.3.5 Phase Field Method.....	27

1.4	Computational Modeling.....	31
1.4.1	Finite Element Method	32
1.4.2	Machine Learning.....	33
1.4.3	Optimization	36
1.5	Motivation	42
1.6	Objectives	43
1.7	Organization of the Thesis.....	44
CHAPTER 2: EXPERIMENTAL WORK ON MACHINING OF Ti-6Al-4V AND IN100 ALLOYS.....		45
2.1	Introduction	45
2.2	Machining (Material Removal) Experiments	47
2.3	Microhardness Measurements	49
2.3.1	Microhardness measurements for Ti-6Al-4V alloy	49
2.3.2	Microhardness measurements for IN100 alloy	52
2.4	Grain Size Measurements.....	56
2.4.1	Specimen preparation.....	56
2.4.2	Grain size measurements for Ti-6Al-4V alloy.....	57
2.4.3	Grain size measurements for IN100 alloy	78
CHAPTER 3: COMPUTATIONAL MICROSTRUCTURE MODELING		90
3.1	Introduction	90

3.2	Microstructure Modeling in Machining Processes with Finite Element Simulations	91
3.2.1	Microstructure Modeling of Ti-6Al-4V Titanium Alloy	94
3.2.2	Microstructure Modeling of IN100 Alloy.....	127
CHAPTER 4: MACHINE LEARNING BASED MODELING OF HARDNESS AND MICROSTRUCTURE		139
4.1	Introduction	139
4.2	Temperature Based Random Forests Model for Hardness Prediction of Ti-6Al-4V	140
4.3	Instantaneous hardness model	141
4.3.1	Hardness after cooldown.....	144
4.4	Grain Size and Process Parameter Based Models for Hardness Prediction of Ti-6Al-4V	148
4.5	Grain Size and Process Parameter Based Models for Hardness Prediction of IN100	153
CHAPTER 5: MACHINING PARAMETER AND MICROSTRUCTURE MODEL OPTIMIZATIONS.....		159
5.1	Introduction	159
5.2	Machining Parameter Optimization.....	160
5.2.1	Minimizing Microstructural Changes and Maximizing Productivity.....	161
5.2.2	Minimizing Machining Temperature and Microstructural Changes	168

5.3	JMAK Microstructure Model Parameter Optimization.....	175
5.3.1	JMAK Model and Parameters.....	176
5.3.2	Initial Parameters of JMAK Model.....	177
5.3.3	Model Parameter Identification Methodology.....	182
5.3.4	Optimization Problem Definition	182
5.3.5	Simulation Queuing & Batch Jobs.....	185
5.3.6	Finite Element Simulations.....	187
5.3.7	Optimization Results and Discussion	193
CHAPTER 6: EXPERIMENTAL ANALYSIS OF IN625 SELECTIVE LASER MELTING.....		197
6.1	Introduction	197
6.2	Selective Laser Melting Process.....	199
6.2.1	Sample Fabrication and Preparation	200
6.3	Image Analysis	204
6.3.1	Scanning Electron Microscopy (SEM) Imaging.....	204
6.3.2	Grain Size Detection	208
6.3.3	Growth Direction Analysis	220
6.3.4	In-situ Thermal Video Analysis.....	238
6.3.5	Spattering	247
6.3.6	Heating and Cooling Rates	254

CHAPTER 7: MICROSTRUCTURAL MODELING OF SLM PROCESS.....	259
7.1 Introduction	259
7.2 3D Thermal Modeling with Finite Element Method	260
7.2.1 Linear 3D FEM Formulation	262
7.2.2 Heat Source Implementation.....	265
7.2.3 Nonlinearities	271
7.2.4 Time Integration.....	275
7.2.5 Verification and Convergence	275
7.2.6 Problem Geometry and Process Parameters	278
7.2.7 Experimental Validation	280
7.2.8 Single-track Simulation Results.....	282
7.2.9 Multi-track Simulations	287
7.3 Microstructure Prediction	293
7.3.1 Thermal Gradients	293
7.3.2 Phase Field Method.....	298
CHAPTER 8: CONTRIBUTIONS AND FUTURE WORK.....	305
APPENDIX A: MICROSTRUCTURAL ANALYSIS - GRAIN SIZE MEASUREMENTS	
.....	308
APPENDIX B: MICROSTRUCTURAL ANALYSIS - GRAIN GROWTH DIRECTION	
MEASUREMENTS	317

APPENDIX C: OPTICAL IMAGE ANALYSIS	326
APPENDIX D: THERMAL IMAGE ANALYSIS	327
REFERENCES	347

LIST OF TABLES

Table 1.1. Typical grain size of IN100 nickel-base alloy.	9
Table 1.2 JMAK parameters and descriptions.	18
Table 2.1 Microhardness measurements on the machined surfaces for Ti-6Al-4V.	50
Table 2.2 Hardness measurement results for IN100 nickel alloy.	52
Table 2.3 Vickers hardness profiles (mean and standard deviation) of machined IN100 for different cutting speeds and tool geometries.	54
Table 2.4 Measured grain sizes and calculated volume fractions on the specimens after machining of Ti-6Al-4V.	60
Table 2.5 Measured grain sizes and calculated volume fractions on the specimens after machining.	78
Table 3.1 Parameters of the FE simulation model.	96
Table 3.2 Modified Johnson-Cook material flow stress model parameters.	101
Table 3.3 Temperature dependent material properties for Ti-6Al-4V FE simulation. ...	102
Table 3.4 JMAK model parameters for Ti-6Al-4V.	103
Table 3.5 Predicted field variables (weighted means over the selected volume) during first and second pass with against the measured grain size of microstructure in machined surfaces.	105
Table 3.6 IN100 alloy FE simulation parameters.	129
Table 3.7 Material flow stress model parameters for IN100 alloy.	130
Table 3.8 Temperature-dependent material properties for IN100 alloy.	130
Table 3.9 JMAK model parameters for IN100 alloy γ matrix grain simulations.	133

Table 3.10 JMAK model parameters for IN100 alloy primary γ' grain simulations.	133
Table 4.1 Hardness measurements at room temperature after cooling down	145
Table 5.1 Input and response variables for the regression models for Ti-6Al-4V and IN100.	163
Table 5.2 Regression model coefficients with R^2 values for machining IN100 nickel and Ti-6Al-4V titanium alloys.....	164
Table 5.3 Input and response variables for the regression models for Ti-6Al-4V and IN100.	170
Table 5.4 Regression model coefficients for Ti-6Al-4V and IN100.	171
Table 5.5 JMAK parameters and descriptions.....	178
Table 5.6 JMAK Parameters for IN718 and Waspaloy.	179
Table 5.7 Different JMAK parameter sets used in the sensitivity analysis study.....	180
Table 5.8 Initial JMAK model parameters for IN100 alloy.....	180
Table 5.9 Simulation parameters for Reduced FE Model 1.....	189
Table 5.10 Simulation parameters for Reduced FE Model 2.....	190
Table 5.11 Constraints used in the optimization runs for Models 1 and 2.	192
Table 5.12 Identified JMAK model parameters using single machining condition with Reduced Model 1.	194
Table 5.13 Identified JMAK model parameters with Reduced Model 2, post-processed with different weights.	194
Table 5.14 Identified JMAK model parameters (with $w_1=0.5$ and $w_2=0.5$) running on full FE simulations.	196
Table 6.1 General Structure of Box-Behnken Design for Three Factors	203

Table 6.2 Processing conditions and grain size analysis results.	213
Table 6.3 Processing conditions and grain growth direction analysis results for 90° rotation.	224
Table 6.4 Processing conditions and grain growth direction analysis results for 67° rotation.	225
Table 6.5 Thermal camera properties.	240
Table 6.6 Thermal video and process parameters.	240
Table 6.7 Type I and Type II meltpool width measurements from thermal and optical imaging.	245
Table 6.8 Correction factor for thermal camera meltpool width measurements.	245
Table 7.1 Finite Element formulations for steady state, transient, linear and nonlinear solution to the diffusion equation.	261
Table 7.2 Natural coordinates of the nodes of a 8-node hexahedron element.	264
Table 7.3 Bulk Material Properties for IN 625.	272
Table 7.4 SLM Process parameters used in the simulation.	279
Table 7.5 SLM process parameters used in the simulation.	288
Table 7.6 Parameters used in the phase field simulations.	301
Table C.1 Meltpool width measurements with optical microscopy.	326

LIST OF FIGURES

Figure 1.1 Processing route for IN100 nickel alloy.	4
Figure 1.2 Alternative processing route for IN100 nickel alloy.	5
Figure 1.3 Typical microstructure of Ti-6Al-4V titanium alloy.	7
Figure 1.4 Typical microstructure of IN100 nickel alloy.	7
Figure 1.5 Description of microstructural features in IN100 and SEM image of the microstructure of IN100.	8
Figure 1.6 Optical image of SLM microstructure showing melt pool boundaries in the build direction (Z).	23
Figure 1.7 Microstructure of SLM processed IN625 Nickel alloy. (a) SEM image of horizontal (XY) section showing cellular/dendritic growth towards the center of the scan track, (b) vertical (YZ) section with dendrites growing towards the track center and in the build direction. Growth direction is marked with red arrows, and laser scan track centers are marked with white arrows.	25
Figure 1.8 SEM 3D combined view of SLM produced IN100 microstructure. The build direction is shown by the arrow.	26
Figure 1.9 Liquid/solid interface representation using order parameter p	28
Figure 1.10 Selection operation.	39
Figure 1.11 One point crossover operation.	39
Figure 1.12 Mutation operation.	40
Figure 1.13 Elitism.	40
Figure 2.1 Experimental configuration used in face turning of Ti-6Al-4V disks.	48

Figure 2.2 Effects of cutting tool edge radius and coating on measured microhardness of the machined surfaces ($v_c=55$ m/min). Comparison boxplots indicate the upper and lower quartiles and variability of the measured hardness.	51
Figure 2.3 Effects of cutting tool edge radius and coating on measured microhardness of the machined surfaces ($v_c=90$ m/min). Comparison boxplots indicate the upper and lower quartiles and variability of the measured hardness.	51
Figure 2.4 Effects of cutting speed (a) and tool type (b) on the microhardness of the machined surface.	53
Figure 2.5 Microhardness profiles of machined IN100 subsurface into depth for different cutting speeds and tool geometries. (a) $v_c = 12$ m/min, (b) $v_c = 24$ m/min.	55
Figure 2.6 IN100 specimens before preparation for grain size measurements.	56
Figure 2.7 (a) Microstructure of machined subsurface, (b) image processing for grain size calculations, and (c) histogram (TiAlN coated WC/Co tool, $v_c=90$ m/min, $f=0.05$ mm/rev).	58
Figure 2.8 SEM image (a) and grain size distribution (b) taken from unmachined surfaces.	59
Figure 2.9 SEM images and grain size distributions of the disk tracks machined with the TiAlN coated WC/Co tool, with different cutting speed and feed rates.	64
Figure 2.10 SEM images and grain size distributions of the disk tracks machined with the WC/Co tool ($r_\beta=25$ μ m), with different cutting speed and feed rates.	68
Figure 2.11 SEM images and grain size distributions of the disk tracks machined with the WC/Co tool ($r_\beta=10$ μ m), with different cutting speed and feed rates.	72

Figure 2.12 SEM images and grain size distributions of the disk tracks machined with the sharp WC/Co tool ($r_\beta=5\text{ }\mu\text{m}$), with different cutting speed and feed rates.	76
Figure 2.13 Comparison of grain sizes calculated from SEM images for different cutting speed and feed rates.	77
Figure 2.14 Microstructure of machined IN100 subsurface (a) (Sharp WC/Co tool, $v_c=12\text{ m/min}$, $f=0.05\text{ mm/rev}$), histograms of primary γ (b) and secondary γ' (c) grains. Grains are marked red.	80
Figure 2.15 Microstructure of machined IN100 subsurface (a) (Sharp WC/Co tool, $v_c=24\text{ m/min}$, $f=0.05\text{ mm/rev}$), histograms of primary γ (b) and secondary γ' (c) grains. Grains are marked red.	81
Figure 2.16 Microstructure of machined IN100 subsurface (a) (TiAlN coated WC/Co tool, $v_c=12\text{ m/min}$, $f=0.05\text{ mm/rev}$), histograms of primary γ (b) and secondary γ' (c) grains. Grains are marked red.	82
Figure 2.17 Microstructure of machined IN100 subsurface (a) (TiAlN coated WC/Co tool, $v_c=24\text{ m/min}$, $f=0.05\text{ mm/rev}$), histograms of primary γ (b) and secondary γ' (c) grains. Grains are marked red.	83
Figure 2.18 Microstructure of machined IN100 subsurface (a) (WC/Co $r_\beta=10\text{ }\mu\text{m}$ tool, $v_c=12\text{ m/min}$, $f=0.05\text{ mm/rev}$), histograms of primary γ (b) and secondary γ' (c) grains. Grains are marked red.	84
Figure 2.19 Microstructure of machined IN100 subsurface (a) (WC/Co $r_\beta=10\text{ }\mu\text{m}$ tool, $v_c=24\text{ m/min}$, $f=0.05\text{ mm/rev}$), histograms of primary γ (b) and secondary γ' (c) grains. Grains are marked red.	85

Figure 2.20 Microstructure of machined IN100 subsurface (a) (WC/Co $r_\beta=25\text{ }\mu\text{m}$ tool, $v_c=12\text{ m/min}$, $f=0.05\text{ mm/rev}$), histograms of primary γ (b) and secondary γ' (c) grains. Grains are marked red.	86
Figure 2.21 Microstructure of machined IN100 subsurface (a) (WC/Co $r_\beta=25\text{ }\mu\text{m}$ tool, $v_c=24\text{ m/min}$, $f=0.05\text{ mm/rev}$), histograms of primary γ (b) and secondary γ' (c) grains. Grains are marked red.	87
Figure 2.22 Effects of cutting speed v_c (left) and tool type (right) on the primary (top) and secondary (bottom) γ' grains.	88
Figure 2.23 Effects of (a) cutting speed v_c and (b) tool type on the primary (f_1) and secondary (f_2) γ' grain volume fractions.	89
Figure 3.1 FE model of the simulation with (a) workpiece geometry and boundary conditions, (b) tool geometry and (c) mesh of the chip and the machined workpiece.	95
Figure 3.2 Finite element model geometry and temperature fields after the first cut;(a) workpiece mesh with removed chip, (b) temperature field after chip removal, (c) temperature field after diffusion, (d) temperature field during second cut, (e) tool and workpiece at the beginning of second pass.	99
Figure 3.3 Temperature dependent material properties for Ti-6Al-4V FE simulation...	102
Figure 3.4 Predicted temperature fields in FE simulations after first pass (left), second pass (right) at the low feed rate ($f=0.05\text{ mm/rev}$).	107
Figure 3.5 Predicted temperature fields in FE simulations after first pass (left), second pass (right) at the high feed rate ($f=0.10\text{ mm/rev}$).	109
Figure 3.6 Predicted dynamic recrystallization volume fraction fields in FE simulations, after first pass (left), second pass (right) at the low feed rate ($f=0.05\text{ mm/rev}$).....	113

Figure 3.7 Predicted dynamic recrystallization volume fraction fields in FE simulations, after first pass (left), second pass (right) at the high feed rate ($f=0.10$ mm/rev).	117
Figure 3.8 Predicted average grain size fields in FE simulations, after first pass (left), second pass (right) at the low feed rate ($f=0.05$ mm/rev).	121
Figure 3.9 Predicted average grain size fields in FE simulations, after first pass (top), second pass (bottom) at the high feed rate ($f=0.10$ mm/rev).	125
Figure 3.10 Comparison of predicted average α -grain sizes (mean and standard deviation) in machined Ti-6Al-4V sub-surfaces.	126
Figure 3.11 3D FE simulation model for turning IN100 alloy.	129
Figure 3.12 Temperature dependent material properties for the IN100 alloy FE simulation.....	131
Figure 3.13 Comparison of predicted and measured (primary γ') average grain size (mean and standard deviation) on IN100 alloy subsurface.	134
Figure 3.14 Predicted grain size fields: TiAlN coated tool $v_c=12$ m/min.....	134
Figure 3.15 Predicted grain size fields: TiAlN coated tool $v_c=24$ m/min.....	135
Figure 3.16 Predicted grain size fields: WC/Co tool $r_\beta=5\mu\text{m}$, $v_c=12$ m/min.	136
Figure 3.17 Predicted grain size fields: WC/Co tool $r_\beta=5\mu\text{m}$, $v_c=24$ m/min.	137
Figure 4.1 Hot hardness measurements at during air cooling for different initial temperatures (different colors).....	141
Figure 4.2 Representation of a regression tree in the instantaneous hardness model.	142
Figure 4.3 Instantaneous hardness RF regression model results, red: whole dataset, blue: predictions on training data, green: predictions on testing data.....	142

Figure 4.4 Temperature in °C (a) and hardness in HV (b) over line section on the workpiece during machining over time.	144
Figure 4.5 Hardness measurements at room temperature after cooling down.....	145
Figure 4.6 Instantaneous hardness (a) prior to chip formation, (b) after the cutting process, and (c) after cooling down to room temperature.	147
Figure 4.7 Random Forests based prediction models for hardness and grain size.	149
Figure 4.8 Measured and predicted average grain sizes for $v_c=55$ m/min and $v_c=90$ m/min.	151
Figure 4.9 Measured and predicted hardness for $v_c=55$ m/min and $v_c=90$ m/min.	152
Figure 4.10 Microhardness profile prediction models for the TiAlN coated and uncoated tools.....	153
Figure 4.11 Surface fit of the microhardness with respect to depth and cutting speed for the TiAlN coated tool. Experimental data points are shown as circles.	155
Figure 4.12 Surface fit of the microhardness with respect to depth and cutting speed for the uncoated tools with $r_\beta=5\mu\text{m}$. Experimental data points are shown as circles.....	155
Figure 4.13 Surface fit of the microhardness with respect to depth and cutting speed for the uncoated tools with $r_\beta=10\mu\text{m}$. Experimental data points are shown as circles.....	156
Figure 4.14 Surface fit of the microhardness with respect to depth and cutting speed for the uncoated tools with $r_\beta=25\mu\text{m}$. Experimental data points are shown as circles.....	156
Figure 4.15 Comparison of experimental microhardness measurements and grain-size based microhardness predictions.	158
Figure 5.1 Multi-objective optimization result for IN100 nickel alloy with objective values (left) and the decision variables (right).....	166

Figure 5.2 Multi-objective optimization result for Ti-6Al-4V titanium alloy with objective values (left) and the decision variables (right).	168
Figure 5.3 Multi-objective optimization result for IN100 nickel alloy with objective values (left) and the decision variables (right).	172
Figure 5.4 Multi-objective optimization result for Ti-6Al-4V titanium alloy with objective values (left) and the decision variables (right).	174
Figure 5.5 Sensitivity analysis on parameter a_8 with different cutting conditions.	181
Figure 5.6 Optimization of JMAK Model Parameters: DEFORM and MATLAB interface.....	184
Figure 5.7 Scheduling and running the JMAK model parameter optimization.....	186
Figure 5.8 Reduced Model 1 geometry after the slicing operation: a) Beginning of the optimization run. b) End of the optimization run.	188
Figure 5.9 Reduced Model 2 geometry and mesh for TiAlN coated tool with $v_c=24$ m/min, (a) beginning of the optimization run (cutting length of $l_1=1.1$ mm) (b) end of the optimization run (cutting length of $l_2=2.6$ mm).	190
Figure 5.10 Comparison of measured and predicted grain sizes by using identified JMAK model parameters under different objective function weights.	195
Figure 6.1 Representation of Selective Laser Melting process.....	198
Figure 6.2 SLM terminology.	200
Figure 6.3 Box-Behnken Design.....	202
Figure 6.4 Build layout, as shown in the EOS M270 software.....	202
Figure 6.5 SEM image of the electropolished XZ surface of the coupon #35, at 100X magnification. B indicates the build direction.	206

Figure 6.6 SEM image of the electropolished XZ surface of the coupon #35, at 1500X magnification (left) showing layers and 8000X magnification (right) showing columnar grains with inclinations. B indicates the build direction.	206
Figure 6.7 SEM image of horizontal (XY) section (top) and vertical (YZ) section (bottom) of coupon #17 showing cellular growth between meltpool regions and columnar growth within meltpool regions.	207
Figure 6.8 8-connected neighborhood for pixel p_{ij}	209
Figure 6.9 Grain size analysis of SLM processed IN625 coupons, (a) coupon #35 (195 W, 800 mm/s, 0.1 mm, 90° rotation scan strategy) and (b) coupon #31 (195 W, 800 mm/s, 0.1 mm, 67° rotation scan strategy).	212
Figure 6.10 Effect of energy intensity.	214
Figure 6.11 Effect of laser power.	215
Figure 6.12 Effect of scanning velocity.	215
Figure 6.13 Effect of hatch distance.	216
Figure 6.14 Effect of laser power and scanning velocity.	218
Figure 6.15 Effect of scanning velocity and laser power.	218
Figure 6.16 Effect of hatch distance and laser power.	219
Figure 6.17 Effect of hatch distance and scanning velocity.	219
Figure 6.18 Positive and negative angles and line coloring.	222
Figure 6.19 Growth directions and histograms of inclination angles for IN 625 test coupons observed from XZ faces, (a) coupon #35 (195 W, 800 mm/s, 0.1 mm, 90° rotation scan strategy) and (b) coupon #31 (195 W, 800 mm/s, 0.1 mm, 67° rotation scan strategy).	226

Figure 6.20 Effect of laser power on dominant positive and negative growth directions, with 90° (top) and 67° (bottom) rotation strategies.	227
Figure 6.21 Effect of scanning speed on dominant positive and negative growth directions, with 90° (top) and 67° (bottom) rotation strategies.	228
Figure 6.22 Effect of hatch distance on dominant positive and negative growth directions, with 90° (top) and 67° (bottom) rotation strategies.	229
Figure 6.23 Effect of energy intensity on dominant positive and negative growth directions, for 90° (top) and 67° (bottom) rotation strategies.	231
Figure 6.24 Effects of laser power and scanning speed on dominant positive and negative growth directions at constant hatch distance ($h=0.1\text{mm}$), for 90° (top) and 67° (bottom) rotation strategies.	233
Figure 6.25 Effects of scanning speed and laser power on dominant positive and negative growth directions at constant hatch distance ($h=0.1\text{mm}$), for 90° (top) and 67° (bottom) rotation strategies.	234
Figure 6.26 Effects of hatch distance and laser power on dominant positive and negative growth directions at constant scanning velocity ($v_s=800\text{mm/s}$), for 90° (top) and 67° (bottom) rotation strategies.	236
Figure 6.27 Effects of hatch distance and scanning speed on dominant positive and negative growth directions at constant laser power ($P=182\text{W}$), for 90° (top) and 67° (bottom) rotation strategies.	237
Figure 6.28 Thermal camera setup, (a) Side-view of the EOS machine, custom door, and thermal camera, (b) Solidworks model of EOS build chamber + custom viewport, (c) optical axis, plane of focus and scene size.....	241

Figure 6.29 Camera signal transformation curves for different emittivity values.....	242
Figure 6.30 Image generated with temperature data obtained from the thermal camera. Emittivity (ϵ) assumed to be 0.2.	242
Figure 6.31 Meltpool visualization from a thermal image. Dimensions are in pixels....	244
Figure 6.32 Meltpool width measurements (calculated and actual) along with attached and detached spattering particles. Dimensions are in pixels.....	244
Figure 6.33 Meltpool width correction.	246
Figure 6.34 Minimum, maximum and average meltpool widths after attached particle and optical image comparison corrections. Error bars represent sample standard deviations.	247
Figure 6.35 Spattering during the process.	248
Figure 6.36 An image captured from the thermal camera plotted in MATLAB showing combined RGB (top-left), red (top-right), green (bottom-left) and blue (bottom-right) channels. Temperature information is not shown here.	250
Figure 6.37 Lens flare removal around the meltpool region with the original frame (top) and the processed frame (bottom).....	251
Figure 6.38 Preprocessed thermal camera image (left), detected particles (right). Centroids or spattering particles are marked blue.....	252
Figure 6.39 Processing steps for spattering particle detection.....	253
Figure 6.40 Frames from the thermal camera video showing the processing of a single track.....	256
Figure 6.41 Minimum, maximum and average temperature histories grouped by the x coordinates: At the beginning of the track (top), middle of the track (middle) and end of	

the track (bottom) across multiple tracks. Error bars represent sample standard deviations. Only the tracks with positive scanning direction (+x) are shown.....	257
Figure 6.42 Minimum, maximum and average temperature histories grouped by the x coordinates: At the beginning of the track (top), middle of the track (middle) and end of the track (bottom) across multiple tracks. Error bars represent sample standard deviations. Only the tracks with negative scanning direction (-x) are shown.....	258
Figure 7.1 Isoparametric 8-node hexahedral element.....	263
Figure 7.2 Node based element capturing under a circular beam. Captured elements are shown in yellow.	266
Figure 7.3 Gaussian beam intensity on the surface.....	267
Figure 7.4 Representation of the beam area (contoured) sampled with points.....	268
Figure 7.5 Power distribution on node-captured elements with Monte-Carlo sampling of the laser beam.	270
Figure 7.6 The affected (heated) and unaffected elements under the beam. Only the elements in the top are affected.	270
Figure 7.7 Problem geometry with hexahedra mesh.	279
Figure 7.8 Comparison of thermal camera and FE results on a single track with medium energy intensity ($P=195$ W, $h=0.1$ mm, $v_s=800$ mm/s). Liquidus and solidus temperatures are marked with dashed lines.....	281
Figure 7.9 FE solution for the high energy intensity ($P=195$ W, $h=0.1$ mm, $v_s=725$ mm/s) case. Temperatures are limited to $T \leq T_L$	282
Figure 7.10 FE solution for the medium energy intensity ($P=195$ W, $h=0.1$ mm, $v_s=800$ mm/s) case. Temperatures are limited to $T \leq T_L$	283

Figure 7.11 FE solution for the low energy intensity ($P=169$ W, $h=0.1$ mm, $v_s=875$ mm/s) case. Temperatures are limited to $T \leq T_L$	283
Figure 7.12 Temperature extraction points.	284
Figure 7.13 Temperature histories at six points for the high energy intensity ($P=195$ W, $h=0.1$ mm, $v_s=725$ mm/s) case.	285
Figure 7.14 Temperature histories at six points for the medium energy intensity ($P=195$ W, $h=0.1$ mm, $v_s=800$ mm/s) case.	285
Figure 7.15 Temperature histories at six points for the low energy intensity ($P=169$ W, $h=0.1$ mm, $v_s=875$ mm/s) case.	286
Figure 7.16 Multi-track simulation geometry with hexahedra mesh.	288
Figure 7.17 Meltpool width calculated from low, medium and high energy intensity FE simulation results showing two tracks of processing.	290
Figure 7.18 Temperature histories at six points along the scanning direction for the high energy intensity ($P=195$ W, $h=0.1$ mm, $v_s=725$ mm/s) case.	291
Figure 7.19 Temperature histories at six points along the scanning direction for the medium energy intensity ($P=195$ W, $h=0.1$ mm, $v_s=800$ mm/s) case.	292
Figure 7.20 Temperature histories at six points along the scanning direction for the low energy intensity ($P=169$ W, $h=0.1$ mm, $v_s=875$ mm/s) case.	292
Figure 7.21 Contour plot of the temperature field and the negative thermal gradients on sampled points at the end of the medium energy intensity ($P=195$ W, $h=0.1$ mm, $v_s=800$ mm/s) simulation.	294

Figure 7.22 YZ view of the negative thermal gradients extracted from the FE solution ($P=195$ W, $h=0.1$ mm, $v_s=800$ mm/s) sampled at various points (shown as blue). Note that the thermal gradients are summed over time.	295
Figure 7.23 YZ view of the negative thermal gradients extracted from the medium energy intensity FE solution ($P=195$ W, $h=0.1$ mm, $v_s=800$ mm/s) sampled at various points (shown as blue). Note that the thermal gradients are summed over time.	295
Figure 7.24 Gradient directions in the XZ plane obtained from FE solutions.....	296
Figure 7.25 Gradient directions in the YZ plane obtained from FE solutions.....	297
Figure 7.26 Initial phase field. The red region ($p=1$) is solid while the blue region ($p=0$) is liquid.	302
Figure 7.27 Microstructure at the end of the phase field simulation that utilizes the temperature field from the high energy intensity ($P=195$ W, $h=0.1$ mm, $v_s=725$ mm/s) FE simulation.....	304
Figure 7.28 Microstructure at the end of the phase field simulation that utilizes the temperature field from the medium energy intensity ($P=195$ W, $h=0.1$ mm, $v_s=800$ mm/s) FE simulation.	304
Figure A.1 Grain size analysis of SLM processed IN625 coupons.	308
Figure B.1 Growth directions and histograms of inclination angles for all IN 625 test coupons.	317
Figure D.1 Thermal images for track #1.....	327
Figure D.2 Thermal images for track #2.....	328
Figure D.3 Thermal images for track #3.....	329
Figure D.4 Thermal images for track #4.....	330

Figure D.5 Thermal images for track #5.....	331
Figure D.6 Thermal images for track #6.....	332
Figure D.7 Thermal images for track #7.....	333
Figure D.8 Thermal images for track #8.....	334
Figure D.9 Thermal images for track #9.....	335
Figure D.10 Thermal images for track #10.....	336
Figure D.11 Thermal images for track #11.....	337
Figure D.12 Thermal images for track #12.....	338
Figure D.13 Thermal images for track #13.....	339
Figure D.14 Thermal images for track #14.....	340
Figure D.15 Thermal images for track #15.....	341
Figure D.16 Thermal images for track #16.....	342
Figure D.17 Thermal images for track #17.....	343
Figure D.18 Thermal images for track #18.....	344
Figure D.19 Thermal images for track #19.....	345
Figure D.20 Thermal images for track #20.....	346

CHAPTER 1: INTRODUCTION

1.1 Background

Manufacturing processes may significantly affect the quality of resultant surfaces and structural integrity of the metal end products. Controlling manufacturing process induced changes to the product's surface and structural integrity may improve the fatigue life and overall performance of the end product. Surface integrity is considered one of the most relevant attributes used for evaluating the quality of finish machined surfaces, as the critical structural components in industry are manufactured with the objective to reach high reliability levels. Surface integrity comprises two aspects, topography and layer characteristics. Topography characteristics are defined by the shape of the surface of a material, such as surface waviness and surface roughness. For instance, feed marks left on the surface of a material after machining and subsequent polishing operations to remove these marks fall in the domain of topography. Having a smooth surface topography after machining is essential in certain areas, such as assemblies that require high precision and moving parts. The second aspect of surface integrity is layer characteristics. As opposed to surface topography, layer characteristics are related to the condition of the material below the surface. For instance, thermal and mechanical loads that result in deformation may leave some stresses in the material even after the loads are removed. This remaining stress, called the residual stress, can greatly affect the strength of a material. Certain processes, such as shot peening and laser peening, aim to generate compressive residual stresses near the surface of a material, increasing its strength against compressive forces. However,

residual stresses may lead to cracks that may yield catastrophic failures if not investigated and treated properly. Another property of layer characteristics is hardness, which can be defined as a material's resistance to indentation, or plastic deformation under compressive stress. While hardness is closely related to the strength of the material, it may not be homogenous throughout the material as it is highly influenced by the material's thermomechanical processing history. A material's properties greatly depend on the condition of its internal structure, called the microstructure. Microstructure can be altered via phase changes, recrystallization and grain growth as a result of thermomechanical processes, such as forging and machining, and these alterations may lead to increased / decreased hardness and residual stresses. Therefore, microstructure of a material plays a critical role in surface integrity, and it has become a topic of interest in manufacturing of certain alloys.

Nickel-base alloys can considerably maintain their strength at high temperatures and long exposures; therefore they are preferred material for components in hot sections of the aircraft and gas turbine engines, nuclear reactors and rocket engines. These alloys can be obtained in the forms of wrought, forged, cast and sintered, through several different processing routes. Inconel 100 (IN100) is a Ni-Co-Cr based super alloy which is used in the cast or powder metallurgy (PM) forms and powder processing provides structural uniformity, high strength, and toughness suitable for engine components operating at intermediate temperature regimes such as disks, spacers, and seals. Although high strength at elevated temperatures and good corrosion resistance are achieved, machining of IN100 alloy is highly difficult due to low thermal conductivity, high rigidity, high toughness,

chemical affinity with tool materials at elevated temperatures and microstructure related hard carbide particles (Axinte et al., 2006). In addition, machining induced surface integrity and alterations to the subsurface microstructure so called “white layer” due to severe plastic deformation (SPD) and abusive thermal loading strongly affects the fatigue life of mission-critical components (Ulutan and Ozel, 2011; M'Saoubi et al., 2014) .

Titanium alloys, specifically Ti-6Al-4V (Ti64), are commonly used in the aerospace industry due to their high strength to weight ratio and toughness. Ti-6Al-4V is known to form a tightly adherent oxide film immediately upon exposure to oxygen, vastly improving its corrosion resistance. They are also considered bio-compatible and can be used in medical devices.

1.1.1 Conventional and Advanced Manufacturing of Titanium & Nickel Based Alloyed Parts

Conventional manufacturing process often starts with a large workpiece prepared through metal forming or powder material compaction and material is removed from this workpiece in certain locations to obtain the final geometry of the product. Such processes are called material removal processes or machining and they are the most commonly used manufacturing processes in the industry. Additive metal manufacturing, often called but not limited to 3-D printing, is an emerging field where the final part is built layer-by-layer by combining the powder material together by utilizing energy sources such as high energy laser or electron beams.

1.1.1.1 Material Removal / Machining Processes

Material removal processes may start with a bulk material obtained via casting, forging or powder compaction manufacturing routes to create a desired geometry, or with a pre-processed part to achieve higher geometrical precision. This research will only focus on machining processes, in particular, the turning process applied on bulk material. Turning process consists of a workpiece rotating around one of its axis, and a tool made from a harder material is forced on the workpiece to remove material from desired locations.

Powder-based materials such as IN100 can be processed in various ways. One typical processing route is given in Figure 1.1 where the powder goes through several steps to obtain its final form. Powder manufacturing processes generally yield a porous microstructure. The material then undergoes sintering and Hot Isostatic Pressing (HIP) in order to achieve a fully dense microstructure. The densified material is then forged into a desired shape, such as a billet. After the forging operation, the final part is obtained via material removal processes. Additionally, residual stresses that may have occurred from previous processes can be removed by heat treatment processes.

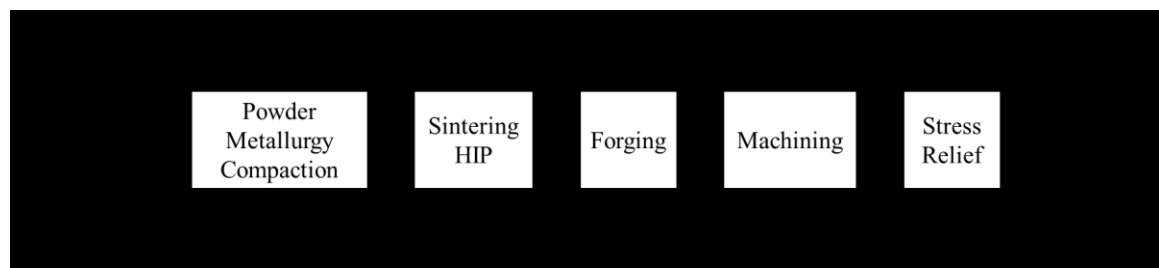


Figure 1.1 Processing route for IN100 nickel alloy.

1.1.1.2 Additive Manufacturing Processes

Additive manufacturing processes such as 3-D printing are most commonly applied to metal alloys and plastics, but more exotic applications include biological tissue and even food printing. Additive manufacturing has become popular because it allows the creation of intricate parts directly from a computer design.

Selective Laser Melting (SLM) is an example of metal printing where a layer of powdered metal is melted at specific locations using a high power laser beam. The desired 3-D geometry is sliced to layers of equal thickness using Computer Aided Design (CAD), and the printer builds the part layer-by-layer by adding a new layer of powder on top of the previously processed layer. At the end, the excess metal powder is vacuumed and can be reused to a certain extent.

Alternative processing routes to that shown in Figure 1.1 has emerged with the advent of additive manufacturing processes. Figure 1.2 shows one such route where the powder Ni alloy is directly processed via SLM. Additional steps such as HIP and precision machining can be included to achieve higher quality parts.

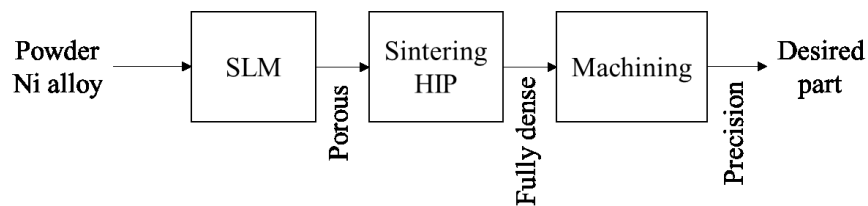


Figure 1.2 Alternative processing route for IN100 nickel alloy.

1.2 Microstructure of Ti-6Al-4V and IN100 Alloys

Regardless of the processing route chosen, surface integrity of the final product depends greatly on its final microstructure. Microstructure of Ti-6Al-4V and IN100 alloys are of particular interest to this research, and they are briefly discussed in this section.

1.2.1 Microstructure of the Ti-6Al-4V alloy

Pure titanium has two phases, the hexagonal close-packed α -phase, and the body-centered cubic β -phase. As stated by Carpenter (Carpenter, 2000), allotropic phase transformation occurs in titanium at 882.5°C from the α -phase to β -phase. The β -phase must be stabilized to exist in room temperature with the use of alloying elements. This allows titanium alloys to be strengthened by heat treating to achieve higher strengths. Therefore, titanium alloys are classified as α -alloys, β -alloys and $\alpha+\beta$ alloys. The first group α -alloys are not heat treatable and may contain natural α -stabilizers such as Al or O. The second group β -alloys are metastable and require the addition of β -stabilizers such as V or Mo to preserve the β phase after quenching. They can benefit greatly from solution treating and aging, resulting in strength increase. The third group, $\alpha+\beta$ alloys, are alloyed with both α and β stabilizers to retain both phases in low and high temperatures. Ti-6Al-4V is an $\alpha+\beta$ alloy, and is by far the most commonly used titanium alloy in the industry. Microstructure of annealed Ti-6Al-4V consists of two phases; α phase with average $d_0= 20 \mu\text{m}$ grain diameters, and β -matrix grains with about 40-60% volume fraction as reported by Nalla et al. (Nalla et al., 2003). A typical microstructure image of Ti-6Al-4V alloy is shown in Figure 1.3.

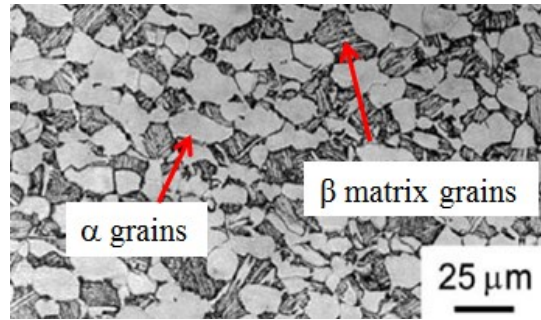


Figure 1.3 Typical microstructure of Ti-6Al-4V titanium alloy.

(Nalla et al., 2003)

1.2.2 Microstructure of the IN100 alloy

IN100 microstructure mainly consists of two phases; γ and γ' . A representative image of the IN100 microstructure is given in Figure 1.4. The γ phase consists of large grains that form the matrix in the material whereas γ' is formed as a result of various processes (Milligan et al., 2004; Wusatowska-Sarnek et al., 2003a; Wusatowska-Sarnek et al., 2003b; Kikuchi et al., 1990). Three types of γ' have been observed: primary γ' , secondary γ' , and tertiary γ' as shown in Figure 1.5.

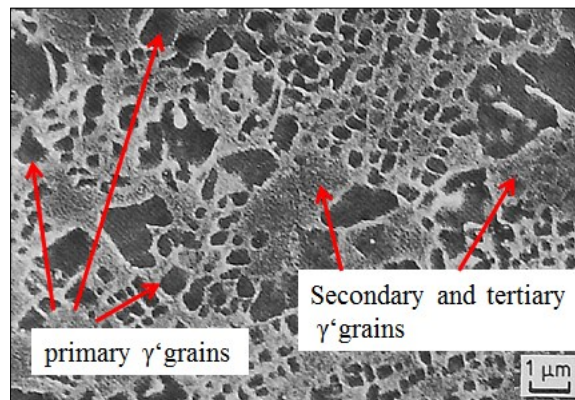


Figure 1.4 Typical microstructure of IN100 nickel alloy.

(Kikuchi et al., 1990)

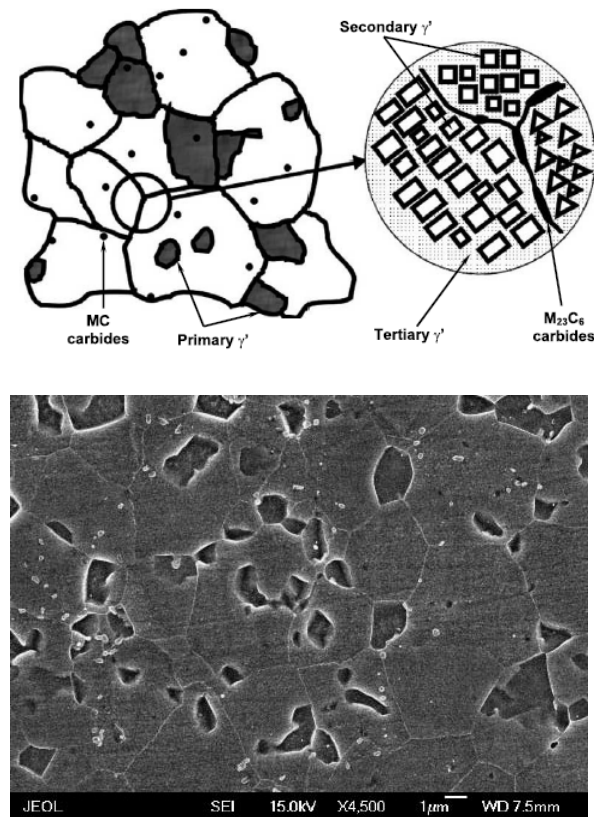


Figure 1.5 Description of microstructural features in IN100 and SEM image of the microstructure of IN100.

(Wusatowska-Sarnek et al., 2003b)

Sizes and distributions of these γ' formations are set by process parameters, for instance, a very fine microstructure may be obtained by a subsolvus heat treatment. Milligan et al. (Milligan et al., 2004) states that by varying the cooling rate after the solutionizing step and the solution heat treatment temperature, it is possible to influence the γ grain sizes as well as γ' grain sizes and distributions. It is stated by Wusatowska-Sarnek et al. (Wusatowska-Sarnek et al., 2003a) that primary γ' is affected by the solution treatment temperature, secondary γ' is affected by the stabilization temperature and forms during cooling from the solution temperature and tertiary γ' is controlled by aging. Primary γ' -

grains are large enough to be compared with the γ -matrix grains, and can be included in the grain size measurement of the matrix. Wusatowska-Sarnek et al. (Wusatowska-Sarnek et al., 2003b) reports the average IN100 γ -matrix grain size as 3.82 μm (see Figure 5b), Kikuchi et al. (Kikuchi et al., 1990) reports as 3.5 μm and Milligan et al. (Milligan et al., 2004) reports it as 4.2 μm . Average diameters of secondary and tertiary γ' -grains are nanocrystalline grains with average sizes of 120 nm and 8.5 nm respectively (see Table 1.1). It is stated that the sizes and distributions of the γ' precipitates play an important role in mechanical properties of IN100. It also reported by Wusatowska-Sarnek et al. (Wusatowska-Sarnek et al., 2003a) that a high strength material is obtained in the two phase field ($\gamma + \gamma'$) by maintaining the temperature below the γ' solvus, 1460K. A subsolvus solution treatment at 1416K is followed by a two-step aging sequence at 1255K and 1005K to form the strengthening phases. Upon investigating the PM IN100 alloy through tensile tests at 260°C and 650°C, Milligan et al. (Milligan et al., 2004) concludes that secondary γ' size and volume fraction has a dominant effect on the strength of the material. It is further claimed that the presence of γ' is important, but its size is not. A decrease in strain hardening is observed with larger secondary γ' particles and with the presence of primary γ' particles.

Table 1.1. Typical grain size of IN100 nickel-base alloy.

(Milligan et al., 2004)

Phase	Grain size [μm]	Volume Fraction
γ grains	4.2	balance
Primary γ' grains	1.28	0.25
Secondary γ' grains	0.109	0.32
Tertiary γ' grains	0.021	0.024

1.2.3 Process Induced Microstructural Changes

Microstructure of the material may be affected by thermal fields and deformations during and after certain manufacturing processes, depending on the process parameters. High temperatures and excessive strain / strain rates often change the microstructure so much that the initial properties of the material are altered, sometimes towards an undesirable state. One example is the severe work/strain hardening effect seen in Ni alloys during machining processes.

1.2.3.1 Machining Induced Microstructural Changes

Microhardness is an important aspect of surface integrity, and it can play an important role throughout the product's lifecycle as reviewed in (Ulutan and Ozel, 2011). It is affected by the machining induced strain, stress and temperature fields in the workpiece. Although there are some analytical modeling efforts for microhardness, they require a great understanding of the microstructure of the specific material and are not easily implemented or generalized (Ulutan and Ozel, 2011; Che-Haron and Jawaaid, 2005). However, it is known that machining parameters such as cutting speed, depth of cut, tool radius and tool coating have an effect on stress and temperature fields; therefore it is possible to obtain a relationship between the machining parameters and microhardness.

Moussaoui et al. (Moussaoui et al., 2013) investigated the effects of milling on microhardness and microstructure in Ti-6Al-4V. It is stated that machining causes a softening effect on the material due to high temperatures during cutting which cause Vanadium to diffuse into the α phase from the β phase of the alloy, without changing the

microstructure. It is also stated that it is difficult to take traditional hardness measurements from two phase alloys such as the Ti-6Al-4V, and the results are dispersed. Jovanovic et al. (Jovanović et al., 2006) investigated how the mechanical properties and microstructure of investment cast Ti-6Al-4V change with different annealing temperatures and cooling rates. It was found out that higher annealing temperatures and faster cooling rates yield higher tensile strength and hardness, and reported hardness measurements of annealed Ti-6Al-4V between 360-375 HV using 10 N force (about 1.02 kg). Moussaoui et al. (Moussaoui et al., 2013) reported microhardness measurements that were made at 300 g force (about 2.94 N) for Ti-6Al-4V as 335.65 HV mean with 19.24 standard deviation. Rotella et al. (Rotella et al., 2014) measured surface and subsurface microhardness values as 354 HV for as received (annealed) Ti-6Al-4V using 50 g force (0.49 N).

1.2.3.2 Selective Laser Melting Generated Microstructure

Selective Laser Melting (SLM) of titanium alloys and nickel alloys is a recent research interest for many researchers. In SLM, powder material is melted using a high powered laser which cools down and solidifies. Anam et al. (Anam et al., 2013b) investigated the microstructure of SLM processed IN625 alloy, and stated that process parameters such as laser beam power and scan speed affect the temperature and cooling rates in the meltpool which in turn determine the formation of constituent phases. Anam et al. (Anam et al., 2014) further studied the SLM processing of IN625 alloy, by observing the microstructure obtained from different scanning strategies. Cellular dendritic grain growth was observed towards the center of the scan track (perpendicular to the scanning direction), however, alternating scan directions between layers caused remelted dendritic structures from

previous layers to grow epitaxially towards the center of the new melt pool. Inter-cellular spacing was found to be less than 1 μm , which was said to contribute to the strength of the material. Coarse cellular structures were also observed in the inter-meltpool regions, which were deemed undesirable and assumed to have a significant impact on hardness and strength.

In nickel based alloys, the matrix phase γ NiCr fcc, γ' $\text{Ni}_3(\text{Al,Ti})$ fcc with primary, secondary, tertiary if exists, γ'' Ni_3Nb bct and δ $(\text{Fe,Ni})_2\text{Nb}$ hcp phases can be found in the microstructure, as well as dendrite formations (Anam et al., 2013b; Anam et al., 2014; DuPont et al., 2001; Jia and Gu, 2014; Amato et al., 2012; Nie et al., 2014; Smith and Patel, 2005). In SLM of IN625, γ and γ'' phases are dominantly observed. Coarser cellular structures are also observed in the inter-meltpool regions (Anam et al., 2014). Amato et al. (Amato et al., 2012) investigated the mechanical behavior and microstructure of SLM fabricated IN718 alloy. It was observed that as-fabricated cylinders oriented in the build direction and perpendicular to the build direction contained columnar grains and arrays of oblate ellipsoidal γ' precipitates. Further processing by Hot Isostatic Pressing (HIP) revealed columnar γ'' Ni_3Nb (bct) phase parallel to the laser beam and build direction whereas annealing of as-processed parts (1160°C for 4h) revealed 50% recrystallization with spheroidal γ' precipitates, densely distributed γ'' precipitates and δ phase recrystallization interfaces and recrystallized grain boundaries. The columnar grains were 0.5-1 μm in width. Microindentation Vickers hardness measurement values were 3.9GPa for as-fabricated, 5.7GPa for HIP processed and 4.6 GPa for the annealed materials. It was concluded that SLM produced parts exhibited similar tensile properties to wrought (cold

work) IN718 alloy. The melt pool width was reported as 75 to 100 μm and the layer thickness was about 50 μm in their study.

DuPont et al. (DuPont et al., 2001) investigated the microstructure of Laser Engineered Net Shaping (LENS) deposited IN718 alloy using optical, scanning and transmission electron microscopy. The LENS process uses a high powered laser beam to create a molten pool of metal powder that is injected during the process. It was found that the thermal cycles of subsequent passes did not affect the underlying layer microstructure. It is stated that γ' , γ'' and δ precipitates appear in the as-cast IN718 at high temperatures, however, it takes about six minutes at 870°C and takes even longer at lower temperatures. Time above peak temperature has been observed to be extremely short in the LENS process, and peak temperature decreases to 850°C five layers below the weld pool, leading to the conclusion that precipitation reactions would not occur during the process. This conclusion was also supported by TEM analysis, and it allowed the as-deposited microstructure to be estimated using only solidification models. The microstructure model used in the paper predicts the types of phases formed during solidification that are necessary to prevent microsegregation.

Gong et al. (Gong et al., 2013) studied the effects of process parameters in SLM and Electron Beam Melting (EBM) processing of Ti-6Al-4V alloy. It was found that energy density, defined by laser power divided by scanning speed, hatch spacing and layer thickness, had an impact on meltpool size and a low energy density could result in voids between hatch lines. Defects such as pits and pores, and their correlations with process

parameters were explored. It was found that in the SLM process, pits can be formed by splashed particles that land and adhere on the processed surface of the material, which were then hit by the recoater blade. Porosity of the as-processed material was also found to be affected by processing conditions, however, a direct correlation could not be found.

The current literature indicates that the final microstructure of the processed material highly depends on the processing conditions, thus, researching experimental analysis and modeling of the microstructure is very compelling.

1.3 Microstructure Modeling

Microstructure is often characterized by grain sizes in the material, before and after processing. Grains are known to be affected by variables such as temperature, strain and strain rates during a process. Sun et al. (Sun et al., 2010) reported the effects of different temperatures and strain rates on the grain sizes of TA15 titanium alloy during hot forging.

Many different models exist for grain diameter prediction in manufacturing processes, such as the Zener-Hollomon (ZH) parameter based model used by Rotella et al. (Rotella et al., 2013), the Kocks-Mecking (KM) based dislocation density model used by Sun et al. (Sun et al., 2010), and the Johnson-Mehl-Avrami-Kolmogorov (JMAK) based recrystallization model used by Yi et al. (Yi et al., 2008). Another model by Arieli and Rosen (Arieli and Rosen, 1977) relates the grain size of the Ti-6Al-4V alloy to flow stress and temperature by a logarithmic relationship. Using initial average grain size, material properties and process outcomes such as strain, strain rate, temperature, and time, the final average grain size can be obtained with these models which is ultimately related to surface integrity. JMAK based recrystallization model, KM based dislocation density model and ZH parameter based recrystallization model are reviewed in this section.

1.3.1 Johnson-Mehl-Avrami-Kolmogorov (JMAK)

The JMAK model, also called Avrami model, defines the transformation kinetics in a material. The JMAK equation relates the volume fraction of (nucleated and grown) crystals in a solidifying liquid with time, and requires the crystal nucleation and growth rates to be known. It can be used to calculate the recrystallized volume fraction inside the material as a function of time. Under the assumption that the nucleation and growth rates are affected by the initial grain size, and variables such as temperature, strain and strain rate, the microstructure evolution for recrystallization can be modeled.

Isothermal JMAK equations describe the volume fraction of the transformed material as a function of temperature and time. Experimental results are used to determine the constants, and subsequent calculations can be made for recrystallized fraction and grain size. There is an implementation of this model in the commercial Finite Element Analysis software DEFORM that includes grain growth, static, dynamic, and metadynamic recrystallization, and it incorporates a modified version of the JMAK equation that takes strains and strain rates the material experiences into account (SFTC; Shen et al., 1995; Shen, 2005). Arrhenius type equations are used to describe model variables with respect to temperature, strain and strain rate empirically which are obtained from the FE solution at a given time step. Dynamic recrystallization occurs when a critical strain $\varepsilon_c = a_2 \varepsilon_p$ is exceeded, where a_2 is a model parameter and the peak strain ε_p is defined by:

$$\varepsilon_p = a_1 d_0^{h_1} \dot{\varepsilon}^{m_1} \exp(Q_1/RT) + c_1 \quad (1.1)$$

Note that the temperature dependence is justified by the fact that in the Finite Element implementation of these equations, they are recalculated at each timestep, and a constant

value of temperature is used in the equation. Furthermore, the model parameters can also be defined as temperature dependent, using different values at distinct temperature ranges. The volume fraction for dynamic recrystallization is defined with the Avrami equation as given by:

$$X_{DRx} = 1 - \exp \left[-\beta_d \left(\frac{\varepsilon - a_{10}\varepsilon_p}{\varepsilon_{0.5}} \right)^{k_d} \right] \quad (1.2)$$

where X_{DRx} is the fraction of dynamically recrystallized material. The strain for 50% recrystallization is given by:

$$\varepsilon_{0.5} = a_5 d_0^{h_5} \varepsilon^{n_5} \dot{\varepsilon}^{m_5} \exp(Q_5/RT) + c_5 \quad (1.3)$$

where R is the universal gas constant. The recrystallized grain size is calculated from,

$$d_{DRx} = a_8 d_0^{h_8} \varepsilon^{n_8} \dot{\varepsilon}^{m_8} \exp(Q_8/RT) + c_8 \quad (1.4)$$

The average grain size is then calculated from the mixture of recrystallized grains and unaffected grains as:

$$d_{avg} = d_0(1 - X_{DRx}) + d_{DRx}X_{DRx} \quad (1.5)$$

Descriptions of parameters in Eqs. (1.1)-(1.5) are given in Table 1.2.

Table 1.2 JMAK parameters and descriptions.

Q_{act} : Activation energy [kJ/mole]
a_1 : Peak strain slope
h_1 : Initial grain size sensitivity exponent
m_1 : Strain rate sensitivity exponent
Q_1 : $Q_{act} m_1$
c_1 : Peak strain intercept
a_2 : Critical strain ratio
a_5 : $\epsilon_{0.5}$ slope
h_5 : Initial grain size sensitivity exponent in $\epsilon_{0.5}$
n_5 : Strain sensitivity exponent in $\epsilon_{0.5}$
m_5 : Strain rate sensitivity exponent in $\epsilon_{0.5}$
Q_5 : $Q_{act} m_5$
c_5 : $\epsilon_{0.5}$ intercept
a_{10} : DRx constant
k_d : DRx exponent
β_d : DRx constant
a_8 : d_{DRx} slope
h_8 : Initial grain size sensitivity exponent in d_{DRx}
n_8 : Strain sensitivity exponent in d_{DRx}
m_8 : Strain rate sensitivity exponent in d_{DRx}
Q_8 : $Q_{act} m_8$
c_8 : d_{DRx} intercept

Yi et al. (Yi et al., 2008) used this model to predict the grain size of aluminum alloy AL7050 during hot forming and the constitutive model was defined by writing the strain rate as a function of flow stress and temperature at high temperatures using an Arrhenius type equation. The dynamic recrystallization is given by:

$$X_{DRx} = 1 - e^{-\left[0.693\left(\frac{\epsilon - 0.8\epsilon_p}{\epsilon_{0.5}}\right)^2\right]} \quad (1.6)$$

The strain for 50% recrystallization is given by:

$$\varepsilon_{0.5} = 1.214 \times 10^{-5} d_0^{0.13} \dot{\varepsilon}^{0.04} e^{\frac{5.335 \times 10^4}{RT}} \quad (1.7)$$

where constants are determined by means of experiments and regression analysis. Dynamic recrystallization is said to occur at a critical strain $\varepsilon_c = 0.8\varepsilon_p$ where ε_p is defined by:

$$\varepsilon_p = 4.107 \times 10^{-3} \dot{\varepsilon}^{0.06} e^{\frac{1.318 \times 10^4}{RT}} \quad (1.8)$$

The grain size after recrystallization is calculated from:

$$d_{DRx} = 78.6022 \dot{\varepsilon}^{-0.03722} e^{-\frac{1902.72}{RT}} \quad (1.9)$$

The average grain size is then calculated using the mixture law, given in Eq. (1.5).

1.3.2 Kocks-Mecking (KM)

The Kocks-Mecking (KM) model (Mecking and Kocks, 1981; Follansbee and Kocks, 1988; Kocks, 1976) relates the flow stress to the square root of dislocation density to explain the work hardening behavior. KM based models that are used in the literature for microstructure modeling. Dislocation density can be related to the shear flow stress, and additional parameters such as grain size can be included in the formulation (Banabic, 2007), allowing to a fuller microstructure modeling. According to the KM model, the shear flow stress (τ) is given in terms of the dislocation density (ρ) as:

$$\tau = \tau_0 + \alpha \mu b \sqrt{\rho} \quad (1.10)$$

where τ_0 is the lattice friction stress, μ is the elastic shear modulus, b is the amplitude of the Burgers vector and α is a constant that takes dislocation interactions into account. The dislocation density rate is written in terms of dislocation density and other state parameters empirically as:

$$\frac{\partial \rho}{\partial t} = k_1 + k_2 \sqrt{\rho} - k_3 \rho \quad (1.11)$$

where the coefficients k_i are assumed to be strain rate and temperature-dependent. This approach allows the modeling of time-dependent and independent behaviors. Following the KM approach, Sun et al. (Sun et al., 2010) developed a model that accounts for static recovery, recrystallization, and static and recrystallized grain growth rates in order to compute the microstructure evolution in TA15 titanium alloy during hot deformation using the internal-state-variable method. The microstructure evolution is determined with the use of Eqs. (1.12) through (1.16).

$$\dot{\rho} = k_1 \sqrt{\rho} \dot{\epsilon} - k_2 \dot{\epsilon}^m e^{-\frac{Q_s}{RT}} - k_3 \rho^n e^{-\frac{Q_s}{RT}} - k_4 \rho \dot{S} / (1 - S) \quad (1.12)$$

$$\dot{d} = \alpha_1 d^{-\gamma_1} - \alpha_2 \dot{S}^{\gamma_3} d^{\gamma_2} \quad (1.13)$$

$$\dot{S} = \beta_1 \gamma \rho e^{-\frac{Q_b}{RT}} / d \quad (1.14)$$

$$\rho_{cr} = \beta_2 \left(\dot{\epsilon} e^{-\frac{Q_z}{RT}} \right)^{\lambda_1} \quad (1.15)$$

$$\gamma = (0.1 + S)^q (1 - S) \rho / \rho_{cr} \quad (1.16)$$

where $\dot{\rho}$ is the dislocation density rate, \dot{S} is the recrystallized volume fraction rate, \dot{d} is the grain growth (or refinement) rate, ρ_{cr} is the critical dislocation density, and k_i , α_i , β_i , γ_i , λ_i , m , n , q , Q_s , Q_b are material constants.

1.3.3 Zener-Hollomon (ZH)

Another common approach in the literature for determining the recrystallized grain size is utilizing an Arrhenius type equation with strain-rate dependency. The Zener-Hollomon parameter combines strain rate and temperature effects and is defined as:

$$Z = \dot{\epsilon} e^{Q/RT} \quad (1.17)$$

where Q is the apparent activation energy for hot deformation. The recrystallized grain size can then be found, independently of the initial grain size, as:

$$d_{DRx} = bZ^m \quad (1.18)$$

where b and m are model constants to be determined that depend on the material and the process. Hot forming of Ti-6Al-4V titanium alloy in the temperature range of 750 – 1100°C and strain rate range of $3 \times 10^{-4} - 10 \text{ s}^{-1}$, and estimated the α and prior β grain sizes for the Ti-6Al-4V based on the Zener-Hollomon parameter as (Seshacharyulu et al., 2002):

$$g_{\alpha} = 1406.4 \times Z^{-0.139} \quad (1.19)$$

$$d_{p\beta} = 1954.3 \times Z^{-0.172} \quad (1.20)$$

where g_{α} is the α grain size (in μm) and $d_{p\beta}$ is the prior β grain size. It was stated that linear fits in the log-log scale between g_{α} - Z and $d_{p\beta}$ - Z suggest that a relationship between Z and grain sizes exists.

In another study (Rotella et al., 2013), microstructural changes in turning of AA7075-T651 aluminum alloy and grain size after recrystallization were calculated using the Zener-Hollomon parameter which was then related to the hardness of the material using the Hall-Petch equation. The Zener-Hollomon parameter can also be related to the flow stress σ as:

$$Z = A[\sinh(\alpha\sigma)]^n \quad (1.21)$$

where A , α and n are parameters that were determined. Note that this form of the ZH parameter comes from substituting the Arrhenian constitutive equation given as:

$$\dot{\epsilon} = A[\sinh(\alpha\sigma)]^n e^{-Q/RT} \quad (1.22)$$

Dynamic recrystallization occurs when the strain exceeds a critical strain value, ϵ_{cr} , which is given as:

$$\epsilon_{cr} = c \left(\frac{Z}{A} \right)^p \quad (1.23)$$

where c and p are model parameters to be obtained. A derivation of this is given in (Quan et al., 2014). The recrystallized grain size, modified to include the initial grain size (d_0) is given by:

$$d = d_0 + bZ^m \quad (1.24)$$

where b and m are two material related empirical constants.

1.3.4 Solidification Microstructure in SLM of IN625

Solidification is an important process that needs to be investigated separately, as it affects the properties of the material significantly based on nucleation and crystallization kinetics due to rapid cooling rates in SLM. Microstructure plays a critical role and will tremendously affect the components' performance and life. Therefore, it is important to know the final state of the microstructure after the SLM process concludes. A typical microstructure obtained after SLM processing is shown in Figure 1.6. Here, the melt pool boundaries are clearly visible.

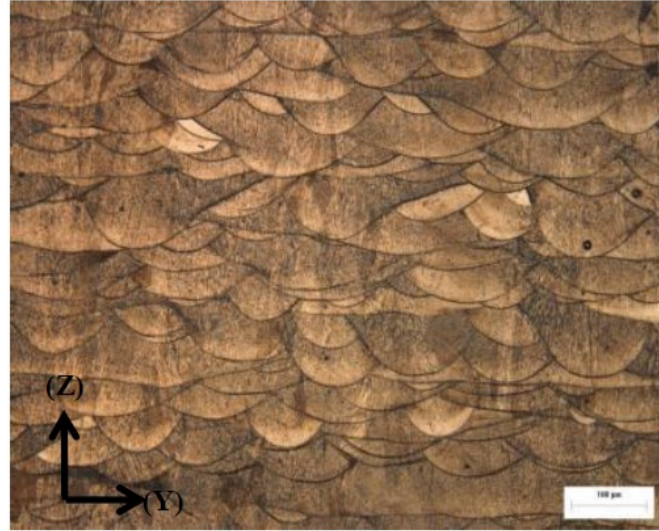


Figure 1.6 Optical image of SLM microstructure showing melt pool boundaries in the build direction (Z).

(Anam et al., 2014).

Microstructure of SLM processed IN625 is given in Figure 1.7 where dendrites are observed to grow in cells. It is seen in Figure 1.7a that the growth direction is toward (or away from) the center of the scan track. Furthermore, in Figure 1.7b, meltpools in different layers are observed with dendritic growth occurring towards the track center in the build (Z) direction. Figure 1.8 shows a 3D view of SLM produced IN100 microstructure. Columnar grains are observed in the build direction in the side views. Moreover, cellular grains are also seen in the top (XY) and side views. Cellular grains in the top view have approximately the same diameter as the width of the columnar grains, and may in fact be appearing due to cross-sectioning of the columnar grains. Li et al. (Li et al., 2015) states that boundaries of the cellular structures are primarily composed of Nb. It is further explained that during solidification, the liquid-solid interface moves at very high speeds,

impeding diffusion. Therefore, solute atoms are trapped in the resulting structure, and solute atoms such as Cr, Mo and Nb are captured by the matrix phase, which prevents phase transition. γ'' and δ phases are instead detected in heat treated samples by inference from the changes in the lattice constant of the matrix phase. Amato et al. (Amato et al., 2012) melt layer banding is observed, with dark contrasts caused by γ'' Ni_3Nb (bct) precipitates distinguishing these bands.

After an SLM process, it is desirable for the workpiece to have a microstructure that is similar to one obtained via traditional manufacturing processes and usually, heat treatments are performed on the finished parts in order to remedy this. Therefore, a microstructure model can be used to determine key characteristics of the microstructure of an SLM processed part, and allow a comparison with other methods in the literature.

The evolution of the microstructure in a process can be roughly estimated by phase fractions, grain shapes and diameters depending on the thermal-mechanical process. Computational methods such as Finite Element Method (FEM) have been successfully utilized in conjunction with theoretical models to accurately predict the resulting microstructure in various manufacturing processes. Yazdipour et al. (Yazdipour et al., 2008) also utilized Cellular Automata (CA) in conjunction with the ZH parameter to model recrystallization. Nie et al. (Nie et al., 2014) utilize a stochastic microstructure model coupled with Finite Element Method to model solidification during laser additive machining of IN718 alloy. While many applications of such models exist widely in the literature for processes like hot forming (Sun et al., 2010; Yi et al., 2008) and machining

(Özel and Arisoy, 2014; Arisoy and Özel, 2014; Arisoy and Özel, 2015) the microstructure of components fabricated using SLM processes has not been adequately studied in a computational framework with a few exceptions (Amato et al., 2012; Jia and Gu, 2014; Wang et al., 2012; Nie et al., 2014).

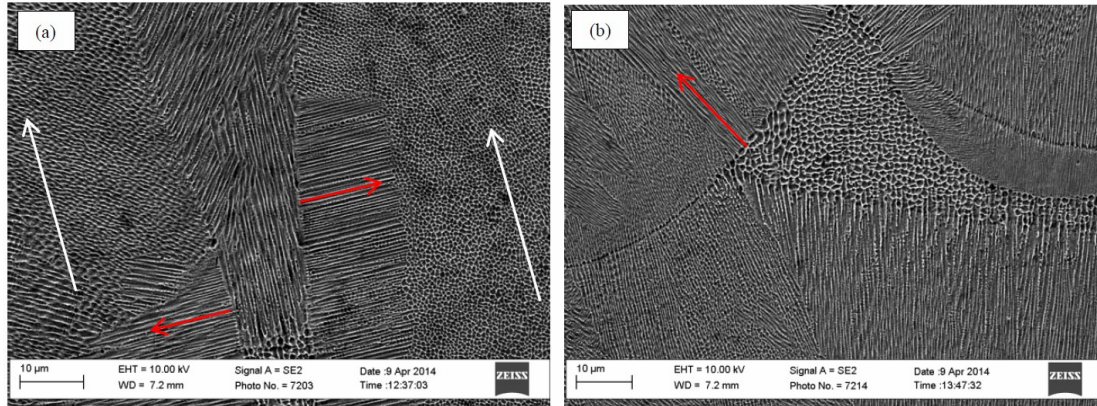


Figure 1.7 Microstructure of SLM processed IN625 Nickel alloy. (a) SEM image of horizontal (XY) section showing cellular/dendritic growth towards the center of the scan track, (b) vertical (YZ) section with dendrites growing towards the track center and in the build direction. Growth direction is marked with red arrows, and laser scan track centers are marked with white arrows.

(Anam et al., 2014).

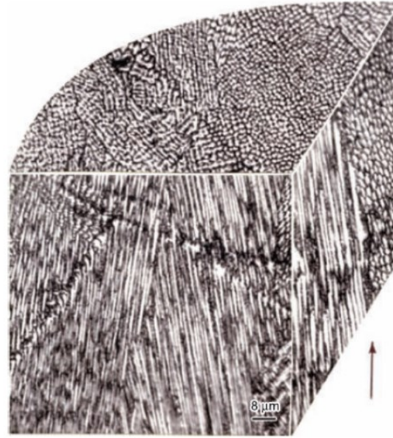


Figure 1.8 SEM 3D combined view of SLM produced IN100 microstructure. The build direction is shown by the arrow.

(Murr et al., 2012).

1.3.5 Phase Field Method

The phase field method is commonly used in computational modeling of solidification due to its ability to model complexities more efficiently than other methods used in solidification. During the solidification process, an interface is formed between different phases of the material, e.g. between the solid and liquid phases in the solidification of a pure metal. The actual location of the interface is not calculated in the phase field method, therefore it provides a massive computational advantage especially when modeling complicated interfaces where meshing is prohibitively hard in problems like dendritic solidification and spinodal decomposition. Rather than explicit tracking of sharp interfaces, diffuse interfaces are employed using continuous order parameters to represent different phases in the system. In the case of solidification of a pure substance from melt, a single order parameter p can be used such that $p=0$ where the material is liquid, and $p=1$ where it is solid. Figure 1.9 illustrates the liquid/solid interface along a line that goes through liquid and solid phases.

It is relatively common to couple additional physical phenomena into the phase field model. For instance, heat and concentration diffusion equations are usually solved in conjunction with the phase field during the evolution.

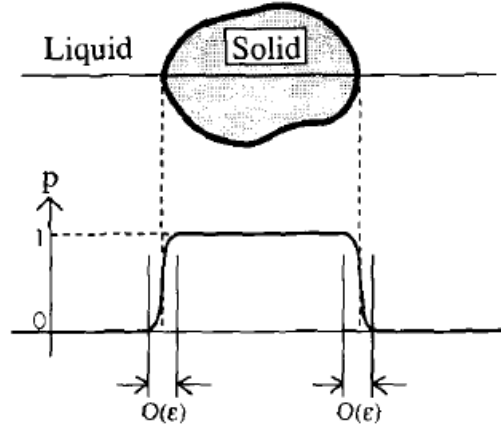


Figure 1.9 Liquid/solid interface representation using order parameter p .

(Kobayashi, 1993)

Kundin et al. (Kundin et al., 2015) investigate the phase field modeling of Inconel 718 alloy during rapid solidification in SLM processing, and compare their predictions with experimental results and theoretical predictions.

The model (and corresponding derivation) by Kobayashi (Kobayashi, 1993) is followed in the following equations. The evolution of the phase field follows the Ginzburg-Landau form given in Eq. (1.25) as the free energy functional Φ is minimized:

$$\tau \frac{\partial p}{\partial t} = - \frac{\delta \Phi}{\delta p} \quad (1.25)$$

Where p is the phase field order parameter, τ is a positive constant characterizing relaxation. Dendritic crystal growth in a single component system using a Ginzburg-Landau type free energy functional with parameter m , is defined as

$$\Phi[p; m] = \int \frac{1}{2} \varepsilon^2 |\nabla p|^2 + F(p; m) dr \quad (1.26)$$

where ε is a parameter that determines the thickness of the interface. Here, F is a double-well free energy potential and can take many forms. Kobayashi (Kobayashi, 1993) uses the following equation:

$$F(p; m) = \frac{1}{4}p^4 - \left(\frac{1}{2} - \frac{1}{3}m\right)p^3 + \left(\frac{1}{4} - \frac{1}{2}m\right)p^2 \quad (1.27)$$

with $|m| < \frac{1}{2}$ controlling the difference of chemical potentials of the two phases that can be a function of temperature. The phase field method, when coupled with a heat diffusion equation can model the growth of dendritic structures while accommodating the latent heat of fusion arising from solidification:

$$\frac{\partial T}{\partial t} = \nabla^2 T + K \frac{\partial p}{\partial t} \quad (1.28)$$

where T is a dimensionless undercooling temperature ($T = 0$ at melting temperature) and K is a dimensionless latent heat parameter. The value of K has a strong effect on the evolution of the microstructure. It is possible to introduce anisotropy by considering that ε is dependent on the direction of the outer normal vector at the interface, which is denoted as $-\nabla p$. Here, ε is a function of vector \mathbf{v} such that $\varepsilon(\lambda \mathbf{v}) = \varepsilon(\mathbf{v})$.

From Eqs. 1.25-1.27, and considering the dependency of ε on $-\nabla p$, the following equation is obtained:

$$\tau \frac{\partial p}{\partial t} = -\nabla \cdot \left(|\nabla p|^2 \varepsilon \frac{\partial \varepsilon}{\partial \mathbf{v}} \right) + \nabla \cdot (\varepsilon^2 \nabla p) + p(1-p) \left(p - \frac{1}{2} + m \right) \quad (1.29)$$

where τ is a small positive constant. The thermodynamical driving force is achieved by the term m that controls the double-well free energy potential F . Furthermore, when a 2D

space is considered, there parameter ε can be made a function of θ , an angle that is between the vector v and a specific direction. Equation 1.29 then becomes:

$$\tau \frac{\partial p}{\partial t} = -\frac{\partial}{\partial x} \left(\varepsilon \frac{\partial \varepsilon}{\partial \theta} \frac{\partial p}{\partial y} \right) + \frac{\partial}{\partial y} \left(\varepsilon \frac{\partial \varepsilon}{\partial \theta} \frac{\partial p}{\partial x} \right) + \nabla \cdot (\varepsilon^2 \nabla p) + p(1-p) \left(p - \frac{1}{2} + m \right) \quad (1.30)$$

Furthermore, the parameter m can be assumed to be a function of temperature to increase the driving force of interfacial motion with supercooling. The following form of m is assumed:

$$m(T) = \left(\frac{\alpha}{\pi} \right) \text{atan}[\gamma(T_e - T)] \quad (1.31)$$

where $0 < \alpha < 1$ to ensure $|m| < \frac{1}{2}$ for all temperature values.

The anisotropy is incorporated by assuming $\varepsilon = \bar{\varepsilon} \sigma(\theta)$ where $\bar{\varepsilon}$ is the mean interface thickness and $\sigma(\theta)$ represents anisotropy such that

$$\sigma(\theta) = 1 + \delta \cos[j(\theta - \theta_0)] \quad (1.32)$$

where δ is the strength of the anisotropy and j is the mode of the anisotropy.

The 2D phase field method is used in conjunction with a 3D Finite Element Method based heat equation solver in Chapter 7 to model the microstructure of the IN625 nickel alloy during the Selective Laser Melting process.

1.4 Computational Modeling

While analytical solutions exist for Ordinary Differential Equations (ODE) and Partial Differential Equations (PDE) for simple geometries, it is extremely hard to apply them over complicated problem geometries. However, computational methods such as Finite Volume Method (FVM) and Finite Element Method (FEM) can be utilized to solve these complicated problems with good accuracy when sufficient computational power is employed.

Finite Volume Method is commonly used in the field of fluid mechanics, for solving the Navier-Stokes equations in Eulerian reference frame. The Finite Element Method on the other hand is widely used for solid mechanics, heat transfer in Lagrangian or Arbitrary Lagrangian-Eulerian (ALE) reference frames, however applications of FEM on fluid mechanics and electromagnetic fields are also very common.

Apart from Finite Element Method, machine learning methods can also be a useful tool in modeling microstructure. Particularly, regression models can find relationships between process parameters and outcomes, using available data. Optimization is another tool in computational modeling that can be applied to both FEM and machine learning. For instance, experimental data can be used to optimize the microstructure model parameters for a better representation.

1.4.1 Finite Element Method

Many applications of FEM exist, such as solid mechanics, fluid mechanics (Navier-Stokes equations), heat transfer and electromagnetic fields (Maxwell's equations). The main advantage of FEM over other methods is that it is highly modular and customizable thanks to different types of elements being used. In addition, it allows complex geometries without having to change the formulation. The accuracy of the solution is affected by how well the discretization is done, however, achieving a high accuracy through mesh convergence studies is a common challenge to the current practice. The number of elements used in an FEM simulation model affects the computational cost but it does not change the problem formulation. This allows easy scalability, and robustness.

At the heart of the FEM lies the discretization of the problem geometry into small elements, via the Mean Weighted Residuals (MWR) method. MWR method is an approximation method for solving differential equations over various domains, and it employs test functions to approximate the field. Galerkin method limits these test functions to be the same as the shape functions of elements in the Finite Element formulation, therefore FEM is often considered to be a special case of the Galerkin method. The elements have properties of their own, and represent the differential equation that is being solved in the local domain. For instance, a heat transfer element may have a conductance and a capacity matrix to represent the convection-diffusion equation, whereas a solid mechanics element may have a stiffness matrix that represents the constitutive equation, a mass matrix, and a dampening matrix for dynamic problems. Each element has a certain number of degrees of freedom, which represent the solution of the problem, such as temperature or displacement.

All of these elements come together to form the geometry, and by assembling the matrices of the elements into global matrices, the problem can be solved over the original domain. Matrix and vector calculus is used extensively in FEM in order to improve the performance, and through clever use of parallelization and high performance clusters, highly complex problems can be solved over large, intricate geometries in a reasonable amount of time.

Many commercially available software exist for solving different types of problems. For large plastic deformation processes such as forging and machining processes, Deform-3D software developed by Scientific Forming Technologies Corporation (SFTC) is a highly customizable and comprehensive software package, and is utilized in this study extensively.

1.4.2 Machine Learning

Machine Learning is an emerging field in statistics and computer science that utilizes complex relationships in large sets of data that would otherwise be impossible to recognize intuitively. Machine learning algorithms inspect, extract and use the relationships and patterns that exist within the given dataset, which is very convenient for the user. Given a set of data that includes inputs $x_{i,j}$ and outputs y_j , a function f can be inferred that defines the relationship between them such that $f(x_{i,j}) = y_j$. Here, i represents different features and j represents different observations or samples. Since y_j 's are known from the dataset, i.e. the data is "labeled", an error can be calculated to evaluate the performance of the model for each observation. This act of inference from labeled data is called supervised learning. Regression falls under the supervised learning category, where after a model is

trained the function f is used to estimate the value of the output $y_{k,k \neq j}$ for new observations $x_{i,k,k \neq j}$. Regression is often used for making predictions, such as forecasting. Another supervised learning method is classification. In classification, each observation x belongs to a class y , and the goal is to determine the classes of incoming observations based on the previous data. Unsupervised learning, such as clustering, deals with data that have no prior labeling, in other words, where y_j 's do not exist.

In unsupervised learning, the user must make certain assumptions to proceed. For instance, in clustering, the data set $x_{i,j}$ is separated into clusters, i.e. groups that contain the observations that are similar to each other. The user often needs to decide the number of clusters that the data will be divided into. Moreover, the data can be clustered using different measures and approaches. Since an error cannot be calculated, there is often no best solution and it becomes the user's responsibility to "supervise" the method.

Various machine learning algorithms exist, and their performance depends on the application, available data and calibration. Among them, Neural Networks (NN), Support Vector Machines (SVM) and Random Forests (RF) are some of the most popular ones for classification and regression. Random Forests (RF) method proposed by Breiman (Breiman, 2001) is used in this research.

RF is an adaptive nearest neighbor algorithm that can be used for classification and regression and it can easily capture nonlinear relationships between an input data set and a target data set. Essentially, it works by dividing the data into regions based on features. As

the name suggests, Random Forests algorithm employs multiple decision (regression) trees to find the relationship between the input and target data. Decision trees work by recursively partitioning the data. Starting from the root node that contains the whole dataset, a tree is grown by generating two branches. For regression, the partitioning is done to minimize the residual sum of squared errors (RSS) over all splitting variables α (input parameters and predictor types) and split points β as shown in Eq. (1.33):

$$RSS = \left[\sum_{i=1}^{N_L} (y_i - \bar{y}_L)^2 + \sum_{i=1}^{N_R} (y_i - \bar{y}_R)^2 \right] \quad (1.33)$$

where L and R denote the first (left) and second (right) regions, N_L and N_R are the number of points in L and R , y_i are the response variables, and \bar{y}_L and \bar{y}_R are the mean values at the left and right nodes, respectively. For classification, the Gini criterion, which is a measure of the frequency of incorrectly labeled points is minimized:

$$Gini = N_L \sum_{i=1}^{N_L} p_{iL}(1 - p_{iL}) + N_R \sum_{i=1}^{N_R} p_{iR}(1 - p_{iR}) \quad (1.34)$$

where p_{iL} and p_{iR} are the proportion of class i in the left and right nodes, respectively.

The splitting process continues at each new node until certain criteria are met; such as meeting a minimum error improvement δ for a split, or setting a minimum number of data points in each branch. When a node cannot be split anymore, it is called a leaf node or a terminal node. Usually, trees are grown until a minimum number of leaves exists. However, overfitting becomes an issue when the trees are grown excessively, yielding a smaller bias. When overfitting occurs, small changes in the training data yield a high variance in the result due to the number of degrees of freedom created in the tree. This can be prevented

by pruning the trees, which in turn reduces the model's ability to capture complicated relationships in the data. However, pruning is generally not used in Random Forests.

Regression trees require a careful selection of data and model. Bootstrap aggregating, or bagging, is a data selection method effective for preventing overfitting and reducing variance, and is a critical component of the Random Forests algorithm. It is performed by randomly sampling and using a different subset of data each for each tree. The number of trees, n_{tree} , is a parameter in the RF algorithm that can affect the computational performance, however, in terms of robustness, similar results can be obtained over a wide range of n_{tree} . Yet another parameter in the RF algorithm is m_{try} , which limits the number of features (m) being used at each branching operation and is typically chosen to be between the square root of number of features (\sqrt{m}) and number of features divided by 3 ($m/3$).

1.4.3 Optimization

Optimization is an important step in design, realization and service phases of a products lifecycle. Various types of optimization exist in different fields, such as in Operations Research, combinatorial optimization techniques are widely used for transportation problems, whereas shape and topology optimization is used in the design of components and systems, such as wings and engines in the aerospace industry.

Industrial applications often require multiple yet often conflicting objectives to be optimized. The process of minimizing or maximizing multiple objective functions

simultaneously is called multi-objective optimization. In most cases of multi-objective optimization, the objectives are in conflict, meaning that the best solution for one may not be the best solution for the other. In this case, a set of candidate designs appears that cannot be improved in the direction of all objectives simultaneously. This set of best candidate designs is called the Pareto set, and the user often faces the question of choosing the best candidate among the Pareto set by considering trade-offs.

Furthermore, the optimization problem can be multi-modal, meaning that multiple good solutions exist, locally or globally. Classical optimization methods, especially a-priori gradient based methods or a-posteriori methods such as bisection or Simplex method perform poorly in multi-modal problems, since they tend to get stuck at one solution only (often at a local minimum or maximum), based on the starting point. Meta-heuristic methods such as evolutionary computational programming such as Genetic Algorithms (Mitchell, 1996; Deb, 2001) or Particle Swarm Optimization (Eberhart and Kennedy, 1995) are good at capturing most of the multiple solutions in a multi-modal problem, and therefore are more resistant to local optima. Moreover, when an analytical or explicit representation of the problem does not exist, it becomes a challenging task to use classical methods. Furthermore, evolutionary computational methods also perform very well when the solution space is large.

Genetic Algorithm (GA) is an evolutionary programming method that mimics the evolution and natural selection process seen in the nature. Starting with an initial population, the individuals of this population mate and evolve towards the optimum solution. Each

individual in the population has a chromosome that represents the current values of the decision variables for that individual. The next generation of individuals containing the offspring is evolved from the current generation, the parents. The algorithm relies on three main operations: Selection, Crossover and Mutation. A child (offspring) must be the product of either crossover, or mutation.

At this point, it is important to note that it is often necessary to impose certain constraints on the problem to limit the solution space, to eliminate unrealistic designs. These constraints are either equality or inequality constraints, and are applied to the decision variables. Solutions that do not satisfy the constraint are called infeasible. In both crossover and mutation operations, the feasibility of the offspring must be satisfied.

During the selection phase, the fitness value of each individual in the current generation is evaluated, using the objective function. The fitness value of an individual represents how close to the solution that individual is. A set of individuals is selected to become parents of the next generation, based on their fitness values. There are various methods for the selection process, such as fitness proportionate selection, truncation selection and tournament selection. In fitness proportionate selection, individuals are selected randomly with replication from the current population with probabilities proportional to the normalized fitness values, as shown in Figure 1.10. Truncation selection selects the best individuals that form an arbitrary upper percentage, and tournament selection selects the individuals with the best fitness values from randomly selected subgroups of individuals.

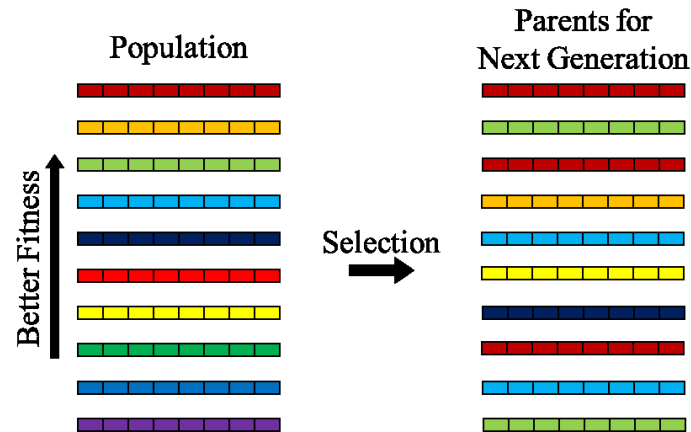


Figure 1.10 Selection operation.

The next step after selection operation is the crossover operation. In this phase, the chromosomes of two parents that are randomly selected from the result set of the selection operation are combined to create two offspring for the next generation. The operation can be performed in various ways, the simplest one being one point crossover where a crossover point is selected after which the chromosomes of two parents are swapped with each other, producing two offspring as shown in Figure 1.11. Alternatively, one parent's genes at certain locations can be selected randomly to be exchanged with another parent. Other methods for crossover exist, such as multi-point crossover and uniform crossover.

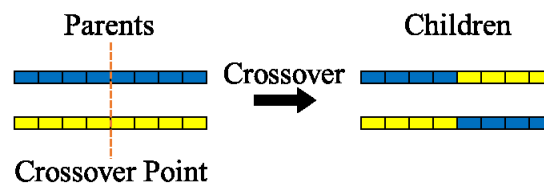


Figure 1.11 One point crossover operation.

The third basic operation in GA is mutation. Mutation is a process where one or more genes (decision variables) in the chromosome are changed to a different value as shown in Figure 1.12. The final value must be within the feasible region of the decision variable, and a distribution such as uniform or Gaussian can be used to assign the value. In some cases, the value is set to the lower or upper boundary of the variable. Mutation allows the population to maintain a genetic diversity, and is crucial for preventing the population from getting stuck in local optima.



Figure 1.12 Mutation operation.

Elitism is another selection method that supplements other operations and allows certain individuals from one generation to survive to the next generation without being altered, as shown in Figure 1.13. It can also be considered as a special case of mutation, with no mutation being applied.



Figure 1.13 Elitism.

The algorithm stops when the change in the best solution between the last two generations becomes smaller than a tolerance value, or when a certain number of generations is reached, whichever happens first. The performance and accuracy of the algorithm depends on the population size, and generation limit.

Genetic algorithms and evolutionary computation have been used in optimization problems in materials and manufacturing processes successfully ranging from carbon nanotubes to the process optimization (Ulutan and Özel, 2013c; Chakraborti et al., 2007; Chakraborti, 2013). Recently, a review was provided on the soft computing techniques used in designing metal alloys based on composition-process-microstructure-property relations (Datta and Chattopadhyay, 2013) and a critical assessment of this field was given in (Chakraborti, 2014).

1.5 Motivation

It is widely discussed in the literature and industry that different manufacturing processes and process settings result in different surface quality and microstructures affecting the fatigue life of the end product. The motivation of this dissertation is to improve the surface integrity of the manufactured parts by identifying the phenomena that result in microstructural alterations and utilizing physics-based process simulations and various computational methods for process optimization purposes. Through this methodology, certain predictions can be made and process parameters can be optimized, ultimately leading to better performance of products in their service life.

1.6 Objectives

The objectives of this study can be summarized as; a) obtaining physics based theoretical models for process simulations and generating experimental data that validates these process simulation models and using them to make viable predictions, b) developing comprehensive computational 3D machining models for studying microstructural changes and c) designing and conducting controlled experiments to quantify microstructural changes occurring during conventional machining processes such as face turning and advanced manufacturing processes such as Selective Laser Melting in processing Titanium and Nickel based alloyed end products.

1.7 Organization of the Thesis

Firstly, experimental work is presented in Chapter 2 including machining experiments and measurement of microhardness, grain sizes and phase fractions on the machined subsurfaces. In Chapter 3, physics based computational models using Finite Element Method are developed with microstructure calculations, and process simulations and relevant results are shown. In Chapter 4, machine learning methods are used in making predictions of hardness, and grain sizes. In Chapter 5, multi-objective machining parameter optimization is performed to minimize the grain size changes, minimize machining temperature and maximize productivity using experimental measurements and Finite Element simulations. Furthermore, JMAK model parameters for the IN100 alloy are identified using optimization. In Chapter 6, experimental work for Selective Laser Melting of IN625 is presented, where grain sizes, growth directions and spattering are measured using image processing. In Chapter 7, the SLM process is investigated computationally via 3-D Finite Element simulations, and a basic phase field model is implemented to compare the relative effects of processing parameters on solidification.

CHAPTER 2: EXPERIMENTAL WORK ON MACHINING OF Ti-6Al-4V AND IN100 ALLOYS

2.1 Introduction

In order to understand the effects of machining on surface integrity of Ti-6Al-4V and IN100 alloys, a series of experiments were conducted. For this purpose, the experimental work includes designing experimental conditions, running the controlled experiments, inspection surfaces generated, hardness testing, polishing and etching surfaces for obtaining Scanning Electron Microscopy imaging and image analysis.

Face turning and cut-off machining operations were utilized to create disk shaped specimens from the bulk material. Each specimen consists of tracks that are machined with different cutting tool, cutting speed, or feed, in order to represent a wider range of machining processing conditions and explore the effects of machining on process induced surface integrity and microstructure. Thermomechanical processing often causes visible alterations in the microstructure of polycrystalline materials. These microstructural alterations may reflect themselves in certain material properties such as surface hardness. Hardness is an important property in machining of metal alloys, as it plays a direct role in the quality and performance of the part, as well as the performance and lifetime of the tool that is being used. For this reason, hardness measurements were taken from the processed surfaces of the specimens. After hardness measurements were taken, surfaces were etched and inspected with Scanning Electron Microscopy (SEM). SEM is a useful tool for obtaining high resolution images of a surface in a very small scale, in the order of

nanometers to microns which reveals the microstructure of the material. Grain and precipitate formations were analyzed via a proprietary image processing algorithm written in MATLAB. The results of these analyses are shown in this chapter, along with further details and analysis on the experiments.

2.2 Machining (Material Removal) Experiments

Machining experiments in face turning configuration were made to investigate the effects of different machining and tool parameters on the microstructure of Ti-6Al-4V and IN100 alloys using the cylindrical workpieces and TPG432 type insert geometry (insert nose radius of $r_\epsilon = 0.8$ mm and relief angle of $\alpha = 11^\circ$).

In the face turning of Ti-6Al-4V cylindrical workpiece, a constant depth of cut ($a_p = 2$ mm), two cutting speed levels ($v_c = 55$ and 90 m/min) and two feed levels ($f = 0.05$ and 0.1 mm) were used under dry cutting conditions. In these experiments, uncoated cutting inserts made of tungsten carbide in cobalt binder (WC/Co) with up-sharp (edge radius of $r_\beta = 5 \pm 0.5 \mu\text{m}$ as measured) and TiAlN coated ($r_\beta = 10 \pm 0.7 \mu\text{m}$ as measured) inserts and edge prepared inserts with abrasive brushing for $r_\beta = 25 \pm 1.0 \mu\text{m}$ (WC25) and $r_\beta = 10 \pm 0.7 \mu\text{m}$ (WC10) were used. These inserts were installed onto a tool holder (CTFPR-164C type). As a result, the inserts were oriented to have lead and side rake angles of 0° and a back rake angle of -5° during face turning. On each face of the disks, three tracks have been machined using high speed cutting condition first and low speed cutting conditions the last along the feed direction. After each set of face turning, a section (approximately 3 mm thickness) of the cylindrical workpiece was cut off gently, for use in hardness testing.

Effects of face turning with different machining and tool parameters on the microstructure of Inconel IN100 were also investigated using a cylindrical workpiece. Figure 2.1 shows the experimental setup, and parameter definitions where a_p is the depth of cut, F_c , F_f , and F_p are the cutting, feed, and thrust forces, and r_β is the cutting edge radius of the tool. IN100

alloy disks used in the experiments are manufactured via powder metallurgy route with a chemical composition of 18.3% Co, 12.3% Cr, 4.9% Al, 4.3% Ti, 3.3% Mo, 0.7% V, 0.1% Fe, 0.06% C, 0.02% B, 0.02% Zr and Ni balance. After face turning, approximately 3-5 mm thick disks from the machined section were cut off at least 5 mm away from the surface of the disk and the new surface was cleaned with very gentle machining. A constant depth of cut ($a_p=1$ mm), two cutting speed levels ($v_c=12$ and 24 m/min) and a constant feed ($f=0.05$ mm/rev) were used under dry cutting conditions. In these experiments, uncoated cutting inserts made of tungsten carbide in cobalt binder (WC/Co) with up-sharp (edge radius of $r_\beta=5\pm0.5\mu\text{m}$ as measured) and edge prepared with abrasive brushing for $r_\beta=25\pm1.0\mu\text{m}$ (WC25) and $r_\beta=10\pm0.7\mu\text{m}$ (WC10), and TiAlN coated inserts ($r_\beta=10\pm0.7\mu\text{m}$ as measured) have been used.

After each machining test and the cutoff operation, the remaining cylindrical workpiece was heat treated in a furnace for annealing and stress relieving. Both Ti-6Al-4V alloy and IN100 alloy cylindrical billets have undergone this operation.

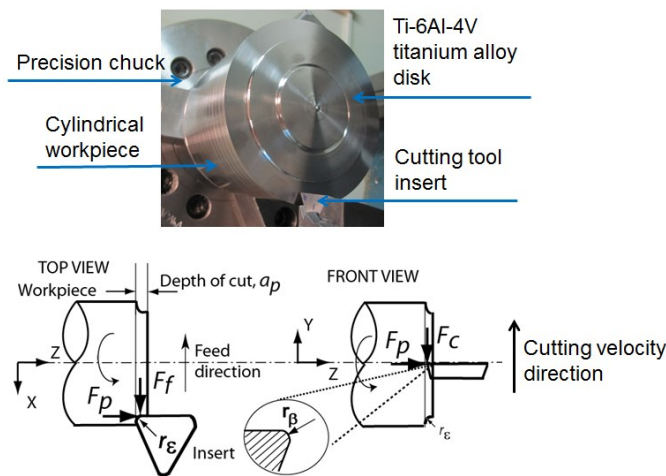


Figure 2.1 Experimental configuration used in face turning of Ti-6Al-4V disks.

2.3 Microhardness Measurements

2.3.1 Microhardness measurements for Ti-6Al-4V alloy

Prior to each machining test, hardness measurements were taken from the untouched back surface of the cylindrical billet after each annealing process using a Rockwell type tester in the HR15N scale (15N or 1.53 kg) and then converted to Vickers Hardness (HV). The mean and standard deviation of hardness of annealed Ti-6Al-4V specimens are reported as 335.7 HV and 13.5 HV respectively. In order to quantify the effects of different cutting conditions and tools on the microstructure, microhardness measurements were taken at different locations by collecting 30 or more data points on the machined tracks of the disks. Their mean and standard deviations are calculated. The varying machining conditions (v_c & f) and tool parameters (r_β & coating) along with the hardness measurements taken on Ti-6Al-4V disk tracks are summarized in Table 2.1. A large experimental scatter is observed.

The effects of machining conditions and tool parameters on hardness of Ti-6Al-4V titanium alloy disk samples are shown in Figure 2.2 and Figure 2.3, for $v_c=55$ m/min and $v_c=90$ m/min, respectively. These figures are commonly known as box-and-whisker plots have whiskers (lines extending vertically from the boxes) indicating variability outside the upper and lower quartiles. It should be noted that outliers are plotted as individual points.

Table 2.1 Microhardness measurements on the machined surfaces for Ti-6Al-4V.

Disk Sample	a_p [mm]	Tool type	r_β [μm]	v_c [m/min]	f [mm/rev]	Mean HV	SD HV
Ti-6Al-4V	2	WC/Co (TiAlN)	10	55	0.05	324.26	9.30
					0.1	324.84	13.01
				90	0.05	313.72	10.09
					0.1	319.20	9.11
		WC/Co	25	55	0.05	327.72	14.90
					0.1	326.51	6.95
				90	0.05	325.03	5.67
					0.1	319.04	9.45
		WC/Co	10	55	0.05	303.76	20.57
					0.1	314.17	12.66
				90	0.05	314.62	8.91
					0.1	311.72	18.09
		WC/Co	5	55	0.05	315.96	14.34
					0.1	324.65	9.46
				90	0.05	321.45	8.39
					0.1	331.78	11.61

In general, it was observed that higher feed rates yield harder surfaces, while faster cutting speeds tend to yield softer surfaces. The dashed line (green) indicates mean annealed hardness of Ti-6Al-4V. Machined surfaces are found to be softer than the annealed surface at room temperature, indicating microstructural changes. As the cutting speed and feed rate are altered, effects of dynamic recrystallization and grain growth can cause such changes in surface hardness. It was observed that machining of Ti-6Al-4V titanium alloy using uncoated WC/Co tool with $r_\beta=5\ \mu\text{m}$ (sharp edge) provided the hardest surface in almost all cutting conditions.

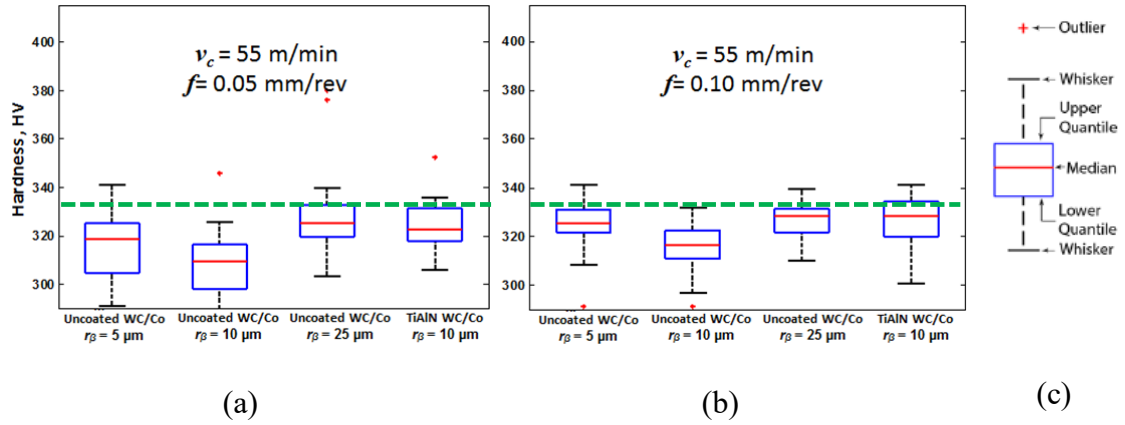


Figure 2.2 Effects of cutting tool edge radius and coating on measured microhardness of the machined surfaces ($v_c=55 \text{ m/min}$). Comparison boxplots indicate the upper and lower quartiles and variability of the measured hardness.

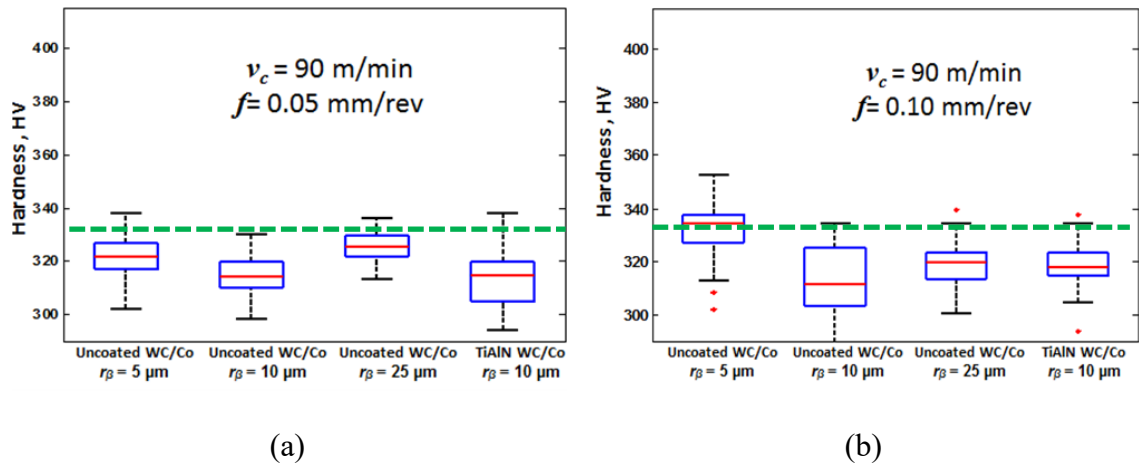


Figure 2.3 Effects of cutting tool edge radius and coating on measured microhardness of the machined surfaces ($v_c=90 \text{ m/min}$). Comparison boxplots indicate the upper and lower quartiles and variability of the measured hardness.

2.3.2 Microhardness measurements for IN100 alloy

In order to quantify the effects of different cutting conditions and tools, hardness measurements were taken on the machined tracks of the disks using a Rockwell-type tester. The measurements were then converted to Vickers Hardness (HV). Different machining conditions (v_c only) and tool parameters (r_β and coating) along with the hardness measurements taken on IN100 nickel-base alloy disk tracks are summarized in Table 2.2. The effects of tool edge radius on hardness indicate that largest edge radius tool generated higher mean surface hardness. However, a clear distinction cannot be made due to the relatively close measurement uncertainties.

Table 2.2 Hardness measurement results for IN100 nickel alloy.

Tool type	r_β [μm]	v_c [m/min]	Mean HV	SD HV
WC/Co	5	12	380.53	5.75
		24	381.3	22.33
	10	12	386.39	7.07
		24	375.77	13.26
	25	12	389.57	6.02
		24	394.49	5.83
WC/Co (TiAlN)	10	12	382.73	9.18
		24	382.51	6.55

Figure 2.4 shows the effects of cutting speed and tool geometry on the measured hardness. The results indicate that in general, increasing cutting speed decreased the hardness but increased hardness variations along the tracks. Dynamic recrystallization caused by different strain rates may be responsible for the increased or decreased hardness. A clear difference between the tools and the effect of cutting speed is also not very clear across the

tools due to experimental spread. It is seen that the largest edge radius tool generated a high surface hardness in IN100 samples, which supports the results shown in Ranganath et al. (Ranganath et al., 2009).

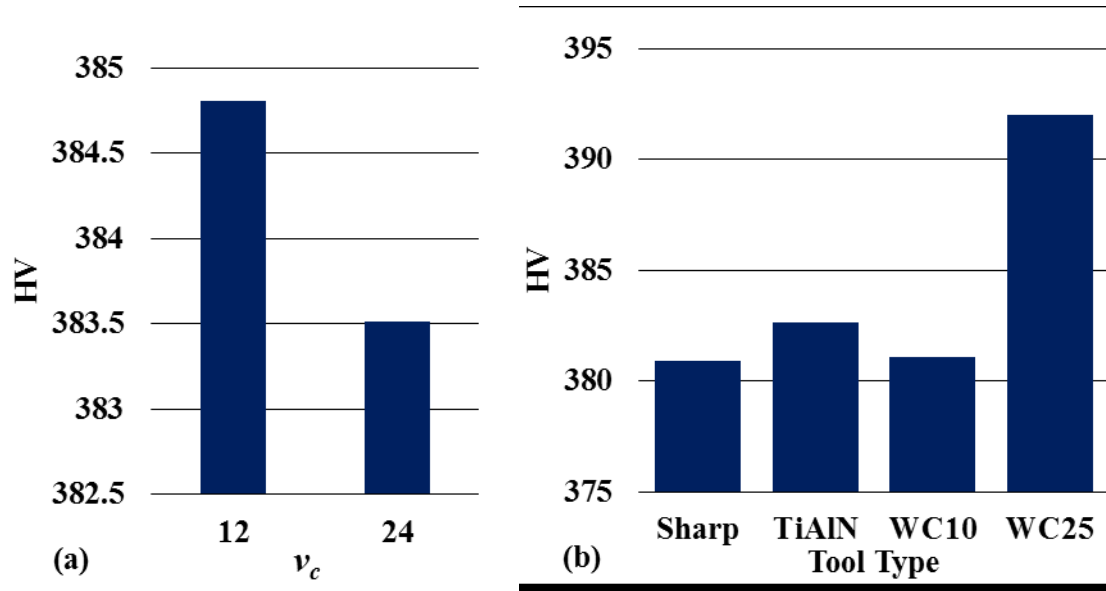


Figure 2.4 Effects of cutting speed (a) and tool type (b) on the microhardness of the machined surface.

Furthermore, a detailed microhardness study on the machined IN100 disks has been conducted by Atilim University as seen in Arisoy et al. (Arisoy et al., 2015). In order to take hardness measurements at various depths, surface layers were removed with Struers LectorPol-5 electro-polishing machine. Struers A2 electrolyte with 20V voltage was used and the process took between 20s and 330s for different specimens and depths. The depth was confirmed with readings from a dial gauge. Microhardness measurements were taken on the machined surfaces in Vickers Hardness (HV) 19.61N scale into the depth with Zwick / Roell ZHV 10 microhardness tester with a testing speed of 25 mm/min. At each

depth level, five microhardness measurements were made for replication. Results of this study are shown in Table 2.3 and Figure 2.5. Overall, a depth of severe plastic deformation (SPD) about 10-25 μm has been observed from microhardness profiles which is clearly seen in Figure 2.5a. Measurements show an increase in the hardness values immediately below the surface followed by softening towards the core of the sample. Increasing the tool edge radius tends to yield hardening at both cutting speeds. Increasing cutting speed decreases the hardness but increases hardness variations indicating possible microstructural changes due to dynamic recrystallization. Among the cutting conditions used for IN100 alloy, it is observed that uncoated WC/Co tool with $r_\beta=25\ \mu\text{m}$ produced abusively severe deformation field and hardest subsurface which should be avoided in industrial applications. Furthermore, TiAlN coated tool provides the lowest hardness profile into the depth of the alloy material.

Table 2.3 Vickers hardness profiles (mean and standard deviation) of machined IN100 for different cutting speeds and tool geometries.

v_c [m/min]	Tool Type	Measurement Depth [μm]					
		0	10	25	50	80	120
12	WC/Co $r_\beta=5\ \mu\text{m}$	439.0 \pm 1.6	445.3 \pm 4.8	424.0 \pm 18.7	397.0 \pm 7.1	396.7 \pm 3.9	390.7 \pm 4.8
	WC/Co $r_\beta=10\ \mu\text{m}$	436.0 \pm 21.6	453.0 \pm 12.1	431.3 \pm 11.2	413.3 \pm 8.7	404.7 \pm 12.4	398.0 \pm 1.6
	WC/Co $r_\beta=25\ \mu\text{m}$	452.0 \pm 4.3	448.0 \pm 1.6	437.0 \pm 4.9	427.0 \pm 8.6	423.7 \pm 2.5	401.3 \pm 6.0
	TiAlN $r_\beta=10\ \mu\text{m}$	430.3 \pm 12.7	434.0 \pm 9.4	434.0 \pm 11.6	409.7 \pm 2.5	393.0 \pm 4.2	402.0 \pm 4.3
24	WC/Co $r_\beta=5\ \mu\text{m}$	451.0 \pm 12.4	444.2 \pm 8.9	426.2 \pm 5.5	402.3 \pm 4.6	396.5 \pm 9.2	399.0 \pm 4.2
	WC/Co $r_\beta=10\ \mu\text{m}$	452.5 \pm 10.6	439.8 \pm 11.0	424.2 \pm 6.2	404.6 \pm 6.4	396.8 \pm 5.9	392.1 \pm 5.8
	WC/Co $r_\beta=25\ \mu\text{m}$	460.7 \pm 17.2	439.3 \pm 5.9	441.5 \pm 10.2	416.1 \pm 8.1	398.4 \pm 6.2	395.8 \pm 4.2
	TiAlN $r_\beta=10\ \mu\text{m}$	440.9 \pm 4.3	419.7 \pm 7.1	413.7 \pm 12.7	400.5 \pm 4.3	384.0 \pm 3.7	389.4 \pm 6.9

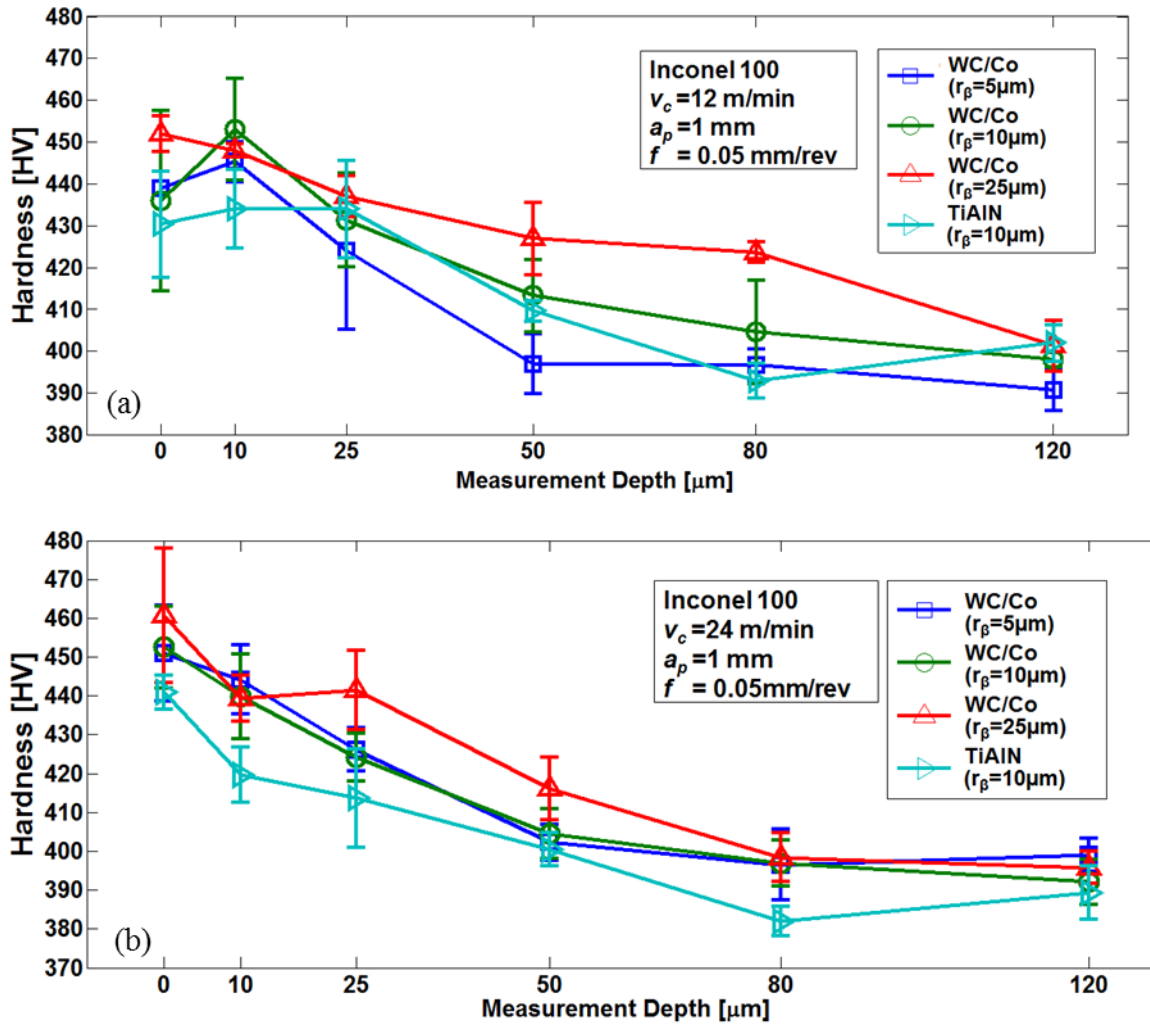


Figure 2.5 Microhardness profiles of machined IN100 subsurface into depth for different cutting speeds and tool geometries. (a) $v_c = 12$ m/min, (b) $v_c = 24$ m/min.

2.4 Grain Size Measurements

2.4.1 Specimen preparation

After the machining operations and hardness tests, Ti-6Al-4V and IN100 disks were prepared in order to perform grain size measurements. First, a sector was cut out from each disk using a band saw at low speed and low feed with plenty of lubricant to prevent overheating that might result in a change in microstructure. A total of eight specimens were obtained, four from Ti-6Al-4V and four from IN100 disks. In the second step, the edges were deburred using mild grinding and a file. In the third step, the specimens were sanded with SiC sand paper by hand, rotating the specimen 45 and 90 degrees while sanding. Multiple stages of sanding was performed on the machined surfaces, with increasing grit up to 1200. In the fourth step, the specimens were polished in multiple stages using diamond compounds with 3 μm and 1 μm particle size using a napless cloth. The specimens were then cleaned using compressed air blasts and with soap and water in an ultrasound bed at low heat between each of the steps. Figure 2.6 shows the IN100 specimens after they were cut out from the disks.



Figure 2.6 IN100 specimens before preparation for grain size measurements.

After the polishing operation, the Ti-6Al-4V specimens were prepared for microstructure analysis. In order to reveal the grains, the specimens were etched using Kroll's reagent, prepared by mixing 2 ml HF, 6 ml HNO₃ and 92 ml distilled water. The mixture was poured on the specimens in droplets, which were allowed to stay for several seconds, after which the specimens were washed with distilled water to stop the reaction.

Similarly, IN100 specimens were etched using 3 ml HF, 5ml HNO₃ and 100 ml H₂O. The IN100 specimens were found to be very resistant hence the etching process was allowed to continue for a longer period of time.

2.4.2 Grain size measurements for Ti-6Al-4V alloy

Grain diameters were determined from the SEM images via a proprietary image processing code written in MATLAB. Figure 2.7 shows a representative SEM image that was processed for the Ti-6Al-4V machining case of TiAlN coated tool, $v_c=90$ m/min, $f=0.05$ mm/rev. Grains were marked individually (see Figure 2.7a) and image processing code was utilized in calculating their volumes and finding corresponding grain diameters as shown in Figure 2.7b. The histogram in Figure 2.7c depicts the frequency of grain sizes within the SEM image evaluated.

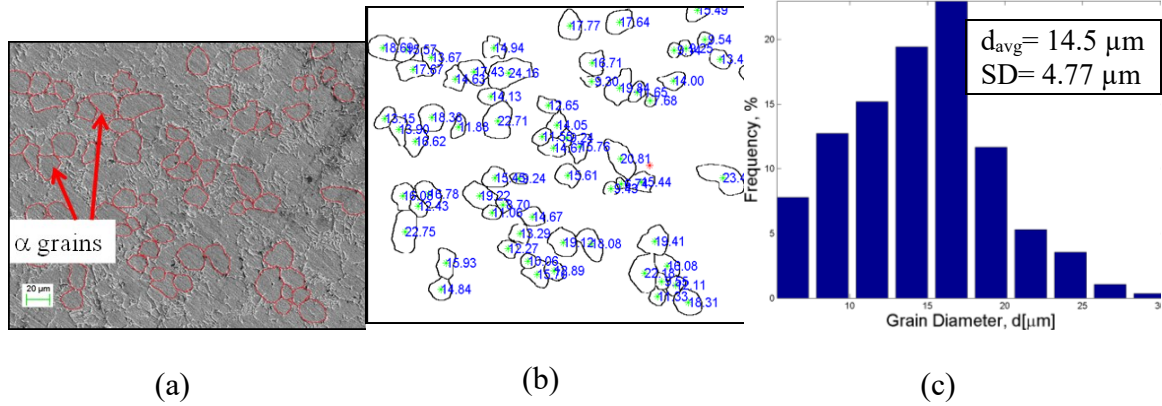


Figure 2.7 (a) Microstructure of machined subsurface, (b) image processing for grain size calculations, and (c) histogram (TiAlN coated WC/Co tool, $v_c=90$ m/min, $f=0.05$ mm/rev).

Several specimens that were obtained from Ti-6Al-4V cylindrical workpiece have been used in analyzing the as-received microstructure. Figure 2.8 shows of these SEM images and grain size distribution. The average grain diameter was found between 15.84 μm and 13.65 μm at the different locations of the cylindrical billet. These observed average grain size values are below the 20 μm that has been commonly reported in the literature, such as in the paper by Nalla et al. (Nalla et al., 2003). This could be related to the fact that the microstructure of these surfaces of the cylindrical billet had been affected by preceding processing. Results of the measurements for all cutting conditions are summarized in Table 2.4.

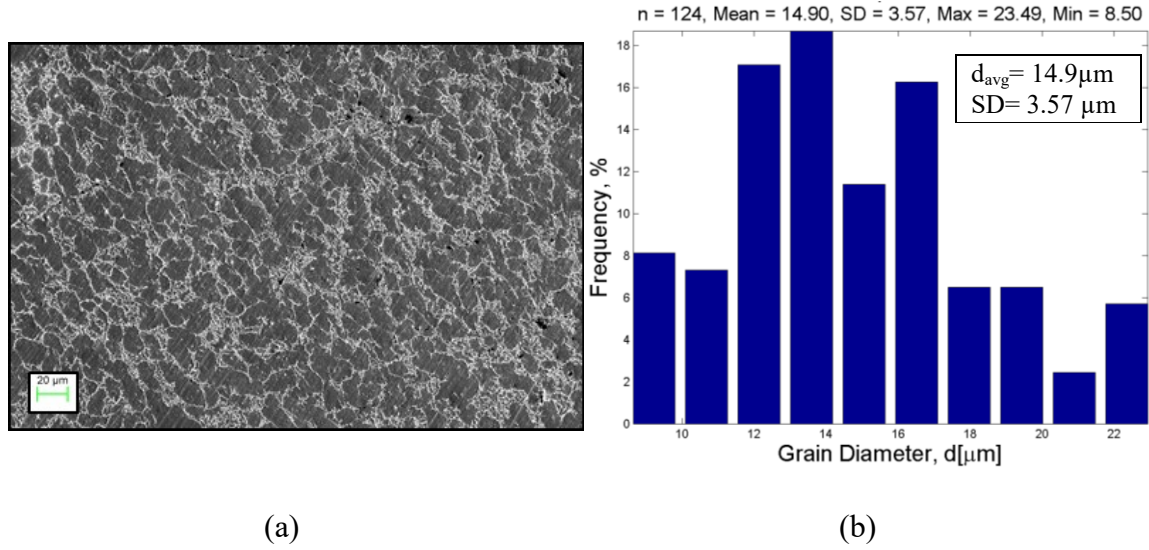


Figure 2.8 SEM image (a) and grain size distribution (b) taken from unmachined surfaces.

Figure 2.9 shows the processed SEM images and grain size distributions the Ti-6Al-4V machining case of TiAlN coated tool, with cutting speeds $v_c=55$ m/min and 90 m/min, and feed rates $f=0.05$ mm/rev and $f=0.10$ mm/rev. Measurements show no significant effect of cutting speed at low feeds ($f=0.05$ mm/rev), but an increase of $2.18 \mu m$ in average diameter is observed when the speed is increased at the high feed cutting condition ($f=0.10$ mm/rev) which can be related to a recovery process. Figures 2.10-2.12 give the results of the same analysis for WC/Co tool ($r_\beta=25 \mu m$), WC/Co tool ($r_\beta=25 \mu m$), and WC/Co tool ($r_\beta=5 \mu m$) respectively. A large variation in grain sizes is observed in some cases. Small grains (less than $\sim 8 \mu m$) observed in these figures indicate recrystallization, as they did not appear in Figure 2.8. Similarly, grains with diameters greater than $\sim 25 \mu m$ can be considered as a product of grain growth. Furthermore, grains as large as $34.3 \mu m$ are observed in the machined tracks, supporting the evidence of grain growth. If an as-received grain size of

about $\sim 15 \mu\text{m}$ is assumed as suggested by Figure 2.7, then by looking at the histograms in Figures 2.9-12, one may infer the evolution of microstructure. For instance, Figures 2.10d and 2.11a suggest a heavily affected microstructure with many grains undergoing recrystallization, yielding a reduction in average grain size. On the other hand, Figure 2.9d suggests that several grains have experienced growth, reaching very large diameters. Figure 2.13 shows the comparison of grain sizes calculated from SEM images for different cutting speed and feed rates.

Table 2.4 Measured grain sizes and calculated volume fractions on the specimens after machining of Ti-6Al-4V.

Disk Sample	Depth of Cut a_p [mm]	Tool Type	Edge Radius r_β [μm]	Cutting Speed v_c [m/min]	Feed f [mm/rev]	Avg. Grain Size d_{avg} (μm)	SD Grain Size d_{avg} (μm)	Volume Fraction of β Matrix Grains
Ti-6Al-4V	2	WC/Co (TiAlN)	10	55	0.05	14.66	3.43	0.17
					0.1	13.09	2.59	0.18
				90	0.05	14.40	3.18	0.19
					0.1	14.95	3.63	0.17
		WC/Co	25	55	0.05	13.03	3.04	0.22
					0.1	14.39	2.73	0.27
				90	0.05	16.17	3.45	0.19
					0.1	13.57	2.85	0.28
		WC/Co	10	55	0.05	13.20	2.69	0.27
					0.1	12.82	2.69	0.24
				90	0.05	14.39	2.79	0.29
					0.1	13.66	2.62	0.23
		WC/Co	5	55	0.05	10.70	2.41	0.34
					0.1	13.63	3.07	0.23
				90	0.05	16.29	2.95	0.25
					0.1	14.57	3.23	0.27

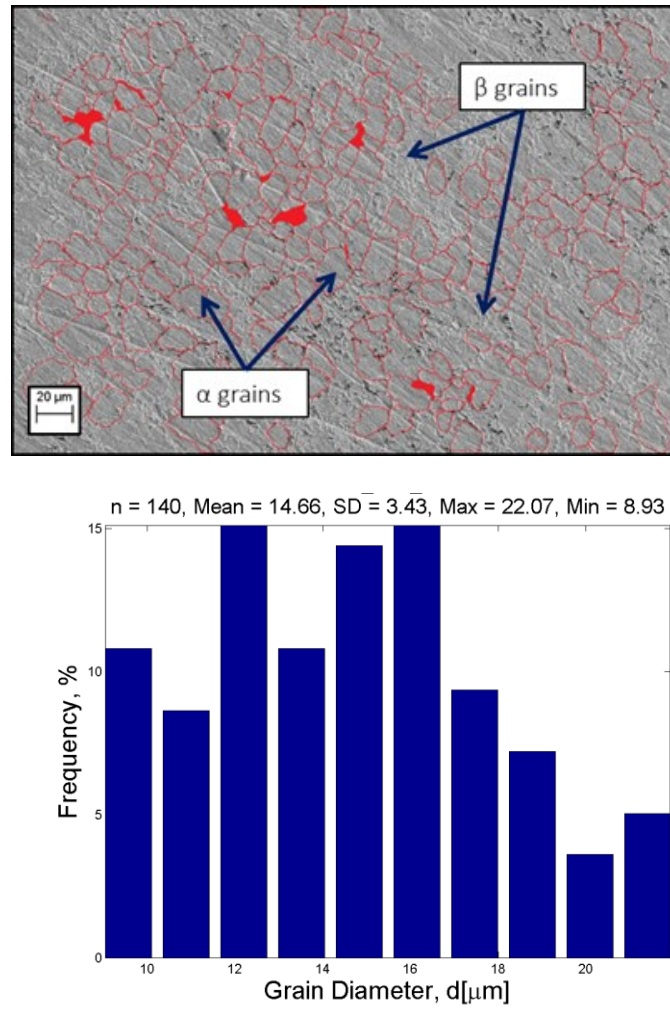


Figure 2.9 (a) TiAlN coated WC/Co tool ($r_\beta=10 \mu\text{m}$), $v_c=55 \text{ m/min}$, $f=0.05\text{mm/rev}$

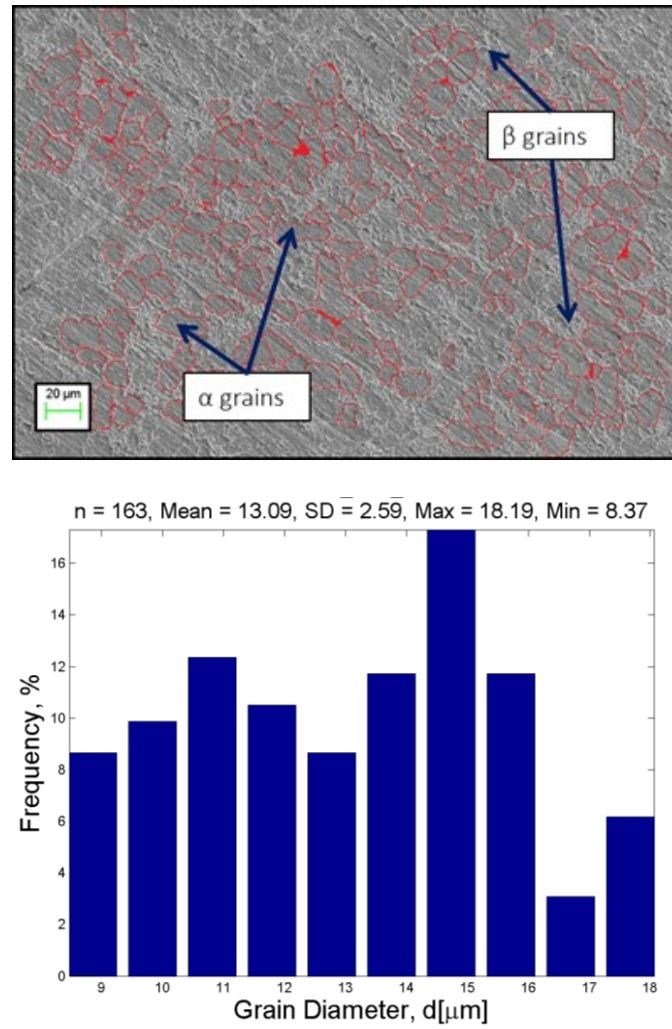


Figure 2.9 (b) TiAlN coated WC/Co tool ($r_\beta=10 \mu\text{m}$), $v_c=55 \text{ m/min}$, $f=0.10\text{mm/rev}$

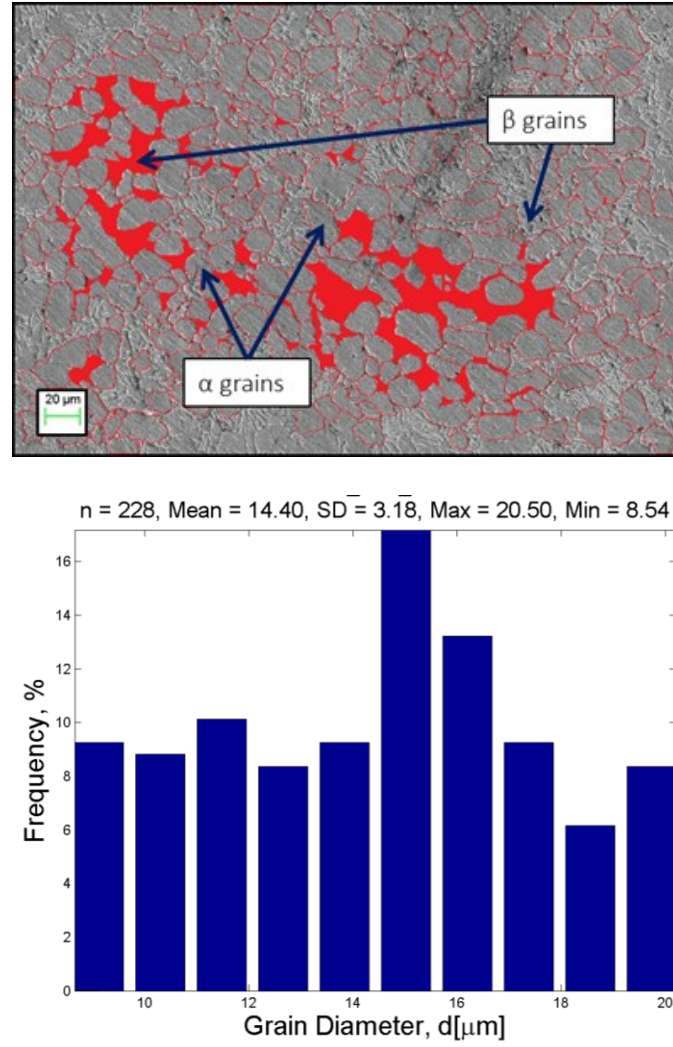


Figure 2.9 (c) TiAlN coated WC/Co tool ($r_\beta=10 \mu\text{m}$), $v_c=90 \text{ m/min}$, $f=0.05\text{mm/rev}$

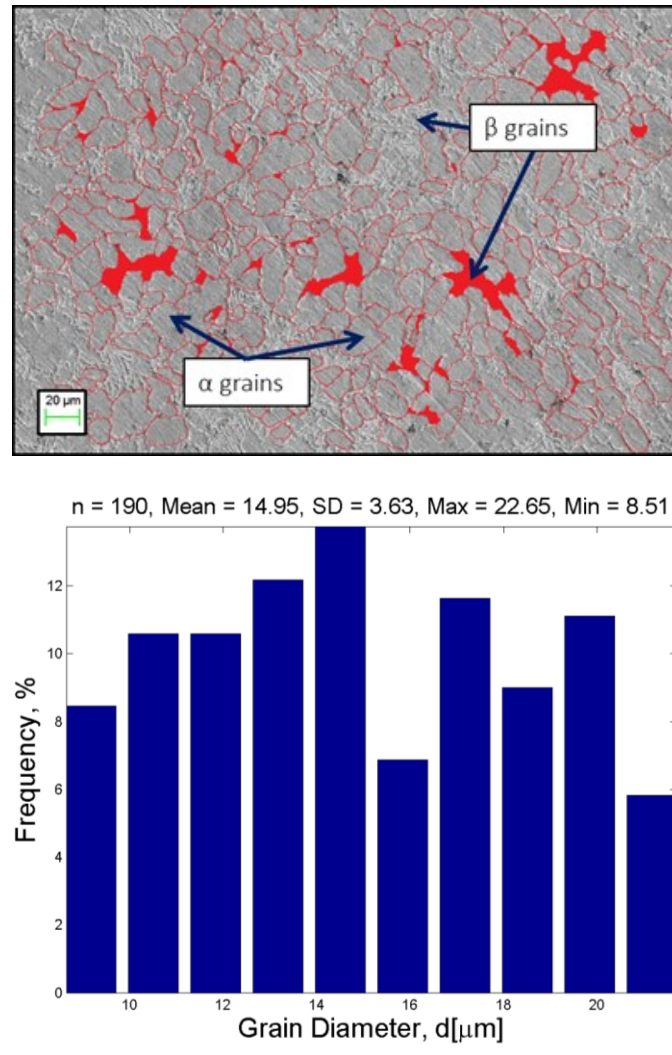


Figure 2.9 (d) TiAlN coated WC/Co tool ($r_{\beta}=10 \mu\text{m}$), $v_c=90 \text{ m/min}$, $f=0.10\text{mm/rev}$

Figure 2.9 SEM images and grain size distributions of the disk tracks machined with the TiAlN coated WC/Co tool, with different cutting speed and feed rates.

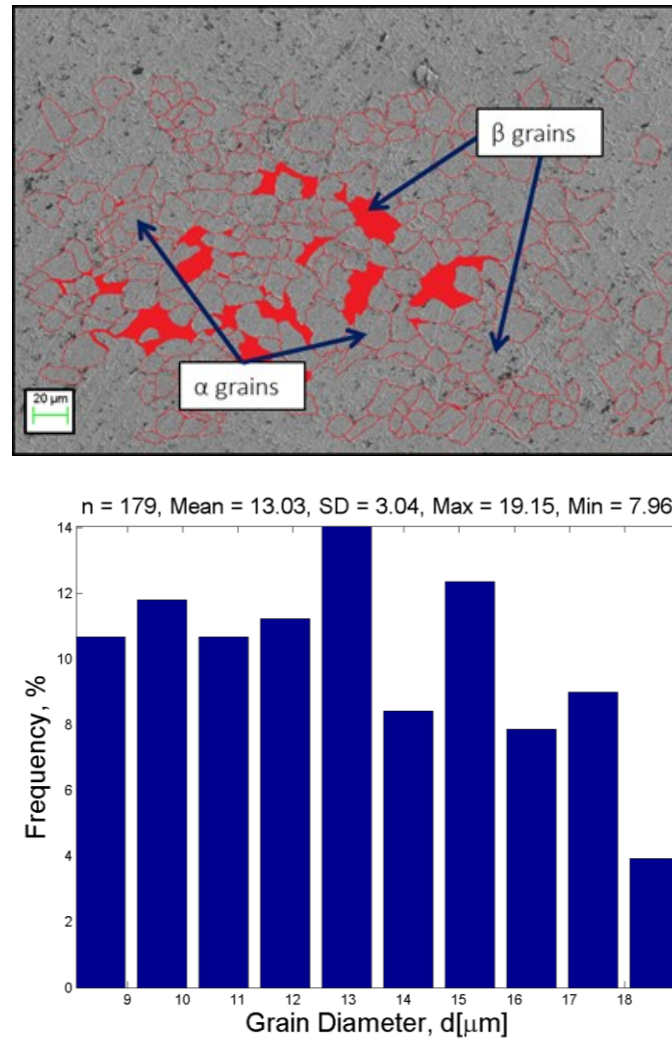


Figure 2.10 (a) WC/Co tool ($r_\beta=25 \mu\text{m}$), $v_c=55 \text{ m/min}$, $f=0.05\text{mm/rev}$

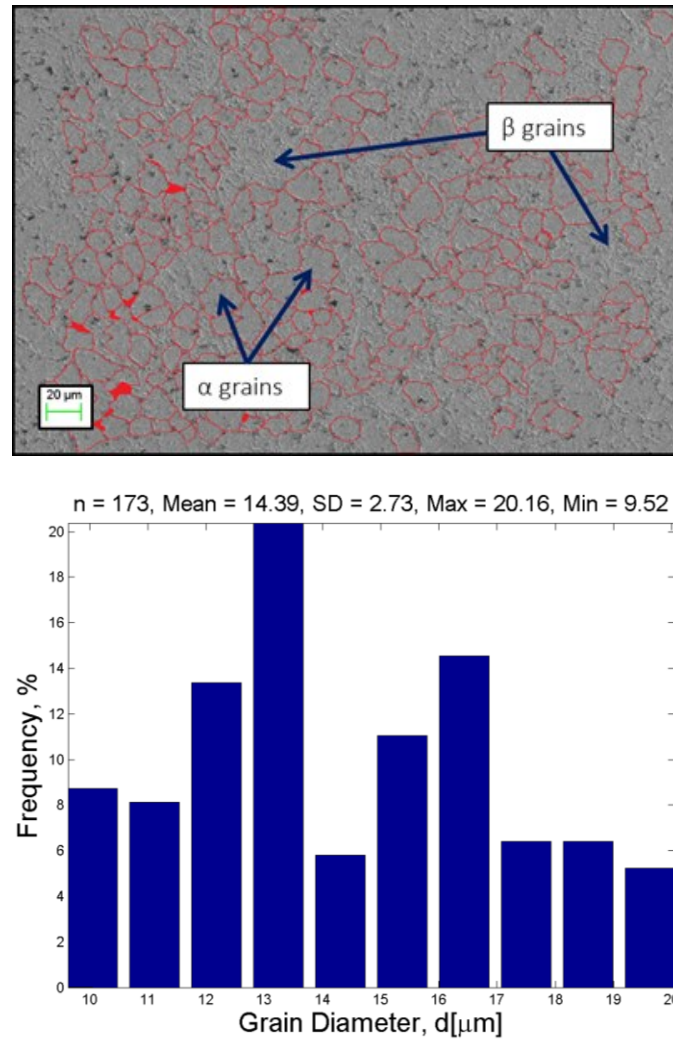


Figure 2.10 (b) WC/Co tool ($r_\beta=25 \mu\text{m}$), $v_c=55 \text{ m/min}$, $f=0.10\text{mm/rev}$

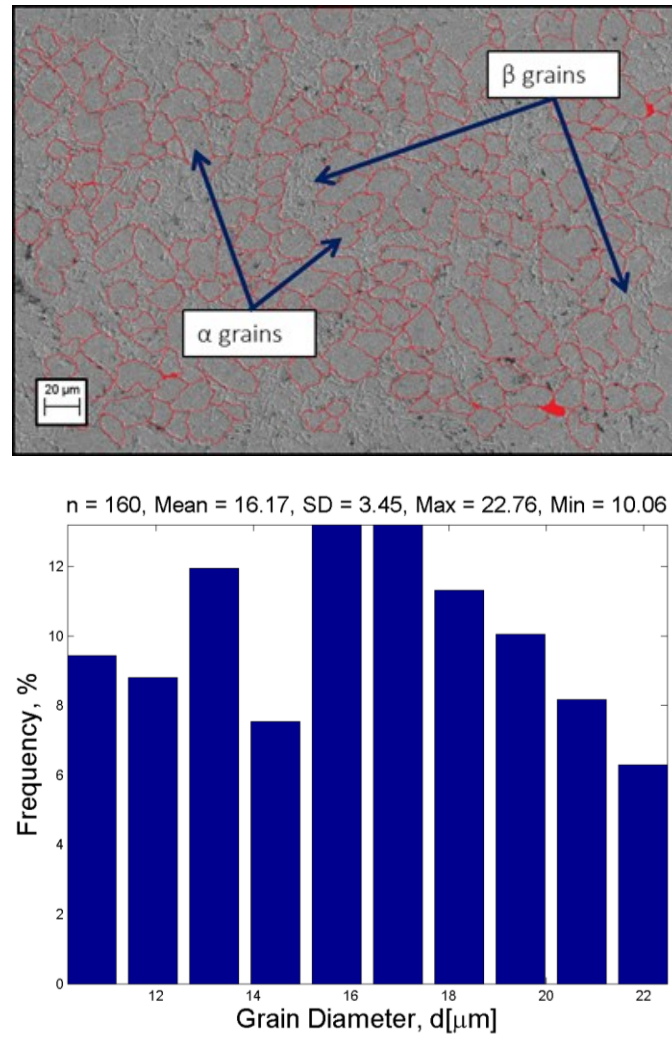


Figure 2.10 (c) WC/Co tool ($r_\beta=25 \mu\text{m}$), $v_c=90 \text{ m/min}$, $f=0.05\text{mm/rev}$

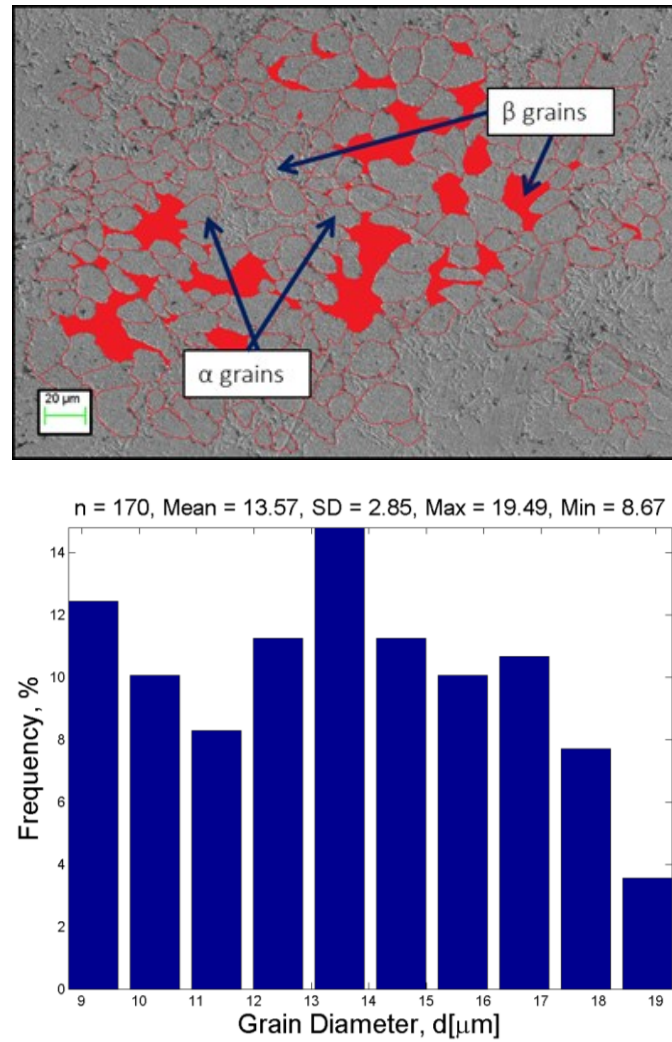


Figure 2.10 (d) WC/Co tool ($r_\beta=25 \mu\text{m}$), $v_c=90 \text{ m/min}$, $f=0.10\text{mm/rev}$

Figure 2.10 SEM images and grain size distributions of the disk tracks machined with the WC/Co tool ($r_\beta=25 \mu\text{m}$), with different cutting speed and feed rates.

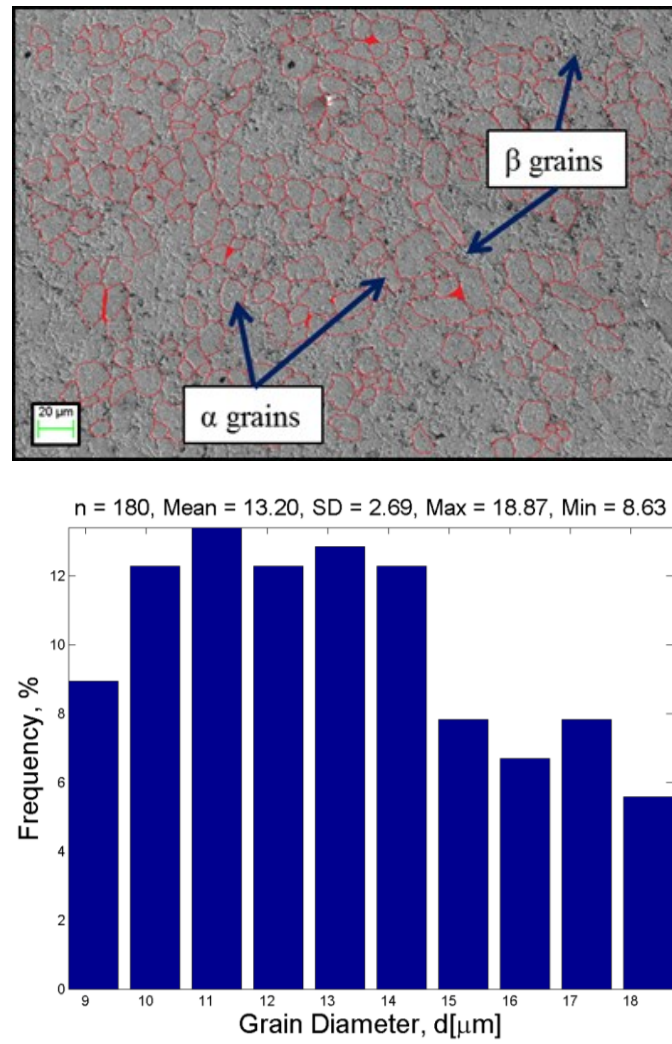


Figure 2.11 (a) WC/Co tool ($r_\beta=10\ \mu\text{m}$), $v_c=55\ \text{m/min}$, $f=0.05\text{mm/rev}$

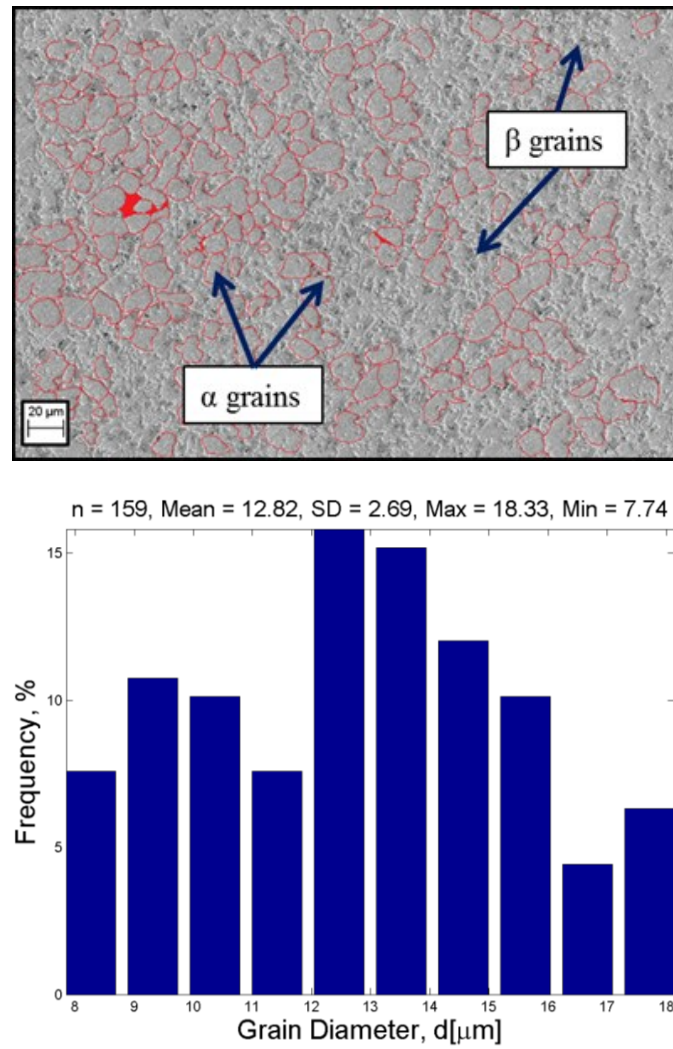


Figure 2.11 (b) WC/Co tool ($r_\beta=10\ \mu\text{m}$),, $v_c=55\ \text{m/min}$, $f=0.10\text{mm/rev}$

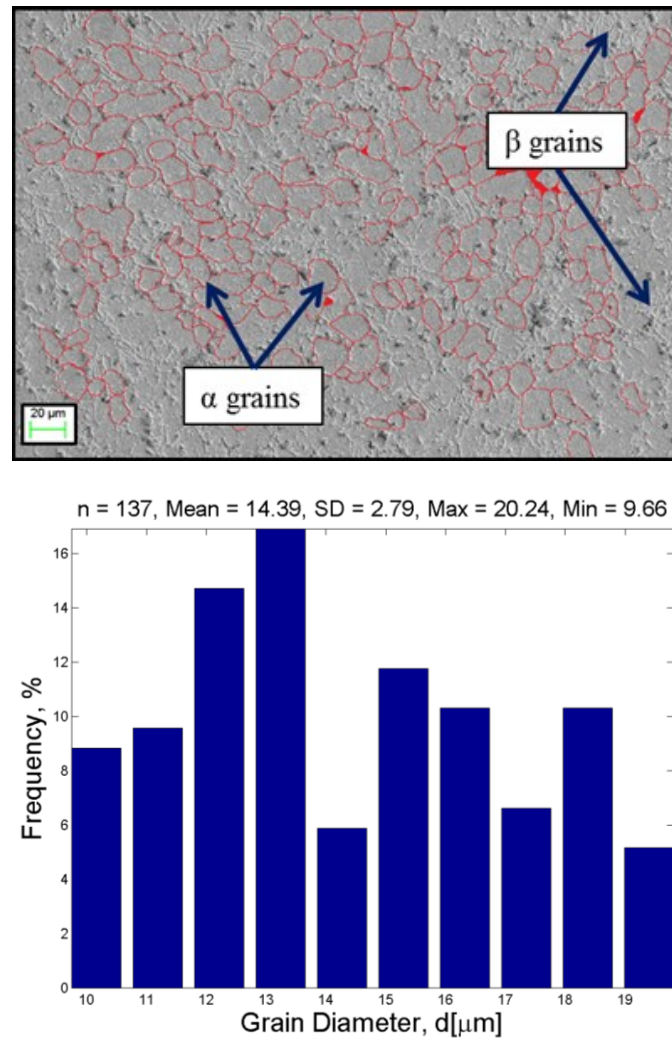


Figure 2.11 (c) WC/Co tool ($r_\beta=10\ \mu\text{m}$), $v_c=90\ \text{m/min}$, $f=0.05\text{mm/rev}$

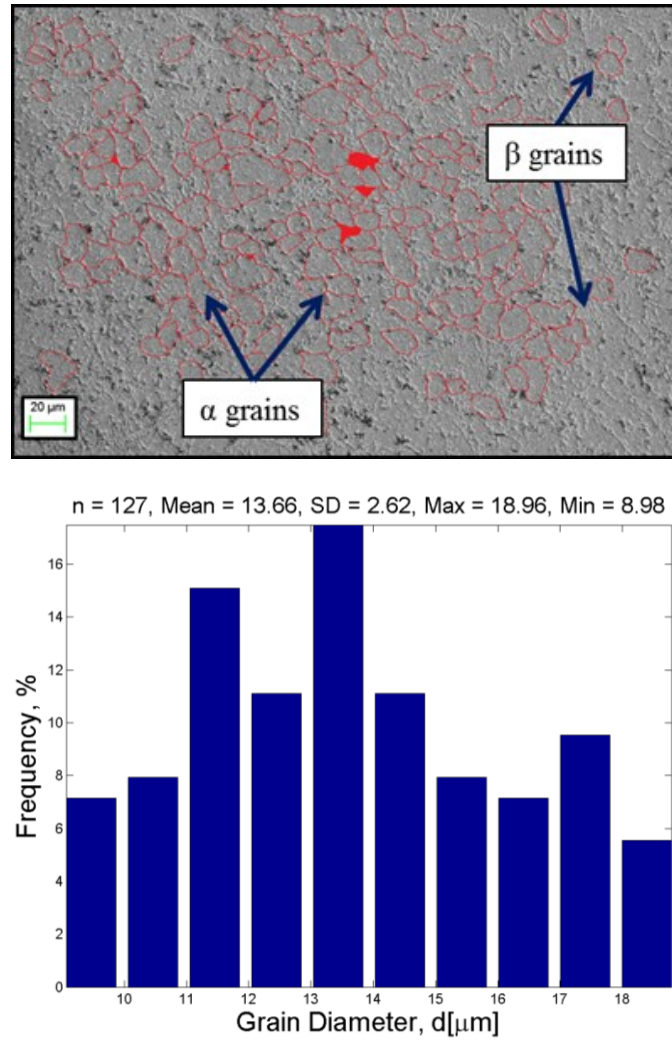


Figure 2.11 (d) WC/Co tool ($r_\beta=10\ \mu\text{m}$), $v_c=90\ \text{m/min}$, $f=0.10\text{mm/rev}$

Figure 2.11 SEM images and grain size distributions of the disk tracks machined with the WC/Co tool ($r_\beta=10\ \mu\text{m}$), with different cutting speed and feed rates.

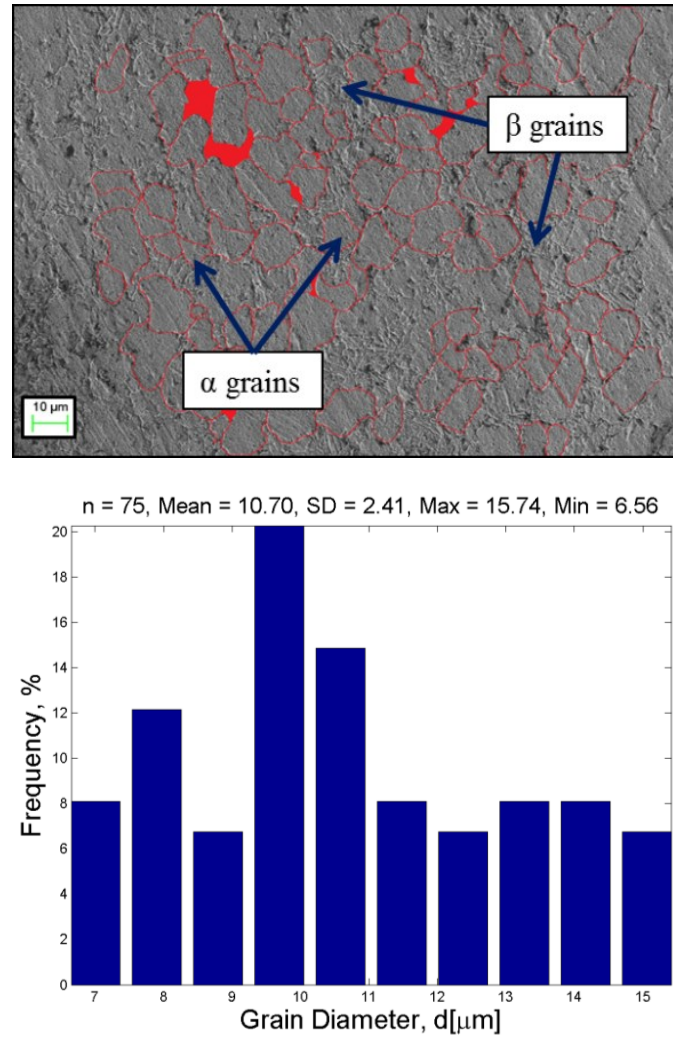


Figure 2.12 (a) WC/Co tool ($r_\beta=5\ \mu\text{m}$), $v_c=55\ \text{m/min}$, $f=0.05\text{mm/rev}$

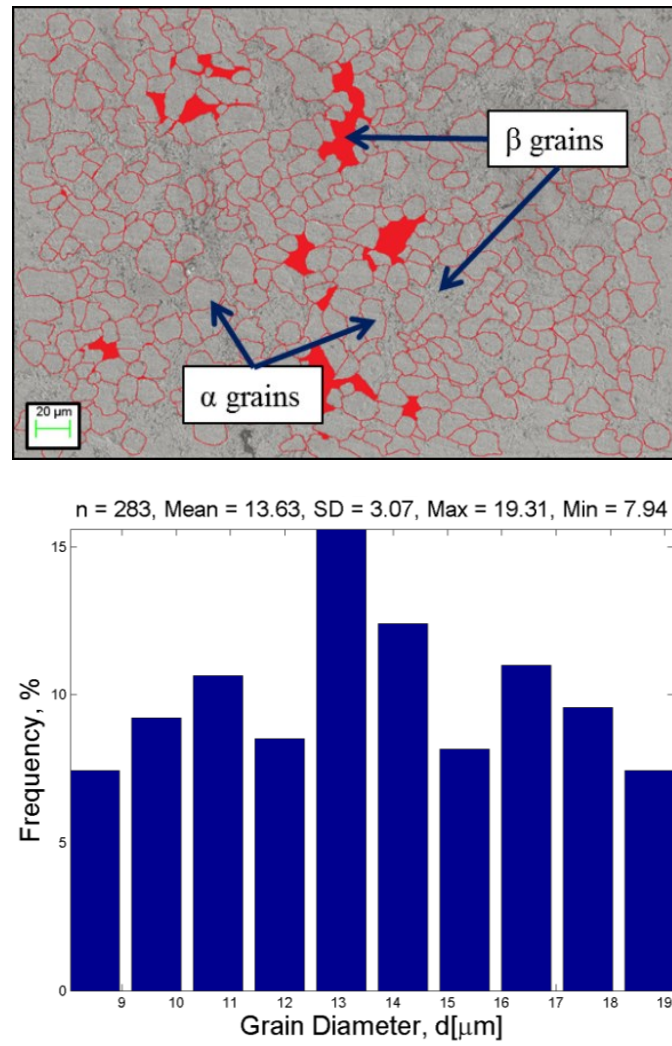


Figure 2.12 (b) WC/Co tool ($r_{\beta}=5 \mu\text{m}$), $v_c=55 \text{ m/min}$, $f=0.10\text{mm/rev}$

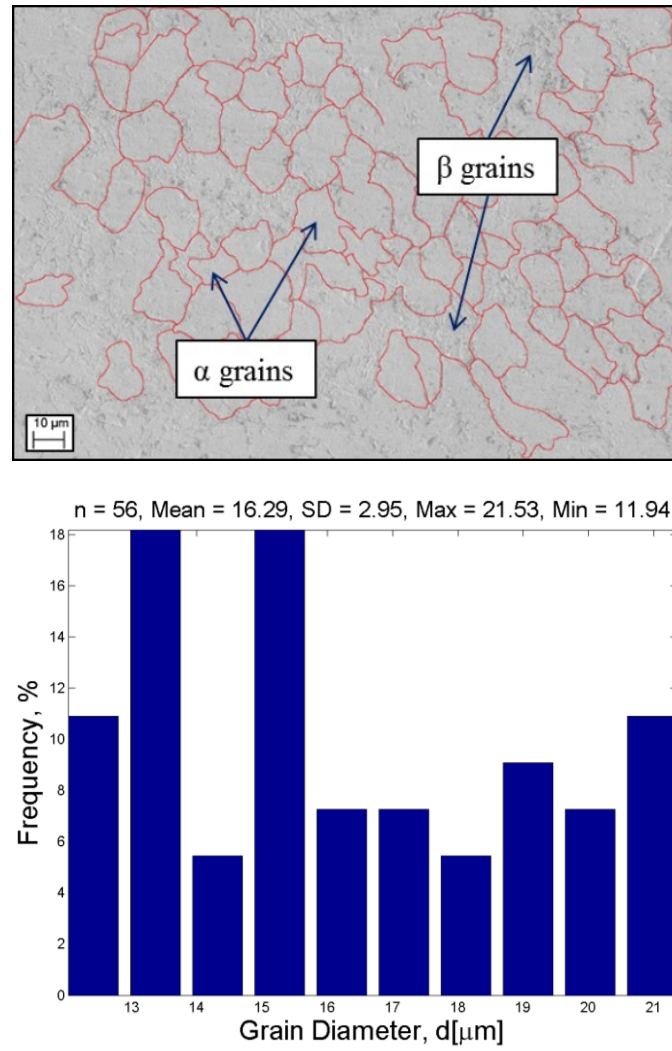


Figure 2.12 (c) WC/Co tool ($r_\beta=5 \mu\text{m}$), $v_c=90 \text{ m/min}$, $f=0.05\text{mm/rev}$

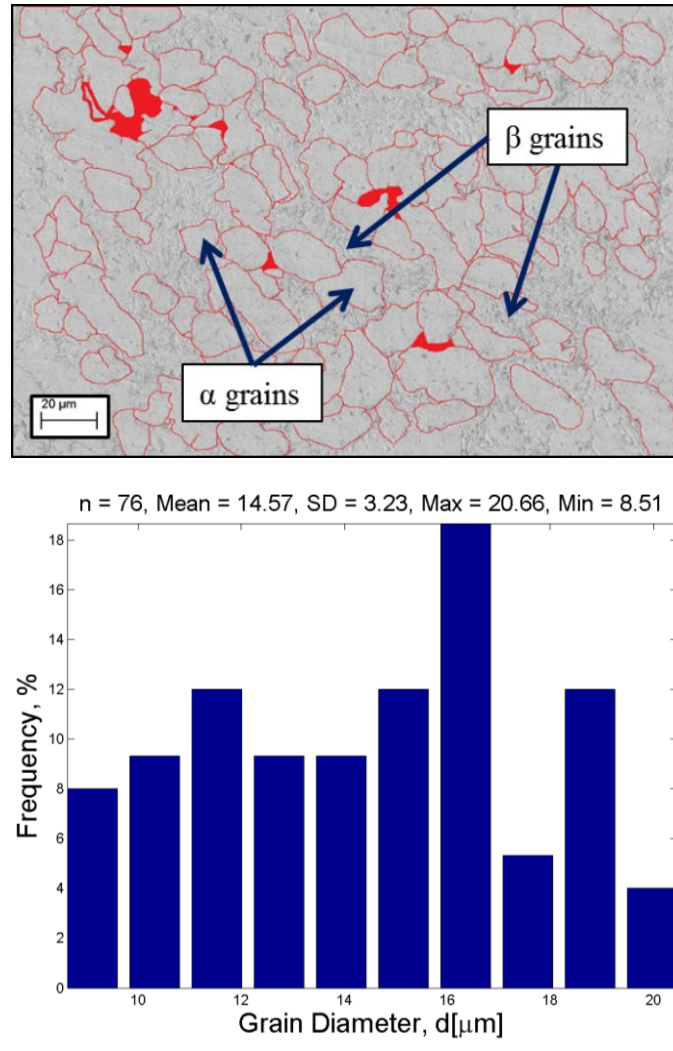


Figure 2.12 (d) WC/Co tool ($r_\beta=5 \mu\text{m}$), $v_c=90 \text{ m/min}$, $f=0.10\text{mm/rev}$

Figure 2.12 SEM images and grain size distributions of the disk tracks machined with the sharp WC/Co tool ($r_\beta=5 \mu\text{m}$), with different cutting speed and feed rates.

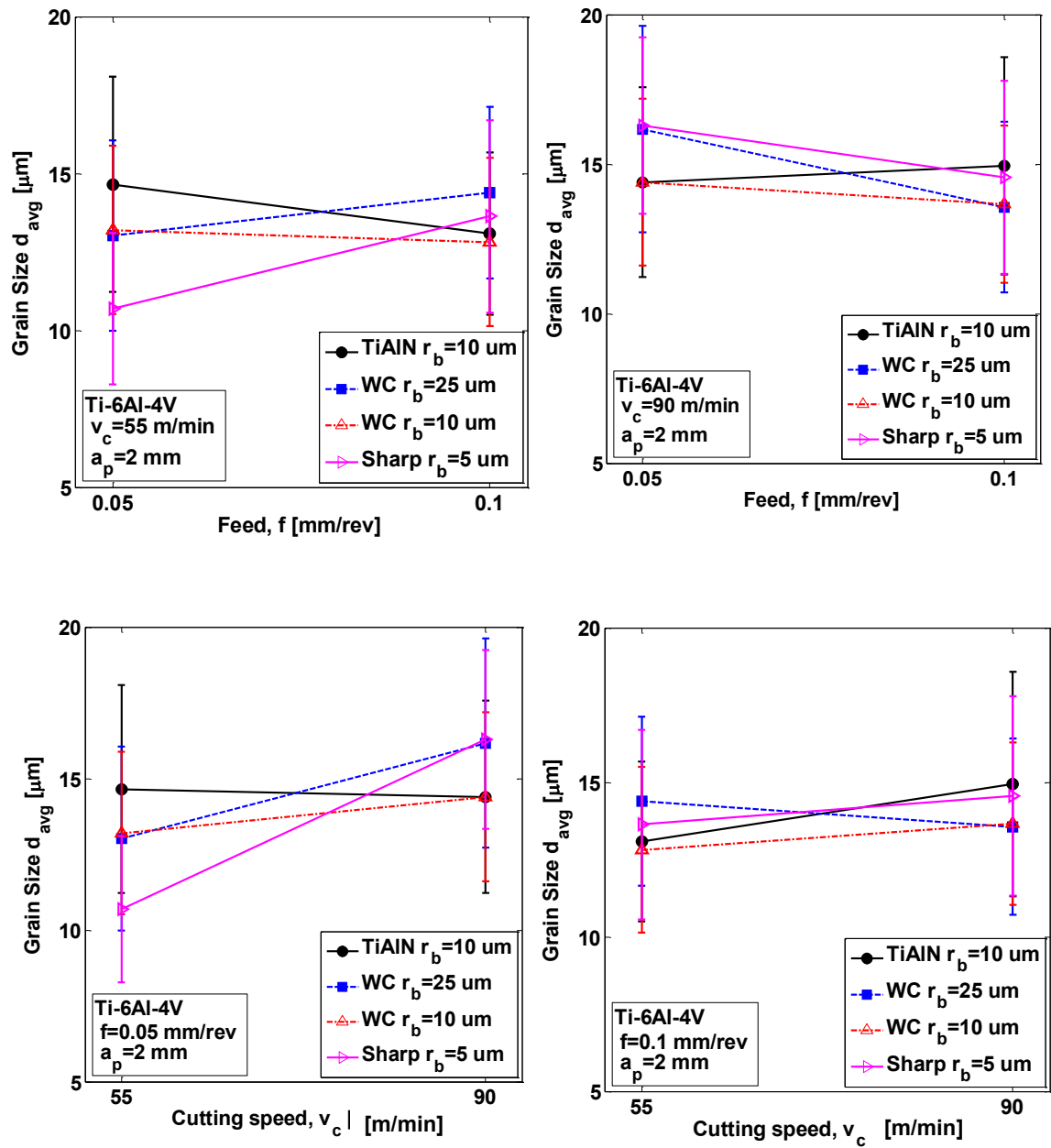


Figure 2.13 Comparison of grain sizes calculated from SEM images for different cutting speed and feed rates.

2.4.3 Grain size measurements for IN100 alloy

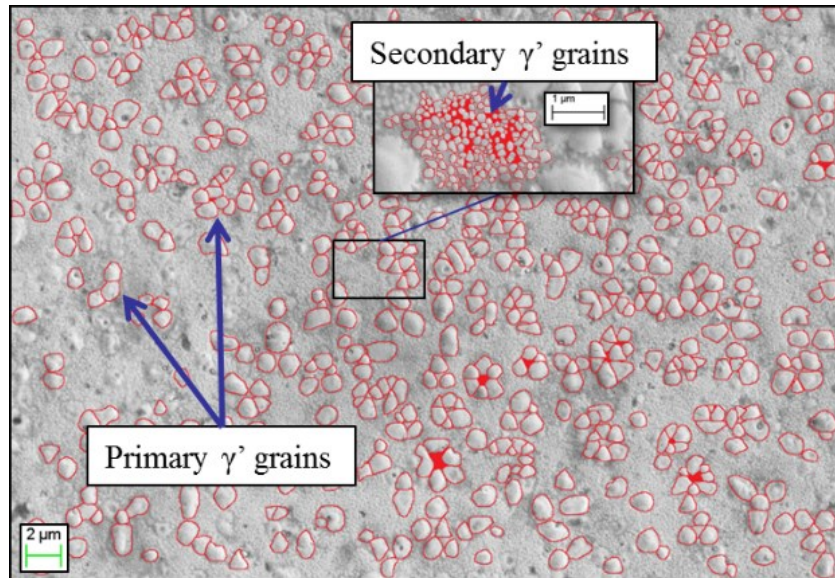
Similar measurements of primary and secondary γ' grain sizes have been taken for the IN100 alloy machined with different conditions. Results of measured grain sizes (d_1 , d_2) and fractions (f_1 , f_2) are summarized in Table 2.5.

Table 2.5 Measured grain sizes and calculated volume fractions on the specimens after machining.

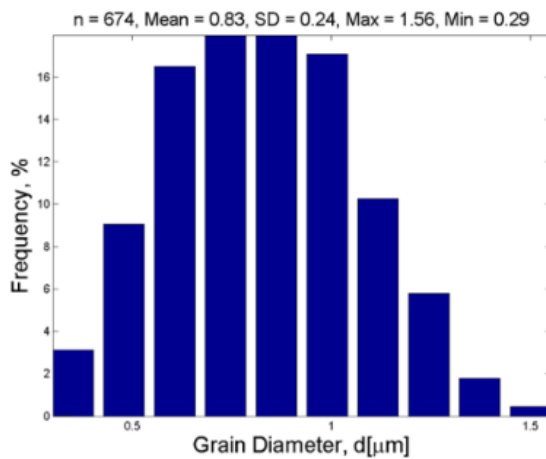
Tool	v_c [m/min]	Primary γ'			Secondary γ'		
		Mean d_1 [nm]	SD d_1 [nm]	Mean f_1	Mean d_2 [nm]	SD d_2 [nm]	Mean f_2
WC/Co $r_\beta=5\mu\text{m}$	12	828	239	0.114	135	45	0.280
	24	941	253	0.106	163	45	0.278
TiAlN $r_\beta=10\mu\text{m}$	12	880	263	0.145	154	48	0.241
	24	728	219	0.060	167	49	0.272
WC/Co $r_\beta=10\mu\text{m}$	12	918	257	0.111	140	40	0.265
	24	783	217	0.107	167	58	0.269
WC/Co $r_\beta=25\mu\text{m}$	12	965	270	0.092	141	39	0.281
	24	814	224	0.065	150	45	0.300

Figures 2.14-2.21 show the processed SEM images together with identified zones of primary and secondary γ' grains. In addition, the distribution of primary and secondary γ' grain sizes are given with histograms in each figure. Figures 2.22-2.23 show the effects of process parameters on grain sizes and volume fractions. Higher cutting speeds tend to yield smaller primary γ' precipitates (d_1), and larger secondary γ' precipitates (d_2). Higher cutting speeds decrease the volume fraction of the primary γ' phase (f_1), but decrease the volume fraction of the secondary γ' phase (f_2). Sharp and WC25 (WC/Co tool with $r_\beta=25\mu\text{m}$) tools yield larger primary γ' precipitates (d_1), followed by the WC10 (WC/Co tool with $r_\beta=10\mu\text{m}$) tool.

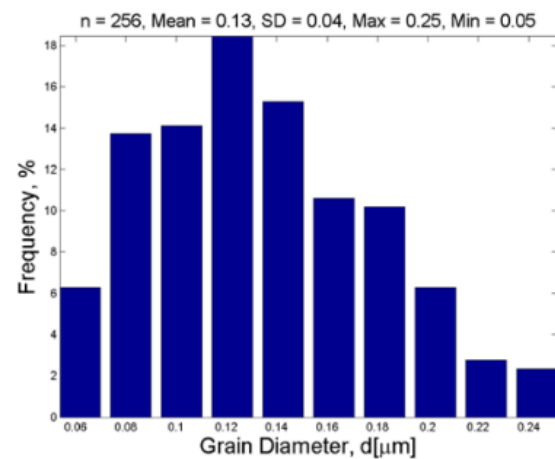
Using TiAlN coated tool results in the smallest average d_1 . An interesting result is that these trends are reversed for the secondary γ' precipitate sizes (d_2) where the TiAlN coated tool generates the largest (d_2). Moreover, TiAlN tool yields the lowest f_2 whereas the WC25 tool yields the lowest f_1 .



(a)



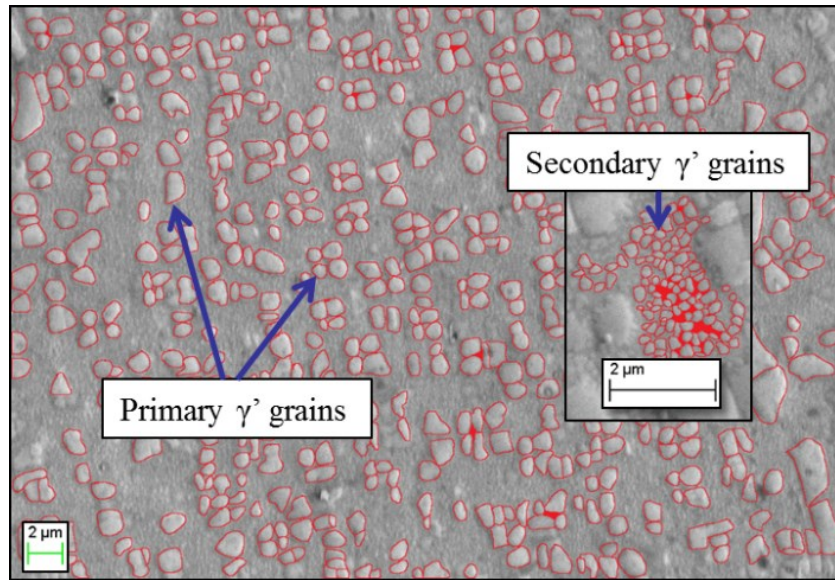
(b)



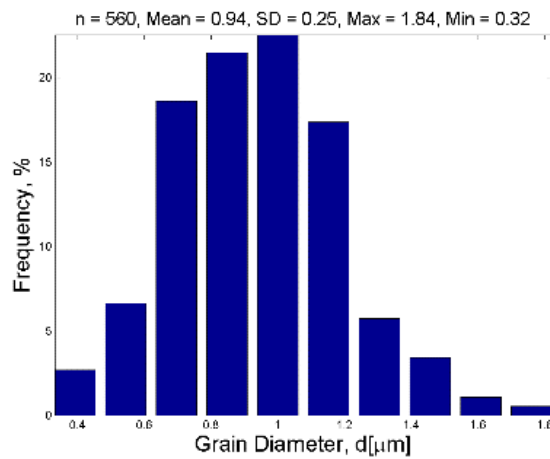
(c)

Figure 2.14 Microstructure of machined IN100 subsurface (a) (Sharp WC/Co tool, $v_c=12$ m/min, $f=0.05$ mm/rev), histograms of primary γ (b) and secondary γ' (c) grains.

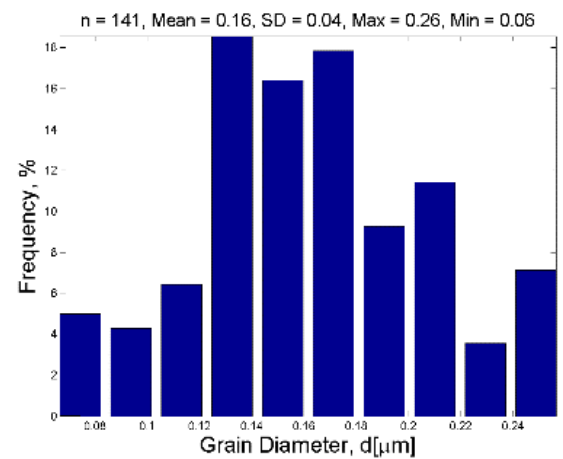
Grains are marked red.



(a)



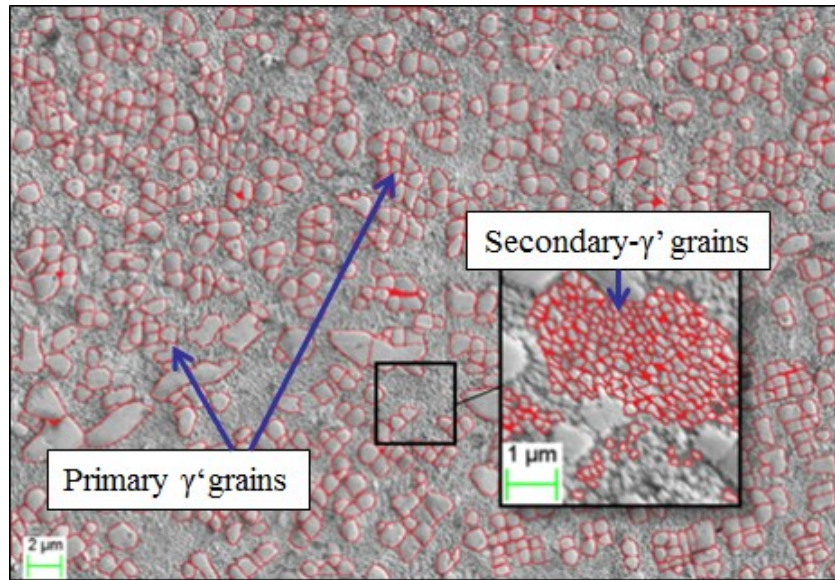
(b)



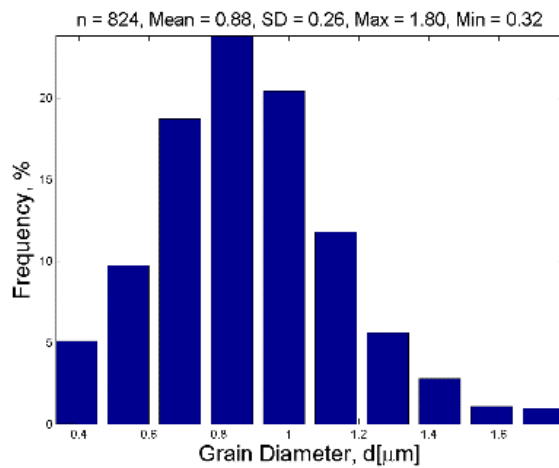
(c)

Figure 2.15 Microstructure of machined IN100 subsurface (a) (Sharp WC/Co tool, $v_c=24$ m/min, $f=0.05$ mm/rev), histograms of primary γ (b) and secondary γ' (c) grains.

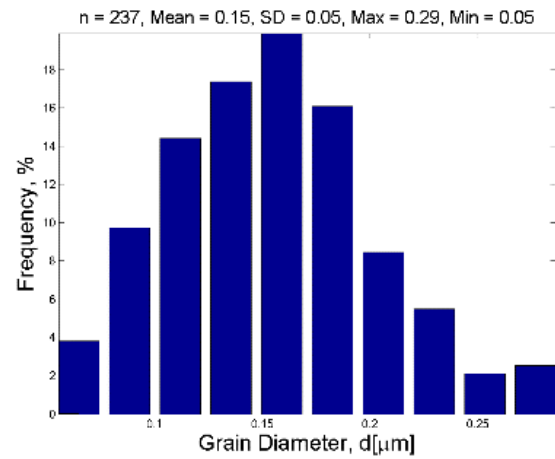
Grains are marked red.



(a)

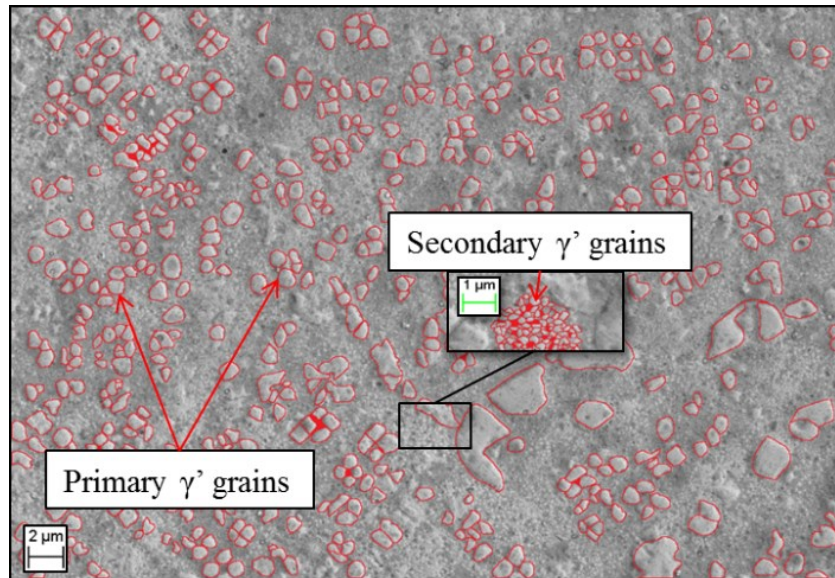


(b)

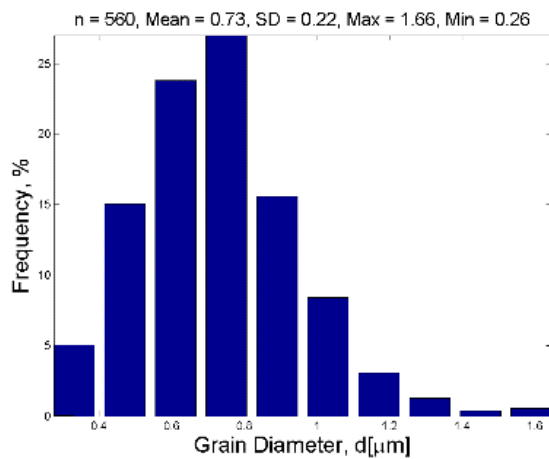


(c)

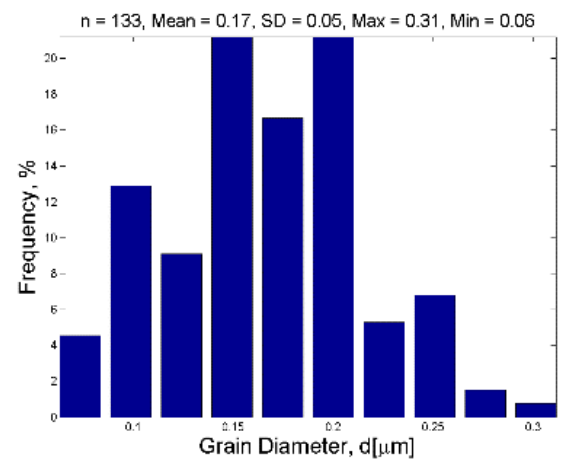
Figure 2.16 Microstructure of machined IN100 subsurface (a) (TiAlN coated WC/Co tool, $v_c=12$ m/min, $f=0.05$ mm/rev), histograms of primary γ (b) and secondary γ' (c) grains. Grains are marked red.



(a)

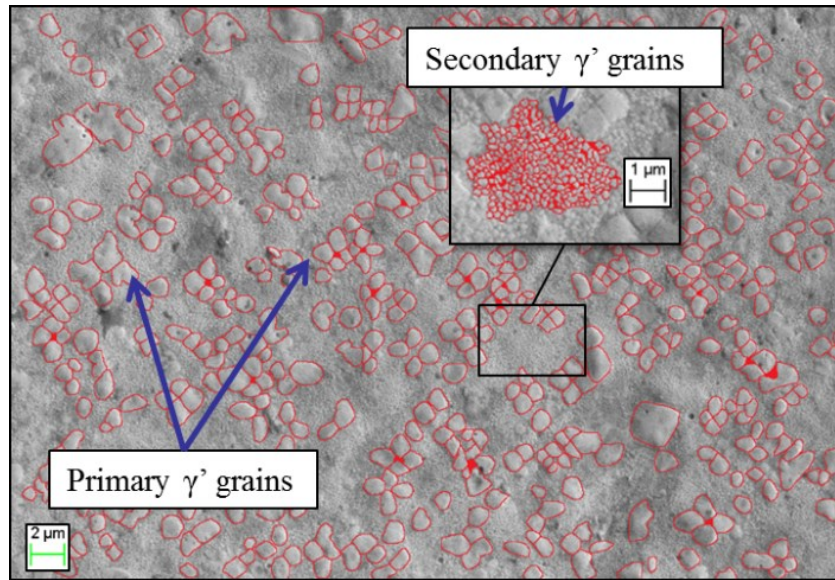


(b)

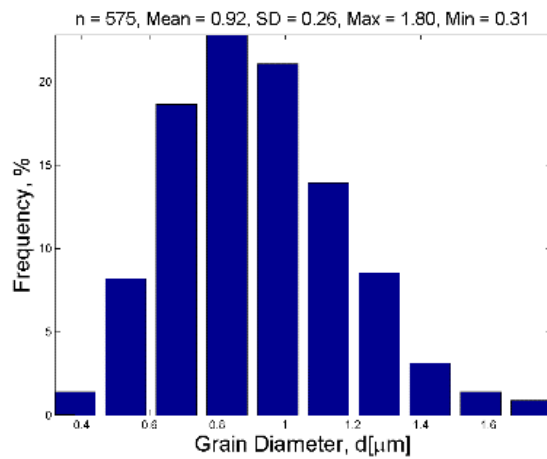


(c)

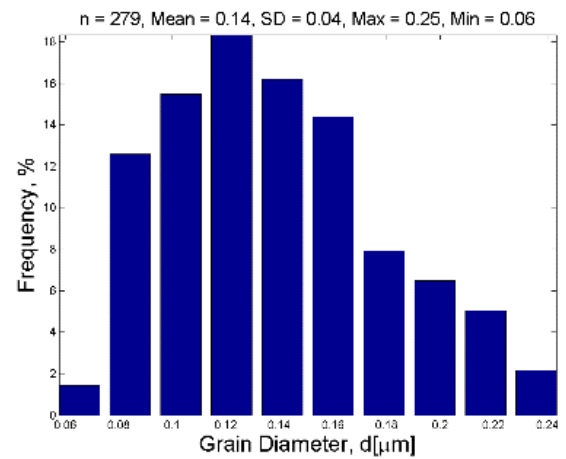
Figure 2.17 Microstructure of machined IN100 subsurface (a) (TiAlN coated WC/Co tool, $v_c=24$ m/min, $f=0.05$ mm/rev), histograms of primary γ (b) and secondary γ' (c) grains. Grains are marked red.



(a)



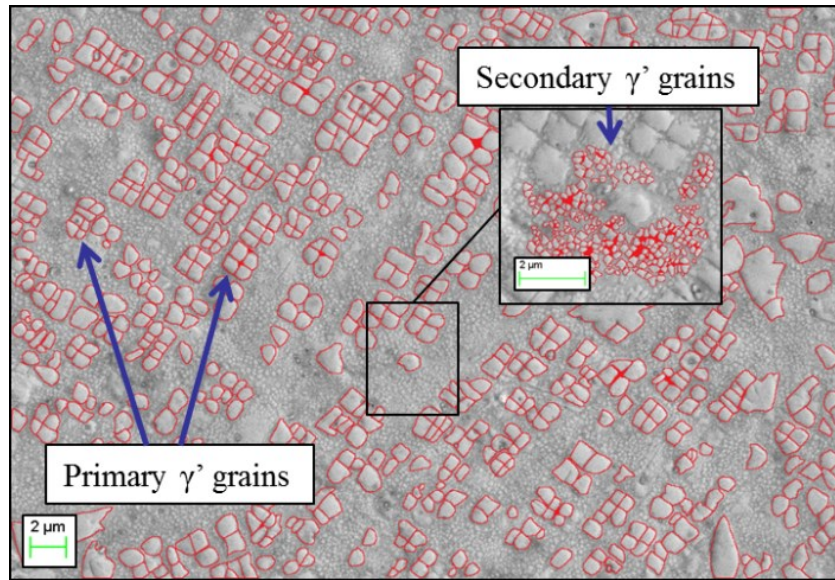
(b)



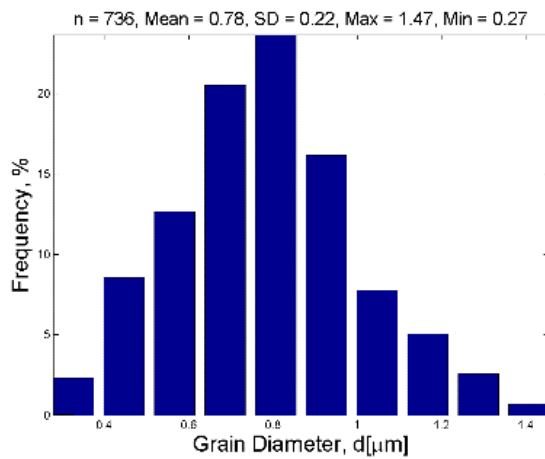
(c)

Figure 2.18 Microstructure of machined IN100 subsurface (a) (WC/Co $r_\beta=10\ \mu\text{m}$ tool, $v_c=12\ \text{m/min}$, $f=0.05\ \text{mm/rev}$), histograms of primary γ (b) and secondary γ' (c) grains.

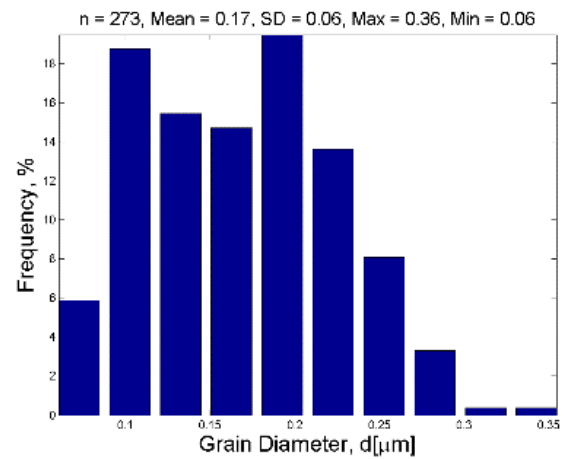
Grains are marked red.



(a)



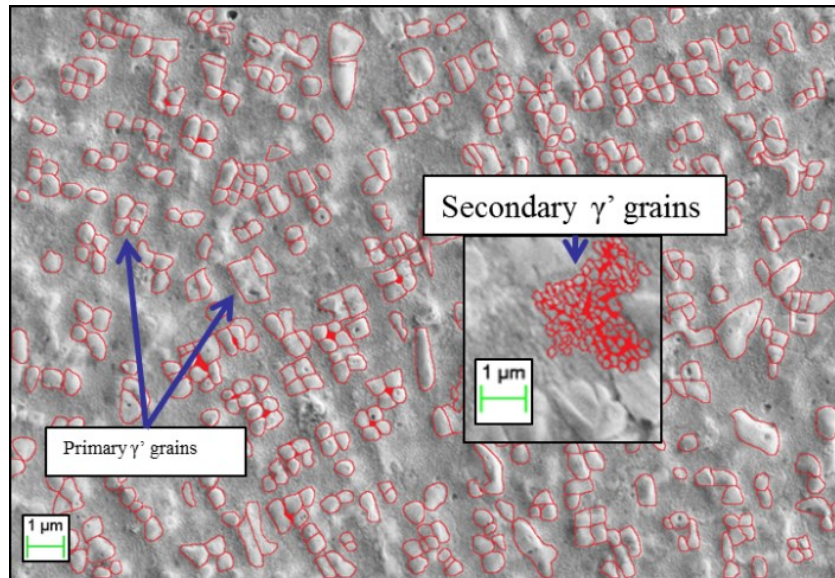
(b)



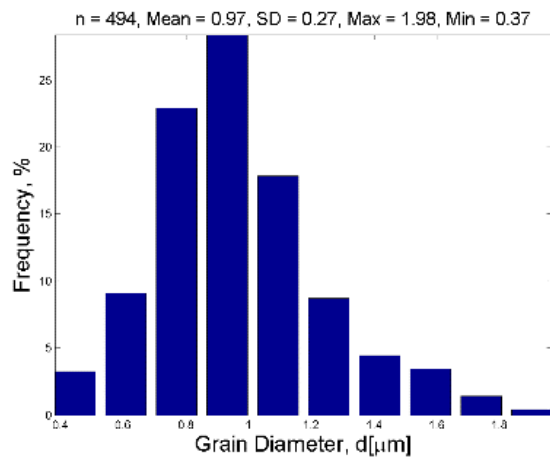
(c)

Figure 2.19 Microstructure of machined IN100 subsurface (a) (WC/Co $r_{\beta}=10\ \mu\text{m}$ tool, $v_c=24\ \text{m/min}$, $f=0.05\ \text{mm/rev}$), histograms of primary γ (b) and secondary γ' (c) grains.

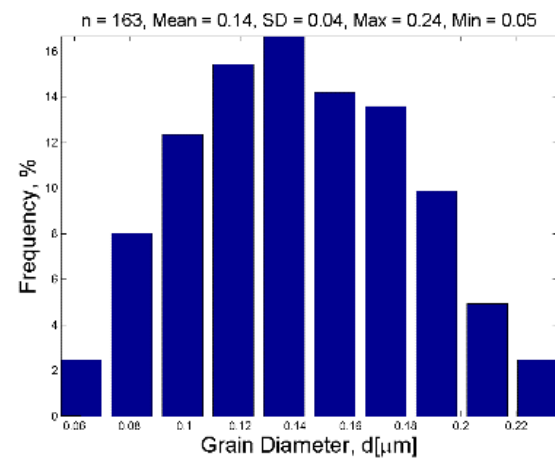
Grains are marked red.



(a)



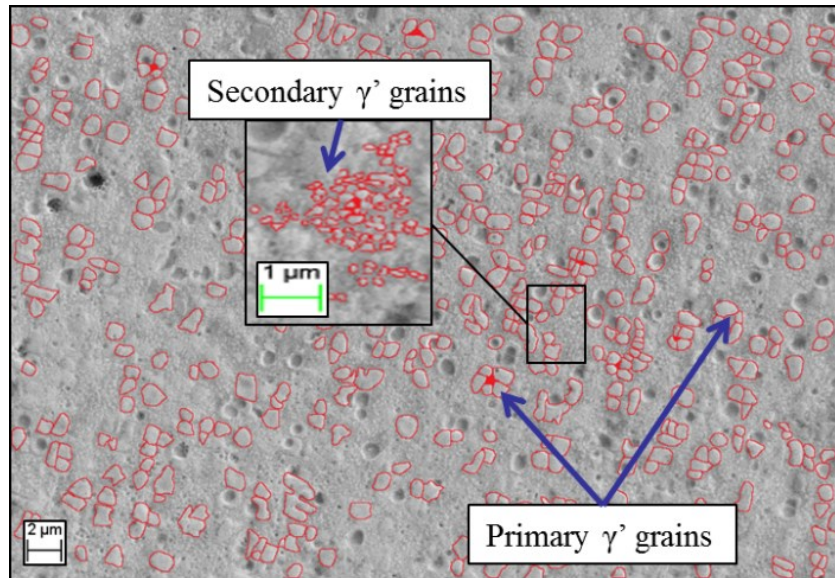
(b)



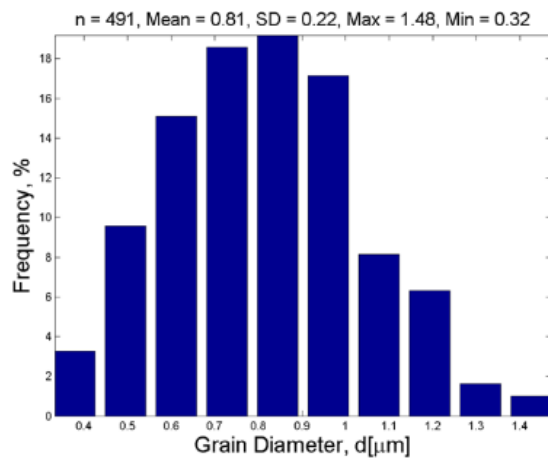
(c)

Figure 2.20 Microstructure of machined IN100 subsurface (a) (WC/Co $r_\beta=25\ \mu\text{m}$ tool, $v_c=12\ \text{m/min}$, $f=0.05\ \text{mm/rev}$), histograms of primary γ (b) and secondary γ' (c) grains.

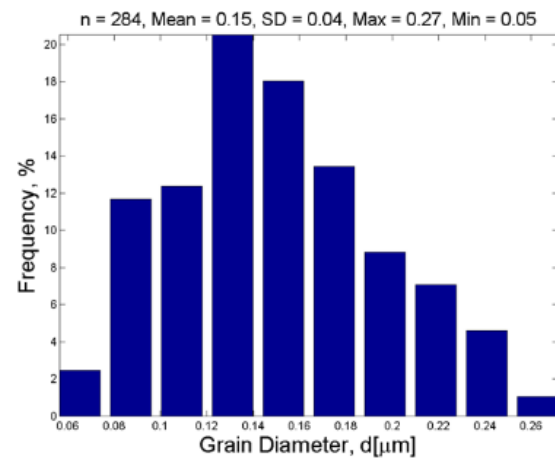
Grains are marked red.



(a)



(b)



(c)

Figure 2.21 Microstructure of machined IN100 subsurface (a) (WC/Co $r_\beta=25\ \mu\text{m}$ tool, $v_c=24\ \text{m/min}$, $f=0.05\ \text{mm/rev}$), histograms of primary γ (b) and secondary γ' (c) grains.

Grains are marked red.

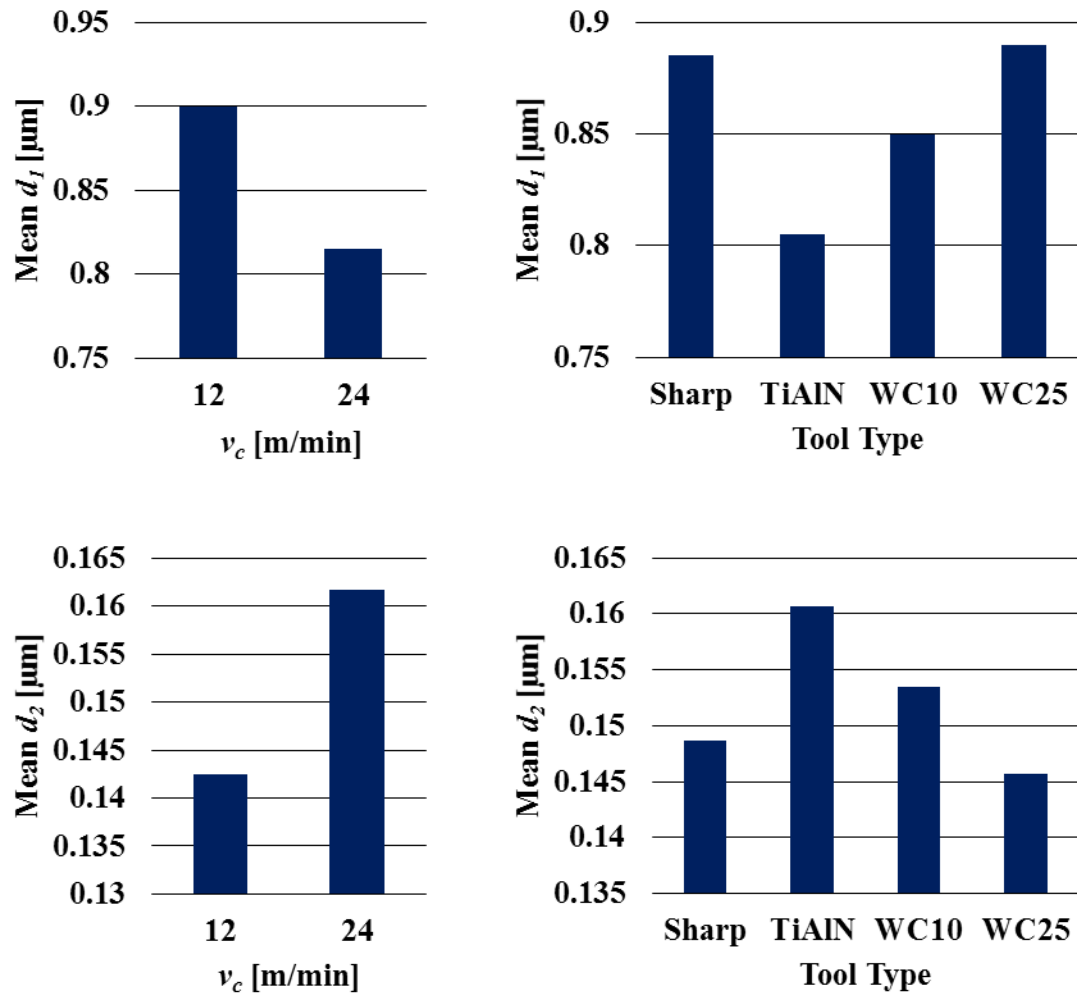


Figure 2.22 Effects of cutting speed v_c (left) and tool type (right) on the primary (top) and secondary (bottom) γ' grains.

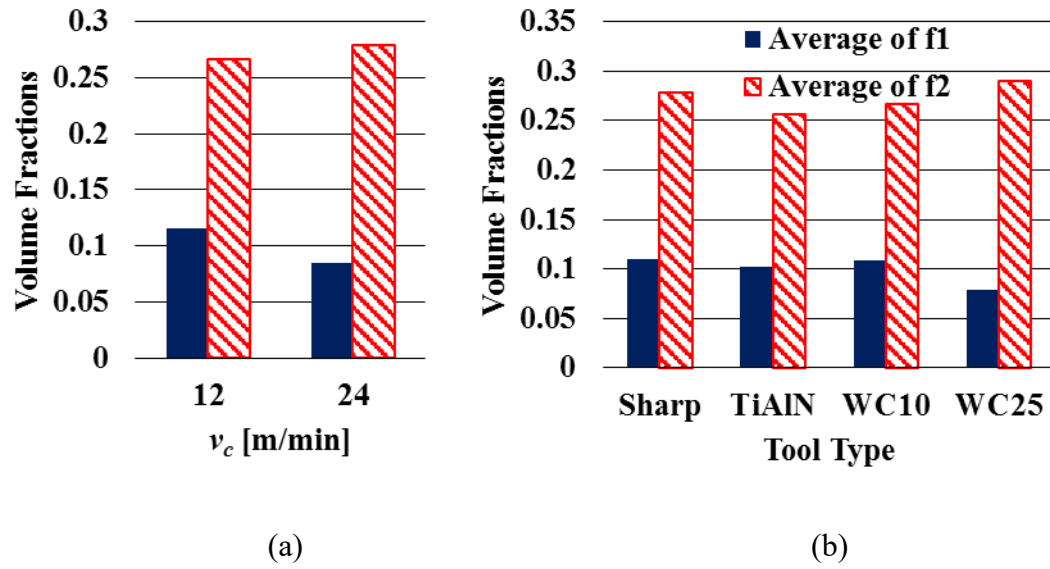


Figure 2.23 Effects of (a) cutting speed v_c and (b) tool type on the primary (f_1) and secondary (f_2) γ' grain volume fractions.

CHAPTER 3: COMPUTATIONAL MICROSTRUCTURE MODELING

3.1 Introduction

The Johnson-Mehl-Avrami-Kolmogorov (JMAK) model has been used to predict the microstructure in the 3-D FE simulations (Arisoy & Özel, 2014; Özel & Arisoy 2014). The JMAK model, also known as Avrami model, defines the transformation kinetics in a material. The JMAK model does not provide a detailed microstructure evolution in terms of grain geometries; however it has been proven to be a very useful tool for modelling nucleation and grain growth phenomena.

There is an implementation of this model in the commercial Finite Element Analysis software DEFORM-3D that includes grain growth, static, dynamic, and metadynamic recrystallization. The implemented model uses temperature, strain, strain rate, activation energies and initial grain size information to model the microstructure evolution. Isothermal JMAK equations describe the volume fraction of the transformed material as a function of temperature and time.

3.2 Microstructure Modeling in Machining Processes with Finite Element Simulations

Microstructure models described in Chapter 1 have been widely used in the literature, by utilizing experimental data. An internal-state-variable based self-consistent constitutive model in order to predict microstructural evolution and flow stresses of Ti-6Al-4V and IMI834 titanium alloys, and considered the KM model and the ZH parameter (Fan and Yang, 2011). Shafaat et al. (Shafaat et al., 2011) performed isothermal hot compression tests on Ti-6Al-4V material in $\alpha + \beta$ phase region and used JMAK equation to model flow curves. Seshacharyulu et al. (Seshacharyulu et al., 2000) investigated the recovery and recrystallization in Ti-6Al-4V in a hot deformation process using the ZH parameter. (Park et al., 2008) also performed isothermal hot compression tests (rolling) on Ti-6Al-4V alloy with martensitic structure, and investigated optimum conditions for achieving dynamic globularization and enhanced superplasticity. An agreement between the Zener-Hollomon parameter with α grain sizes under various temperatures was reported.

The evolution of the microstructure in a process can be roughly estimated by the grain diameter and it is established that there is a relationship between strain, strain rate and temperature during a process and the grain diameter in the material so that Finite Element (FE) based simulations can be used to predict the grain size and microstructure.

Ti-6Al-4V alloy microstructure after manufacturing processes has been investigated by various researchers, using Finite Element Method in conjunction with microstructure

models. (Buffa et al., 2013) used FE simulations to model α - β phase transformations and volume fractions using the Avrami model in friction stir welding of Ti-6Al-4V. Similarly, (Vo et al., 2008) modeled the static recrystallization behavior of the near- α Ti alloy IMI834 during hot compression with FE simulations using Avrami-type equation. (Ding et al., 2002) investigated microstructural evolution of Ti-6Al-4V alloy during thermomechanical processing using ZH parameter and calculated recrystallized grain size in hot deformation process. (Rotella et al., 2014) conducted experiments for machining induced surface integrity in Ti-6Al-4V under various cooling conditions. Furthermore, (Rotella and Umbrello, 2014) investigated machining induced microstructure in orthogonal cutting of Ti-6Al-4V alloy by using 2-D FE modeling with flow softening adjusted flow stress curves and Z-H parameter for grain size and Hall-Petch model for hardness.

Finite Element based microstructure modeling has been demonstrated in other materials as well. (Pu et al., 2014) investigated the microstructure of AZ31B magnesium alloy after dry and cryogenic machining, and calculated dynamically recrystallized grain sizes using the Zener-Hollomon parameter. (Umbrello and Filice, 2009) studied machining induced microhardness alteration and related white layer formation in AISI52100 steel using FE modeling and hardness based flow stress modeling. (Rotella et al., 2013) reported dynamic recrystallization during turning of AA7075-T651 alloy and utilized FE modeling to predict grain refinement and hardness modifications on machined surfaces of this alloy. They found that both the cutting speed and the tool nose radius affect the machined surface and subsurface integrity since both dynamic recrystallization and higher hardness values are observed. Additionally, various computational methods have been used for microstructure

modeling. (Yazdipour et al., 2008) modeled the microstructure of 304 austenitic stainless steel using irregular cellular automata and performed hot torsion tests. (Chun et al., 2006) developed a methodology to model the recrystallization of commercial-purity Titanium after cold-rolling process using Electron Backscatter Diffraction (EBSD) measurements, Monte-Carlo simulations, JMAK and Speich-Fischer (SF) models.

Since dynamic recrystallization has been observed during machining of titanium alloys, the Johnson-Mehl-Avrami-Kolmogorov (JMAK) model which is readily implemented in the DEFORM-3D software has been used. DEFORM-3D has a database that contains the JMAK model parameters and material properties for certain materials, including some aluminum alloys (Yi et al., 2008) and nickel alloys such as Waspaloy (Shen et al., 1995; Shen, 2005). However, most of the JMAK parameters are tailored towards forging applications and work at high temperatures.

3.2.1 Microstructure Modeling of Ti-6Al-4V Titanium Alloy

3.2.1.1 Finite Element Simulation Setup for Machining of Ti-6Al-4V Alloy

Finite element method based 3-D face turning simulations using DEFORM-3D machining software have been investigated in various papers (Özel and Ulutan, 2012; Ozel et al., 2013; Ulutan and Özel, 2013a; Ulutan and Özel, 2013b; Ulutan and Özel, 2013c; Özel and Arisoy, 2014; Arisoy and Özel, 2014; Arisoy and Özel, 2015). In the 3-D FE simulations, curved workpiece geometry was modeled as viscoplastic and represented with high number of elements. The finite element mesh was generated by using DEFORM-3D software's mesh generation system with linear tetrahedral elements. The sensitivity of the mesh size (i.e. number of elements) on the simulation outputs suggested that a mesh size of 50,000 elements for workpiece is optimum for obtaining fast and accurate results. A higher mesh density was used in a 1 mm-long section behind the chip to better resolve the temperature and strain fields that are necessary for the microstructure calculations on the machined surface as shown in Figure 3.1.

Friction between the tool and the workpiece was described with a hybrid model including shear friction and Coulomb friction along the rake and flank faces of the tool. The hybrid friction model is summarized in Eq. (3.1), where m and μ are friction coefficients for shear and Coulomb friction models, and τ , k , τ_f and σ_n are material shear stress, shear flow stress, frictional stress and normal stress on the tool face, respectively.

$$\mu = \frac{\tau_f}{\sigma_n}, \quad \sigma_n \text{ low}$$

$$m = \frac{\tau}{k}, \quad \sigma_n \text{ high}, 0 \leq m \leq l$$
(3.1)

The heat transfer coefficient between tool and workpiece was set to a very high value ($h=100000 \text{ N/ s mm } ^\circ\text{C}$) in order to allow temperature field to reach near its steady-state in a short period of time. This is a necessary step in order to simulate the process more accurately considering the simulation is very short compared to the real process. Some key simulation parameters are listed in Table 3.1.

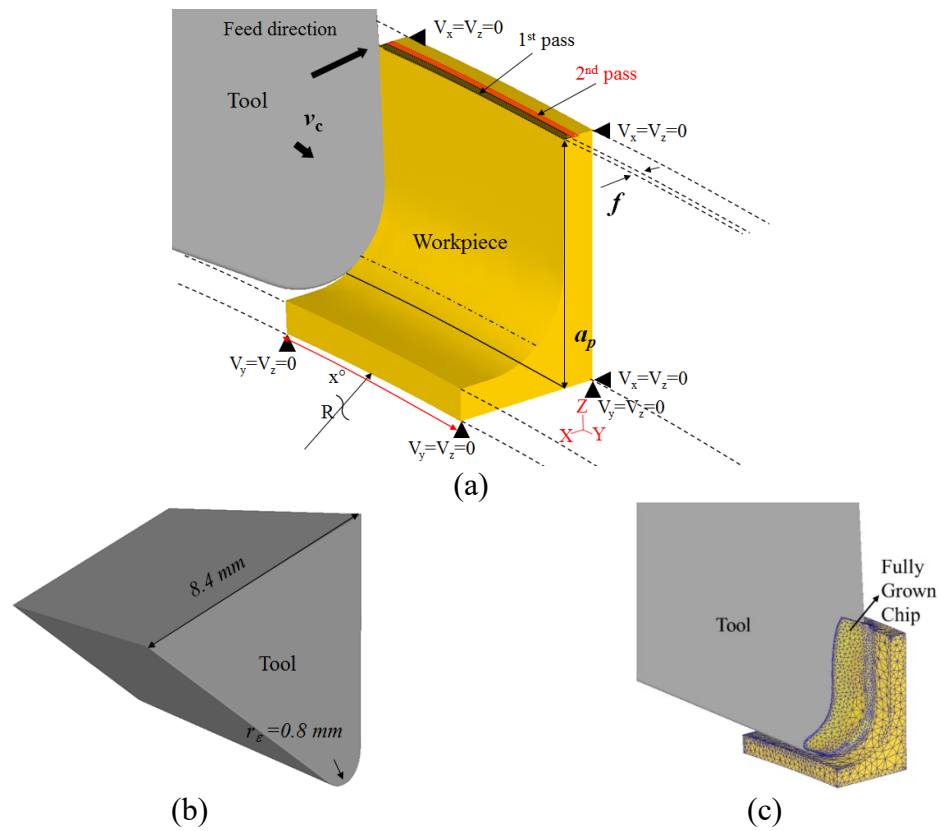


Figure 3.1 FE model of the simulation with (a) workpiece geometry and boundary conditions, (b) tool geometry and (c) mesh of the chip and the machined workpiece.

Table 3.1 Parameters of the FE simulation model.

Tool	Length [mm]		Number of elements		Friction factor and coefficient			
	Workpiece	Cutting	Tool	Work	Rake		Flank	
					m	μ	m	μ
WC/Co	2.5	1.8	120,000	50,000	0.95	0.6	0.9	0.5
TiAlN	2.5	1.8	120,000	50,000	0.95	0.7	0.9	0.5

All 3-D FE simulations were run until a fully grown chip formation occurs at a fixed cutting length at respective cutting speeds. Each simulation takes about 12 hours on a PC with Intel i7-2600 3.4 GHz processor. In each simulation, it is concluded that the machining process reaches near its steady-state conditions in terms of generating acceptable fields of strain, strain rate and temperature for predicting the microstructure.

In order to fully calculate the microstructure resulting from continuous cutting, the effects of consecutive passes (cuts) can be investigated. Consecutive passes may change the microstructure due to increasing temperatures and different strain fields. In order to take these effects into account, an additional cutting pass is implemented in the 3-D FE simulations. To achieve this, the tool was first moved away from the workpiece upon reaching a fixed cutting length by moving it in the negative feed direction. The chip that had been generated after the first pass was then manually removed via element deletion close to its root, allowing disposal of excess heat stored in the chip. Upon the deletion of the chip, the workpiece was remeshed while preserving the element data. Then, the remaining heat in the workpiece was allowed to diffuse within the workpiece during the time the tool completes its revolution to begin a new cut. The tool travels in the feed direction during its revolution around the cutting axis. During this period where the tool is

not in contact with the workpiece, temperature and heat flux boundary conditions were removed from the workpiece and the tool to trap the heat within. This is an acceptable approach as in reality, other areas in the workpiece would be processed during this time that would lead to more heat generation in the surrounding areas, slowing down the cooling. Moreover, the thermal conductivity of the tool was set to 0 in order to preserve the hot zone at the tool tip to induce a realistic continuous cutting effect. After one revolution, the conductivity of the tool was restored upon contact with the workpiece, and boundary conditions on the tool and the workpiece were enabled again. When the tool touches the workpiece, tool elements were joined with the workpiece elements via contact conditions and the cutting process for the second pass begins. The cutting length for the second pass was chosen to be sufficiently long, while avoiding contact with the remaining chip root from the previous cut. Figure 3.2 shows the workpiece after chip removal, and temperature field on the workpiece at different stages of this process. After each pass (cut), simulation results were extracted from DEFORM-3D, and processed in MATLAB over a selected volume (extending up to 1 mm behind the chip in the machined zone) for each simulation (consistent among materials and feeds) using normalized element volumes as weights to accurately represent the given volume.

For the cases with the TiAlN coated WC/Co tool, the temperatures in the beginning of the 2nd cut range between 100-202 °C ($v_c=55$ m/min, $f=0.05$ mm/rev), 110-237 °C ($v_c=55$ m/min, $f=0.1$ mm/rev), 115-207 °C ($v_c=90$ m/min, $f=0.05$ mm/rev) and 102-274 °C ($v_c=90$ m/min, $f=0.1$ mm/rev). For the uncoated WC/Co tool ($r_\beta=25$ μ m), the temperatures range between 100-161 °C ($v_c=55$ m/min, $f=0.05$ mm/rev), 109-234 °C ($v_c=55$ m/min, $f=0.1$

mm/rev), 112-193 °C ($v_c=90$ m/min, $f=0.05$ mm/rev) and 100-267 °C ($v_c=90$ m/min, $f=0.1$ mm/rev). These initial temperature fields, sustained from the previous pass in the workpiece affect the subsequent simulation results.

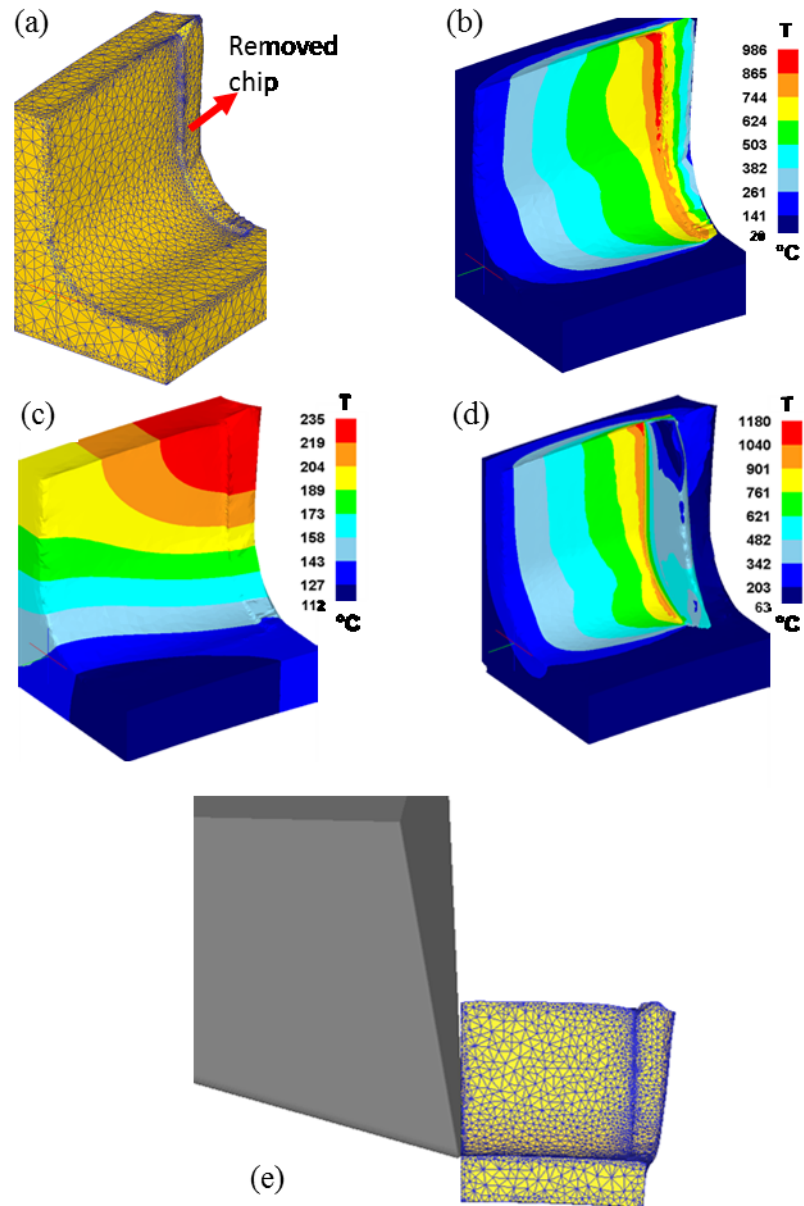


Figure 3.2 Finite element model geometry and temperature fields after the first cut;(a) workpiece mesh with removed chip, (b) temperature field after chip removal, (c) temperature field after diffusion, (d) temperature field during second cut, (e) tool and workpiece at the beginning of second pass.

3.2.1.2 Modified Material Constitutive Model

In 3-D FE simulations, a material constitutive model with modification to the Johnson-Cook (JC) material model to represent temperature-dependent flow softening behavior of high temperature titanium and nickel alloys has been used. The modified material model is given in Eq. (3.2) where flow stress (σ) of the material is being represented in terms of strain (ε), strain rate ($\dot{\varepsilon}$), and temperature (T) and where $\dot{\varepsilon}_0$ is the reference strain rate, T_0 is the ambient temperature, and T_m is the melting temperature of the material. This model includes the JC material model parameters (A, B, C, n, m) and modification parameters (a, b, d, r, s) that are used to describe temperature-dependent flow softening.

$$\sigma = \left[A + B\varepsilon^n \left(\frac{1}{\exp(\varepsilon^a)} \right) \right] \times \left[1 + C \ln \frac{\dot{\varepsilon}}{\dot{\varepsilon}_0} \right] \times \left[1 - \left(\frac{T - T_r}{T_m - T_r} \right)^m \right] \times \left[D + (1 - D) \left[\tanh \left(\frac{1}{(\varepsilon + p)^r} \right) \right]^s \right] \quad (3.2)$$

where $D = 1 - \left(\frac{T}{T_m} \right)^d$, and $p = \left(\frac{T}{T_m} \right)^b$.

Model parameters, given in Table 3.2, have been determined for Ti-6Al-4V titanium alloy by using experimental and simulated forces in 3-D FE simulations in an earlier study by (Ulutan and Özel, 2013b). First, the parameters of the original Johnson-Cook model, given in Eq. (3.3), were obtained from the literature (Lee and Lin, 1998) for the Ti-6Al-4V alloy $A=724.7, B=683.1, n=0.47, C=0.035, m=1$.

$$\sigma = \left[A + B\varepsilon^n \left(\frac{1}{\exp(\varepsilon^a)} \right) \right] \times \left[1 + C \ln \frac{\dot{\varepsilon}}{\dot{\varepsilon}_0} \right] \times \left[1 - \left(\frac{T - T_r}{T_m - T_r} \right)^m \right] \quad (3.3)$$

Using these parameters as basis, additional parameters of the modified JC model (Eq. 3.2) were obtained via an iterative procedure that compared the forces obtained from experiments with 3D FE simulations while varying model parameters B , n , a , b , d , r and s , within the ranges reported by various references (Calamaz et al., 2008; Sima and Özel, 2010). Parameters A , C and m were kept constant in order to preserve the flow stress at zero strain, the strain rate and temperature effects compared to the original JC model, respectively. However, parameters B , n , and a were varied until the combined prediction error in forces (F_c , F_p , F_f) was minimized. The differences between forces in all directions between the experiments and each simulation were used to calculate a normalized square error, and the parameters that minimized this error were chosen as final parameters.

Table 3.2 Modified Johnson-Cook material flow stress model parameters.

(Ulutan and Özel, 2013a)

Alloy	A	B	n	C	m	a	b	d	r	s
Ti-6Al-4V	725	300	0.65	0.035	1	0.5	2	0.5	12	-0.05

In order to fully utilize temperature-dependent modified material constitutive model in 3-D FE simulations, temperature-dependent physical, mechanical, and thermal properties of titanium alloy Ti-6Al-4V along with tool material and coating have been used as given in Table 3.3, and also their temperature dependent behavior is shown in Figure 3.3.

Table 3.3 Temperature dependent material properties for Ti-6Al-4V FE simulation.

(Ulutan and Özel, 2013a)

Property	WC/Co	TiAlN	Ti-6Al-4V
E [GPa]	5.6×10^2	6.0×10^2	$7.4 \times 10^{-4}T + 113$
α [$1/^\circ\text{C}$]	4.7×10^{-6}	9.4×10^{-6}	$3 \times 10^{-9}T + 7 \times 10^{-6}$
k [W/m $^\circ\text{C}$]	55	$8.1 \times 10^{-3}T + 11.95$	$7.039 \times e^{0.0011T}$
c_p [N/mm 2 $^\circ\text{C}$]	$5 \times 10^{-4}T + 2.07$	$3 \times 10^{-4}T + 0.57$	$2.24 \times e^{0.0007T}$

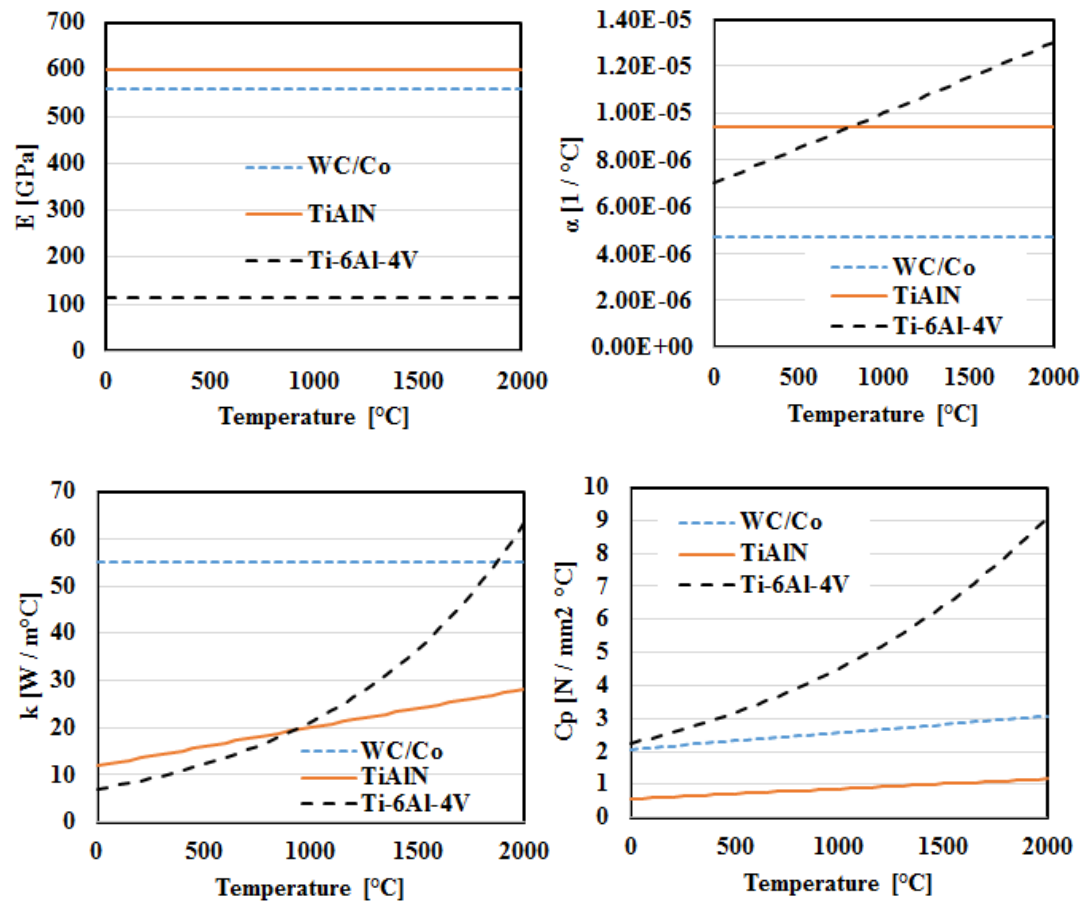


Figure 3.3 Temperature dependent material properties for Ti-6Al-4V FE simulation.

3.2.1.3 Microstructure Modeling Using JMAK Model

It has been reported that the machining process affects the Ti-64 microstructure and its grain size (Arrazola et al., 2009; Nalla et al., 2003). In thermal-mechanical processing of metal alloys, the onset of thermal recovery/recrystallization generally occurs at about $0.4-0.5 \times T_m$ which is 500-690°C for Ti-64 alloy ($T_m=1922\text{K}$). Therefore dynamic recrystallization will take place in the regions of such temperatures combined with large plastic deformations. For this reason, JMAK grain size model given in Eqs. (1.1)-(1.5) has been utilized to study the effects of machining parameters in machining Ti-64. The JMAK model parameters have been identified after running a sweep / sensitivity analysis on DEFORM-3D FE simulations by monitoring average α -grain size. These parameters are partially based on (Yi et al., 2008) with the activation energy for Ti-6Al-4V taken as $Q_{act}=218$ [kJ/mol] as reported by (Ding et al., 2002), and are given in Table 3.4.

Table 3.4 JMAK model parameters for Ti-6Al-4V.

Peak Strain								
a_1	h_1		m_1		$m_1 \times Q_{act}$	c_1	a_2	
2	0		0.006		1308	0	0.8	
DRx Kinetics								
a_5	h_5	n_5	m_5	$m_5 \times Q_{act}$	β_d	c_5	k_d	a_{10}
1.21×10^{-5}	0.13	0	0.04	8720	0.693	0	2	0
DRx Grain Size								
a_8	h_8	n_8	m_8		$m_8 \times Q_{act}$	c_8		
150	0	0	-0.03		-6540	0		

3.2.1.4 Microstructure Prediction Results

3-D FE simulations for all cutting conditions in turning of Ti-6Al-4V were conducted by using the microstructure model given in the previous section. Thermal-mechanical transformation kinetics including dynamic recrystallization were predicted and resultant field variables such as temperature (T), peak strain (ε_p), dynamic recrystallized volume fraction (X_{DRx}) and grain size (d_{DRx}), and average grain size including the recrystallized grains (d_{avg}) were extracted. Their volume weighted averages for all of these process variables were calculated in MATLAB and their histograms together with mean and standard deviations were obtained after first and second cutting passes. These predicted field variables and measured average grain sizes are given in Table 3.5 for machining Ti-6Al-4V. Predicted temperature (T) fields are shown for different cutting conditions and tools (coated and uncoated) in Figures 3.4-3.5. In addition, the dynamic recrystallized volume fraction (X_{DRx}) and average grain size (d_{avg}) are shown in Figures 3.6-3.7 and Figures 3.8-3.9 respectively.

Table 3.5 Predicted field variables (weighted means over the selected volume) during first and second pass with against the measured grain size of microstructure in machined surfaces.

Tool	v_c [m/min]	f [mm/rev]	Predicted field variables (Pass 1)					Predicted field variables (Pass 2)					Exp. d_{avg} [μm]
			T	ε_p	X_{DRx}	d_{DRx}	d_{avg}	T	ε_p	X_{DRx}	d_{DRx}	d_{avg}	
			[$^{\circ}\text{C}$]			[μm]	[μm]	[$^{\circ}\text{C}$]			[μm]	[μm]	
WC/Co (TiAlN)	55	0.05	302.86	2.16	0.37	7.46	17.38	406	2.00	0.39	7.81	17.57	14.66
		0.1	414.46	2.37	0.39	7.81	17.07	473	2.11	0.37	7.40	17.23	13.09
	90	0.05	307.21	2.22	0.31	6.18	17.60	443	1.98	0.43	8.47	17.91	14.40
		0.1	439.32	2.31	0.39	7.69	17.40	530	2.05	0.45	8.94	17.75	14.95
WC25	55	0.05	265.30	2.24	0.29	5.86	17.41	387	2.05	0.39	7.64	17.35	13.03
		0.1	402.82	2.33	0.35	7.00	17.03	477	2.16	0.36	7.14	16.96	14.39
	90	0.05	289.96	2.24	0.30	5.98	17.62	431	2.02	0.43	8.47	17.77	16.17
		0.1	436.28	2.30	0.40	8.04	17.30	500	2.03	0.43	8.55	17.72	13.57

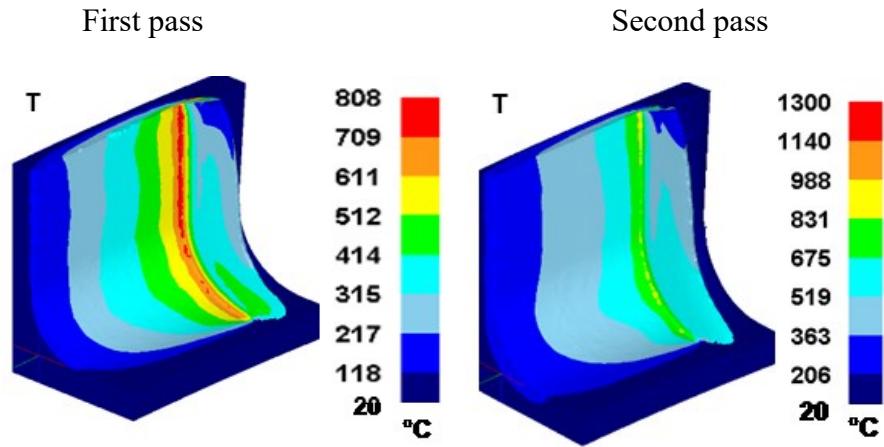


Figure 3.4 (a) TiAlN coated WC/Co tool ($r_f=10\text{ }\mu\text{m}$), $v_c=55\text{ m/min}$, $f=0.05\text{ mm/rev}$

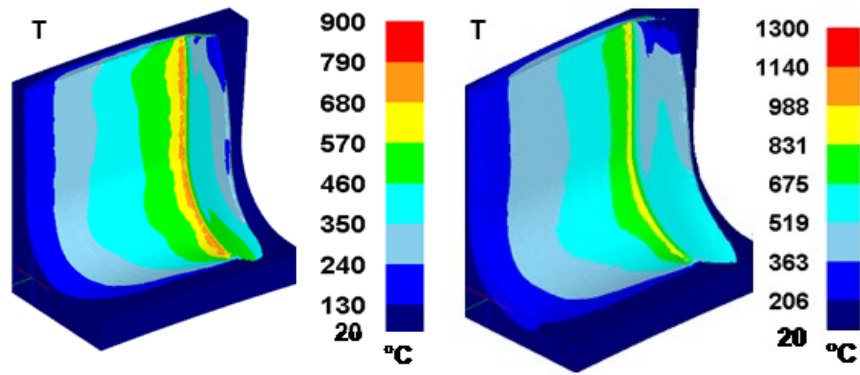


Figure 3.4 (b) TiAlN coated WC/Co tool ($r_f=10\text{ }\mu\text{m}$), $v_c=90\text{ m/min}$, $f=0.05\text{ mm/rev}$

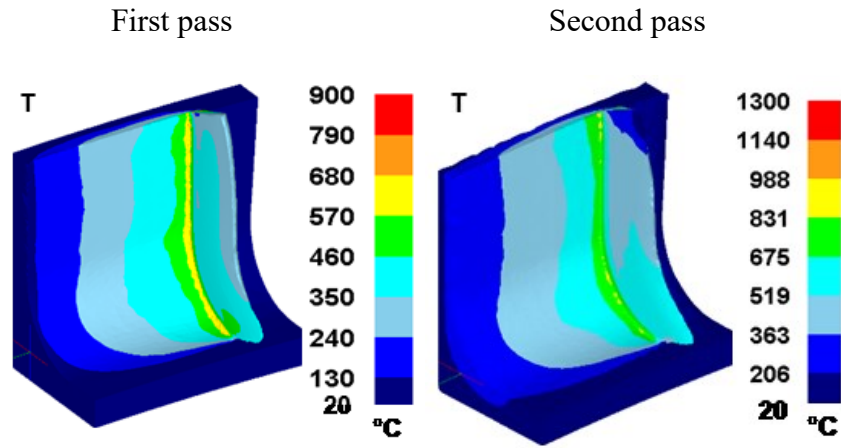


Figure 3.4 (c) WC/Co tool ($r_\beta = 25 \mu\text{m}$), $v_c = 55 \text{ m/min}$, $f = 0.05 \text{ mm/rev}$

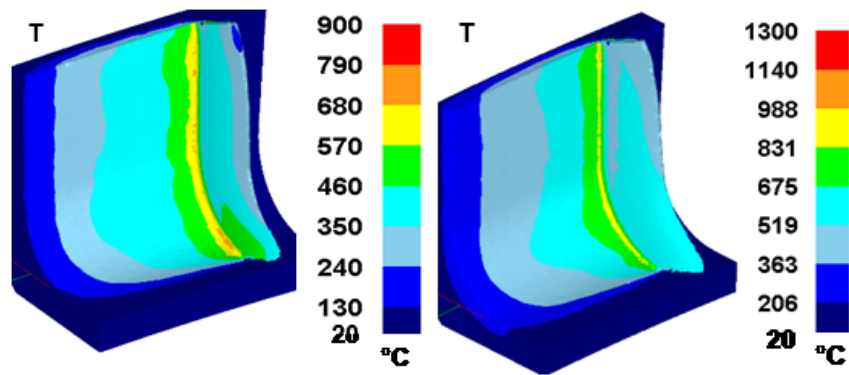


Figure 3.4 (d) WC/Co tool ($r_\beta = 25 \mu\text{m}$), $v_c = 90 \text{ m/min}$, $f = 0.05 \text{ mm/rev}$

Figure 3.4 Predicted temperature fields in FE simulations after first pass (left), second pass (right) at the low feed rate ($f = 0.05 \text{ mm/rev}$).

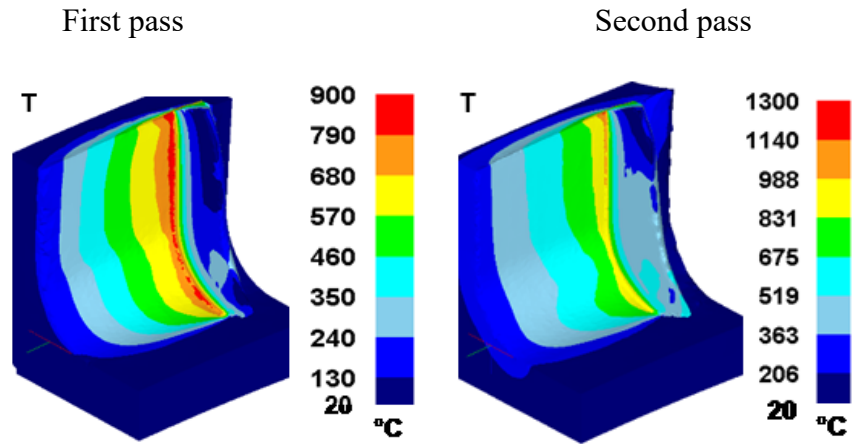


Figure 3.5 (a) TiAlN coated WC/Co tool ($r_\beta=10$ μm), $v_c=55$ m/min, $f=0.10$ mm/rev

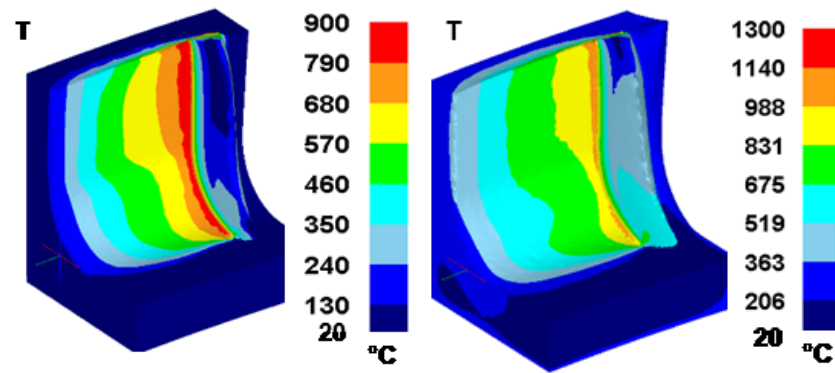


Figure 3.5 (b) TiAlN coated WC/Co tool ($r_\beta=10$ μm), $v_c=90$ m/min, $f=0.10$ mm/rev

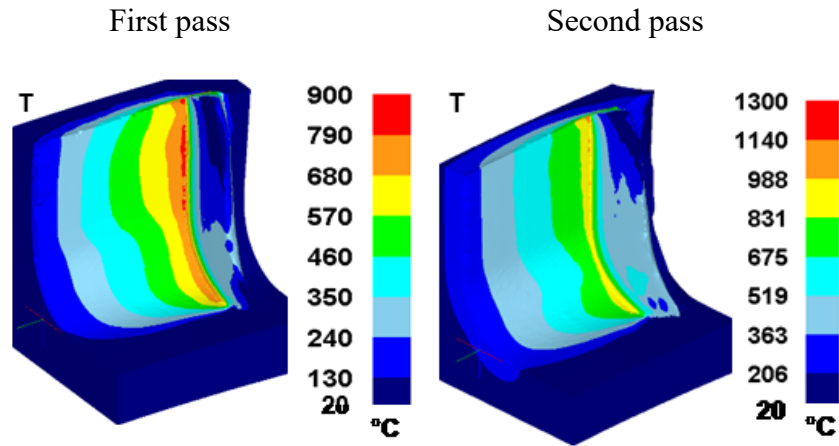


Figure 3.5 (c) WC/Co tool ($r_\beta=25\ \mu\text{m}$), $v_c=55\ \text{m/min}$, $f=0.10\ \text{mm/rev}$

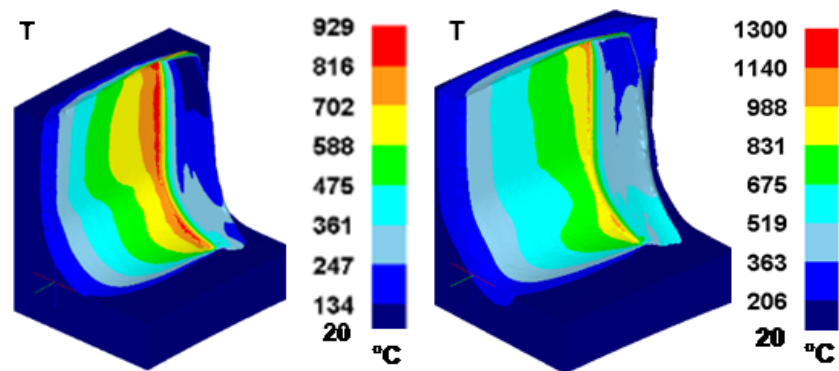


Figure 3.5 (d) WC/Co tool ($r_\beta=25\ \mu\text{m}$), $v_c=90\ \text{m/min}$, $f=0.10\ \text{mm/rev}$

Figure 3.5 Predicted temperature fields in FE simulations after first pass (left), second pass (right) at the high feed rate ($f=0.10\ \text{mm/rev}$).

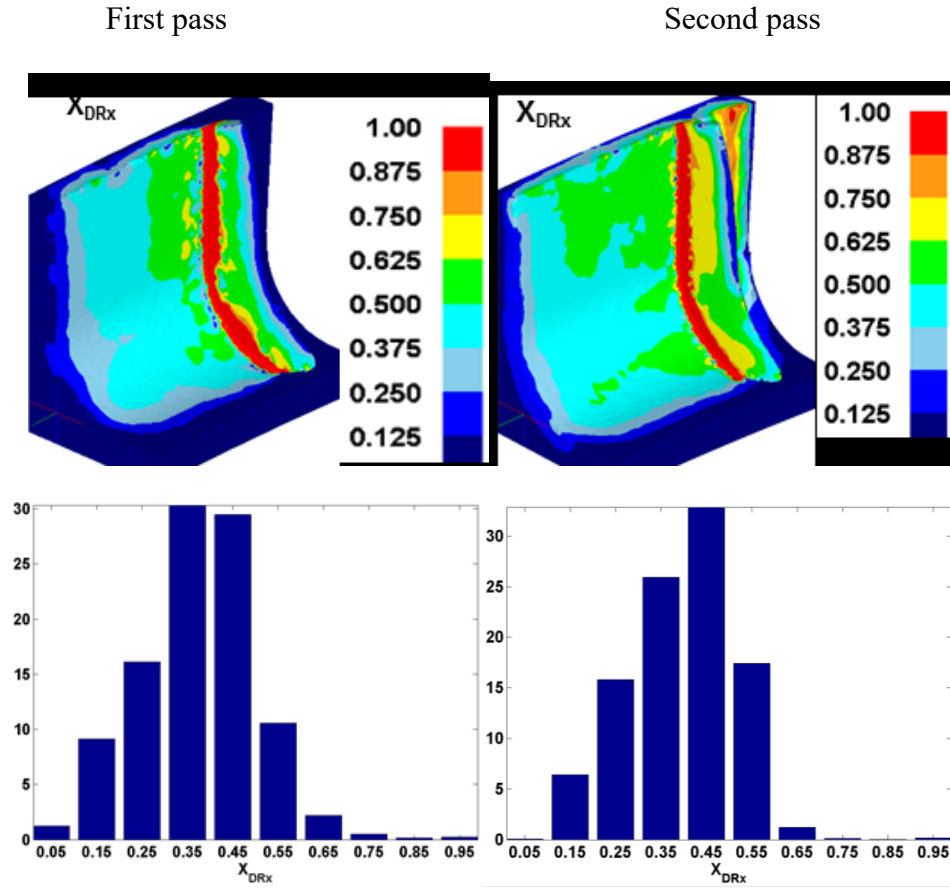


Figure 3.6 (a) TiAlN coated WC/Co tool ($r_f=10\text{ }\mu\text{m}$), $v_c=55\text{ m/min}$, $f=0.05\text{ mm/rev}$

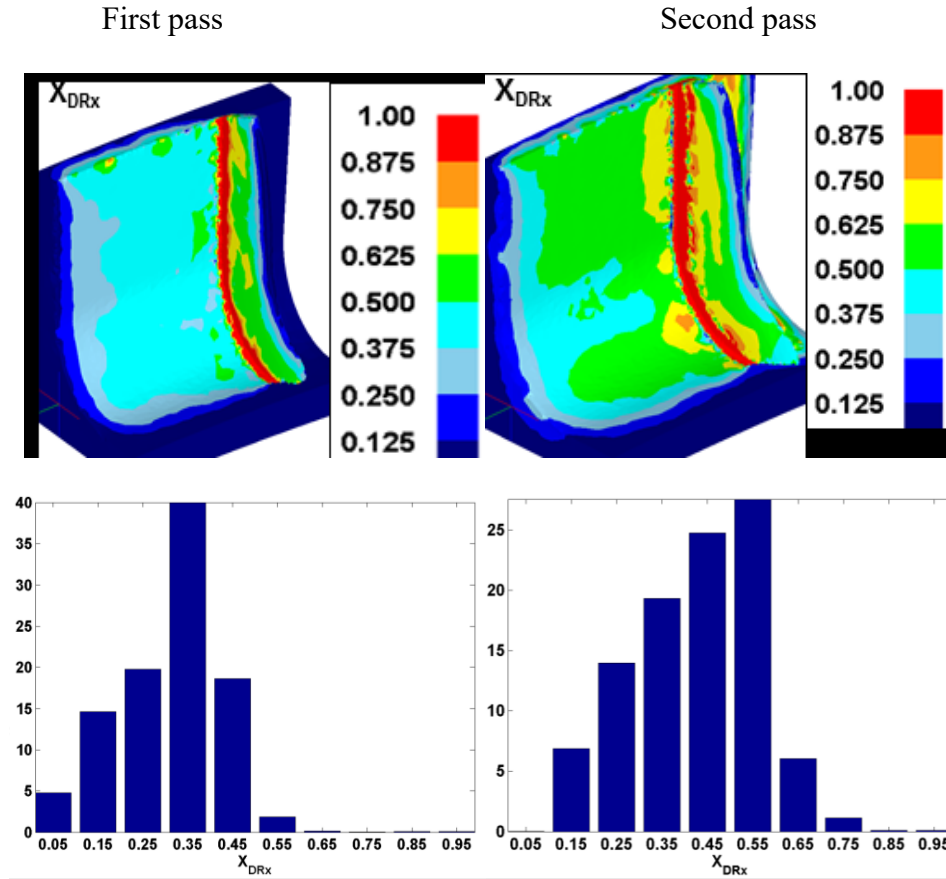


Figure 3.6 (b) TiAlN coated WC/Co tool ($r_\beta=10\ \mu\text{m}$), $v_c=90\ \text{m/min}$, $f=0.05\ \text{mm/rev}$

First pass

Second pass

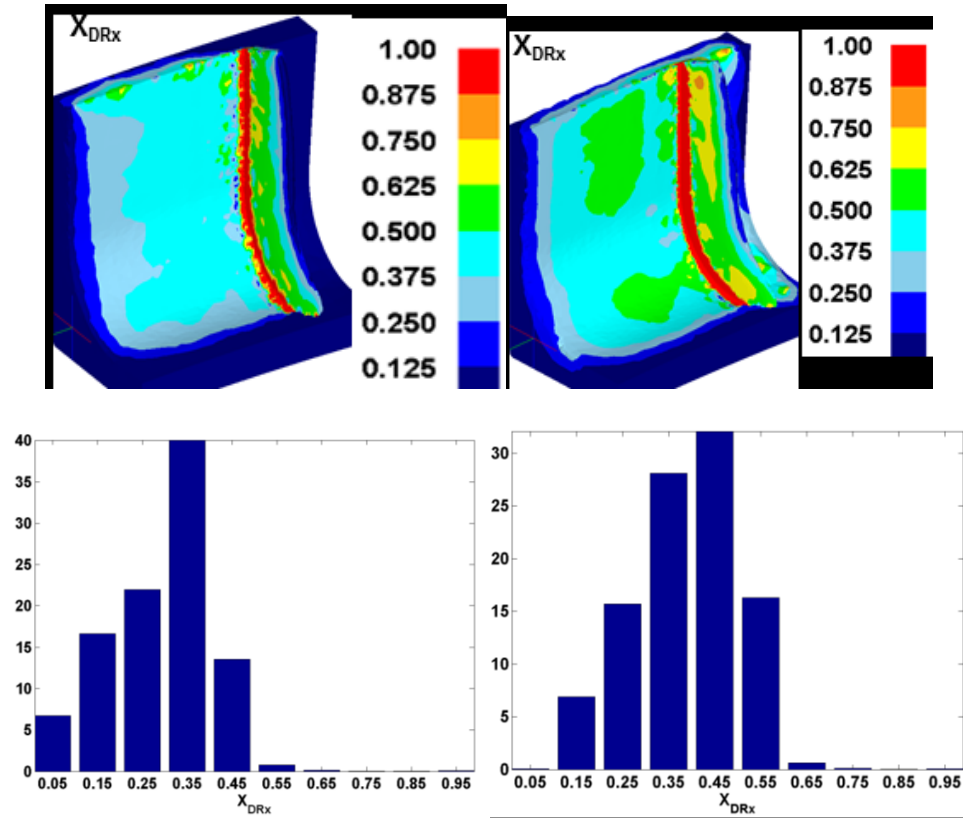


Figure 3.6 (c) WC/Co tool ($r_\beta=25\ \mu\text{m}$), $v_c=55\ \text{m/min}$, $f=0.05\ \text{mm/rev}$

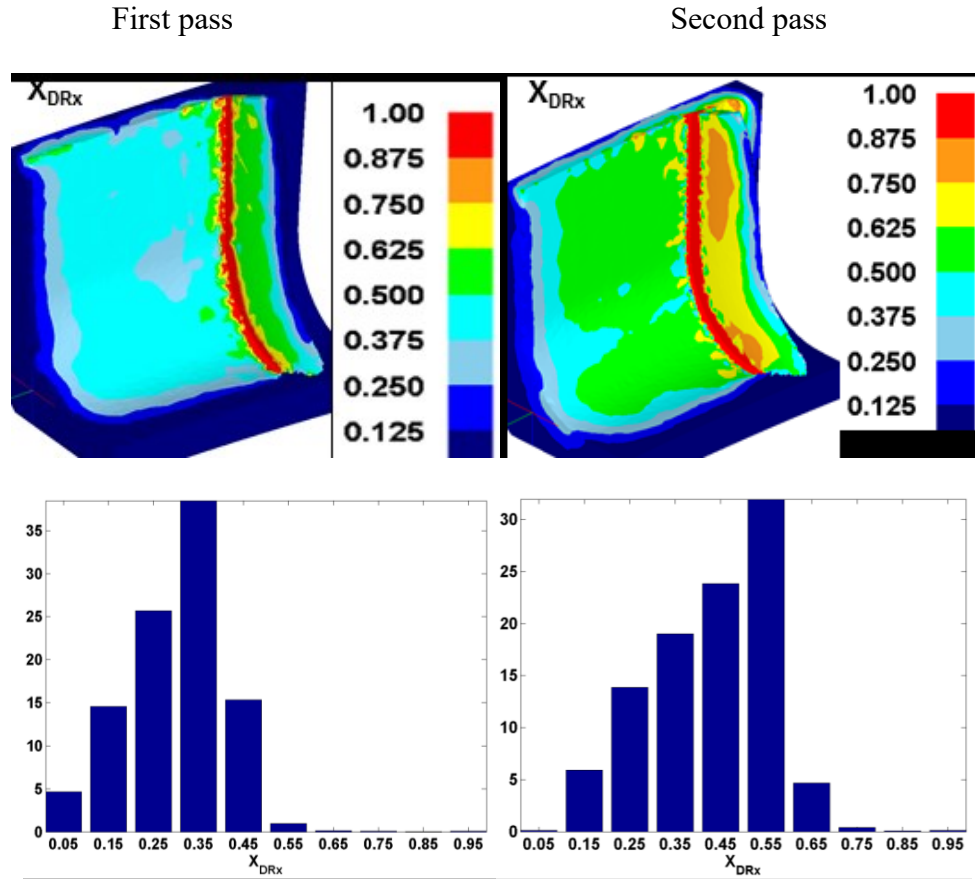


Figure 3.6 (d) WC/Co tool ($r_\beta=25\ \mu\text{m}$), $v_c=90\ \text{m/min}$, $f=0.05\ \text{mm/rev}$

Figure 3.6 Predicted dynamic recrystallization volume fraction fields in FE simulations, after first pass (left), second pass (right) at the low feed rate ($f=0.05\ \text{mm/rev}$).

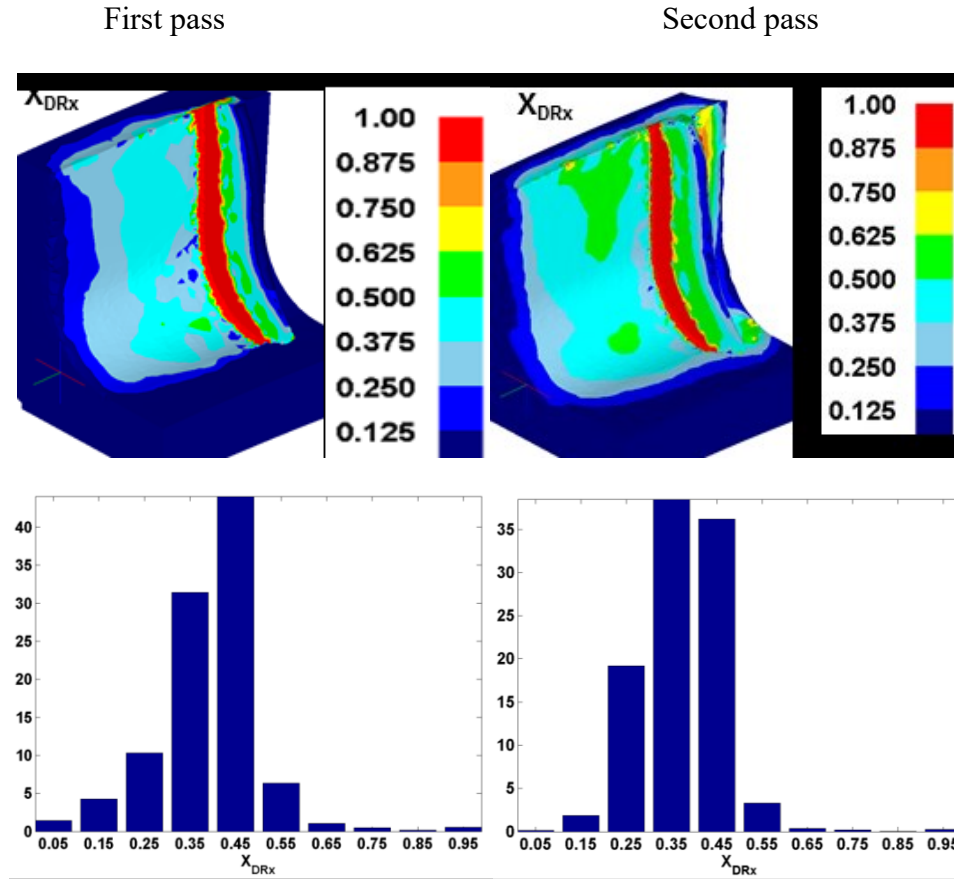


Figure 3.7 (a) TiAlN coated WC/Co tool ($r_\beta=10\ \mu\text{m}$), $v_c=55\ \text{m/min}$, $f=0.10\ \text{mm/rev}$

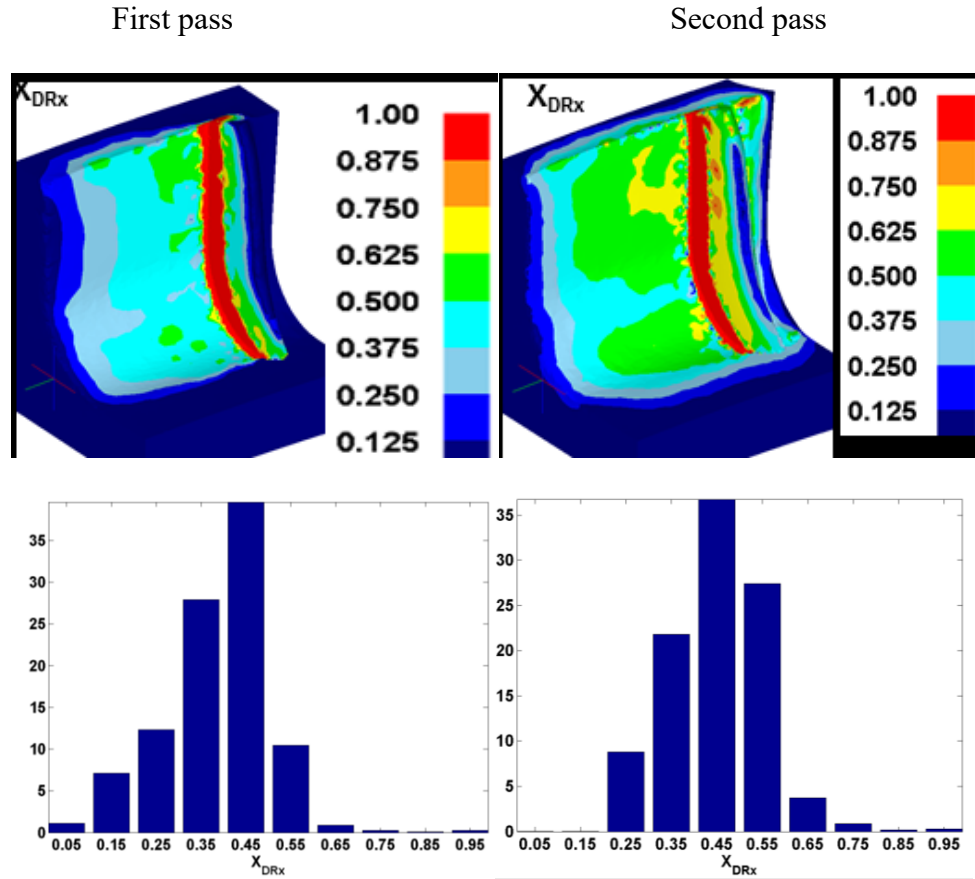


Figure 3.7 (b) TiAlN coated WC/Co tool ($r_\beta=10\ \mu\text{m}$), $v_c=90\ \text{m/min}$, $f=0.10\ \text{mm/rev}$

First pass

Second pass

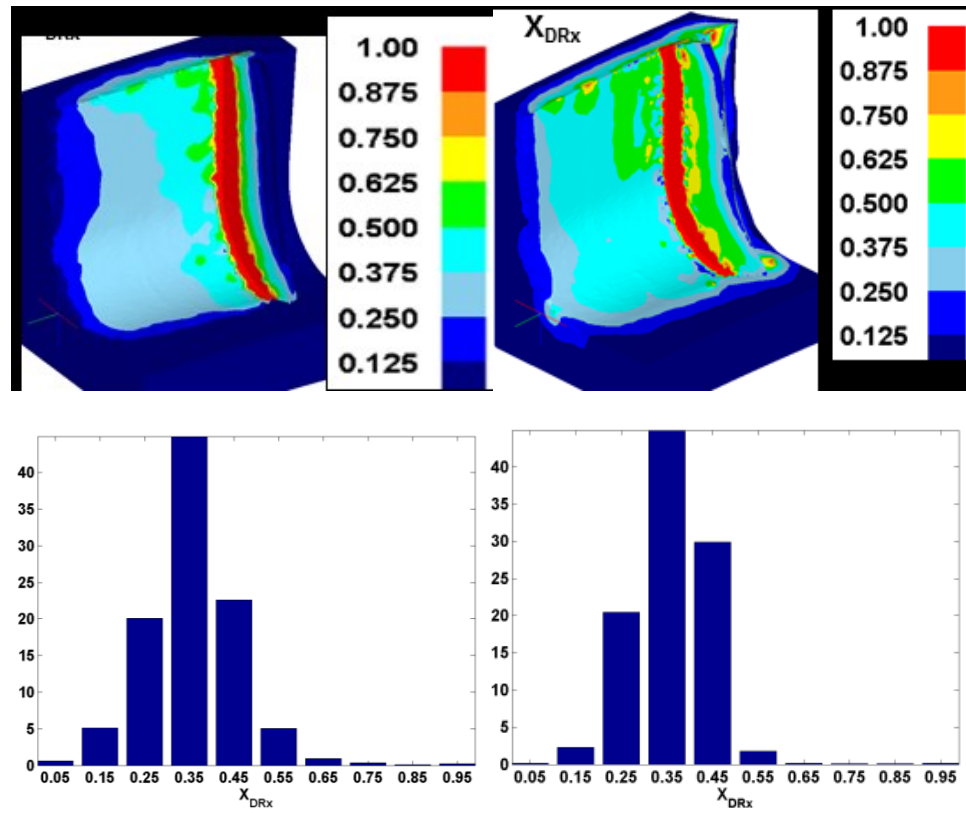


Figure 3.7 (c) WC/Co tool ($r_\beta = 25 \mu\text{m}$), $v_c = 55 \text{ m/min}$, $f = 0.10 \text{ mm/rev}$

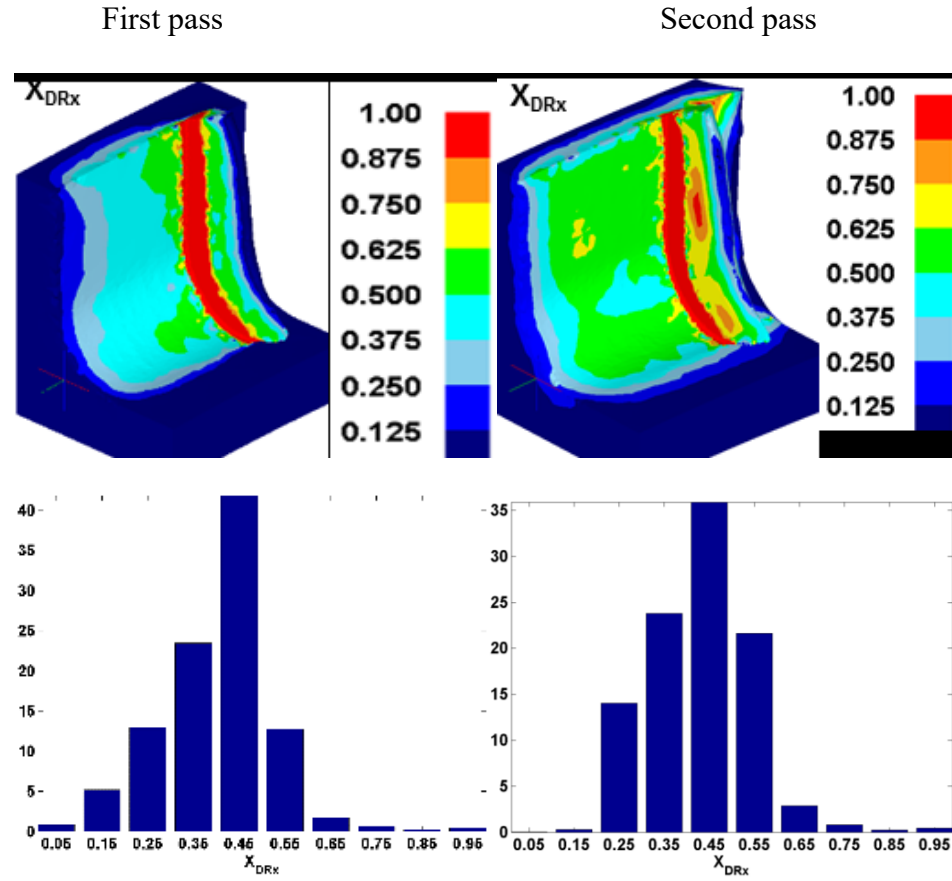


Figure 3.7 Predicted dynamic recrystallization volume fraction fields in FE simulations, after first pass (left), second pass (right) at the high feed rate ($f=0.10\ \text{mm/rev}$).

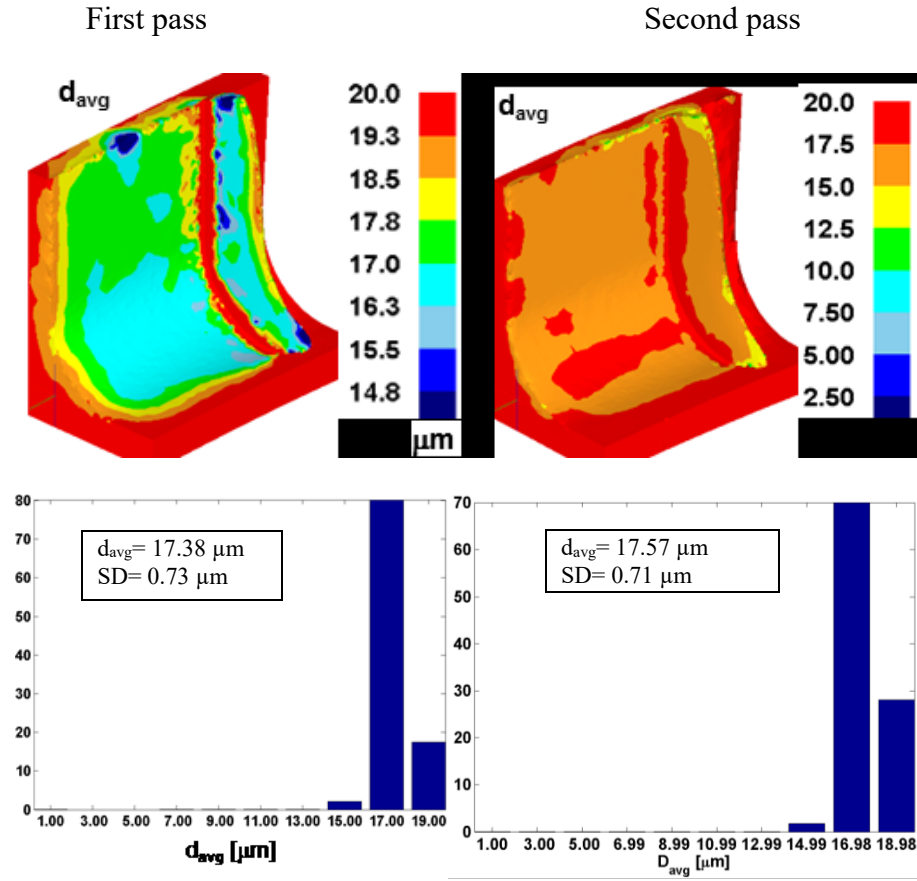


Figure 3.8 (a) TiAlN coated WC/Co tool ($r_\beta=10 \mu\text{m}$), $v_c=55 \text{ m/min}$, $f=0.05 \text{ mm/rev}$

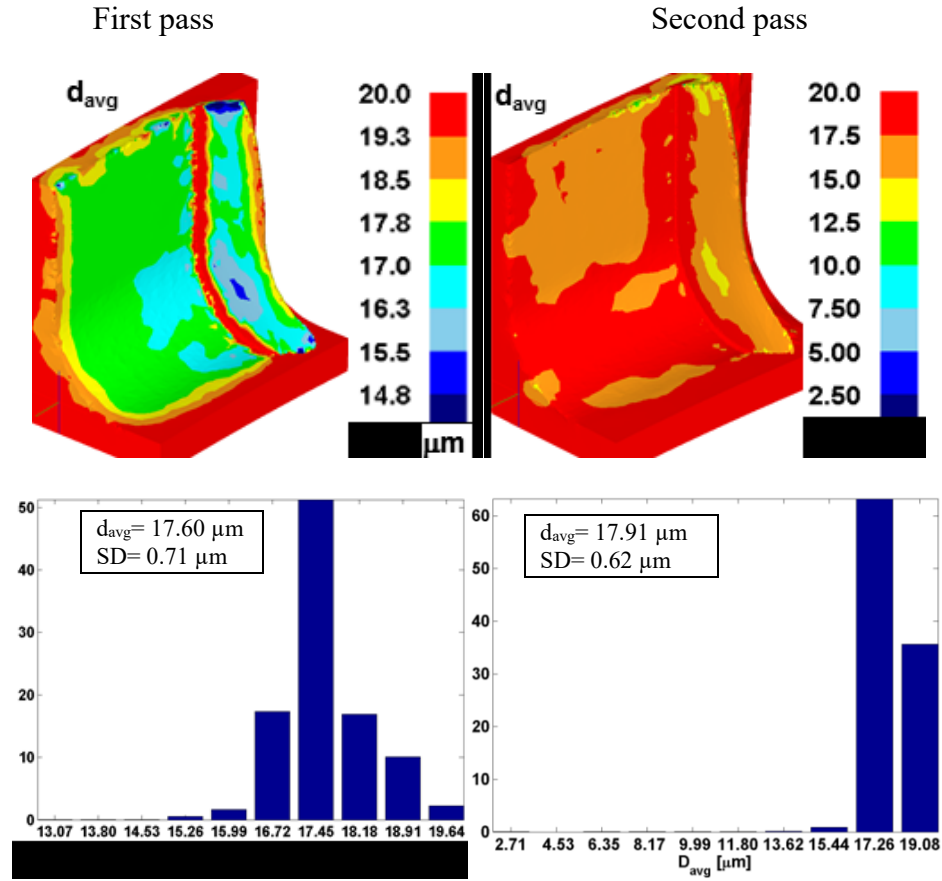


Figure 3.8 (b) TiAlN coated WC/Co tool ($r_{\beta}=10 \mu\text{m}$), $v_c=90 \text{ m/min}$, $f=0.05 \text{ mm/rev}$

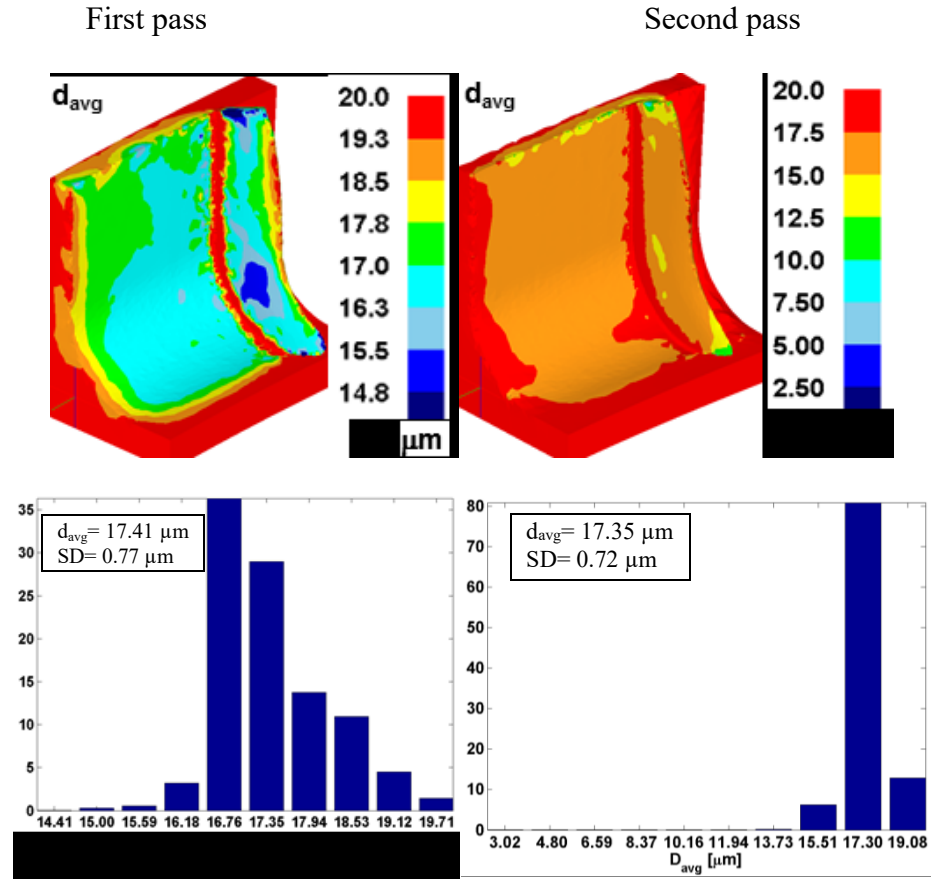


Figure 3.8 (c) WC/Co tool ($r_\beta=25 \mu\text{m}$), $v_c=55 \text{ m/min}$, $f=0.05 \text{ mm/rev}$

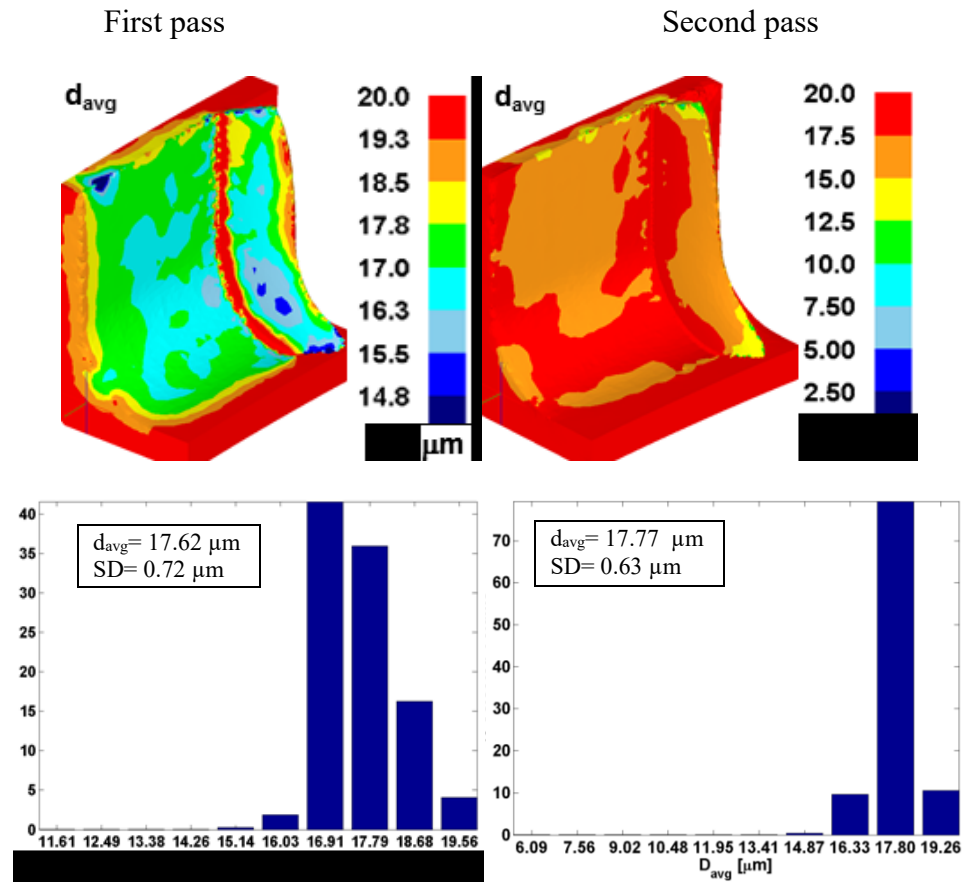


Figure 3.8 (d) WC/Co tool ($r_\beta=25 \mu m$), $v_c=90$ m/min, $f=0.05$ mm/rev

Figure 3.8 Predicted average grain size fields in FE simulations, after first pass (left), second pass (right) at the low feed rate ($f=0.05$ mm/rev).

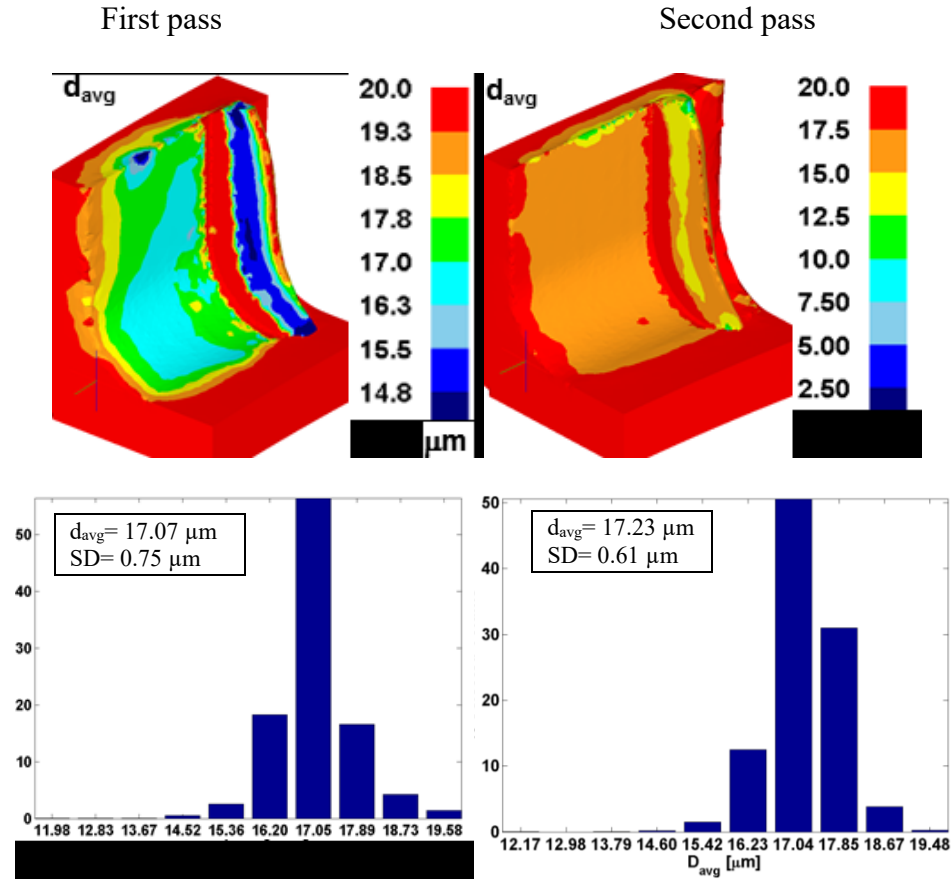


Figure 3.9 (a) TiAlN coated WC/Co tool ($r_\beta=10 \mu\text{m}$), $v_c=55 \text{ m/min}$, $f=0.10 \text{ mm/rev}$

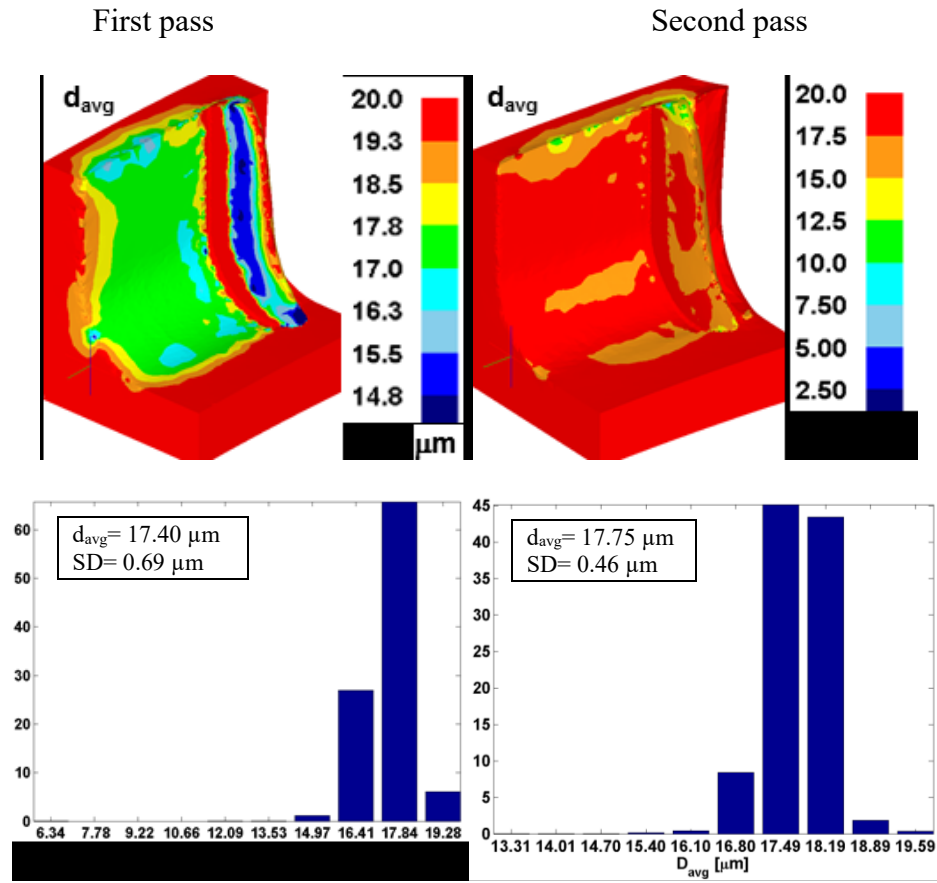


Figure 3.9 (b) TiAlN coated WC/Co tool ($r_\beta=10 \mu\text{m}$), $v_c=90 \text{ m/min}$, $f=0.10 \text{ mm/rev}$

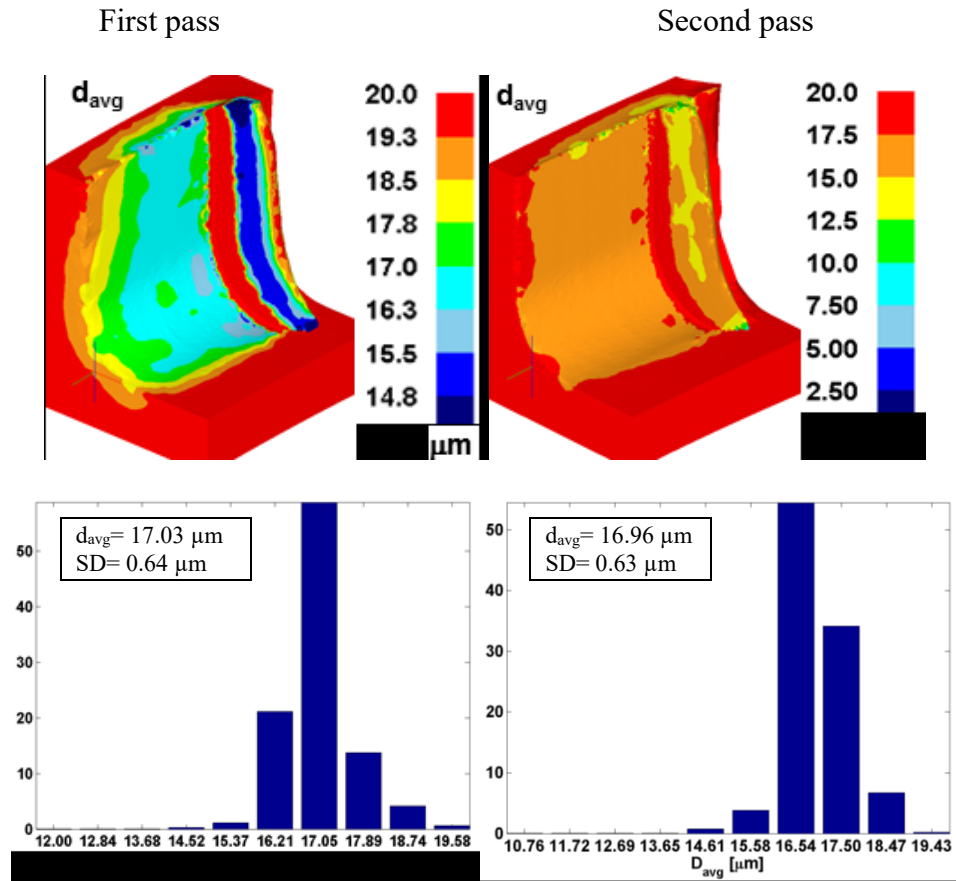


Figure 3.9 (c) WC/Co tool ($r_\beta=25 \mu\text{m}$), $v_c=55 \text{ m/min}$, $f=0.10 \text{ mm/rev}$

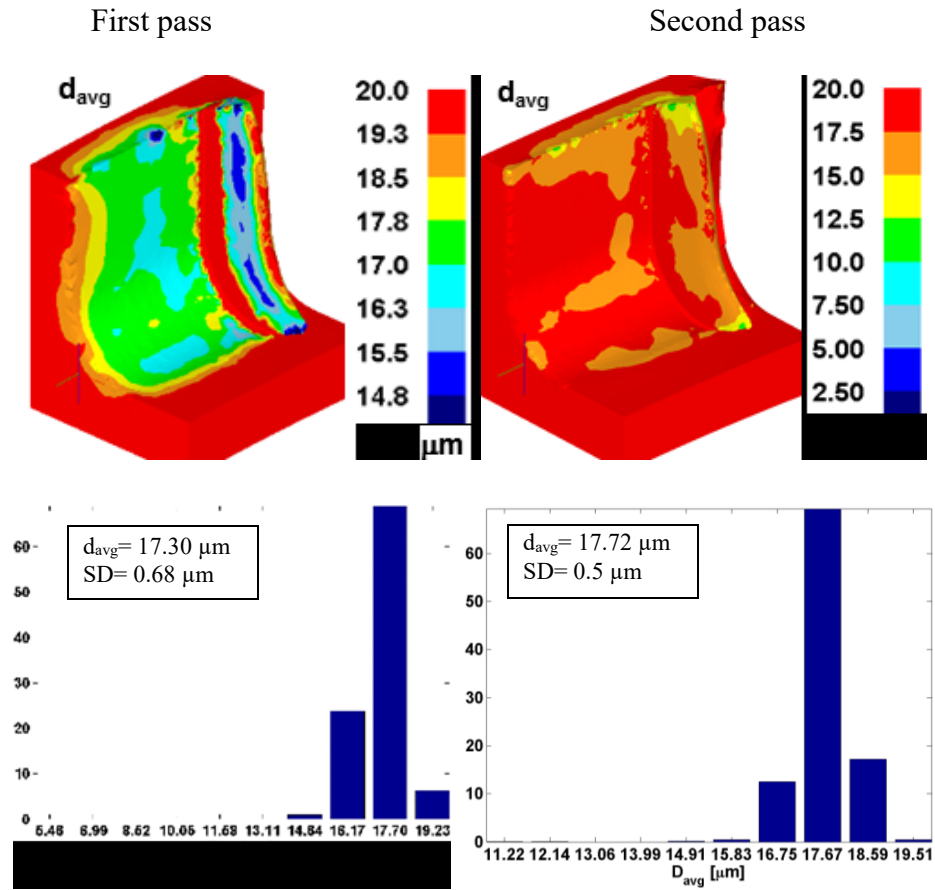


Figure 3.9 (d) WC/Co tool ($r_\beta=25 \mu m$), $v_c=90$ m/min, $f=0.10$ mm/rev

Figure 3.9 Predicted average grain size fields in FE simulations, after first pass (top), second pass (bottom) at the high feed rate ($f=0.10$ mm/rev).

Comparison plots for predicted average grain diameter (or size) from first and second passes are given in Figure 3.10 for machining Ti-6Al-4V. It is observed that the dynamic recrystallized volume fraction is about 30-40% in machining Ti-6Al-4V. The average grain size became smaller (compared to the initial grain size $d_0 = 20 \mu\text{m}$) in all machining conditions for both Ti-6Al-4V indicating that the recrystallized grains contribute to this smaller average grain size hence machining affected microstructure. It should be noted that grain growth (from annealing) is not being considered in FE simulations due to rapid cooling rates of the machined surfaces.

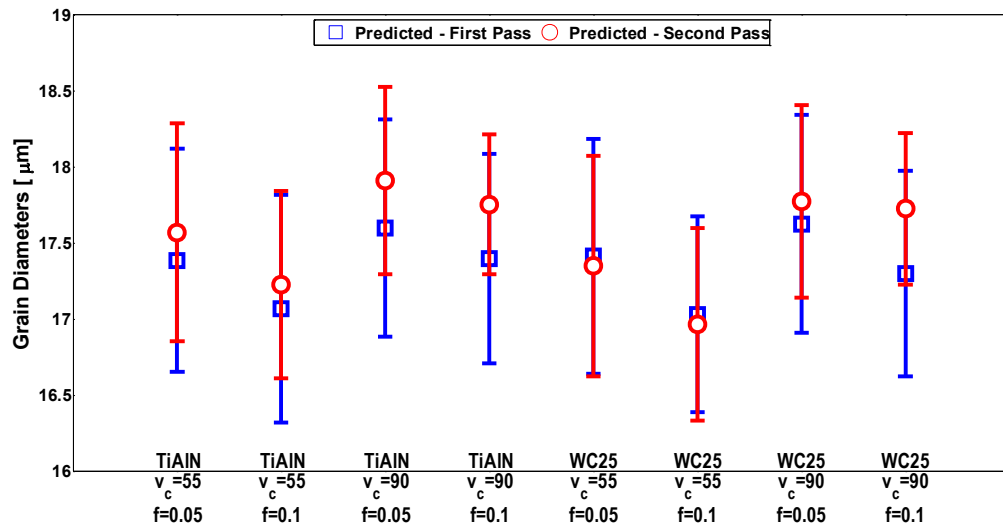


Figure 3.10 Comparison of predicted average α -grain sizes (mean and standard deviation) in machined Ti-6Al-4V sub-surfaces.

3.2.2 Microstructure Modeling of IN100 Alloy

As described in Chapter 1, IN100 microstructure mainly consists of two phases; γ and γ' where γ phase consists of the large grains that form the matrix in the material whereas γ' is formed as a result of various processes (Kikuchi et al., 1990; Wusatowska-Sarnek et al., 2003a; Wusatowska-Sarnek et al., 2003b; Milligan et al., 2004). The face-centered-cubic austenitic γ phase consists of large grains (3-4 μm) that form the matrix in the material whereas precipitating γ' phase grains (<1.5 μm) are formed as a result of various processes. Three sizes of γ' grains have been observed: primary γ' (1.25-1.3 μm with 25% volume fraction), secondary γ' (\sim 0.1 μm with 32% volume fraction) and tertiary γ' (\sim 20 nm with 0.24% volume fraction).

During the machining process, the microstructure is altered due to large plastic deformations and temperatures. Work hardening is often observed during machining of IN100 and is linked to white layer formation, which is a region close to the surface where a large amount of recrystallization occurs that results in much smaller grains and increased strength. The name is attributed to the white color of the region in optical microscopy imaging. Ranganath et al. (Ranganath et al., 2009) investigated the white layer formation in IN100 after machining using orthogonal cutting and finite element simulations. While the white layer formation was not detected due to relatively short cutting times, the effects of machining caused strain hardening was evident, with elongated grains near the machined surface. They also found out that low speed machining with large edge radius produced harder surfaces, with deformed layers being 2-3 times harder when compared to the bulk material.

M'Saoubi et al. (M'Saoubi et al., 2014) investigated the effect of abusive drilling on Nickel superalloys Alloy 718, Waspaloy, Alloy 720Li and RR1000 using Electron Backscatter Diffraction (EBSD), X-Ray Diffraction (XRD), Transmission Electron Microscopy (TEM), SEM and nano indentation. Nano-sized grains were observed in the severe plastic deformation (SPD) zone and plastic slip bands in sub-surface layers. Nano indentation results suggested a work hardening near the machining surface, and the TEM results show equiaxed ultra-fine grained microstructure that was attributed to recrystallization. RR1000 and Alloy 720Li exhibited a larger SPD zone and higher nanohardness compared to the other two alloys. Additionally, the Zener-Hollomon parameter was used to obtain the grain size based on strain rate and temperature.

In order to study the effects of machining parameters in machining IN100 alloy, finite element simulations have been performed using the JMAK grain size model, as discussed before.

3.2.2.1 Finite Element Simulation Setup for Machining of IN100 Alloy

3D FE simulations for face turning have been conducted for selected experimental conditions using DEFORM-3D software similar to the previous studies (Ulutan and Ozel, 2011; Sun et al., 2010). In the 3D FE simulations, curved workpiece geometry was modelled as viscoplastic. A higher mesh density was used in a 3 mm-long section behind the chip to better resolve the temperature and strain fields that are necessary for the microstructure calculations on the machined surface as shown in Figure 3.11. The friction between the tool and the workpiece was described with a hybrid model including shear

The same material constitutive model given in Eq. 3.2 has been used for IN100 alloy, with different parameters. Model parameters for the IN100 alloy have been determined by matching experimental and simulated forces through iterations in 3D FE simulations (Ulutan and Özel, 2013b) and are given in Table 3.7. Temperature-dependent physical, mechanical, and thermal properties of IN100 alloy along with tool material and coating used in FE simulations are given in Table 3.8 and Figure 3.12.

Table 3.7 Material flow stress model parameters for IN100 alloy.

(Ulutan and Özel, 2013a)

<i>A</i>	<i>B</i>	<i>n</i>	<i>C</i>	<i>m</i>	<i>a</i>	<i>b</i>	<i>d</i>	<i>r</i>	<i>s</i>
1350	1750	0.65	0.017	1.3	1.5	10	0.01	1.5	-0.4

Table 3.8 Temperature-dependent material properties for IN100 alloy.

(Ulutan and Özel, 2013a)

Property	WC/Co	TiAlN	IN100
E [GPa]	5.6×10^5	6.0×10^5	$-72 \times T + 217000$
α [1/°C]	4.7×10^{-6}	9.4×10^{-6}	1.1×10^{-5}
k [W/m×°C]	55	$0.0081T + 11.95$	$10.3 \times e^{0.0008 \times T}$
c_p [N/mm ² °C]	$5 \times 10^{-4}T + 2.07$	$0.0003T + 0.57$	$3.62 \times e^{0.0004 \times T}$

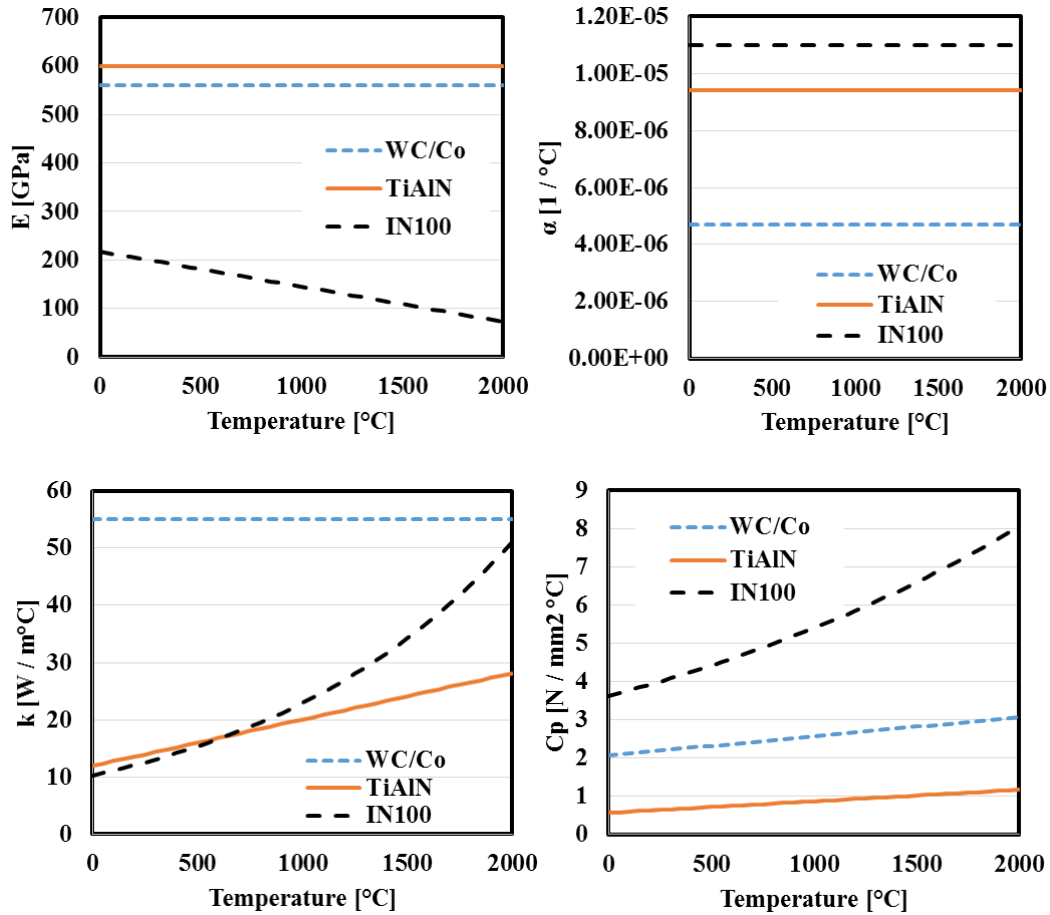


Figure 3.12 Temperature dependent material properties for the IN100 alloy FE simulation.

3.2.2.2 Microstructure Prediction Results

Experimental microstructure results under hot deformation conditions are often used to determine the constants for recrystallized fraction and grain size. Two sets of FE simulations have been run for predicting γ matrix grains and primary γ' grains. The JMAK model parameters for the first set of simulations for γ matrix grains have been obtained using the parameters of a similar Nickel based alloy as a starting point (Shen, 2005), and

modifying them through a careful sensitivity analysis. Since the γ matrix grains could not be identified in the SEM measurements shown in Chapter 2, the average γ matrix grain size was taken as $d_0=3.5 \mu\text{m}$ (Kikuchi et al., 1990). JMAK parameters are given in Table 3.9.

For the second set of simulations to predict primary γ' grains, JMAK model parameters have been identified using Genetic Algorithm based optimization on the FE simulations to minimize the difference with FE predicted and SEM measured average grain sizes. A reduced model of the Sharp tool, $v_c = 12 \text{ m/min}$, $f = 0.05 \text{ mm/rev}$ simulation was used and parameters $a_1, h_1, m_1, a_2, a_5, h_5, m_5, a_8, n_8$ and m_8 were changed while other parameters were kept constant. Population size was selected as 8 in order to run 8 simulations in parallel for each generation. Initial population included the JMAK parameters for Waspoloy (Shen, 2005), and the final parameters are given in Table 3.10. Once the optimum JMAK parameters were found, they were used for all cutting conditions and tools to predict primary γ' grains. Apparent activation energy of $Q_{act}=348000 \text{ J/mol}$ (Kikuchi et al., 1990) was used for both cases, and initial grain sizes of $d_0= 3.5 \mu\text{m}$ for γ matrix grains and $d_0= 1.28 \mu\text{m}$ for primary γ' grains (Milligan et al., 2004) were used. The methodology is further explained in Chapter 5.

Substantial recrystallization with dynamic recrystallized volume fraction of 30-35% has been predicted in the simulations. A comparison plot for predicted and measured average grain size for primary gamma prime (γ') grains is given in Figure 3.13 indicating mostly reasonable agreements. 3D FE simulation results of average grain sizes for both γ matrix

and primary γ' grains on machined surfaces using uncoated WC/Co and TiAlN coated tools are shown in Figures 3.14-3.17.

Table 3.9 JMAK model parameters for IN100 alloy γ matrix grain simulations.

a_1	h_1	m_1	c_1	a_2	β_d
0.293	0	0.0102	0	0.8	0.693
a_5	h_5	m_5	n_5	c_5	k_d
0.145	0.32	0.03	0	0	3
a_8	h_8	m_8	n_8	c_8	a_{10}
8103	0	-0.16	0	0	0

Table 3.10 JMAK model parameters for IN100 alloy primary γ' grain simulations.

a_1	h_1	m_1	c_1	a_2	β_d
0.293	0.34	0.039	0	0.38	0.693
a_5	h_5	m_5	n_5	c_5	k_d
0.145	0.48	0.03	0	0	3
a_8	h_8	m_8	n_8	c_8	a_{10}
8103	0	-0.16	0.43	0	0

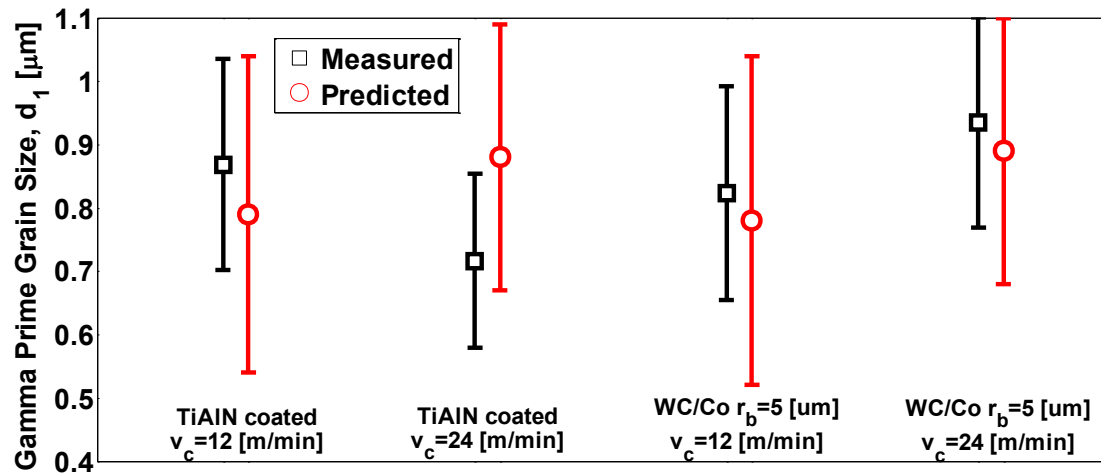


Figure 3.13 Comparison of predicted and measured (primary γ') average grain size (mean and standard deviation) on IN100 alloy subsurface.

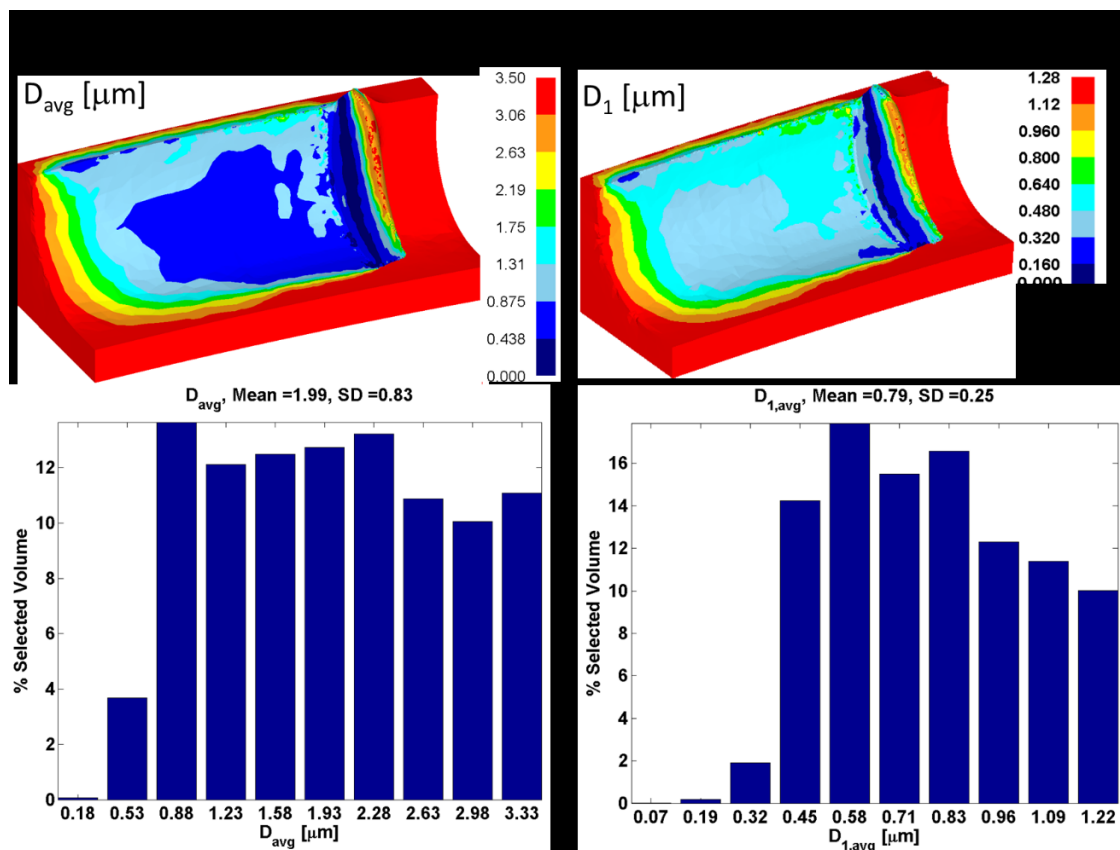


Figure 3.14 Predicted grain size fields: TiAlN coated tool $v_c=12$ m/min.

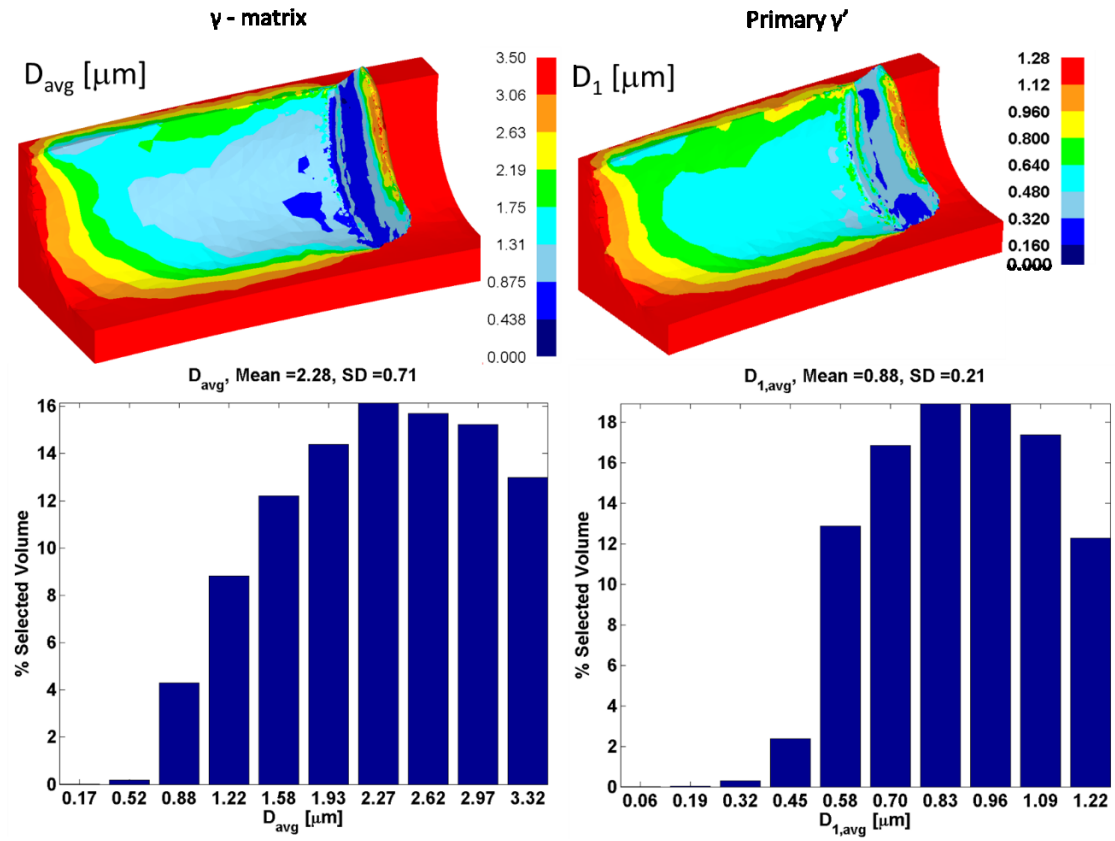


Figure 3.15 Predicted grain size fields: TiAlN coated tool $v_c=24$ m/min.

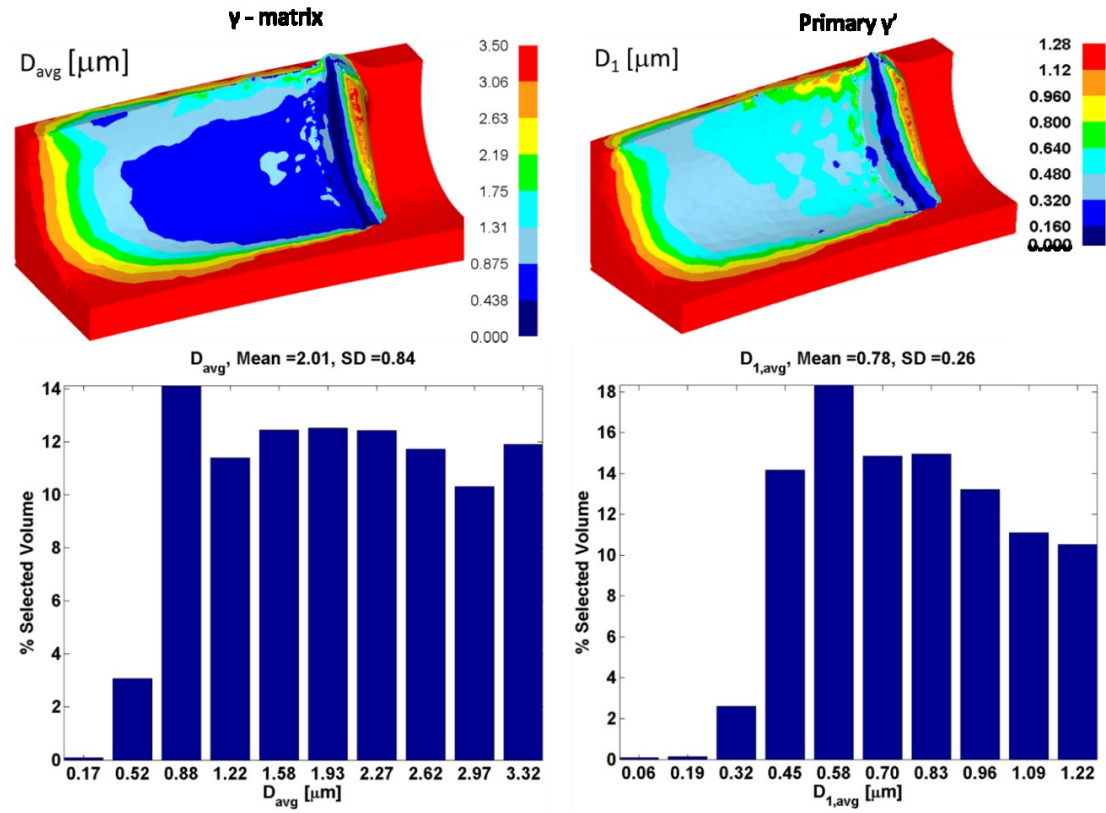


Figure 3.16 Predicted grain size fields: WC/Co tool $r_\beta=5\mu\text{m}$, $v_c=12$ m/min.

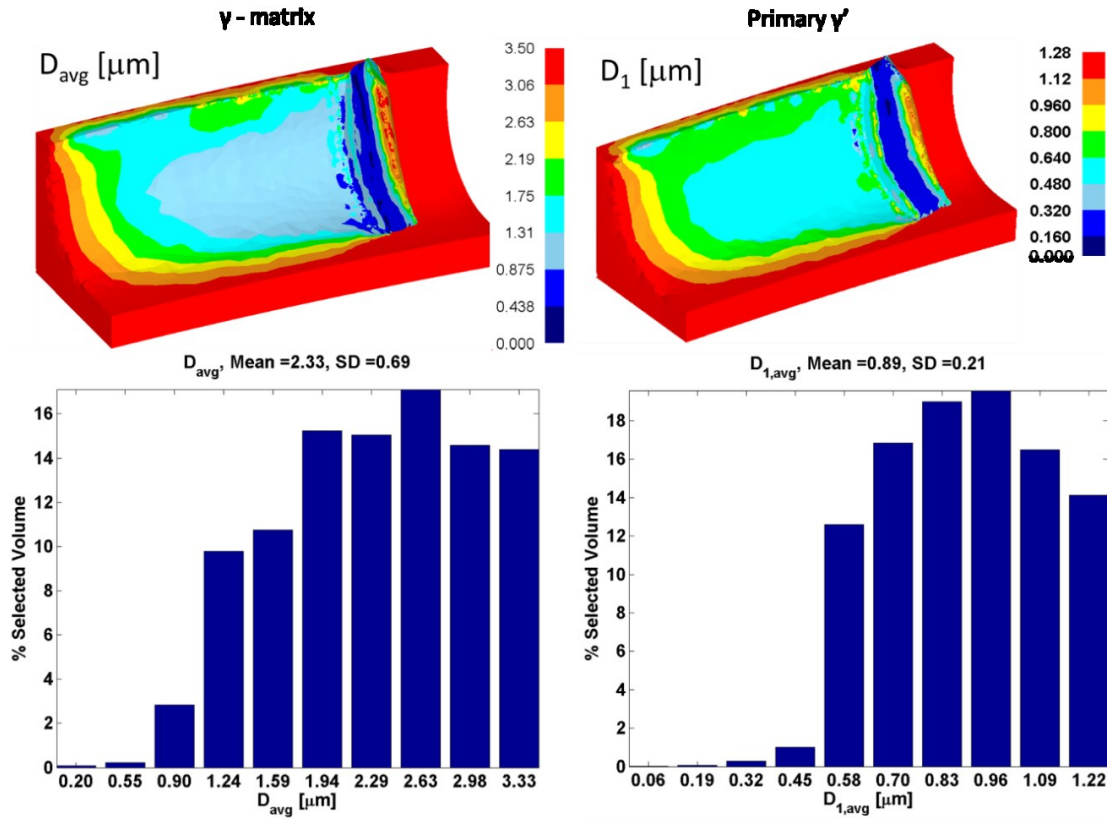


Figure 3.17 Predicted grain size fields: WC/Co tool $r_\beta=5\mu\text{m}$, $v_c=24$ m/min.

3.2.2.3 Microhardness Prediction

Using the grain sizes and distributions obtained via SEM and FEM analysis, an expression is constructed for predictive modeling of hardness on the machined subsurface (at about 25 μm into the depth) as suggested in (Milligan et al., 2004). Following this Hall-Petch type approach, a generalized model of the following form is proposed:

$$HV = c_0 + c_1[d_1^{m_1}f_1^{n_1}] + c_2[d_2^{m_2}f_2^{n_2}] + c_3[d_3^{m_3}f_3^{n_3}] + c_4[d_{avg}^{m_4}] \quad (3.4)$$

where HV is microhardness, d_{avg} , d_1 , d_2 , d_3 are the γ -matrix, primary, secondary and tertiary γ' grain sizes and f_1 , f_2 , f_3 are related volume fractions, respectively. The c_0 , c_1 , c_2 , c_3 , c_4 are model constants and m_1 , n_1 , m_2 , n_2 , m_3 , n_3 , m_4 are model exponents that define the relationship between different grains and volume fractions and the hardness. Model parameters are obtained via nonlinear optimization using Genetic Algorithm from SEM measurements for gamma prime grain sizes and volume fractions, γ matrix grain sizes calculated from 3D FE simulations along with the microhardness measurements. The resultant microhardness model for IN100 which can be used for hardness predictions is given as:

$$HV = 110.36 + 168.75[d_1^{0.38}f_1^{0.007}] + 2858.91[d_2^{-0.74}f_2^{0.35}] + 60.97[d_3^{-0.33}f_3^{0.41}] + 97.43[d_{avg}^{0.25}] \quad (3.5)$$

This predictive microhardness model could also be used to estimate the expected hardness of so called “white layer” from measured and/or predicted grains sizes and phase fractions.

CHAPTER 4: MACHINE LEARNING BASED MODELING OF HARDNESS AND MICROSTRUCTURE

4.1 Introduction

Machine learning methods can be used to predict the outcomes of a process without experiments or simulations. Using experimental and simulation data, a metamodel can be generated that links inputs to outputs, or targets. Inputs and targets must first be determined carefully in order to train a model that achieves desirable results. Inputs are composed of different features that represent different physical attributes, and observations that represent the measurements of each feature. When designing such models, one should always keep the Occam's Razor (*lex parsimoniae*) principle in mind, keeping the model as simple as possible, since making many assumptions and including unnecessary information into the model reduces the accuracy and robustness of it.

4.2 Temperature Based Random Forests Model for Hardness Prediction of Ti-6Al-4V

Following this line of thought, two separate RF models for regression were constructed; one for predicting the instantaneous hardness during machining and another for predicting the final hardness of the workpiece after cooling down to room temperature (Ozel et al., 2013; Arisoy and Özel, 2014). For the prediction phase, FE simulation data was extracted in the form of nodal temperatures and passed to MATLAB. A line of 0.1 mm depth from the surface was selected close to the middle of the workpiece in order to see the effects of the tool. The temperature data was interpolated using MATLAB. The resulting data was fed into the RF model, and hardness values were calculated. It is important to note that current model is purely temperature dependent and is not intended to capture the work deformation induced effects. For instance, localized heating, an important factor that affects surface integrity during machining, is not present in the hot hardness measurements. Moreover, plastic deformation was not included in this current model. However, a more complicated and accurate model can be developed in a similar manner.

4.3 Instantaneous hardness model

The training of the instantaneous model is performed using hot hardness measurements as the target, where the temperature and hardness values were measured and recorded. Hot hardness measurements during cooling from given annealing temperatures are shown in Figure 4.1.

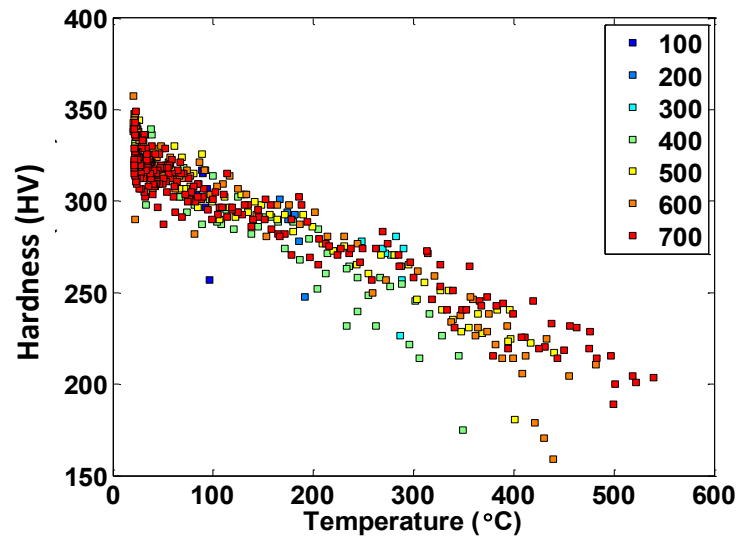


Figure 4.1 Hot hardness measurements at during air cooling for different initial temperatures (different colors).

Inputs are chosen as maximum temperature, instantaneous temperature and the cooling time since these are factors that are known to play an important role in microstructure alterations. An input matrix is constructed from the data such that each column is a feature and each row is a different measurement. A representative tree from the model is shown in Figure 4.2. During the training of the model, 10% of the input data was reserved as test

data and was not used in training. Figure 4.3 shows the goodness of fit. The fit has $R^2=0.965$, $MAE=0.51$ and $RMSE=0.933$.

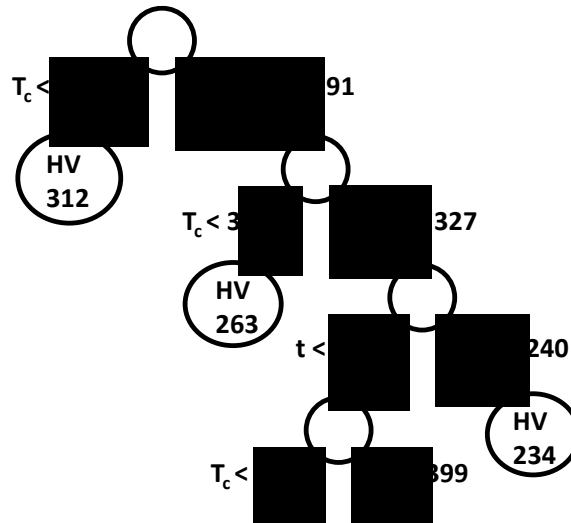


Figure 4.2 Representation of a regression tree in the instantaneous hardness model.

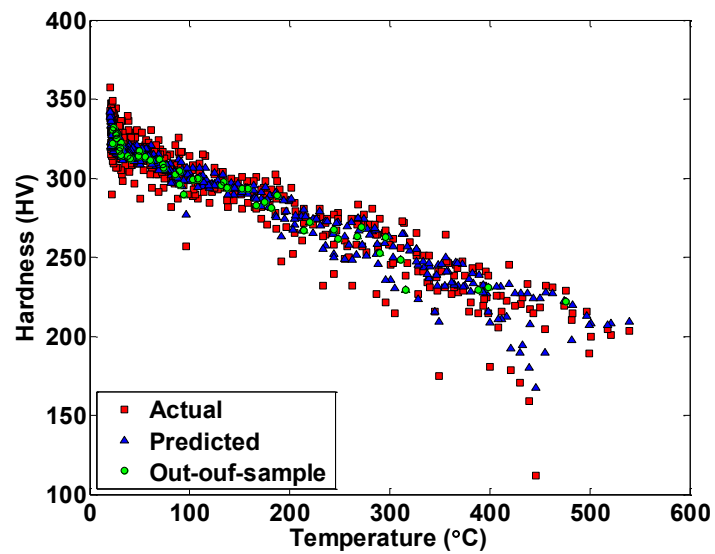


Figure 4.3 Instantaneous hardness RF regression model results, red: whole dataset, blue: predictions on training data, green: predictions on testing data.

After the model is trained, FE simulation results are used as inputs to the model to obtain instantaneous hardness values during the machining operations. Temperature field over time towards the depth is extracted from FE simulations, showing the increase and decrease in temperature as the tool moves over the selected location. Figure 4.4 shows the result temperature vs depth over time at the selected location, and the predicted hardness from the instantaneous hardness model for a representative cutting condition, TiAlN coated WC/Co tool with $v_c = 90$ m/min and $f = 0.1$ mm / rev. Note that the temperature rise and cooldown happens extremely fast, due to the nature of the FE simulation where only a small portion of the workpiece geometry is considered and thermal coefficients are amplified in order to reach steady state quickly as explained in Chapter 3. This amplification can be justified by the fact that the tool processes a much larger area on the workpiece in reality, and the simulated region can be a region that is processed after the tool has already reached the thermal steady state after processing other regions. The results indicate a significant drop in hardness as temperature increases, which is supported by the experimental data. Formation of a hardened layer (shown in lighter blue) is observed between 20-70 μm below the surface at the last time step. The machined surface layer experiences an instantaneous hardness state due to localized heating and cooling during cutting process. During this repeated heating and cooling process, machined surface and subsurface go through changes in the microhardness.

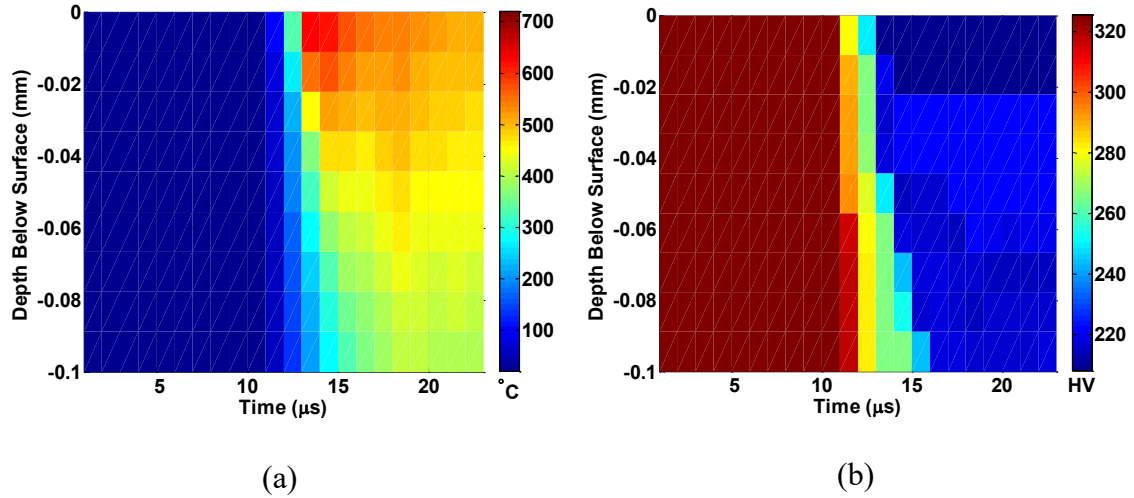


Figure 4.4 Temperature in °C (a) and hardness in HV (b) over line section on the workpiece during machining over time.

4.3.1 Hardness after cooldown

The secondary RF model was trained to calculate the hardness of the cooled down workpiece. The temperatures shown in Figure 4.5 and Table 4.1 were used as the input dataset and the hardness measurements are used as the target dataset, with the exception of the hardness measurements from the furnace cooled 704°C data which was used as the default room temperature hardness for the model to converge to, by setting the temperature to 20°C instead.

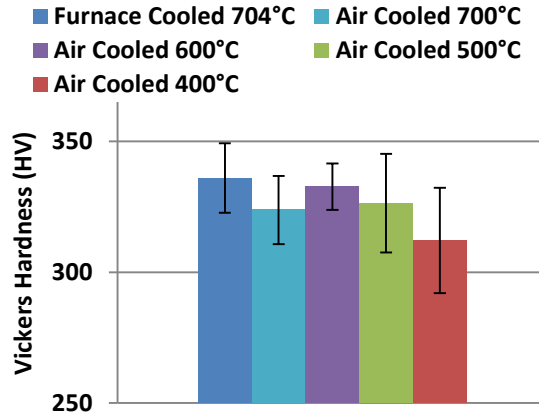


Figure 4.5 Hardness measurements at room temperature after cooling down.

Table 4.1 Hardness measurements at room temperature after cooling down

Condition	Temperature [°C]	Mean Hardness [HV]	SD Hardness [HV]
Furnace Cooled	704	335.8	13.3
Air Cooled	700	323.8	13.1
Air Cooled	600	332.8	8.9
Air Cooled	500	326.4	18.9
Air Cooled	400	312.1	20.1

Figure 4.5 shows the combined result of instantaneous and cooled hardness models along with the effects of different cutting conditions and tool coating on instantaneous and final hardness during various stages of the machining process. Microhardness state into the depth below the surface is shown just prior to chip formation (cutting) process for all cutting conditions in Figure 4.6a. Higher feeds create larger change in surface hardness while this effect diminishes after 50 μm depth into the machined surface. In general coated tool influences hardness more than uncoated tool. In addition, instantaneous hardness change prior to and after the cutting process was also investigated. Machined surface was cooled down to the room temperature and resultant hardness profile was calculated as

shown in Figure 4.6b and c. Higher feed rate and a larger edge radius are found responsible for greater alterations in microhardness profiles. Figure 4.6b shows that the heated surface is predicted to be softer than the relatively colder interior parts of the workpiece, which follows the hot hardness measurement data. Figure 4.6c shows the predicted final hardness of the surface using the second RF model after the process is over, and reveals the differences between different cutting conditions. The hardened layer seen in Figure 4.4b is also evident in Figure 4.6c for the TiAlN coated WC/Co tool with $v_c = 90$ m/min and $f = 0.1$ mm/rev condition. However, this layer is not seen in other conditions.

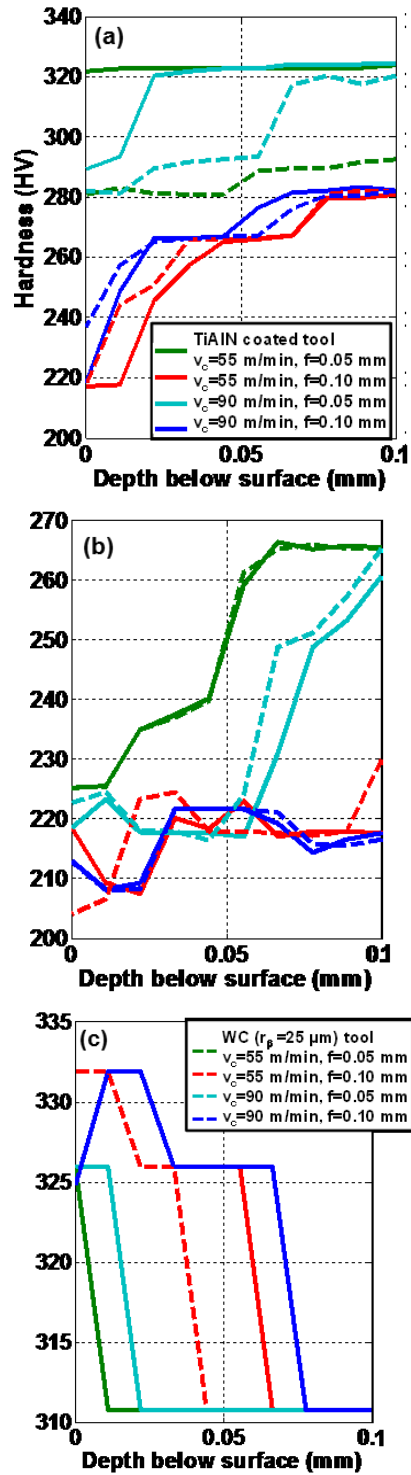


Figure 4.6 Instantaneous hardness (a) prior to chip formation, (b) after the cutting process, and (c) after cooling down to room temperature.

4.4 Grain Size and Process Parameter Based Models for Hardness Prediction of Ti-6Al-4V

Random Forests were also used to create predictive models that relate cutting conditions, grain size and fractions, and hardness measurements to each other. Figure 4.7 shows the 3 different RF models. The $RF_1(\mathbf{x})$ model predicts hardness (HV) from cutting conditions, $RF_2(\mathbf{x})$ model predicts Ti-6Al-4V's α grain size (d_{avg}) from cutting conditions, and the $RF_3(\mathbf{x})$ model predicts hardness from grain size and volume fractions. Cutting conditions are given as v_c, f, r_β , and c , which represent cutting speed, feed rate, tool edge radius, and a binary parameter that describes whether coating exists or not (i.e. uncoated $c=0$ WC/Co uncoated and $c=1$ for TiAlN coating) respectively. Therefore, the input variable set for $RF_1(\mathbf{x})$ and $RF_2(\mathbf{x})$ is $\mathbf{x} = \{v_c, f, r_\beta, c\}$ and for $RF_3(\mathbf{x})$ is $\mathbf{x} = \{d_{avg}, f_\alpha\}$. Mean values of the hardness and grain size measurements were obtained for each of the 16 cutting conditions (2 levels of cutting speed and feed, and 4 different tools). The data was partitioned into training and testing sets such that the testing set contained 4 conditions, selected from 4 different tool types at varying cutting speeds and feeds. The training set contained the remaining 12 conditions.

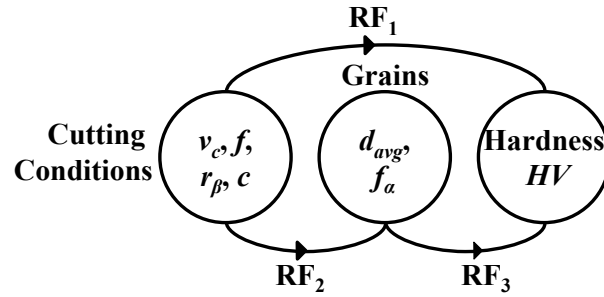


Figure 4.7 Random Forests based prediction models for hardness and grain size.

In addition, using the grain sizes and distributions obtained via SEM, an expression was constructed and proposed to estimate microhardness based on grain size and phase fraction relation and by following a general Hall-Petch (H-P) type equation for grain size and strength relation available in literature:

$$HV = c_0 + c_1[d_{avg}^{m_1} f^{n_1}] \quad (4.1)$$

where HV is microhardness, d_{avg} , and f are α grain size and α or β volume fraction, respectively. The c_0 and c_1 are model constants and m_1 and n_1 are exponents. Model parameters were obtained via nonlinear optimization using Genetic Algorithm from SEM measurements for α grain sizes and β volume fractions (Eq. 4.2) and α grain sizes and α volume fractions (Eq. 4.3) to generate a hardness model for predicting machining induced microhardness in Ti-6Al-4V titanium alloy. These equations can be used to determine the hardness of the particular material that has undergone similar machining conditions from microstructure information.

$$HV = 175.79 + 112.36[d_{avg}^{0.07} f_{\beta}^{-0.04}] \quad (4.2)$$

$$HV = 176.26 + 120.53[d_{avg}^{0.08} f_{\alpha}^{0.11}] \quad (4.3)$$

Predicted α grain sizes in Ti-6Al-4V using $RF_2(x)$ model were compared against measured ones and predicted microhardness of machined surfaces using $RF_3(x)$ model and Hall-Petch type equation as given in Eqs. (4.2) and (4.3) against measured mean microhardness given in Table 2.1. Figure 4.8 shows the grain size comparisons between measurements and $RF_2(x)$ model predictions for different cutting speeds, feeds and tools. The predicted values are very close to each other, and while they follow a trend, the accuracy is not spectacular even for the training set, with $MSE = 0.9203$ (across testing data). This suggests that there are other factors that should be taken into account that determine the final grain size. In fact, it is known that grain sizes in the machined subsurfaces are determined by strain, strain rate and temperature history of the area, which cannot be accurately described solely by the machining conditions. Figure 4.9 shows the hardness comparisons between measurements, $RF_3(x)$ model predictions (and predictions based on the H-P like equation. In this case, the RF_3 model performs better than Eq. (4.3), with $MSE = 38.3370$ (across testing data) and $MSE = 59.9408$ (across all data) for H-P like equation. However, standard deviations of measured grain size and Microhardness which represent uncertainty are utilized in obtaining separate RF models and used in predicting these uncertainties (as error bars) in Figures 4.8 and 4.9.

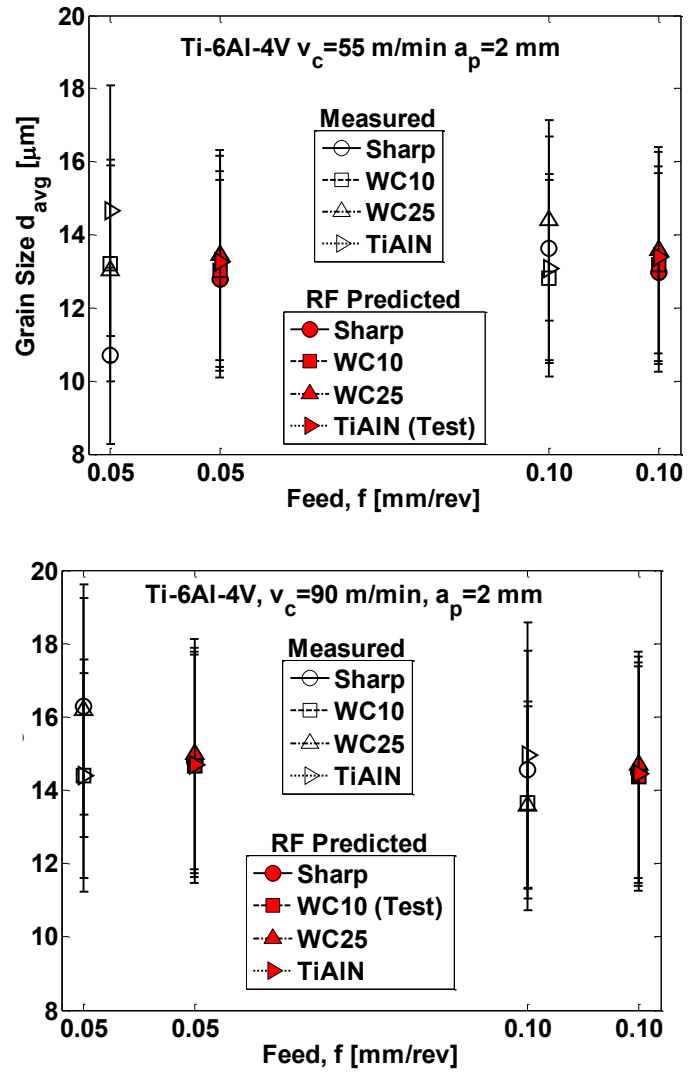


Figure 4.8 Measured and predicted average grain sizes for $v_c=55 \text{ m/min}$ and $v_c=90 \text{ m/min}$.

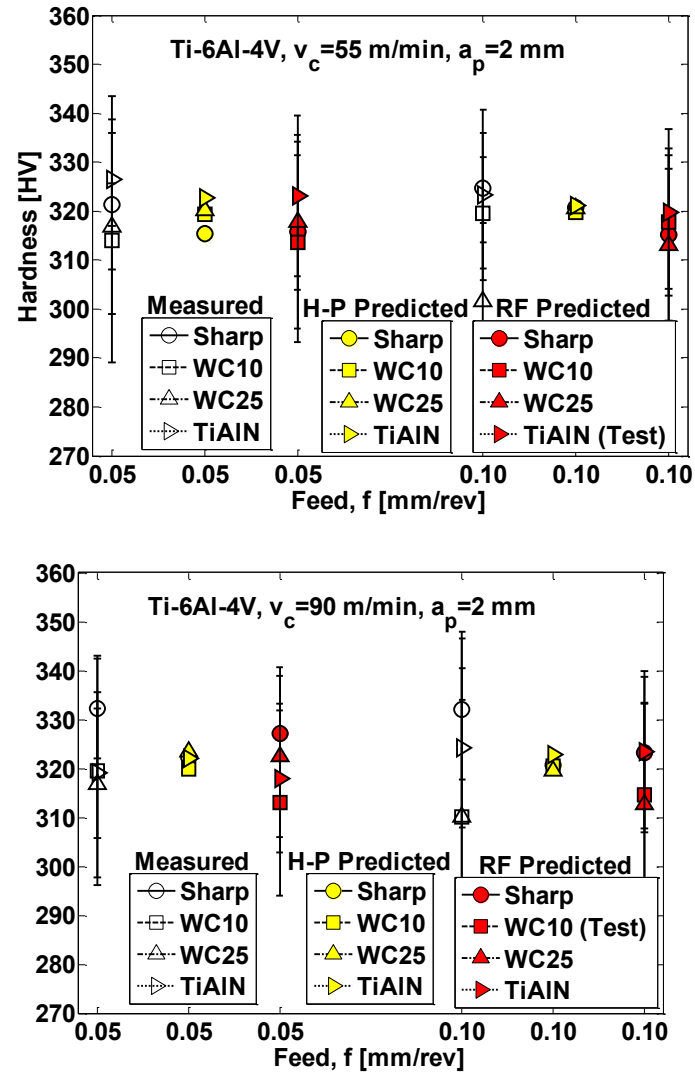


Figure 4.9 Measured and predicted hardness for $v_c = 55 \text{ m/min}$ and $v_c = 90 \text{ m/min}$.

4.5 Grain Size and Process Parameter Based Models for Hardness Prediction of IN100

The microhardness of machined IN100 nickel alloy can also be predicted by following a similar methodology to the one seen in previous section. In addition to surface hardness values, depth based microhardness analysis has also been conducted by Arisoy et al. (Arisoy et al., 2015), as described in Chapter 2.

Two separate regression based models have been created to relate the cutting conditions to the microhardness profiles shown in Figure 2.5 and Table 2.3 in Chapter 2. As shown in Figure 4.10, the first model predicts the hardness with respect to depth h and cutting speed v_c for the TiAlN coated tool. The second model is created for uncoated tools with edge radii $r_\beta=5\mu\text{m}$, $10\mu\text{m}$ and $25\mu\text{m}$, and these tool edge radii have been included in the model.

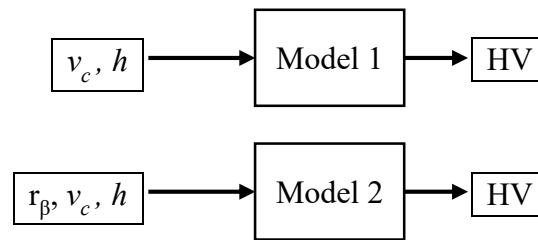


Figure 4.10 Microhardness profile prediction models for the TiAlN coated and uncoated tools.

Rather than utilizing machine learning as in the previous section, both models utilize explicit equations with exponentially decaying function to represent the depth. Model 1 is given by:

$$HV = 396.05 + 51.09v_c^{-0.002}e^{-0.02h} - 0.14v_c^{1.46} \quad (4.4)$$

where h is the positive depth below surface. Model 2 includes the tool edge radius effect in addition to cutting speed and depth, and is shown in Eq. (4.5).

$$HV = 389.51 + 54.61v_c^{0.09}r_\beta^{-0.05}e^{-0.02h} - 1.17v_c^{0.72} + 0.86r_\beta^{0.93} \quad (4.5)$$

The equation parameters are obtained with least squares regression. The R^2 values for Eqs. (4.4) and (4.5) are found as 0.87 and 0.91, respectively. Note that more complicated models with additional terms can be constructed at the expense of generalization power.

Figure 4.11 shows the surface that is obtained from Eq. (4.4) for TiAlN coated WC/Co cutting tool while Figures 4.12 through 4.14 show the surfaces obtained from Eq. (4.5) for uncoated WC/Co tools at different tool edge radii. Note that the tool edge radii are kept constant (at their respective values) in order to create Figures 4.12-4.14.

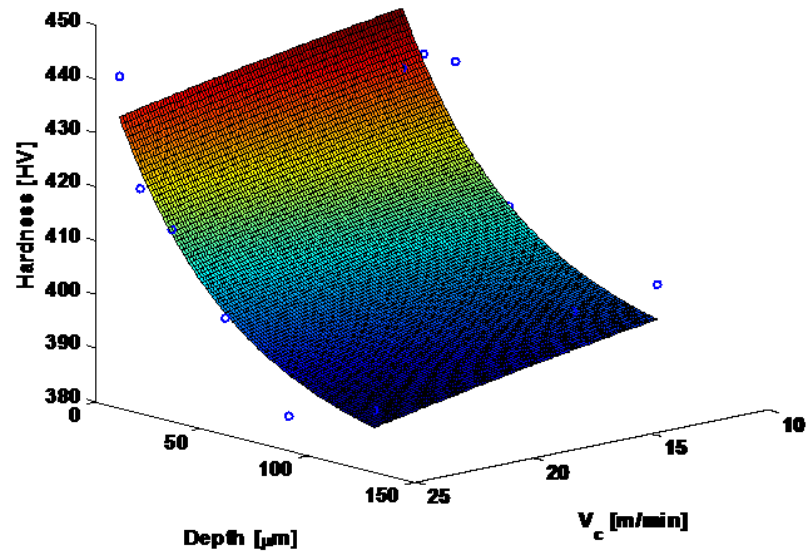


Figure 4.11 Surface fit of the microhardness with respect to depth and cutting speed for the TiAlN coated tool. Experimental data points are shown as circles.

(Y. M. Arisoy, 2016)

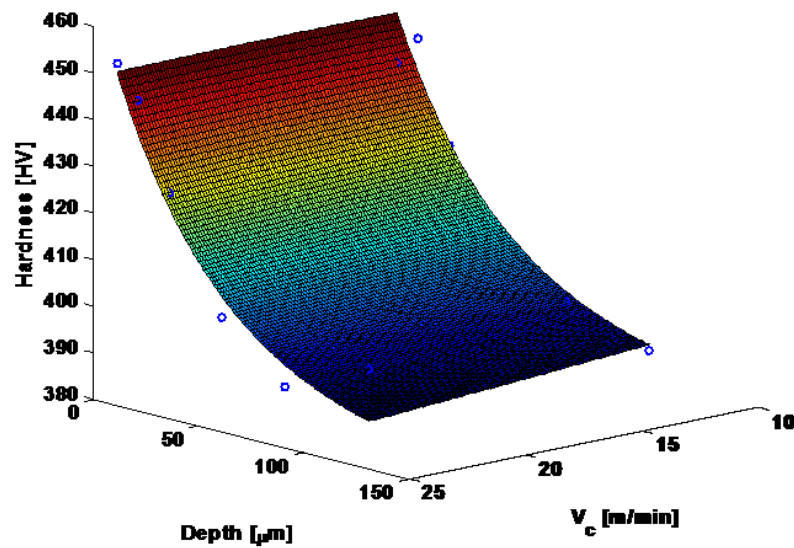


Figure 4.12 Surface fit of the microhardness with respect to depth and cutting speed for the uncoated tools with $r_{\beta}=5\mu\text{m}$. Experimental data points are shown as circles.

(Y. M. Arisoy, 2016)

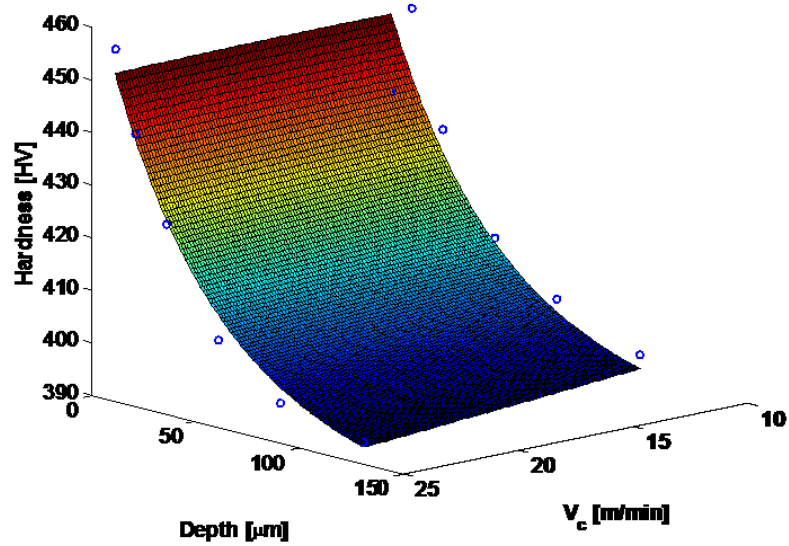


Figure 4.13 Surface fit of the microhardness with respect to depth and cutting speed for the uncoated tools with $r_\beta=10\mu\text{m}$. Experimental data points are shown as circles.

(Y. M. Arisoy, 2016)

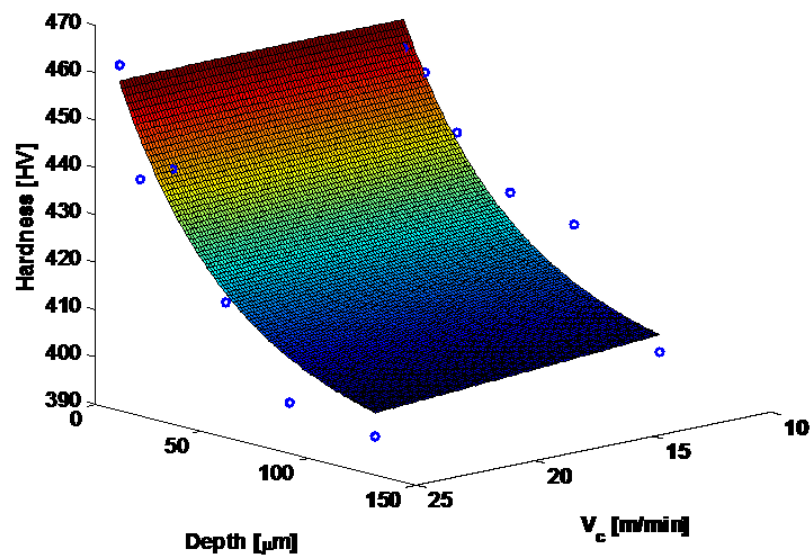


Figure 4.14 Surface fit of the microhardness with respect to depth and cutting speed for the uncoated tools with $r_\beta=25\mu\text{m}$. Experimental data points are shown as circles.

(Y. M. Arisoy, 2016)

Furthermore, using the grain sizes and distributions obtained via SEM, an expression is constructed for predictive modeling of hardness on the machined subsurface as suggested in Milligan et al. (Milligan et al., 2004), with modifications. Following this Hall-Petch type approach, a generalized model of the following form is proposed:

$$HV = c_0 + c_1[d_1^{m_1}f_1^{n_1}] + c_2[d_2^{m_2}f_2^{n_2}] \quad (4.6)$$

where HV is microhardness, d_1 and d_2 are the primary and secondary γ' grain sizes and f_1 and f_2 are their respective volume fractions. The c_0 , c_1 , c_2 , m_1 , n_1 , m_2 , n_2 , m_3 , n_3 , m_4 are model parameters that are obtained computationally, utilizing the SEM measurements for gamma prime grain sizes and volume fractions obtained at 120 μm depth. The resultant microhardness model for IN100 which can be used for hardness predictions is given as:

$$HV = 269.2016 + 3.4203d_1^{0.4943}f_1^{0.0313} + 5.72d_2^{0.3995}f_2 \quad (4.7)$$

The model has $R^2=0.8$, indicating that there are other factors that contribute to the hardness. The model is compared to experimental data in Figure 4.15. The model provides a fine match to the microhardness profiles shown in Figure 2.5 in Chapter 2 and could be used to estimate the hardness of white layer formation from measured or predicted grains sizes and phase fractions.

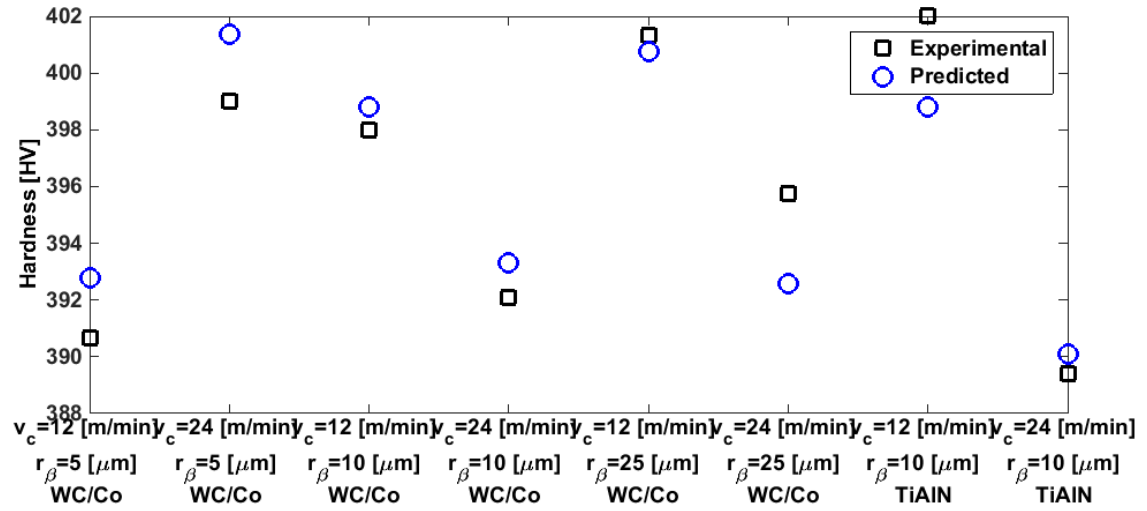


Figure 4.15 Comparison of experimental microhardness measurements and grain-size based microhardness predictions.

CHAPTER 5: MACHINING PARAMETER AND MICROSTRUCTURE MODEL OPTIMIZATIONS

5.1 Introduction

This chapter focuses on two major tasks: (i) the optimization of machining process parameters for IN100 and Ti-6Al-4V alloys, and (ii) the optimization of JMAK model parameters that are used in the Finite Element simulations of the machining IN100 alloy. For the first task, optimal machining parameters (such as cutting speed, feed rate, tool type and tool edge radius) are determined to improve the quality of the parts by minimizing microstructural changes induced while increasing productivity and process efficiency. For the second task, the JMAK model parameters are identified with an objective for accurate representation of the microstructure resulting from the machining process.

5.2 Machining Parameter Optimization

Machining process productivity can be improved by increasing the cutting speed and feed rate so that higher volume of material is removed per unit time during the process. However, using abusive machining parameters can lead to significant microstructural changes which is certainly not desirable. Furthermore, the process efficiency can also be improved, by minimizing the heat generation hence maximizing energy for material removal in the process. For this purpose, two separate optimization studies are conducted in this section in order to improve the machining process productivity and efficiency while reducing microstructural changes. The first optimization study aims to maximize the process rate via increasing the cutting speed and feed rate of the process and at the same time reduce the microstructural changes due to machining by minimizing recrystallization (or maximizing the grain size). The second optimization process aims to reduce the resultant temperature of the workpiece obtained from Finite Element simulations while minimizing the microstructural changes. Since these objectives are in conflict or competing against each other, a multi-objective optimization approach is suggested to identify optimal machining parameters. Regression equations for process outcomes such as average grain diameter and resultant temperature are utilized as objective functions for the multi-objective optimization problems. The following initial grain sizes are used as described in Chapter 3, $d_I=1.28\text{ }\mu\text{m}$ for the IN100 primary γ' grains and $D_{avg}=20\text{ }\mu\text{m}$ for the Ti-6Al-4V α grains.

5.2.1 Minimizing Microstructural Changes and Maximizing Productivity

At first, a multi-objective optimization study is performed to maximize the productivity while minimizing the microstructural changes. This would allow machining operations used in finishing to be done at an optimum speed without altering the existing microstructure.

Rather than pursuing a non-parametric approach such as the Random Forests explained in Chapter 4, a first-order (linear) regression model with interactions is utilized to establish the input-output relationship between response (e.g. grain size or resultant temperature) and controllable processes variables effectively. The model has the following form:

$$y = \beta_0 + \sum_{i=1}^k \beta_i x_i + \sum_{i \neq j=1}^k \beta_{ij} x_i x_j + \varepsilon \quad (5.1)$$

where y is the response, x_i are the input variables, β are the coefficients of the estimation and ε is the residual or error. After subtracting the response and input variables, the equation becomes:

$$\begin{aligned} D_{avg} \text{ or } d_1 = & \beta_0 + \beta_1 r_\beta + \beta_2 v_c + \beta_3 f + \beta_{12} r_\beta v_c + \beta_{13} r_\beta f \\ & + \beta_{23} v_c f + \varepsilon \end{aligned} \quad (5.2)$$

where the left hand side denotes the grain size obtained from SEM images, d_1 for primary γ' in IN100 and D_{avg} for alpha grain size in Ti-6Al-4V and r_β is the tool edge radius. The data used in obtaining the model coefficients are summarized in Table 5.1. The coefficients of the model were determined using Minitab software, and are listed in Table 5.2 along

with calculated R^2 values that describes the determination coefficient for the goodness of the fit to the data for IN100 and Ti-6Al-4V alloys.

Productivity in a machining process can be related to how much material is removed per second, defined by the material removal rate MRR [mm^3/s] as follows:

$$MRR = v_c \times f \times a_p \quad (5.3)$$

Where a_p [mm] is the depth of cut, v_c [mm/s] is the cutting speed (in converted units) and f is the feed [mm/rev]. For clarity, further analysis for Ti-6Al-4V and IN100 alloys are performed separately. The optimization problems formulated in the following sections are solved using the Multi-objective Genetic Algorithm (Deb, 2001) in MATLAB. A population size of 1000 is used, with the following settings: The crossover fraction, which controls the ratio of children that are created via crossover rather than mutation, is set to 0.8, and the Pareto faction setting that limits the number of solutions on the Pareto front is set to 0.35.

Table 5.1 Input and response variables for the regression models for Ti-6Al-4V and IN100.

	Input Variables			Response (Experimental Data)
Material	Tool	v_c [m/min]	f [mm/rev]	d_I – IN100 [μm]
IN100	WC/Co, $r_\beta=5\mu\text{m}$	12	0.05	0.83
		24	0.05	0.94
	WC/Co, $r_\beta=10\mu\text{m}$	12	0.05	0.92
		24	0.05	0.78
	WC/Co, $r_\beta=25\mu\text{m}$	12	0.05	0.97
		24	0.05	0.81
Material	Tool	v_c [m/min]	f [mm/rev]	D_{avg} – Ti-6Al-4V [μm]
Ti-6Al-4V	WC/Co, $r_\beta=5\mu\text{m}$	55	0.05	10.70
		55	0.1	13.63
		90	0.05	16.29
		90	0.1	14.57
	WC/Co, $r_\beta=10\mu\text{m}$	55	0.05	13.20
		55	0.1	12.82
		90	0.05	14.39
		90	0.1	13.66
	WC/Co, $r_\beta=25\mu\text{m}$	55	0.05	13.03
		55	0.1	14.39
		90	0.05	16.17
		90	0.1	13.57

Table 5.2 Regression model coefficients with R^2 values for machining IN100 nickel and Ti-6Al-4V titanium alloys.

	Regression Model for IN100 Grain Size	Regression Model for Ti-6Al-4V Grain Size
Coefficient	d_l [mm]	D_{avg} [mm]
β_0	0.745	-2.43
β_1	0.0168	0.266
β_2	0.66	0.2098
β_3	-	132.8
β_{12}	-0.00891	0.00225
β_{13}	-	-0.96
β_{23}	-	1.707
R^2	0.612	0.783

5.2.1.1 Multi-objective Optimization of Productivity and Microstructure of IN100

In this case, machining productivity is considered by maximizing cutting speed so that the maximum material removal rate is achieved. Since feed rate is often limited by the rapid work hardening of the IN100 material, a constant feed rate was used in the machining experiments shown in Chapter 2. The objective of the optimization problem is to minimize the microstructural changes while maximizing the material removal rate. The optimization problem is defined as follows:

$$\begin{aligned} \text{Min.} \quad & \left\{ (d_1^{exp}(v_c, r_\beta) - d_1)^2, -MRR(v_c) \right\} \\ \text{s.t.} \quad & 12 \leq v_c \leq 24 \\ & 5 \leq r_\beta \leq 25 \end{aligned} \quad (5.4)$$

where d_1^{exp} is the average primary γ' size calculated from the regression equation given in Eq. (5.2) along with the coefficients given in Table 5.2, and $d_1=1.28 \mu\text{m}$ is the reference value for the primary γ' sizes as reported in Chapter 3. The average grain diameter obtained after machining of IN100 is considered as a measure for microstructural changes. Note that in calculation of MRR, constant feed rate $f=0.05 \text{ mm/rev}$ and depth of cut $a_p=1 \text{ mm}$ is used.

The results of the multi-objective optimization are given for as the Pareto front and the corresponding decision variables as shown in Figure 5.1. For visualization and easier identification, the Pareto front is grouped into 4 regions using k-means clustering in MATLAB, and each group is shown with a different color. It can be seen from the objective function space that two groups of non-dominating solutions are obtained. One set of solutions for maximizing cutting speed is grouping along the cutting speed value of 24

m/min or the upper limit of the velocity constraint and another set of non-dominating solutions is forming a trend line which represents a conflicting relations for minimizing the microstructural alterations and maximizing the MRR at the same time.

Depending on the importance of the individual objectives, an optimum cutting speed and a tool can be selected. For instance, if the surface integrity of the part is of utmost importance and productivity can be sacrificed to achieve that, then $v_c < 14$ m/min and $r_\beta = 25$ μm tool (blue region in Figure 5.1) can be used. If the part is not mission critical therefore the microstructural changes are not very important, then $v_c = 24$ m/min and $r_\beta = 5$ μm tool can be used to maximize the productivity (orange region in the figure).

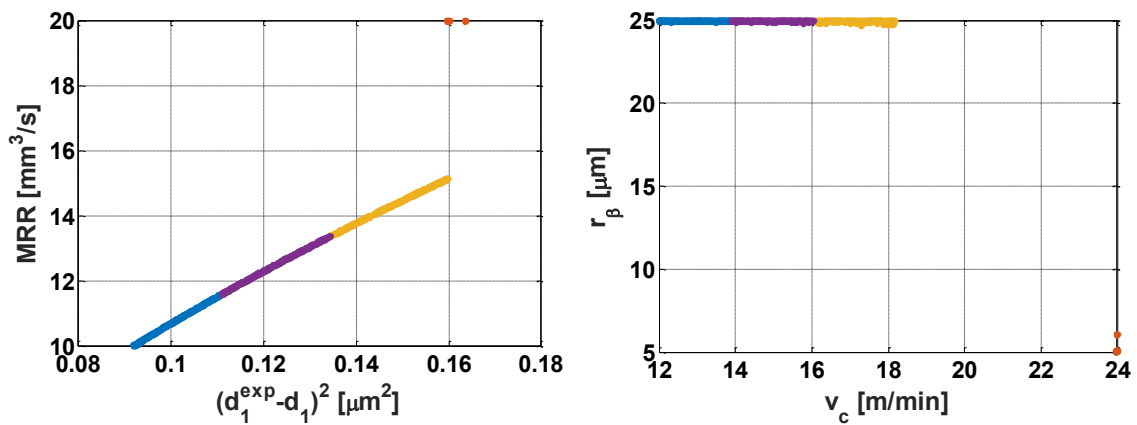


Figure 5.1 Multi-objective optimization result for IN100 nickel alloy with objective values (left) and the decision variables (right).

5.2.1.2 Multi-objective Optimization of Productivity and Microstructure of Ti-6Al-4V

A similar optimization problem can be constructed for the Ti-6Al-4V material. Since the machining experiments were done with two different feed rates (0.05 and 0.1 mm/rev), feed rate is included as a decision variable in the problem. Thus, the optimization problem is defined as follows:

$$\begin{aligned}
 \text{Min.} \quad & \left\{ (D_{avg}^{exp}(v_c, r_\beta) - D_{avg})^2, -MRR(v_c, f) \right\} \\
 \text{s.t.} \quad & 55 \leq v_c \leq 90 \\
 & 5 \leq r_\beta \leq 25 \\
 & 0.05 \leq f \leq 0.1
 \end{aligned} \tag{5.5}$$

where D_{avg}^{exp} is the average α grain size calculated from the regression equation given in Eq. (5.2) along with the coefficients given in Table 5.2, and $D_{avg} = 20 \mu\text{m}$ is the reference value for the α grain sizes as reported in Chapter 3. For the machining of Ti-6Al-4V, the depth of cut a_p is 2 mm.

The Pareto front obtained from the final generation and the corresponding decision variables are shown in Figure 5.2. It is seen that $v_c = 90$ [m/min] is the preferred cutting speed. Again, two dominant groups are observed in the Pareto front, with small and large tool edge radii ($r_\beta = 5 \mu\text{m}$ and $r_\beta = 25 \mu\text{m}$). The small edge radius tool can be used with high feed rates to achieve the best MRR at the cost of high microstructural alterations (purple and yellow regions in the figure). In contrast, the large edge radius tool can be utilized along with a slow feed setting to minimize the grain size difference, at the cost of productivity (orange region in the figure).

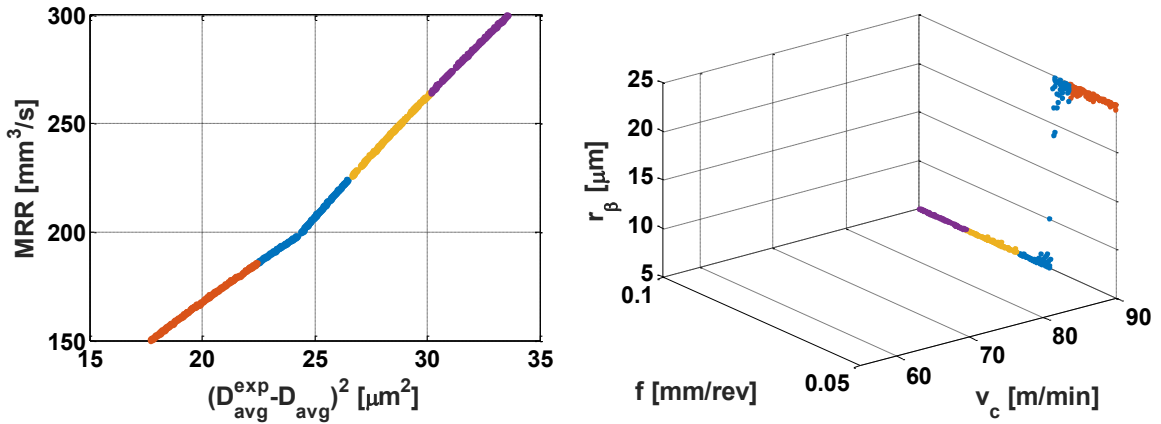


Figure 5.2 Multi-objective optimization result for Ti-6Al-4V titanium alloy with objective values (left) and the decision variables (right).

5.2.2 Minimizing Machining Temperature and Microstructural Changes

High temperatures and residual stress build up during can lead to problems after the process is completed. More specifically, the variation in temperature at different locations in the workpiece generates thermal stresses caused by uneven thermal expansions at different locations, which can result in part distortion after cooling. This effect can be seen more dominantly in more intricate parts, such as thin walled structures. This distortion is highly undesired in parts such as those used in the aerospace industry that must have high dimensional accuracy and standards. By minimizing the machining temperature, part distortions can be reduced.

Machining temperature can roughly be estimated by the final temperature of the workpiece. However, keeping the microstructural alterations minimized is also important. Lower

temperatures will possibly lead to less significant changes (in terms of recrystallization) in the microstructure, therefore, these objectives may not necessarily conflict with each other.

Similar to Eq. (5.1), a first-order regression model with interactions is utilized to establish the input-output relationship between the process parameters and the final average temperature:

$$T_{avg} = \beta_0 + \beta_1 t + \beta_2 v_c + \beta_3 f + \beta_{12} tv_c + \beta_{13} tf + \beta_{23} v_cf + \varepsilon \quad (5.6)$$

T_{avg} [°C] is the final average temperature of the workpiece from the FEM simulations, and t is a variable denoting the tool type ($t=0$ for the WC/Co $r_\beta = 25 \mu\text{m}$ tool and $t=1$ for the TiAlN coated $r_\beta = 10 \mu\text{m}$ tool). Note that since only 2 tools out of 4 were used in the IN100 and Ti-6Al-4V FE simulations, the value of t represents a combination of tool edge radius and coating. The variable t is allowed to be continuous so that different tool types in terms of edge radius and coating can also be considered qualitatively. Alternatively, a mixed-integer programming approach can be used to constrain the variable t to be an integer, however, it is not implemented here. Furthermore, feed was kept constant across all IN100 simulations and it is not used in the equation ($\beta_3 = \beta_{13} = \beta_{23} = 0$). The data used in obtaining the model coefficients are summarized in Table 5.3. The coefficients of the model were determined using Minitab software, and are listed in Table 5.4 along with calculated R^2 values for IN100 and Ti-6Al-4V alloys.

Table 5.3 Input and response variables for the regression models for Ti-6Al-4V and IN100.

Material	Tool Type t	Cutting Speed v_c [mm/min]	Feed f [mm/rev]	Average Temperature T_{avg} [°C]	d_I IN100 [μm]
IN100	1 (TiAlN, $r_\beta = 10 \mu\text{m}$)	12	0.05	359	0.88
	1 (TiAlN, $r_\beta = 10 \mu\text{m}$)	24	0.05	524	0.73
	0 (WC/Co, $r_\beta = 25 \mu\text{m}$)	12	0.05	383	0.97
	0 (WC/Co, $r_\beta = 25 \mu\text{m}$)	24	0.05	552	0.81
Material	Tool Type t	Cutting Speed v_c [mm/min]	Feed f [mm/rev]	Average Temperature T_{avg} [°C]	D_{avg} Ti-6Al-4V [μm]
Ti-6Al-4V	1 (TiAlN, $r_\beta = 10 \mu\text{m}$)	55	0.05	302.86	14.66
	1 (TiAlN, $r_\beta = 10 \mu\text{m}$)	55	0.1	414.46	13.09
	1 (TiAlN, $r_\beta = 10 \mu\text{m}$)	90	0.05	307.21	14.4
	1 (TiAlN, $r_\beta = 10 \mu\text{m}$)	90	0.1	439.32	14.95
	0 (WC/Co, $r_\beta = 25 \mu\text{m}$)	55	0.05	265.3	13.03
	0 (WC/Co, $r_\beta = 25 \mu\text{m}$)	55	0.1	402.82	14.39
	0 (WC/Co, $r_\beta = 25 \mu\text{m}$)	90	0.05	289.96	16.17
	0 (WC/Co, $r_\beta = 25 \mu\text{m}$)	90	0.1	436.28	13.57

Table 5.4 Regression model coefficients for Ti-6Al-4V and IN100.

	Regression Models for IN100 Grain Size and Temperature		Regression Models for Ti-6Al-4V Grain Size and Temperature	
Coefficient	d_l [μm]	T_{avg} [$^{\circ}\text{C}$]	D_{avg} [μm]	T_{avg} [$^{\circ}\text{C}$]
β_0	1.116	214	10	121
β_1	-0.084	-20	0.57	77.4
β_2	-0.01258	14.08	0.073	0.202
β_3	-	-	26	2231
β_{12}	-0.000083	-0.3333	-0.0103	-0.413
β_{13}	-	-	2.2	-401
β_{23}	-	-	-0.53	8.37
R^2	0.278	0.907	0.398	0.995

5.2.2.1 Multi-objective Optimization of Machining Temperature and Microstructure of IN100

An optimization problem for minimizing the machining temperature and microstructural changes is formulated as follows using the variables described previously:

$$\begin{aligned}
 &\text{Min.} && \left\{ (d_1^{exp}(v_c, r_\beta) - d_1)^2, T_{avg}(v_c, t) \right\} \\
 &\text{s.t.} && 12 \leq v_c \leq 24 \\
 &&& 0 \leq t \leq 1
 \end{aligned} \tag{5.7}$$

The Pareto front and the corresponding decision variables are shown in Figure 5.3. It is seen that the low cutting speed ($v_c = 12$ m/min) is preferred, and the tool type is the deciding factor for the competing objectives. According to the regression equations and the result of the optimization, lower cutting speed results in lower temperatures and less microstructural alterations. The TiAlN coated tool has higher thermal conductivity and lower friction, therefore generates less heat during machining. An interesting result is that

even though the TiAlN coated tool yields lower temperatures, it results in a more refined microstructure that could be explained by dynamic recrystallization.

The results indicate that if the minimization of microstructural changes is more important than the minimization of the average temperature, then the WC/Co $r_\beta = 25 \mu\text{m}$ tool can be used with $v_c=12 \text{ m/min}$ cutting speed (orange region in the figure). If the temperature minimization is more critical, the coated tool can be used with $v_c=12 \text{ m/min}$ cutting speed (yellow region in the figure).

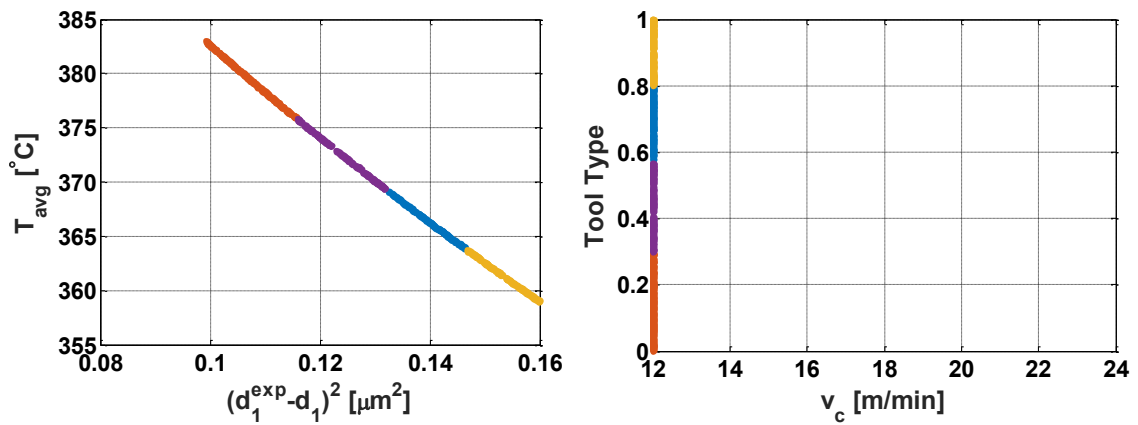


Figure 5.3 Multi-objective optimization result for IN100 nickel alloy with objective values (left) and the decision variables (right).

5.2.2.2 Multi-objective Optimization of Efficiency and Microstructure of Ti-6Al-4V

The optimization problem for minimizing the grain size change and the machining temperature of Ti-6Al-4V titanium alloy is formulated as follows:

$$\begin{aligned}
 \text{Min.} \quad & \left\{ (D_{avg}^{exp}(v_c, r_\beta) - D_{avg})^2, T_{avg}(v_c, t, f) \right\} \\
 \text{s.t.} \quad & 12 \leq v_c \leq 24 \\
 & 0 \leq t \leq 1 \\
 & 0.05 \leq f \leq 0.1
 \end{aligned} \tag{5.8}$$

The Pareto front and corresponding decision variables are shown in Figure 5.4. It is observed that the Pareto front is contained in the slow feed rate ($f = 0.05$ mm/rev) solutions which could be explained by the dominant effect of feed rate on the heat generation during machining. Interestingly, the WC/Co $r_\beta = 25$ μm tool ($t = 0$) is preferred even though the TiAlN coated tool has higher thermal conductivity and lower friction, which could only be attributed to microstructural alterations. Reducing the cutting speed yields lower temperatures as well, which is desirable for efficiency. However, lower cutting speeds create a significant differences between the reference and predicted grain sizes. The WC/Co $r_\beta = 25$ μm tool ($t = 0$) can be used with $f = 0.05$ mm/rev and $v_c = 90$ m/min can be used to minimize the microstructural alterations at the expense of higher temperatures, as shown as the yellow region in the figure. Alternatively, the same tool can be used with $f = 0.05$ mm/rev and $v_c = 55$ m/min to obtain lower temperatures, shown as the blue region in the figure.

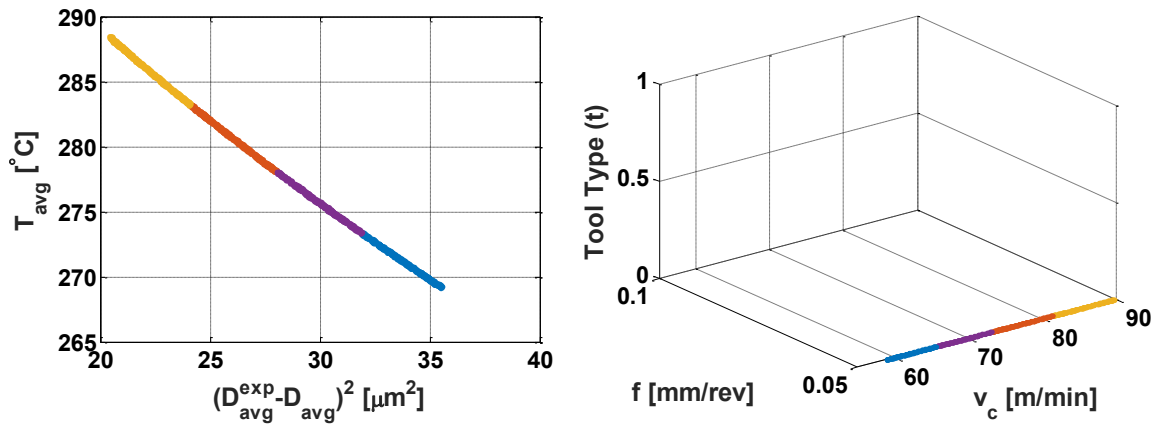


Figure 5.4 Multi-objective optimization result for Ti-6Al-4V titanium alloy with objective values (left) and the decision variables (right).

5.3 JMAK Microstructure Model Parameter Optimization

Although the finite element simulations provide a way to predict the grain size distribution after machining under different conditions, they can be further improved via a methodical search for model parameters. However, designing and running a large amount of simulations manually is a tedious task. Fortunately, this can be achieved using heuristic search methods such as Genetic Algorithms as discussed in this section. By designing FEM simulations and tying them to an optimization algorithm, the JMAK microstructure model parameters can be optimized to achieve a better match between FEM predicted grain sizes and actual grain sizes. Mean grain sizes obtained from SEM measurements at different cutting conditions can be utilized as target values to improve the accuracy predictions of the recrystallization model.

The proposed optimization scheme will be applied to IN100 alloy material, to primary γ' grains. The original JMAK parameters determined for γ matrix grains in the previous chapters can be supplied as the initial population to the GA algorithm. Moreover, certain parameters such as the activation energy can be selected to remain constant via equality constraints, while others can be bound by inequality constraints at reasonable ranges.

5.3.1 JMAK Model and Parameters

The JMAK model described in Chapter 1 utilizes temperature, strain and strain rates calculated during the simulations to predict dynamic recrystallization and grain sizes using model parameters and material properties. Dynamic recrystallization occurs when a critical strain $\varepsilon_c = a_2 \varepsilon_p$ is reached. The JMAK model equations given in Eqs. (1.1)-(1.5) are repeated below:

$$\varepsilon_p = a_1 d_0^{h_1} \dot{\varepsilon}^{m_1} \exp(Q_1/RT) + c_1 \quad (5.9)$$

$$X_{DRx} = 1 - \exp \left[-\beta_d \left(\frac{\varepsilon - a_{10} \varepsilon_p}{\varepsilon_{0.5}} \right)^{k_d} \right] \quad (5.10)$$

$$\varepsilon_{0.5} = a_5 d_0^{h_5} \varepsilon^{n_5} \dot{\varepsilon}^{m_5} \exp(Q_5/RT) + c_5 \quad (5.11)$$

$$d_{DRx} = a_8 d_0^{h_8} \varepsilon^{n_8} \dot{\varepsilon}^{m_8} \exp(Q_8/RT) + c_8 \quad (5.12)$$

$$d_{avg} = d_0(1 - X_{DRx}) + d_{DRx} X_{DRx} \quad (5.13)$$

The apparent activation energy for IN100 nickel alloy is taken as $Q_{act}=348,000$ J/ mol (Kikuchi et al., 1990) and the initial grain size for primary γ' grains is $d_0= 1.28 \mu\text{m}$ (Milligan et al., 2004) as described previously. Brief descriptions of the JMAK parameters implemented in the DEFORM-3D software are given in Table 5.5.

5.3.2 Initial Parameters of JMAK Model

In order to determine initial IN100 parameters, a sensitivity analysis sweep was run based on Waspaloy (Shen, 2005) and IN718 AMTC parameters. Further analyses were performed using Mathematica in order to obtain reasonable ranges by looking at effects of parameters on the equations. Table 5.6 shows the existing JMAK parameters in the DEFORM-3D database for Nickel-base alloys IN718 and Waspaloy. These parameters served as a basis for the parameter search. Table 5.7 shows the different sets of parameters that were used in the analysis.

IN100 base JMAK model parameters, obtained by running sensitivity analyses on parameters given in (Shen et al., 1995; Shen, 2005) for Waspaloy, IN718 JMAK parameters in DEFORM 3D (IN718-AMTC set) are given in Table 5.8. The JMAK-based dynamic recrystallization model implemented in the DEFORM-3D software uses parameters a_1 , h_1 , m_1 , c_1 and a_2 along with the strain rate $\dot{\epsilon}$ to calculate the peak strain value ϵ_p as shown in Eq. (5.9), which is in turn used to determine whether recrystallization occurs or not. As the IN100 primary γ' grains have different morphologies, compositions and sizes than the γ -matrix grains, it is assumed that $\epsilon_{p,\gamma\text{-matrix}} \neq \epsilon_{p,\text{primary } \gamma'}$. Therefore, the parameters a_1 , h_1 , m_1 and a_2 are included in the parameter identification study. Moreover, parameters a_5 and h_5 , which are the exponents of initial grain size d_0 and ϵ in Eq. (5.11) contribute to the strain for 50% recrystallization, $\epsilon_{0.5}$, are included in the scheme. Furthermore, in Eq. (5.12), the exponent ϵ denoted n_8 and the scaling parameter a_8 contribute to the recrystallized grain size d_{DRx} , therefore they are also included in the parameter identification. Parameters m_5 and m_8 which are the strain rate exponents in

calculation of $\varepsilon_{0.5}$ and d_{DRx} are kept constant as strain rate fluctuates greatly with the FE mesh and location. Finally, the parameter h_8 is set to 0 ($h_8 = 0$) in order to disable the effect of initial grain size d_0 to recrystallized grain size d_{DRx} . Recrystallization kinetics parameters, β_d and k_d are kept at their initial values. Lastly, values of c_1 , c_5 and c_8 are taken as constant ($c_1 = c_5 = c_8 = 0$).

Table 5.5 JMAK parameters and descriptions.

Q_{act} : Activation energy [kJ/mole]
a_1 : Peak strain slope
h_1 : Initial grain size sensitivity exponent
m_1 : Strain rate sensitivity exponent
Q_1 : $Q_{act} m_1$
c_1 : Peak strain intercept
a_2 : Critical strain ratio
a_5 : $\varepsilon_{0.5}$ slope
h_5 : Initial grain size sensitivity exponent in $\varepsilon_{0.5}$
n_5 : Strain sensitivity exponent in $\varepsilon_{0.5}$
m_5 : Strain rate sensitivity exponent in $\varepsilon_{0.5}$
Q_5 : $Q_{act} m_5$
c_5 : $\varepsilon_{0.5}$ intercept
a_{10} : DRx constant
k_d : DRx exponent
β_d : DRx constant
a_8 : d_{DRx} slope
h_8 : Initial grain size sensitivity exponent in d_{DRx}
n_8 : Strain sensitivity exponent in d_{DRx}
m_8 : Strain rate sensitivity exponent in d_{DRx}
Q_8 : $Q_{act} m_8$
c_8 : d_{DRx} intercept

Table 5.6 JMAK Parameters for IN718 and Waspaloy.

Parameters		IN718 AMTC DEFORM-3D	Waspaloy (Shen, 2005)
	Q_{act}	N/A	468000
Peak Strain	a_1	0.004659	0.0005375
	h_1	0	0.54
	m_1	0.1238	0.106
	Q_1	49520	49610
	c_1	0	0
	a_2	0.83	0.83
DRX Kinetics	a_5	294	0.1449
	h_5	340	0.32
	n_5	512	0
	m_5	593	0.03
	Q_5	600	14040
	c_5	0	0
	β_d	0	0.693
	k_d	0	3
	a_{10}	0	0
DRX Grain Size	a_8	4.85×10^{10}	8103
	h_8	0	0
	n_8	-0.41	0
	m_8	-0.028	-0.16
	Q_8	-240000	-74880
	c_8	0	0

Table 5.7 Different JMAK parameter sets used in the sensitivity analysis study.

Peak Strain						DRX Kinetics										DRX Grain Size					
a_1	h_1	m_1	Q_1	c_1	a_2	a_5	h_5	n_5	m_5	Q_5	c_5	β_d	k_d	a_{10}	a_8	h_8	n_8	m_8	Q_8	c_8	
0.000538	0.5 4	0.106	49610	0	0.8 3	0.1449	0.3 2	0	0.0 3	1404 0	0	0.69 3	3	0	8103	0	0	-0.16	-74880	0	
0.004659	0	0.123 8	49520	0	0.8 3	294	340	51 2	593	600	0	0	0	0	4.85× 10 ¹⁰	0	- 0.41	- 0.028	- 240000	0	
0.000538	0	0.106	36888	0	0.8	0.1449	0.3 2	0	0.0 3	1044 0	0	0.69 3	3	0	8103	0	0	-0.16	-55680	0	
2.99×10 ⁻⁷	0	0.106	36888	0	0.8	0.1449	0.3 2	0	0.0 3	1044 0	0	0.69 3	3	0	8103	0	0	-0.16	-55680	0	
3×10 ⁻⁷	0.5	0.01	3480	0	0.8	0.05	0.2	0	0.0 3	1044 0	0	0.69 3	2	0	8103	0	0	-0.16	-55680	0	
0.3	0.5	0.01	3480	0	0.8	0.05	0.2	0	0.0 3	1044 0	0	0.69 3	2	0	8103	0	0	-0.16	-55680	0	
2	0	0.006	1308	0	0.8	1.21×10 ⁻⁵	0.1 3	0	0.0 4	8720	0	0.69 3	2	0	150	0	0	-0.03	-6540	0	
2	0	0.006	2088	0	0.8	1.21×10 ⁻⁵	0.1 3	0	0.0 4	1392 0	0	0.69 3	2	0	150	0	0	-0.03	-10440	0	
0.293	0	0.010 2	3549. 6	0	0.8	0.145	0.3 2	0	0.0 3	1044 0	0	0.69 3	3	0	8103	0	0	-0.16	-55680	0	
0.293	0	0.010 2	3549. 6	0	0.8	0.145	0.3 2	0	0.0 3	1044 0	0	0.69 3	3	0	4000	0	0	-0.1	-34800	0	

Table 5.8 Initial JMAK model parameters for IN100 alloy.

a_1	h_1	m_1	c_1	a_2	β_d
0.293	0	0.0102	0	0.8	0.693
a_5	h_5	m_5	n_5	c_5	k_d
0.145	0.32	0.03	0	0	3
a_8	h_8	m_8	n_8	c_8	a_{10}
8103	0	-0.16	0	0	0

Furthermore, a sensitivity analysis has been performed on the parameter a_8 . Figure 5.5 shows the results obtained from SEM measurements, and three different simulation sets that have been run with four different cutting conditions. The SEM measurement results are shown in black while the results obtained with the initial parameter set from Table 5.8 are shown in red, denoted as original parameters, with $a_8=8103$. The green and blue bars represent the results from the same parameter set with modifications to the a_8 parameter at two levels ($a_8=5000$ and $a_8=10000$). It is seen that increasing the a_8 term increases the predicted grain sizes, however a nonlinear response is present in comparison to measurements. The nonlinear response of different tools and cutting speeds to the grain sizes is the motivation to perform a heuristic search on the JMAK model parameters by utilizing the Genetic Algorithm.

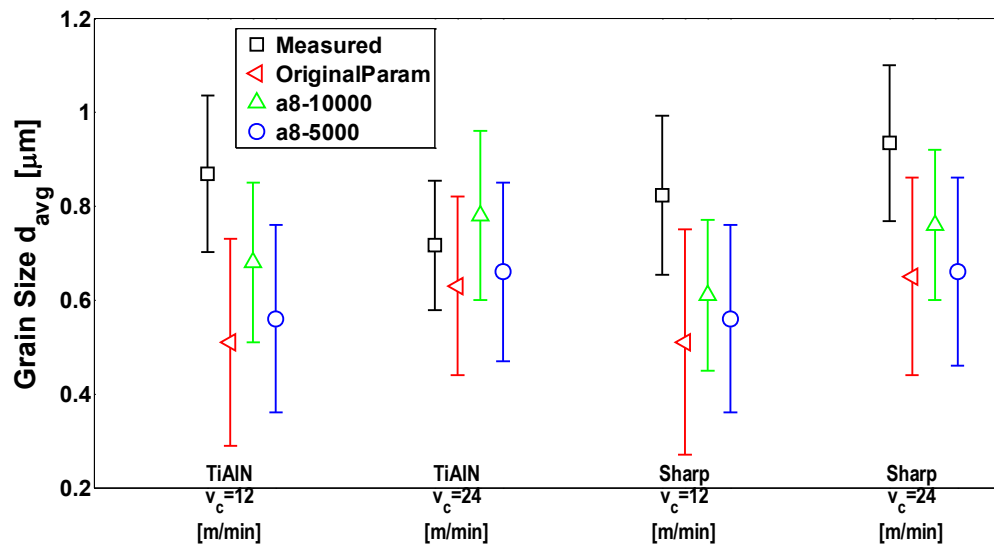


Figure 5.5 Sensitivity analysis on parameter a_8 with different cutting conditions.

5.3.3 Model Parameter Identification Methodology

Model parameter identification is performed by minimizing the difference in measured and predicted average grain sizes on primary γ' grains using FE simulations of machining IN100 alloy. The methodology can be summarized in three steps.

Step 1: Select model parameters to be identified ($a_1, h_1, m_1, a_2, a_5, h_5, a_8, n_8$) together with their constraints (e.g. $a_{1,min} \leq a_1 \leq a_{1,max}$).

Step 2: Develop optimization schemes for obtaining the set of model parameters heuristically as explained in later sections. FE simulations have been run repeatedly until a certain criterion is met.

Step 3: Analyze the results and identify a suitable set of JMAK model parameters.

5.3.4 Optimization Problem Definition

The optimization problem for minimizing the difference of measured and predicted grain sizes for a particular cutting condition with JMAK model parameters x is defined as:

$$\text{Min.} \quad (d_1^{exp} - d_1^{sim}(x))^2 \quad (5.14)$$

$$\text{s.t.} \quad Ax = b \quad (5.15)$$

$$Cx \leq d \quad (5.16)$$

$$l \leq x \quad (5.17)$$

$$x \leq u \quad (5.18)$$

where d_1^{exp} is the mean of the primary γ' grain sizes obtained from experimental measurements and d_1^{sim} is the mean grain sizes obtained from simulations, respectively.

Constraints shown in Eqs. (5.15)-(5.19) are chosen based on suitable values and ranges for each of the JMAK parameters. The decision variable vector \mathbf{x} is given in terms of JMAK parameters as:

$$\mathbf{x} = [a_1 \ n_1 \ m_1 \ Q_1 \ c_1 \ a_2 \ a_5 \ h_5 \ n_5 \ m_5 \ Q_5 \ c_5 \ \beta_d \ k_d \ a_{10} \ a_8 \ h_8 \ n_8 \ m_8 \ Q_8 \ c_8] \quad (5.19)$$

with $Q_i = m_i \times Q_{act}$ where Q_{act} is the activation energy which can be satisfied using Eq. (5.15). Furthermore, the following equality constraints are used to form the matrix A and vector b in Eq. (5.15).

$$x_5 = x_9 = x_{12} = x_{15} = x_{17} = x_{21} = 0, \quad (5.20)$$

$$x_8 = 0.48732, \ x_{10} = 0.03, \ x_{13} = 0.693, \ x_{14} = 3$$

There are no coupled inequality constraints in this problem, therefore Eq. (5.16) is not used in the optimization. Lower and upper bounds, \mathbf{l} and \mathbf{u} are used in the form of Eqs. (5.17) and (5.18) instead, which are given as in Eqs. (5.21) and (5.22).

$$\mathbf{l} = [0.2, 0.1, 0.01, 0, 0, 0.1, 0.1, 0.4, 0, 0.01, 0, 0, 0, 0, 0, 5000, 0, 0.1, -0.5, -\infty, 0] \quad (5.21)$$

$$\mathbf{u} = [0.4, 0.5, 0.1, \infty, 0, 0.5, 0.5, 0.5, 1, 0.1, \infty, 0, 1, 3, 0, 11000, 1, 0.5, -0.1, 0, 0] \quad (5.22)$$

The optimization problem can easily be solved in MATLAB using the built in packages. However, Finite Element simulations must be designed and run in batch mode, autonomously. To achieve this, the MATLAB program has to create the simulations using a template file, make the changes as required by the optimization algorithm, submit the simulations to DEFORM 3D software and extract the outputs when the simulations are over. The optimization process is shown in Figure 5.6. First, a DEFORM Key file is created using an existing simulation by the user. This key file contains the necessary information such as material properties, JMAK model parameters, geometry, mesh, and solver settings,

and is in a text format. Standard MATLAB I/O procedures can be used to manipulate this key file to convey the information that is coming from the optimization algorithm, such as changing the JMAK model parameters. Next, the KEY file is converted to a DEFORM database (DB) file that is used to run the simulation and save the finite element solution. At the end of the simulation, the DB file is parsed and grain size information is extracted from the elements. These extracted results are passed on to the optimization algorithm, and the whole cycle is repeated until an optimum solution is found. Furthermore, since each simulation takes a considerable amount of time to be completed, multiple simulations are run at the same time, on a multicore processor. We are currently limited to an Intel i-7 quad-core processor that is capable of running eight simulations at the same time using hyper-threading. However, this limits the population size to 8 as well, therefore a queue must be implemented to run the simulations in batches of 8 if larger population sizes are desired.

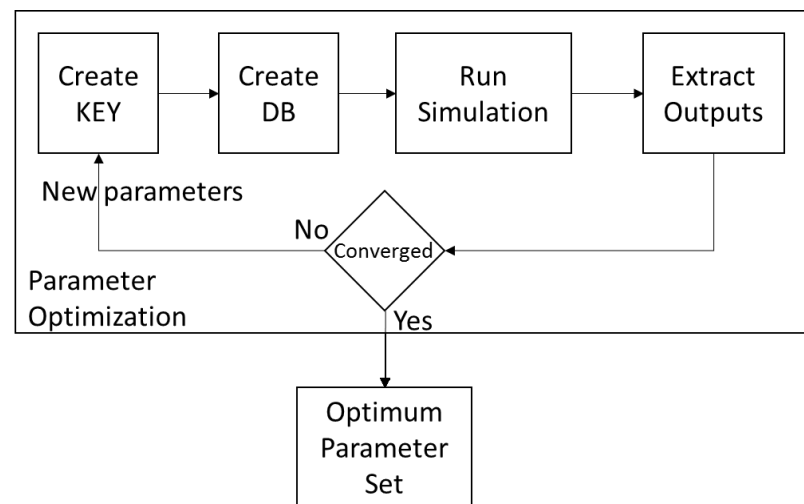


Figure 5.6 Optimization of JMAK Model Parameters: DEFORM and MATLAB interface.

In an attempt to generalize the fit of the parameters, the problem is formulated as multi-objective optimization utilizing i different cutting conditions with the weighted sum approach. A linear scalarization with weights w_j is used to convert the problem to a single-objective problem as shown in Eqs. (5.23)-(5.27).

$$\text{Min.} \quad \sum_{j=1}^i w_{2j-1} \left(\frac{\mu_{exp,j} - \mu_{sim,j}(x)}{\mu_{exp,j}} \right)^2 + w_{2j} \left(\frac{\sigma_{exp,j} - \sigma_{sim,j}(x)}{\sigma_{exp,j}} \right)^2 \quad (5.23)$$

$$\text{s.t.} \quad \sum_{j=1}^{2i} w_j = 1 \quad (5.24)$$

$$Ax = b \quad (5.25)$$

$$x \geq l \quad (5.26)$$

$$x \leq u \quad (5.27)$$

Two cutting conditions are used and the objective function is modified accordingly to give equal weights to the errors from both simulations.

5.3.5 Simulation Queuing & Batch Jobs

The simulation queuing is performed via an in-house developed C# program. Figure 5.7 shows the scheduling and running of the optimization. Firstly, model parameters determined by the optimization algorithm in MATLAB are saved in a SQL database. Next, a C# application periodically checks for new inputs to the database and captures them. In the event of a new simulation input, the C# application creates the DEFORM KEY and DB files, then runs these simulations in batches. Once the simulations are over, the application writes the results to the SQL database. Meanwhile, the optimization algorithm in MATLAB waits for the results to be written in the database. Once the results are in, it

calculates the objective function value and continues the optimization process to generate new parameters. The process continues until an optimum parameter set is obtained. The stopping condition is set such that the difference between the objective function values of the best generation and the newest generation is less than 10^{-5} . The advantage of this approach is that larger population sizes are made available through queuing. Moreover, because parallelization itself does not affect the performance of individual simulations in the proposed solution, it is also possible to create a cluster of workstations in this manner by running the C# application on different computers that monitor the database and share the workload without having to write complex Message Passing Interface (MPI) calls and network operations for parallelization of the whole process, and without having to purchase additional expensive software packages.

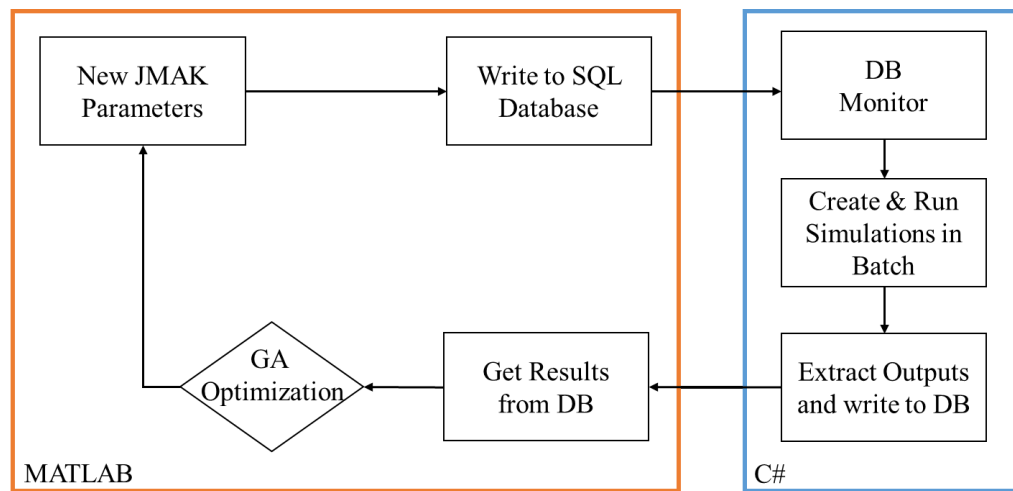


Figure 5.7 Scheduling and running the JMAK model parameter optimization

This effort yields JMAK model parameters that are then used in predicting grain sizes for other cutting conditions including cutting tools with uncoated WC/Co and TiAlN coated WC/Co, two levels of cutting speed ($v_c=12$ m/min and 24 m/min).

5.3.6 Finite Element Simulations

The Finite Element simulations created for modeling the IN100 turning process described in Chapter 3 are utilized in the optimization problem. However, as hundreds of simulations are needed for the optimization to converge, the computational time it takes to run these simulations becomes an issue. Therefore, in order to reduce the simulation times, the problem geometry is simplified, and two separate simulation models are created.

5.3.6.1 Reduced Simulation Model - 1

In order to speed up the optimization process, reduced models of the simulations shown in Chapter 3 are created. The full simulation is first run until the tool has traveled a certain distance in the feed (x) direction. Since the feed is kept constant in all IN100 simulations, this also means that the tool travels the same distance in the cutting direction in all simulations. The simulation is stopped when the x -stroke reaches 394 nm. Then, the length of the workpiece is reduced by removing a portion of it that has already been processed. The length of the workpiece is reduced to 1.9 mm down from the initial 3.5mm while leaving the boundary conditions and solution fields on the remaining part untouched. The new workpiece is then utilized in the optimization study, where simulations are run until the x -stroke reaches 0.00417. The reduced workpiece, containing approximately 30000 elements is shown Figure 5.8, at the beginning and end of the optimization run. The results

are extracted from the processed region, which is about 0.5 mm in the y direction. This approach has reduced the average simulation time to 2 hours. A summary of the simulation parameters is given in Table 5.9.

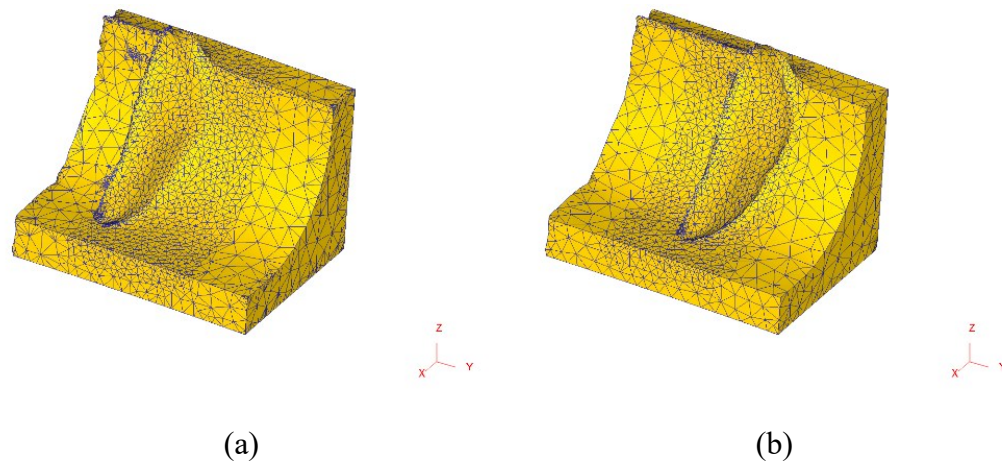


Figure 5.8 Reduced Model 1 geometry after the slicing operation: a) Beginning of the optimization run. b) End of the optimization run.

The microstructure data is then initialized, and a Deform KEY file is created from the simulation. The KEY file is modified accordingly to let MATLAB write in the new set of JMAK parameters. This allows the optimization algorithm to modify the parameters in the FE simulation.

Table 5.9 Simulation parameters for Reduced FE Model 1.

Length [mm]		No. of elements		Friction coefficients	
Workpiece	Cutting	Tool	Work	Rake	Flank
1.9	0.5	120,000	30,000	$\mu=0.8$ WC/Co	$\mu=0.6$ WC/Co

5.3.6.2 Reduced Simulation Model 2

Next, we look at improving the accuracy of the simulations by increasing the area where the data is extracted from, while keeping the simulation times low. In order to achieve this, the original geometry show in Chapter 3 is utilized, however, it is discretized with fewer elements. Figure 5.9 shows the model geometry and mesh, and Table 5.10 shows the summary of the simulation parameters. Once again, the full simulations are run until the tool has travelled a certain distance in the cutting (y) direction starting from a cutting length of $l_1=1.1$ mm until a cutting length of $l_2=2.6$ mm (see Figure 5.9). After this distance is reached, the simulation is stopped and remeshed using 50000 elements, down from 100000 in the beginning of the simulation. Afterwards, the boundary conditions and existing solution fields (temperature, displacement, etc.) are interpolated on to the new mesh. Note that different machining conditions yield different chip geometries and fields (such as temperature), therefore this process has to be repeated for each different machining condition to obtain different geometries if multiple simulations are required.

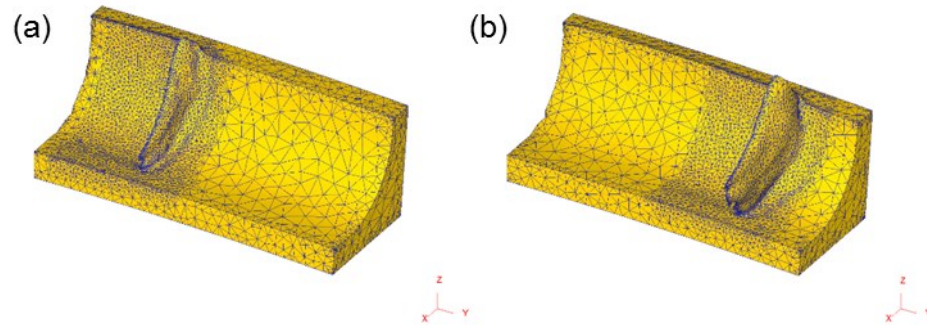


Figure 5.9 Reduced Model 2 geometry and mesh for TiAlN coated tool with $v_c=24$ m/min, (a) beginning of the optimization run (cutting length of $l_1=1.1$ mm) (b) end of the optimization run (cutting length of $l_2=2.6$ mm).

Table 5.10 Simulation parameters for Reduced FE Model 2.

Length [mm]		No. of elements		Friction coefficients	
Workpiece	Cutting	Tool	Work	Rake	Flank
3.5	$\Delta l=l_2-l_1=1.5$	120,000	50,000	$\mu=0.8$ WC/Co	$\mu=0.6$ WC/Co
				$\mu=0.6$ TiAlN	$\mu=0.5$ TiAlN

As discussed in the previous section, Deform KEY files are created from simulations, and they are modified to allow MATLAB to write the new set of JMAK parameters in them during the optimization.

5.3.6.3 Simulation Runs

Using the Reduced Models explained in the previous sections, two separate optimization studies have been performed. First, the optimization problem defined in Eqs. (5.14)-(5.22) is solved using FE simulations with the Reduced Model 1 with a single machining condition, WC/Co tool with $r_\beta=5\ \mu\text{m}$ and $v_c=12\ \text{m/min}$ cutting speed. The second optimization study utilizes WC/Co tool with $r_\beta=5\ \mu\text{m}$ tool, $v_c=12\ \text{m/min}$ cutting speed and TiAlN coated tool with $v_c=24\ \text{m/min}$ cutting speed conditions to create two simulations to be run simultaneously, using Eqs. (5.20)-(5.27). Table 5.11 shows the constraints used in the optimization runs for Models 1 and 2 for each JMAK parameter. The weights were selected as $w_1=w_3=0.35$ and $w_2=w_4=0.15$, with a total of seventy percent of the weights being distributed to the means. Thirty percent of the weights were given to the standard deviations, in order to better represent the grain size distributions seen in the measurements. Note that each machining condition uses a different geometry for reduced model 2.

Table 5.11 Constraints used in the optimization runs for Models 1 and 2.

Parameters		Constraints for Model 1	Constraints for Model 2
Peak Strain	Q_{act}	$Q_{act}=348000$	$Q_{act}=348000$
	a_1	$0 \leq a_1 \leq 0.5$	$0.2 \leq a_1 \leq 0.4$
	h_1	$0 \leq h_1 \leq 0.5$	$0.1 \leq h_1 \leq 0.5$
	m_1	$0 \leq m_1 \leq 0.5$	$0.01 \leq m_1 \leq 0.1$
	Q_1	$Q_1=Q_{act} \times m_1$	$Q_1=Q_{act} \times m_1$
	c_1	$c_1=0$	$c_1=0$
	a_2	$0 \leq a_1 \leq 1$	$0.1 \leq a_1 \leq 0.5$
DRX Kinetics	a_5	$0 \leq a_5 \leq 0.5$	$0.1 \leq a_5 \leq 0.5$
	h_5	$0 \leq n_5 \leq 0.5$	$h_5=0.48732$
	n_5	$n_5=0$	$n_5=0$
	m_5	$0 \leq m_5 \leq 0.5$	$m_5=0.03$
	Q_5	$Q_5=Q_{act} \times m_5$	$Q_5=Q_{act} \times m_5$
	c_5	$c_5=0$	$c_5=0$
	β_d	$\beta_d=0.693$	$\beta_d=0.693$
	k_d	$k_d=3$	$k_d=3$
	a_{10}	$a_{10}=0$	$a_{10}=0$
DRX Grain Size	a_8	$5000 \leq a_8 \leq 10000$	$5000 \leq a_8 \leq 11000$
	h_8	$h_8=0$	$h_8=0$
	n_8	$0 \leq n_8 \leq 0.5$	$0.1 \leq n_8 \leq 0.5$
	m_8	$-0.5 \leq m_8 \leq 0$	$-0.5 \leq m_8 \leq -0.1$
	Q_8	$Q_8=Q_{act} \times m_8$	$Q_8=Q_{act} \times m_8$
	c_8	$c_8=0$	$c_8=0$

5.3.7 Optimization Results and Discussion

The identified JMAK model parameters using reduced Model 1 are given in Table 5.12. It is seen that h_1 , m_1 , a_2 , h_5 and n_8 parameters show differences to the γ -matrix grain parameters shown in Table 5.8 used as initial values.

The results obtained from the multiple simulation case with reduced Model 2 are given in Table 5.13, in the first row. Furthermore, a post-process analysis is performed using the simulation results to determine the effects of the weights w_j in the weighted sum objective function shown in Eq. (5.23). Rows 2 and below show the result of this post processing analysis, where the weights of the standard deviation terms (w_2 , w_4) are set to 0, and weights of the mean grain size terms (w_1 , w_3) are varied at 5 different cases. Based on the different weights, a new set of parameters has been chosen to better represent the model. Figure 5.10 shows a comparison between the optimization results, and the initial parameters. Results denoted by MultiOpt-Reduced in Figure 5.10 belong to the model (SetMulti_Opt,1) obtained from the post-process analysis whose parameters are given later. It is seen that the single simulation case with reduced Model 1 outperforms the reduced Model 2 on TiAlN $r_\beta=10\ \mu\text{m}$, $v_c=12\ \text{m/min}$ and WC/Co $r_\beta=5\ \mu\text{m}$, $v_c=24\ \text{m/min}$ conditions, while the multiple simulation case with reduced Model 2 is best at TiAlN $r_\beta=10\ \mu\text{m}$, $v_c=24\ \text{m/min}$ and WC/Co $r_\beta=5\ \mu\text{m}$, $v_c=12\ \text{m/min}$ conditions.

Table 5.12 Identified JMAK model parameters using single machining condition with Reduced Model 1.

a_1	h_1	m_1	c_1	a_2	β_d
0.293	0.34	0.039	0	0.38	0.693
a_5	h_5	m_5	n_5	c_5	k_d
0.145	0.48	0.03	0	0	3
a_8	h_8	m_8	n_8	c_8	a_{10}
8103	0	-0.16	0.43	0	0

Table 5.13 Identified JMAK model parameters with Reduced Model 2, post-processed with different weights.

Objective Weights				a_1	h_1	m_1	a_2	a_5	h_5	a_8	n_8	WC /Co $v_c=12$ m/min		TiAlN $v_c=24$ m/min	
												D_{avg_mes} 0.828 μm	SD_{mes} 0.239 μm	D_{avg_mes} 0.728 μm	SD_{mes} 0.219 μm
												D_{avg_sim} [μm]	SD_{sim} [μm]	D_{avg_sim} [μm]	SD_{sim} [μm]
w_1	w_2	w_3	w_4												
0.3 5	0.1 5	0.3 5	0.1 5	0.2871 8	0.2724 9	0.010 2	0.1161 3	0.2654	0.4873 2	860 3	0.3388 1	0.9817 4	0.3634 9	0.9350 2	0.2636 5
1	0	0	0	0.2871 8	0.1318 4	0.010 2	0.1161 3	0.1079	0.4873 2	810 1	0.3388 1	0.8303 8	0.4582 5	0.7187 7	0.3726 6
0.7	0	0.3	0	0.2871 8	0.1318 4	0.010 2	0.1161 3	0.1079	0.4873 2	810 1	0.3388 1	0.8303 8	0.4582 5	0.7187 7	0.3726 6
0.5	0	0.5	0	0.2871 8	0.1318 4	0.010 2	0.1161 3	0.1079	0.4873 2	810 1	0.3388 1	0.8303 8	0.4582 5	0.7187 7	0.3726 6
0.3	0	0.7	0	0.2871 8	0.1318 4	0.010 2	0.1161 3	0.1156 5	0.4873 2	813 0	0.3388 1	0.8374	0.4552 6	0.7354 3	0.3667 8
0	0	1	0	0.2871 8	0.1318 4	0.010 2	0.1161 3	0.1156 5	0.4873 2	813 0	0.3388 1	0.8374	0.4552 6	0.7354 3	0.3667 8

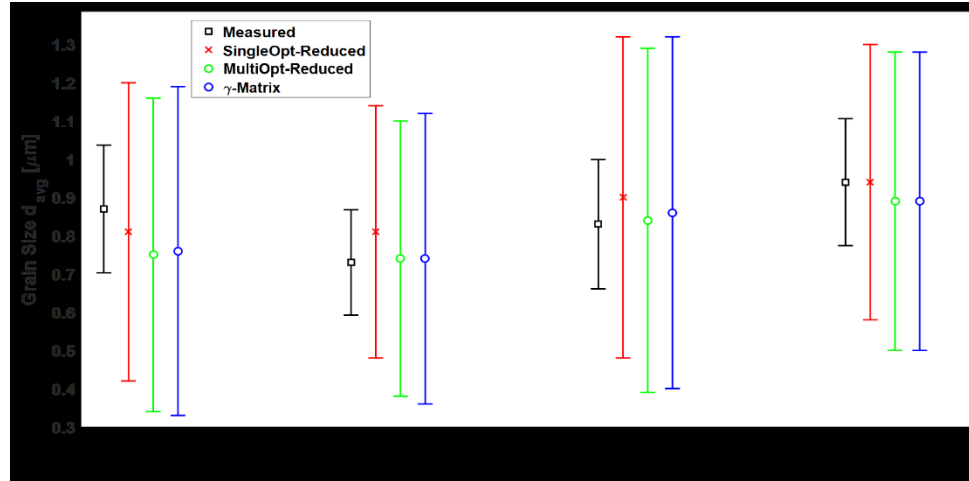


Figure 5.10 Comparison of measured and predicted grain sizes by using identified JMAK model parameters under different objective function weights.

Furthermore, to complete the analysis, parameter sets obtained via reduced Model 1 and reduced Model 2 are run on the FE simulation models (full FE models) given in Chapter 3, and the results are given in Table 5.14. On the full simulations, the JMAK parameters identified with the reduced Model 1 simulation (with WC/Co $r_{\beta}=5 \mu\text{m}$, $v_c=12 \text{ m/min}$) outperforms the reduced Model 2 (with two machining conditions) in all conditions, except the TiAlN $v_c=24 \text{ m/min}$ condition. The difference can be related to two reasons. Firstly, it is possible that the TiAlN, $v_c=24 \text{ m/min}$ condition is dissimilar to the other conditions, and a better generalization is achieved with the WC/Co $r_{\beta}=5 \mu\text{m}$, $v_c=12 \text{ m/min}$ condition that is used as the sole condition in the case of the reduced Model 1. Secondly, the difference in the Reduced Models could have also caused the difference.

On the other hand, it is important to note that smaller grain sizes are linked with hardening in IN100, which causes increased difficulty in machining. The reduced Model 1 parameters

overestimate the grain sizes in one cases by a significant margin, while the reduced Model 2 parameters underestimate the grain sizes in the other two. It is preferable to err on the side of caution, and predicting a more refined microstructure is more desirable. Ultimately, the optimization problem could be run on the full set of simulations given sufficient computational power and time to achieve improvements on these parameters.

Table 5.14 Identified JMAK model parameters (with $w_1=0.5$ and $w_2=0.5$) running on full FE simulations.

Parameter / Condition	*SetSingle_Opt	**SetMulti_Opt,1	**SetMulti_Opt,2
a_1	0.293	0.28718	0.28718
h_1	0.34	0.13184	0.13184
m_1	0.039	0.0102	0.0102
a_2	0.38	0.11613	0.11613
a_5	0.145	0.11565	0.1079
h_5	0.48	0.48732	0.48732
a_8	8103	8130.4	8101.1
n_8	0.43	0.33881	0.33881
TiAlN, $v_c=12$ m/min, $D_{avg,exp}$ 0.87 [μm]	0.79	0.709	0.708
TiAlN, $v_c=24$ m/min, $D_{avg,exp}$ 0.728 [μm]	0.88	0.72	0.715
WC/Co $r_\beta=5$ μm , $v_c=12$ m/min, $D_{avg,exp}$ 0.828 [μm]	0.78	0.726	0.721
WC/Co $r_\beta=5$ μm , $v_c=24$ m/min, $D_{avg,exp}$ 0.94 [μm]	0.89	0.738	0.764

*SetSingle_Opt = Set of model parameters identified from a single machining simulation (WC/Co, Sharp, $v_c=12$ m/min) by using the reduced FE Model 1.

**SetMulti_Opt = Set of model parameters identified from multiple machining simulations (WC/Co, Sharp, $v_c=12$ m/min and TiAlN $v_c=24$ m/min) by using the reduced FE Model 2 and further analysis using the results.

CHAPTER 6: EXPERIMENTAL ANALYSIS OF IN625 SELECTIVE LASER MELTING

6.1 Introduction

Additive manufacturing of metals is becoming increasingly popular in aerospace, automotive and medical industries as it allows production of intricate parts directly from a computer design. Selective Laser Melting (SLM) is a metal additive manufacturing method where a layer of powdered metal is melted at specific locations using a high power laser beam. The desired 3D geometry is sliced into 2D layers of equal thickness using Computer Aided Design (CAD) software, and the printer builds the part layer-by-layer by adding a new layer of powder on top of the previously processed layer. Once the process is completed, the excess metal powder is vacuumed and can be reused to a certain extent. Figure 6.1 provides a graphical representation of the SLM process.

While the 3D printing allows manufacturing of parts with sophisticated features, the quality of the printed parts are often not up to the industry level standards, and require further operations to improve quality and surface integrity. The surface integrity and layer characteristics of the processed parts play an important role in the products reliability and service life. Microstructures of IN625 parts obtained from SLM are significantly different than parts obtained with other processes. Selective Laser Melting of powder metals has not been fully studied and documented yet and consequently, investigation of the microstructure is of great importance.

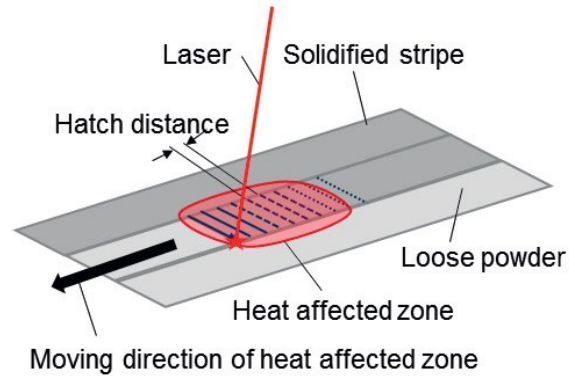


Figure 6.1 Representation of Selective Laser Melting process.

(Krauss et al., 2014)

In this Chapter, Selective Laser Melting processing of IN625 alloy is analyzed using test coupons that were fabricated with different process conditions. Grain size and columnar grain growth directions are measured from SEM images. Furthermore, an in-situ thermal camera video recording is analyzed for melt pool widths, spattering particles and heating and cooling rates.

6.2 Selective Laser Melting Process

The SLM process works by melting desired locations on the powder bed on a layer. The area to be processed is first divided into stripes. Each stripe consists of multiple tracks, separated by a hatch distance, and each track is processed with the laser beam at a constant scanning velocity. After a track is completed by the movement of laser in one direction, the laser shifts towards the next unprocessed track and starts moving in the opposite direction of the previous track as shown in Figure 6.2. The size of the molten region in the powder bed, called the meltpool, is determined by the process parameters such as scanning velocity (v_s), laser power (P), hatch distance (h), laser spot size (d) and the powder material mesh size (MS). Material properties such as thermal conductivity (k), specific heat (C_p), density (ρ) and reflectivity (R), as well as the process environment also has an effect on the meltpool. After a layer is finished, a new layer of powder, with a predefined thickness (s) is placed on the powder bed. Another process parameter in the SLM process is the rotation angle between consecutive layers, which allows the parts to be built in different scanning directions at each layer. Note that the 90° rotation angle means that after each layer, the scanning directions are rotated by 90° which essentially means that the scanning directions coincide after every other layer whereas the 67° angle rotation strategy yields a different design.

For a successful build, it is critical that the meltpool size is large enough to connect the tracks and stripes in each layer and deep enough to connect to the previous layer. Inadequate process parameters can easily cause incomplete fusion which leads to

catastrophic failures during or after the process. Furthermore, process parameters also have a significant effect on the underlying microstructure of the part, which affects the mechanical properties of the material significantly.

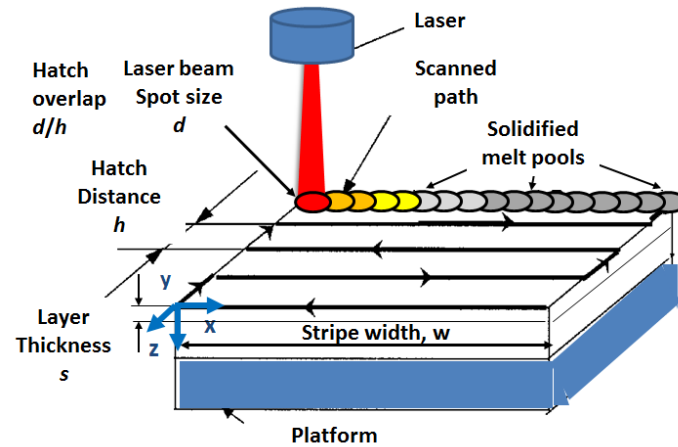


Figure 6.2 SLM terminology.

(Criales et al., 2015)

6.2.1 Sample Fabrication and Preparation

In order to analyze the SLM processing of IN625, thirty six specimens have been manufactured at the National Institute for Standards & Technology (NIST) facility in Gaithersburg, MD, using an EOS M270 DMLS machine. Fabricated test coupons are $16 \times 16 \times 15$ mm in dimension. The coupons were removed from the base plate using wire Electrical Discharge Machining (EDM) which results in final coupon heights less than 15mm. Coupons are processed with 4mm stripes, with a 0.1 mm overlap between each stripe to ensure the stripes are fused together. Process parameters follow the Box-Behnken design with ranges such that the resulting energy intensities coincide with the acceptable

builds shown in Anam et al. (Anam et al., 2013a). Three process parameters are considered at three levels, namely, laser power (P), scanning velocity (v_s) and hatch distance (h). The rotation angle scan strategy was not included as a factor in the design, rather, two separate designs were made for 90° and 67° rotation strategies, with otherwise identical parameters. The three factor Box-Behnken design is shown in Figure 6.3 that represents the process space where the treatment combinations appear at the center of the cube as well as on the midpoints of the edges. Table 6.1 shows the standardized values of factors for each experiment in a 3-factor, 3-level Box-Behnken design where low, medium and high settings of each factor are shown. The selected Box-Behnken design requires 15 coupons to be processed with distinct parameters, as well as 3 additional replications at the default setting. Therefore, 36 coupons were built in total for the experiments. It is important to note that the 67° setting is the recommended setting by EOS. Locations of these coupons were assigned randomly prior to the build, and the build layout is shown in Figure 6.4.

Box-Behnken design was utilized in designing of experiments it requires less number of experiments compared to other designs such as full factorial designs, while maintaining rotatability. Furthermore, it allows the analysis of results via Response Surface Methodology (RSM) which is a popular tool for creating predictive models from experimental data.

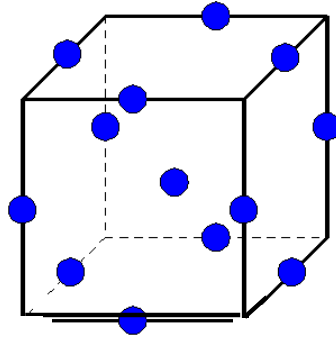


Figure 6.3 Box-Behnken Design.

(National Institute of Standards and Technology, 2015)

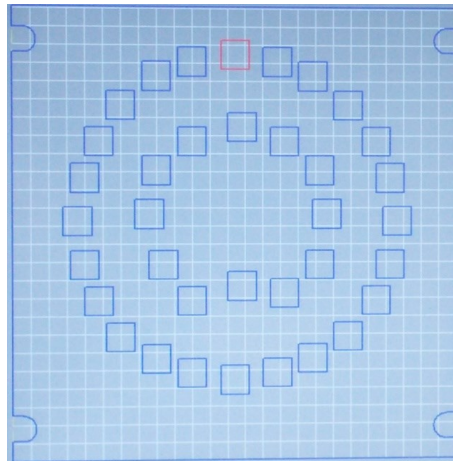


Figure 6.4 Build layout, as shown in the EOS M270 software.

In order to analyze the microstructure of SLM processed IN 625, specimens have been built as explained in the next sections. Due to the nature of the SLM process, processed layers are reheated many times during the processing of new layers, and the effect of reheating on the microstructure can only be observed from the interior layers. Moreover, because of convective and radiative heat transfer with the environment, the “skin” of the coupons are likely to experience a higher cooling rate than the core which may also affect

the microstructure. Furthermore, the SLM machine processes the outer regions of the specimens with the so called “skin” parameters that are different than the user prescribed parameters. Therefore, coupons obtained via SLM were first ground to remove approximately 500 μm from the outside surfaces. After the grinding operation, the SLM coupons were electropolished to reveal the microstructure.

Table 6.1 General Structure of Box-Behnken Design for Three Factors

Power P [W]	Scanning Velocity v_s [mm/s]	Hatch Distance h [mm]
169	725	0.1
195	725	0.1
169	875	0.1
195	875	0.1
169	800	0.09
195	800	0.09
169	800	0.11
195	800	0.11
182	725	0.09
182	875	0.09
182	725	0.11
182	875	0.11
182	800	0.1
182	800	0.1
182	800	0.1

6.3 Image Analysis

Grain sizes and growth directions are indicative of cooling rates, and can affect the mechanical properties of the material significantly. Utilizing a similar methodology to Chapter 2, grain size information can be extracted from SEM images that are taken from SLM produced coupon samples.

6.3.1 Scanning Electron Microscopy (SEM) Imaging

SEM images were obtained from the prepared test coupons using the InLens and Secondary Electron (SE2) detectors, from XY, XZ and YZ surfaces at multiple locations and magnification levels. The images reveal a dendritic microstructure with cross sections of dendrites appearing as equiaxed grains in different cross-sections of the coupons. The dendrites appear to be growing in 2 main directions, in the build (Z) direction and also in a direction perpendicular to the laser's scanning path. During the processing, the scanning path changes many times, thus creating dendrites in different directions. The growth of dendrites in these two directions can be explained by temperature gradients as dendritic growth is observed when large gradients of temperature or concentration are present. In the case of SLM, the temperature gradient is largest in the build direction as the cooling occurs towards the base plate via conduction, and towards the environment at the top layer dominantly via radiation (due to high temperatures) and to some extent convection (the chamber is not in vacuum).

Figure 6.5 shows the XZ view of the coupon #35 (195 W, 800 mm/s, 0.1 mm, 90° rotation scan strategy). Here, the build direction (Z) is shown with a white arrow. Coupon #35 is of specific importance as it was processed with the default settings. Layers can be seen approximately 20 μm apart and the layer thickness varies along each layer as the meltpools intrude and join with the previously solidified layers. Figure 6.6 shows the XZ view of the coupon at larger magnifications. Columnar grains are observed in the build direction, with approximately 0.75 μm in width. Figure 6.7 shows the XY and YZ views of coupon #17 (182 W, 800 mm/s, 0.1 mm, 90° rotation scan strategy), produced with a different set of parameters. It is observed that the region between two curved meltpool boundaries contains equiaxed grains, whereas columnar grains as well as equiaxed grains are observed within the meltpool boundaries.

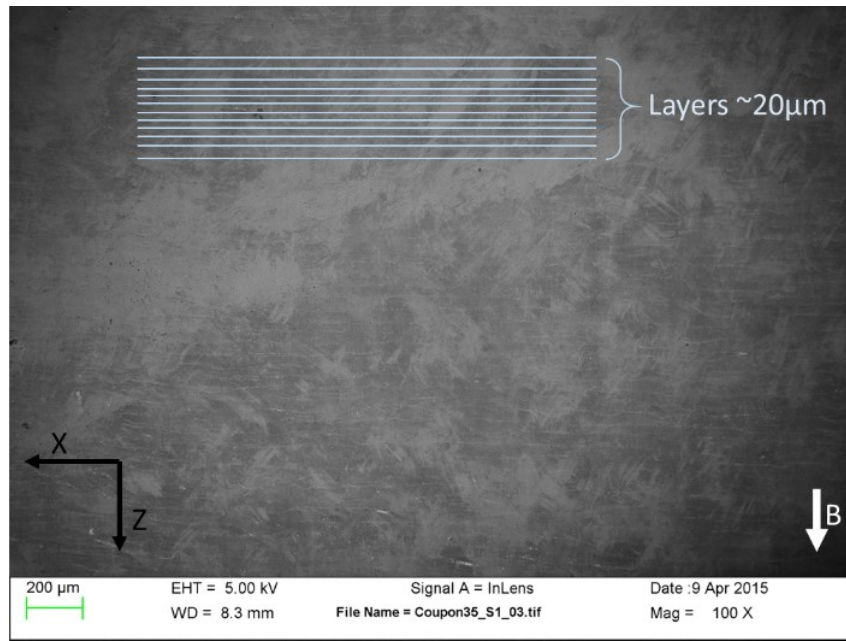


Figure 6.5 SEM image of the electropolished XZ surface of the coupon #35, at 100X magnification. B indicates the build direction.

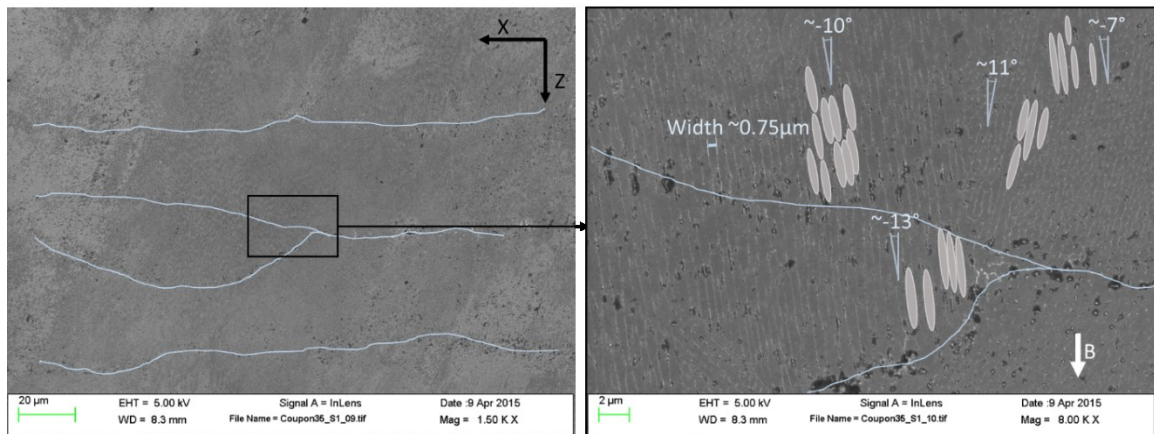


Figure 6.6 SEM image of the electropolished XZ surface of the coupon #35, at 1500X magnification (left) showing layers and 8000X magnification (right) showing columnar grains with inclinations. B indicates the build direction.

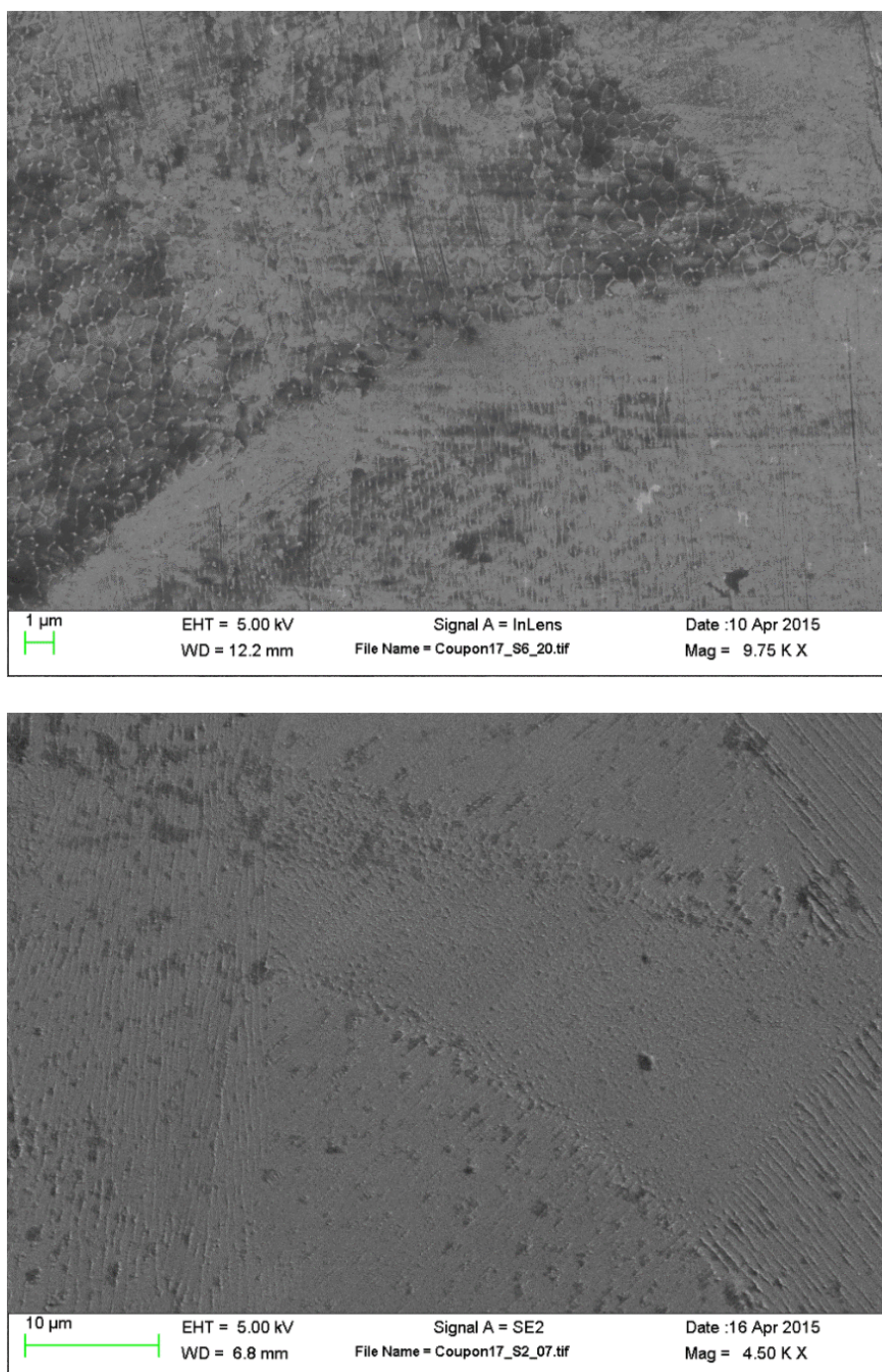


Figure 6.7 SEM image of horizontal (XY) section (top) and vertical (YZ) section (bottom) of coupon #17 showing cellular growth between meltpool regions and columnar growth within meltpool regions.

6.3.2 Grain Size Detection

An image processing procedure is applied on SEM images by marking grain boundaries in order to calculate the average diameters of the cellular grains commonly seen in the XY plane. However, manually marking the grains on each SEM image, as shown in Chapter 2, is a very challenging task given the sheer amount of grains and images involved. The task can be made easier by utilizing various image analysis methods and machine learning, as explained in the next section.

6.3.2.1 Semi-Automatic Edge Detection of Grains Using Machine Learning

Machine learning algorithms can be utilized to mark the grain boundaries, greatly reducing the workload for manual marking. Feature selection is an important task in constructing machine learning algorithms, especially when a large amount of data is involved. A standard SEM image consists of 1024 by 768 pixels, and the grayscale color information of each pixel is coded as an integer between 0-255.

After various trial and error experiments, the best testing performance was obtained after the image was processed in the following way: (1) Canny edge detection is applied on the images. (2) A brightness threshold is applied separately on the images. After the brightness threshold is applied, the pixels are processed with a radial filter. (3) The resulting images are superimposed with different weights applied at each image as a coefficient for the color information.

Features are then extracted from the resulting image to be used in Random Forests based classification in the following manner. The 8-connected pixel neighborhood, similar to the Moore's neighborhood is obtained for each pixel as shown in Figure 6.8. Here, pixel $p_{i,j}$ is the central pixel, with color $c_{i,j}$.

$p_{i-1,j+1}$	$p_{i,j+1}$	$p_{i+1,j+1}$
$p_{i-1,j}$	$p_{i,j}$	$p_{i+1,j}$
$p_{i-1,j-1}$	$p_{i,j-1}$	$p_{i+1,j-1}$

Figure 6.8 8-connected neighborhood for pixel $p_{i,j}$

Each pixel in this neighborhood is used to form a vector of features using their color value, along with the central pixel. The vector is then normalized in order to improve generalization power. Additionally, the initial color of the central pixel is also included in the feature vector which is given by:

$$c = [\hat{c}_{i-1,j+1} \ \hat{c}_{i,j+1} \ \hat{c}_{i+1,j+1} \ \hat{c}_{i-1,j} \ \hat{c}_{i,j} \ \hat{c}_{i+1,j} \ \hat{c}_{i-1,j-1} \ \hat{c}_{i,j-1} \ \hat{c}_{i+1,j-1} \ c_{i,j}] \quad (6.1)$$

In this methodology, each pixel must have an 8-connected neighborhood, therefore, the pixels at the four edges of the original image are not treated as observations as they don't have the required amount of neighboring pixels. Consequently, predictions can't be performed on the edge pixels of the image. After the input matrix is constructed, Principal Component Analysis (PCA) is performed to further reduce the number of features.

A binary output variable for each pixel is defined in the classification problem to suggest whether the pixel is on the boundary (edge) of a grain, or not. This information comes from the preprocessed image (edge detection + thresholding) as explained previously. Each pixel is then treated as an observation, and subsequently, input and output matrices are constructed. Finally, a Random Forests classification model is trained with 4 trees using the input matrix and the output vector is defined.

The grain size calculation algorithm explained in Chapter 2 requires convex and continuous (with no gaps in the perimeter) boundaries to be marked on the image. While the proposed machine learning algorithm is successful at detecting edges, the process results in disconnected edge detection, i.e. some pixels are missing along the contour of the grain. This prevents the grain size calculation operation. Therefore, a manual post-processing step is applied after the RF-predictions.

An image processing procedure is applied on SEM images in order to calculate the average diameters of the cellular grains commonly seen in the XY plane. The calculation is performed by manually tracing the boundaries of the grains on the SEM images with RF-predictions first, and then calculating their diameters in MATLAB.

6.3.2.2 Results and Analysis

Figure A1 in Appendix A shows the processed SEM images of XY views of all coupons showing marked grains and calculated grain diameters. The number of grains identified in each image varies between 126 and 547, which is sufficient for statistical analysis. Only one image per condition is chosen to be processed and further analysis can yield more general results. Figure 6.9 shows the grain size measurements from two of the coupons; coupon #35 (195 W, 800 mm/s, 0.1 mm, 90° rotation scan strategy) and (b) coupon #31 (195 W, 800 mm/s, 0.1 mm, 67° rotation scan strategy). Measurements for all coupons are summarized in Table 6.2, showing average grain diameters for each coupon, along with the processing conditions.

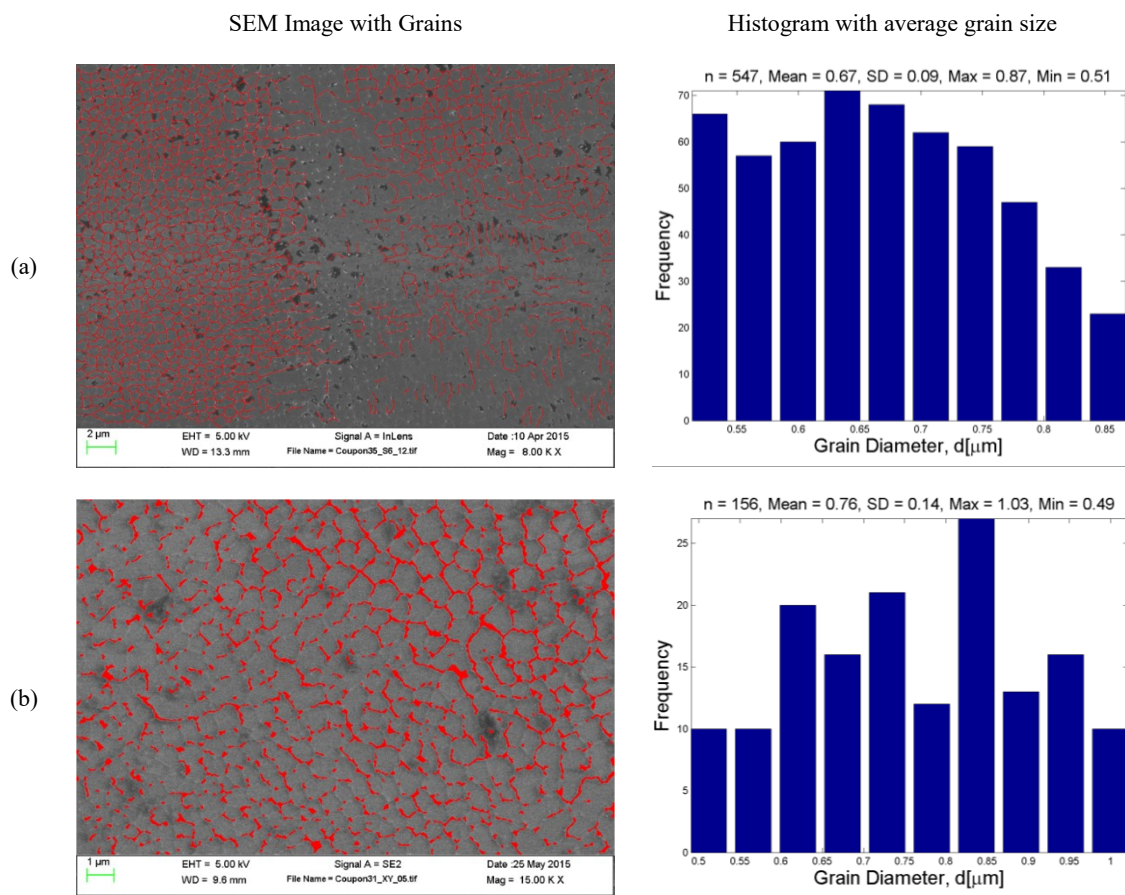


Figure 6.9 Grain size analysis of SLM processed IN625 coupons, (a) coupon #35 (195 W, 800 mm/s, 0.1 mm, 90° rotation scan strategy) and (b) coupon #31 (195 W, 800 mm/s, 0.1 mm, 67° rotation scan strategy).

Table 6.2 Processing conditions and grain size analysis results.

Coupon #	Rotation [°]	Laser Power P [W]	Scanning Velocity v_s [mm/s]	Hatch Distance h [mm]	Energy Intensity E [J/mm ³]	Average Grain Diameter D_{avg} [μm]	Standard Deviation of Grain Diameters SD_{avg} [μm]
1	90	169	875	0.1	96.57	0.6809	0.0913
2	67	169	725	0.1	116.55	0.5247	0.1226
3	67	195	725	0.1	134.48	0.5175	0.1111
4	90	195	875	0.1	111.43	0.5588	0.1033
5	67	169	800	0.09	117.36	0.5728	0.0885
6	90	182	875	0.09	115.56	0.4893	0.0838
7	67	182	800	0.1	113.75	0.6003	0.0809
8	90	182	725	0.11	114.11	0.4659	0.0942
9	90	195	800	0.11	110.8	0.5158	0.1049
10	67	182	725	0.11	114.11	0.7336	0.1313
11	67	169	875	0.1	96.57	0.4961	0.093
12	90	182	725	0.09	139.46	0.7546	0.1069
13	67	195	800	0.09	135.42	0.615	0.0881
14	90	182	800	0.1	113.75	0.6567	0.1395
15	90	182	800	0.1	113.75	0.4946	0.1046
16	90	195	725	0.1	134.48	0.71	0.11
17	90	182	800	0.1	113.75	0.66	0.1
18	90	182	875	0.11	94.55	0.5052	0.0866
19	67	195	875	0.1	111.43	0.4826	0.2071
20	90	169	725	0.1	116.55	0.615	0.1194
21	90	169	800	0.09	117.36	0.5469	0.0964
22	67	182	800	0.1	113.75	0.3943	0.1505
23	90	169	800	0.11	96.02	0.5607	0.0845
24	67	182	800	0.1	113.75	0.5487	0.1521
25	67	195	800	0.11	110.8	0.5044	0.0909
26	67	182	875	0.09	115.56	0.5129	0.0719
27	67	182	725	0.09	139.46	0.4411	0.1512
28	67	182	875	0.11	94.55	0.3857	0.0613
29	90	195	800	0.09	135.42	0.65	0.11
30	67	169	800	0.11	96.02	0.6062	0.1449
31	67	195	800	0.1	121.88	0.7622	0.1424
35	90	195	800	0.1	121.88	0.67	0.09

Figures 6.10-6.13 show the main effects of energy intensity, laser power, scanning speed and hatch distance on the measured average grain sizes respectively. In general, increasing the energy intensity causes an increase in the average grain sizes. Laser power does not seem to affect the grain sizes significantly in both 67° and 90° rotation strategies. Increasing scanning speed tends to decrease the grain sizes in both 67° and 90° rotation strategies. Increasing hatch distance tends to reduce the grain average grain diameters in the case of 90° rotation, whereas in the 67° rotation the change is not as significant.

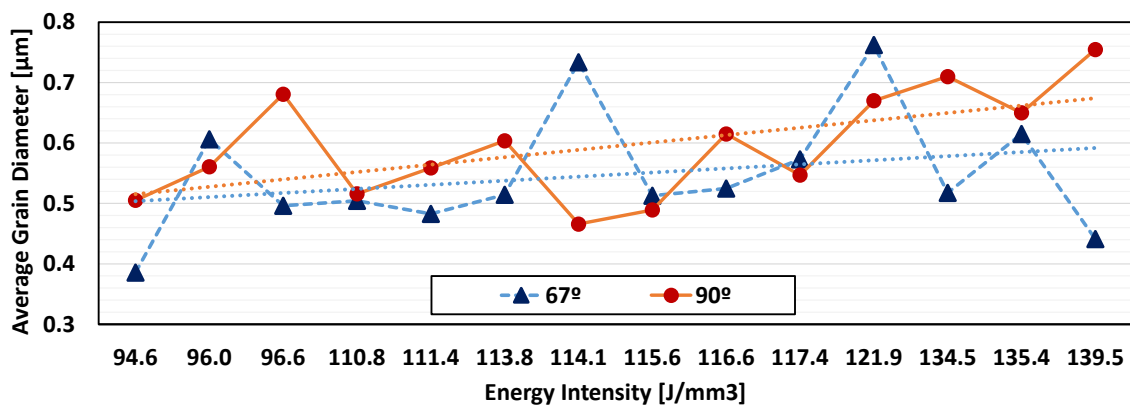


Figure 6.10 Effect of energy intensity.

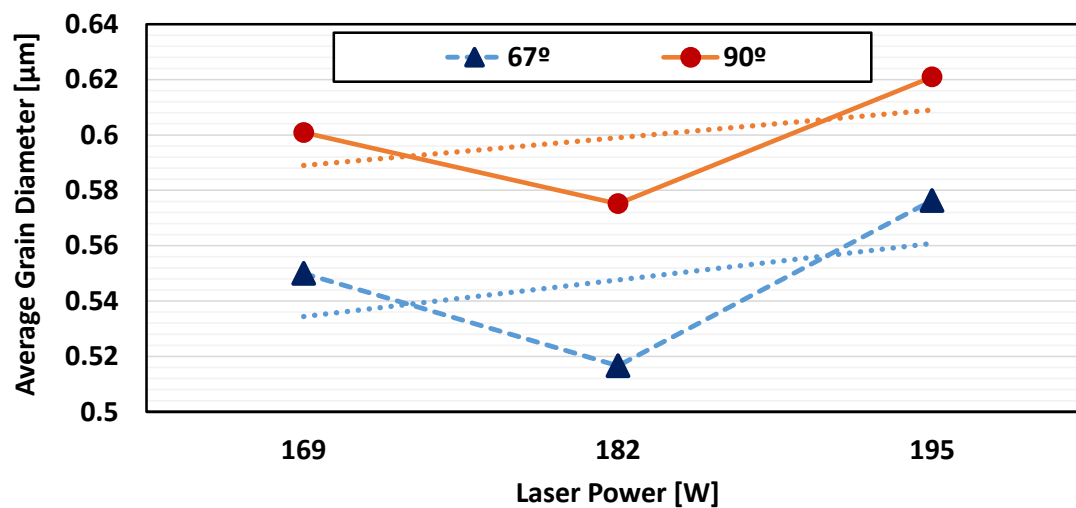


Figure 6.11 Effect of laser power.

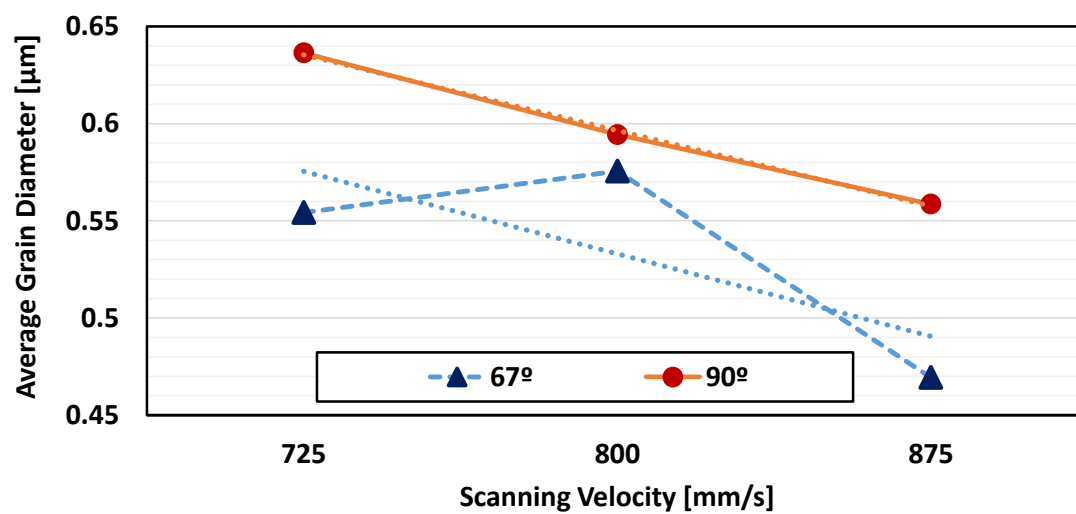


Figure 6.12 Effect of scanning velocity.

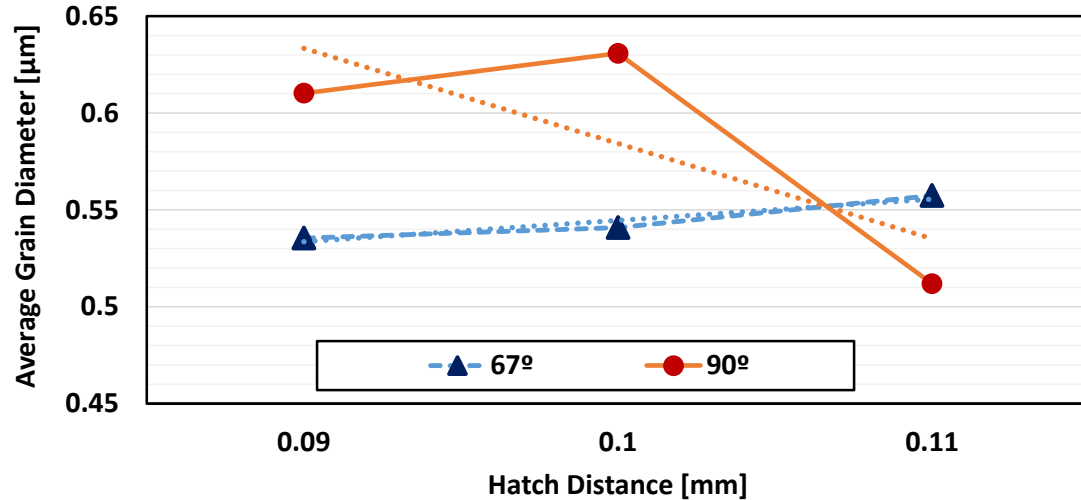


Figure 6.13 Effect of hatch distance.

In order to better understand the effect of each process parameter, a detailed analysis is carried out by looking at effects of two process parameters at different levels while keeping the third process parameter constant at the medium level, as shown in Figures 6.14-17. In these figures, the error bars represent sample standard deviations. It is clear that there are many factors affecting the microstructural evolution. Figure 6.14 shows that at a low laser power, increasing the scanning speed causes an increase in the average grain sizes for 90° rotation strategy and a decrease in the average grain sizes for the 67° rotation strategy. At the high power level (195 W), increasing scanning speed decreases the average grain size for 90° rotation, and a nonlinear effect is observed for the 67° rotation. Figure 6.15 shows that at low and medium scanning speeds, increasing the laser power tends to increase the average grain size for 90° rotation, while at the high scanning speed level the effect is reversed. For 67° rotation, a clear trend is not observed for low and high speeds, but at the medium speed average grain sizes are increased with increasing power. Figure 6.16 shows that at low and medium hatch distance settings, increasing laser power tends to increase

the average grain size for both 67° and 90° rotation strategies while at the high level hatch distance setting ($h=0.11\text{mm}$), increasing power decreases the average grain size for both strategies. Finally, Figure 6.17 shows that at the low level hatch distance setting ($h=0.09\text{mm}$), increasing the scanning speed decreases the average grain size for 90° rotation whereas at the high level hatch distance setting, the effect is reversed. For the 67° rotation strategy, increasing the scanning speed increases the average grain size at the low hatch distance setting but decreases it at the high hatch distance setting. It is important to note the sharp changes in the average grain size (diameter) in Figure 6.17 that are caused by large changes in the scanning speed.

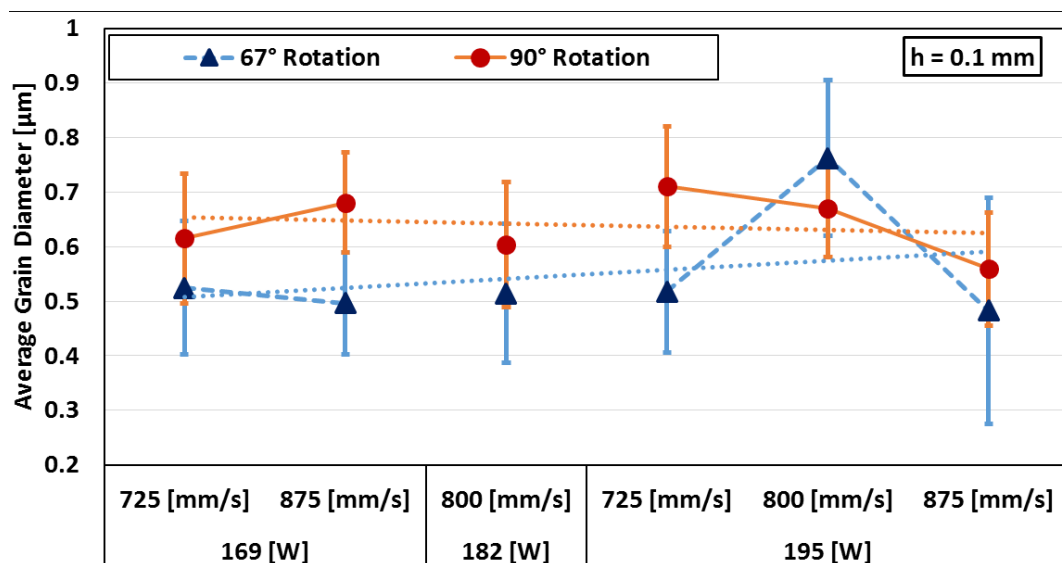


Figure 6.14 Effect of laser power and scanning velocity.

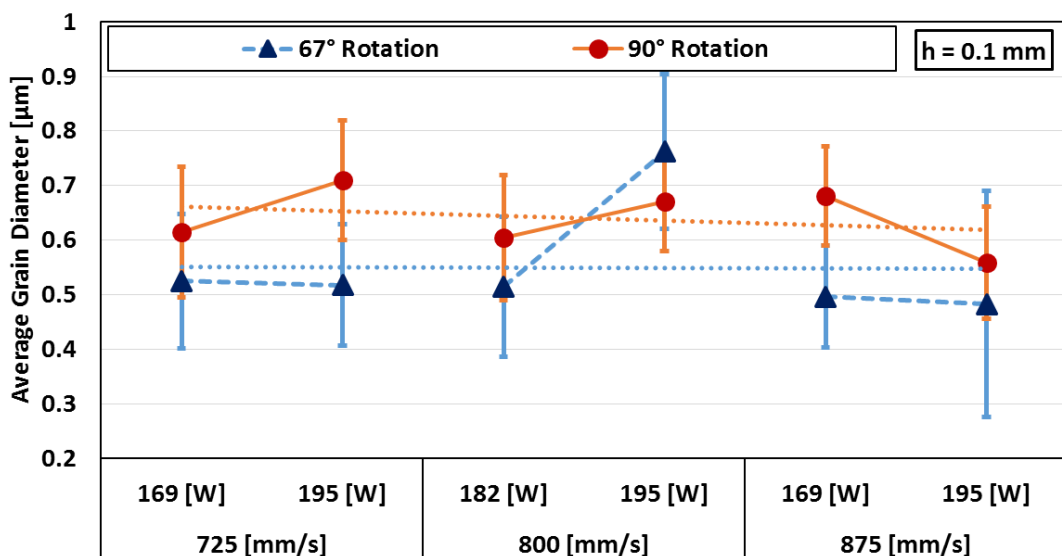


Figure 6.15 Effect of scanning velocity and laser power.

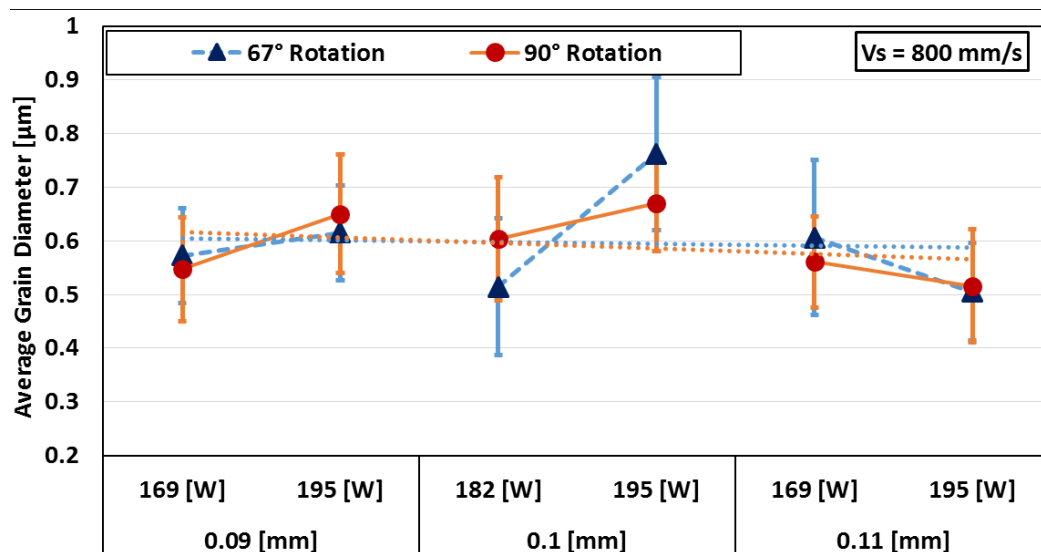


Figure 6.16 Effect of hatch distance and laser power.

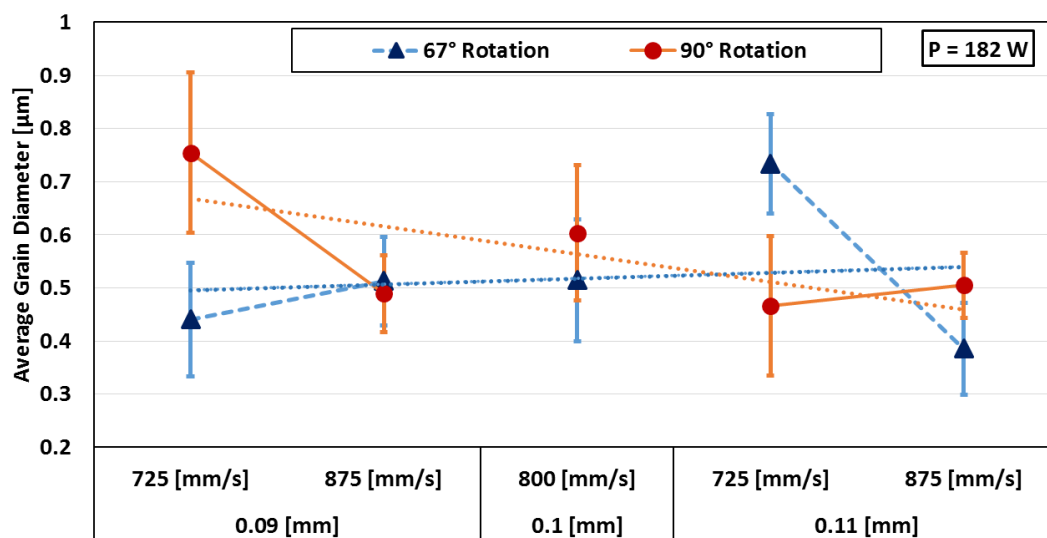


Figure 6.17 Effect of hatch distance and scanning velocity.

6.3.3 Growth Direction Analysis

Growth directions provide valuable information about how the processing parameters affect the microstructure as they are indicative of cooling rates and directions. The images reveal a dendritic microstructure with cross sections of dendrites appearing as equiaxed grains in different cross-sections of the coupons. The dendrites appear to be growing in 2 main directions, in the build (Z) direction and also in a direction perpendicular to the laser's scanning path. During the processing, the scanning path changes many times, thus creating dendrites in different directions. The growth of dendrites in these two directions can be explained by temperature gradients as dendritic growth is observed when the growth is diffusion driven, due to large gradients of temperature or concentration being present. In the case of SLM, the temperature gradient is largest in the build direction as the cooling occurs towards the base plate via conduction, and towards the environment at the top layer. Analyzing the orientation of the dendrites may reveal the effect of different heating/cooling cycles resulting from process parameters on the microstructure of the IN625.

The dendritic microstructure observed in the SLM processed IN625 coupons indicate that the solidification is diffusion driven and largely affected by thermal gradients. Analyzing the orientation of the dendrites may reveal the effect of different heating/cooling cycles resulting from process parameters on the microstructure of the IN625. In this section, directionality in the different microstructures resulting from various process conditions is identified via image analysis. By looking at the XZ cross-section of the test coupons, the boundaries of dendrites are identified and their directions with respect to the z axis (build direction) are obtained using MATLAB. Looking at YZ cross-sections would also yield

similar results due to the rotational scanning strategies. The image processing algorithm identifies growth directions in the SEM images in the following way:

Step 1: Regions of interest on the image are marked manually. Each image is processed regionally for each of the marked areas.

Step 2: The contrast of the image is adjusted. The image is filtered and processed to remove the noise and thresholding is applied to reveal boundaries.

Step 3: The region of interest (ROI) is divided into $n \times m$ sub-regions where $n \times m$ are determined based on the size of the ROI and pixel size (pixels per μm ; depends on the image resolution and zoom level of SEM) of the image.

Step 4: Hough transform is applied and top 80% of the peaks are selected. Lines corresponding to these peaks with sufficient minimum line length and acceptable gap size per line, defined as a function of pixel size and sub-region size, are selected. The inclination angles of detected lines are constrained between -30° and 30° with respect to the z axis. Corrections are made to reduce the errors.

Step 5: Histograms are constructed using all sub-regions and regions in an image.

Calculated angles are positive in the counter-clockwise direction from the Z axis, as shown in Figure 6.18. Lines with positive inclination are shown in blue whereas lines with negative inclination are shown in red. Note that the coloring gets stronger with increasing angle magnitude. Figure B1 in Appendix B shows the analyzed SEM images along with histograms for detected lines in each image.

Note that the coupons were aligned with the SEM detector using coupon edges at the time of recording in order to minimize the error coming from tilting in the images. Also note that coupon #29 (195 W, 800 mm/s, 0.09 mm, 90° rotation scan strategy) YZ surface is being used instead of XZ surface due to technical difficulties and it is considered to be not significantly different than what the XZ surface would yield.

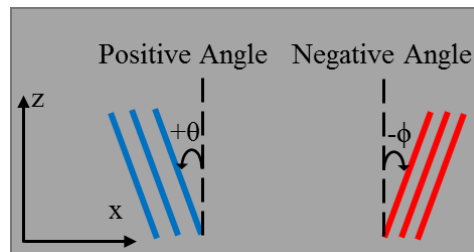


Figure 6.18 Positive and negative angles and line coloring.

6.3.3.1 Results and Analysis

Measurements for all coupons are summarized in Tables 6.3-6.4, showing bin centers and averages for positive and negative dominant angles, along with the processing conditions. Figure 6.19 shows the measurements from coupons #35 (195 W, 800 mm/s, 0.1 mm, 90° rotation scan strategy) and #31 (195 W, 800 mm/s, 0.1 mm, 67° rotation scan strategy). From the figure, it is evident that a decrease in the scanning velocity between these two coupons caused the growth directions in the measurement area to lean towards the positive angles. As dendrites grow towards cooler areas, the skewness of the histogram indicate directional heating or cooling caused by the SLM process.

For further analysis, dominant positive and negative directions are chosen from each image. These directions are compared against each other to better understand the effect of process parameters. Figures 6.20-6.22 show the main effects of laser power, scanning speed and hatch distance on positive and negative growth directions, with dashed lines showing the overall trend. The values are obtained from the histogram bin centers shown in Figure A1 in Appendix A. Note that missing values in these figures means that no dominant direction (positive or negative) was identified for that case. Overall, it is seen that increasing laser power increases the magnitude of both positive and negative dominant angles for the 90° rotation strategy whereas it tends to decrease the positive dominant angle and not affect the negative dominant angle for the 67° rotation strategy. Increasing the scanning speed also causes an increase in both positive and negative dominant angles in the 90° rotation strategy setting, whereas a decrease in the positive angle and an increase in magnitude in the negative angle is observed for the 67° rotation strategy. Finally, increasing the hatch distance tends to increase the magnitude of both negative and positive dominant angles in both 90° and 67° rotation strategies. Although the effects are nonlinear in most cases, these plots provide an insight on how the process parameters may alter the microstructure.

Table 6.3 Processing conditions and grain growth direction analysis results for 90° rotation.

Coupon #	Laser Power P [W]	Scanning Velocity v_s [mm/s]	Hatch Distance h [mm]	Energy Intensity $[J/mm^3]$ $E=P/v_s \times h \times s$	θ^+	Average of θ^+	SD of θ^+	θ^-	Average Of θ^-	SD Of θ^-
1	169	875	0.1	96.6	20	19.29	2.66	-10	-9.47	2.52
4	195	875	0.1	111.4	30	27.76	1.86	-10	-11.48	2.52
6	182	875	0.09	115.6	10	11.74	2.51	0	3.72	1.17
8	182	725	0.11	114.1	20	19.87	2.46	-10	-11.01	2.76
9	195	800	0.11	110.8	30	27.84	1.56	-10	-11.20	2.88
12	182	725	0.09	139.5	0	-1.78	2.27	-10	-10.04	2.60
14	182	800	0.1	113.8	30	27.73	1.66	-10	-9.89	2.62
15	182	800	0.1	113.8	10	10.56	2.70	0	1.36	2.34
16	195	725	0.1	134.5	30	27.55	0.66	-10	-13.24	1.24
17	182	800	0.1	113.8	10	9.80	2.87	-20	-22.17	2.10
18	182	875	0.11	94.6	20	18.98	2.20	-20	-19.78	2.38
20	169	725	0.1	116.6	20	21.13	2.92	0	1.96	2.48
21	169	800	0.09	117.4	0	-0.92	2.76	-10	-9.23	2.43
23	169	800	0.11	96.0	20	18.21	2.50	0	1.18	2.07
29	195	800	0.09	135.4	30	27.96	1.81	-10	-12.08	2.08
35	195	800	0.1	121.9	10	10.58	2.48	0	3.53	1.14

Table 6.4 Processing conditions and grain growth direction analysis results for 67° rotation.

Coupon #	Laser Power P [W]	Scanning Velocity v_s [mm/s]	Hatch Distance h [mm]	Energy Intensity $[J/mm^3]$ $E=P/v_s \times h \times s$	$\theta+$	Average of $\theta+$	SD of $\theta+$	$\theta-$	Average Of $\theta-$	SD Of $\theta-$
2	169	725	0.1	116.6	10	9.58	2.87	0	-0.57	2.73
3	195	725	0.1	134.5	10	10.24	2.65	0	2.60	1.97
5	169	800	0.09	117.4	10	11.73	2.34	-10	-9.22	2.90
7	182	800	0.1	113.8	20	19.03	2.85	-10	-9.91	2.74
10	182	725	0.11	114.1	20	19.63	3.00	-20	-20.09	2.85
11	169	875	0.1	96.6	20	19.08	2.31	-20	-19.50	2.36
13	195	800	0.09	135.4	10	10.07	2.67	-10	-10.43	2.39
19	195	875	0.1	111.4	0	-3.61	1.43	-10	-12.09	2.22
22	182	800	0.1	113.8	10	12.26	2.04	0	4.40	0.54
24	182	800	0.1	113.8	20	19.26	3.05	0	12.15	2.04
25	195	800	0.11	110.8	30	28.46	1.71	-10	-11.53	2.38
26	182	875	0.09	115.6	30	27.95	1.72	-10	-11.38	2.69
27	182	725	0.09	139.5	30	27.99	1.80	-20	-20.66	2.89
28	182	875	0.11	94.6	10	10.54	2.81	-20	-19.51	2.75
30	169	800	0.11	96.0	30	28.23	1.61	-20	-19.89	3.47
31	195	800	0.1	121.9	0	-2.71	1.98	-30	-27.83	1.47

SEM Image with Marked Directions

Histogram with Direction Angles

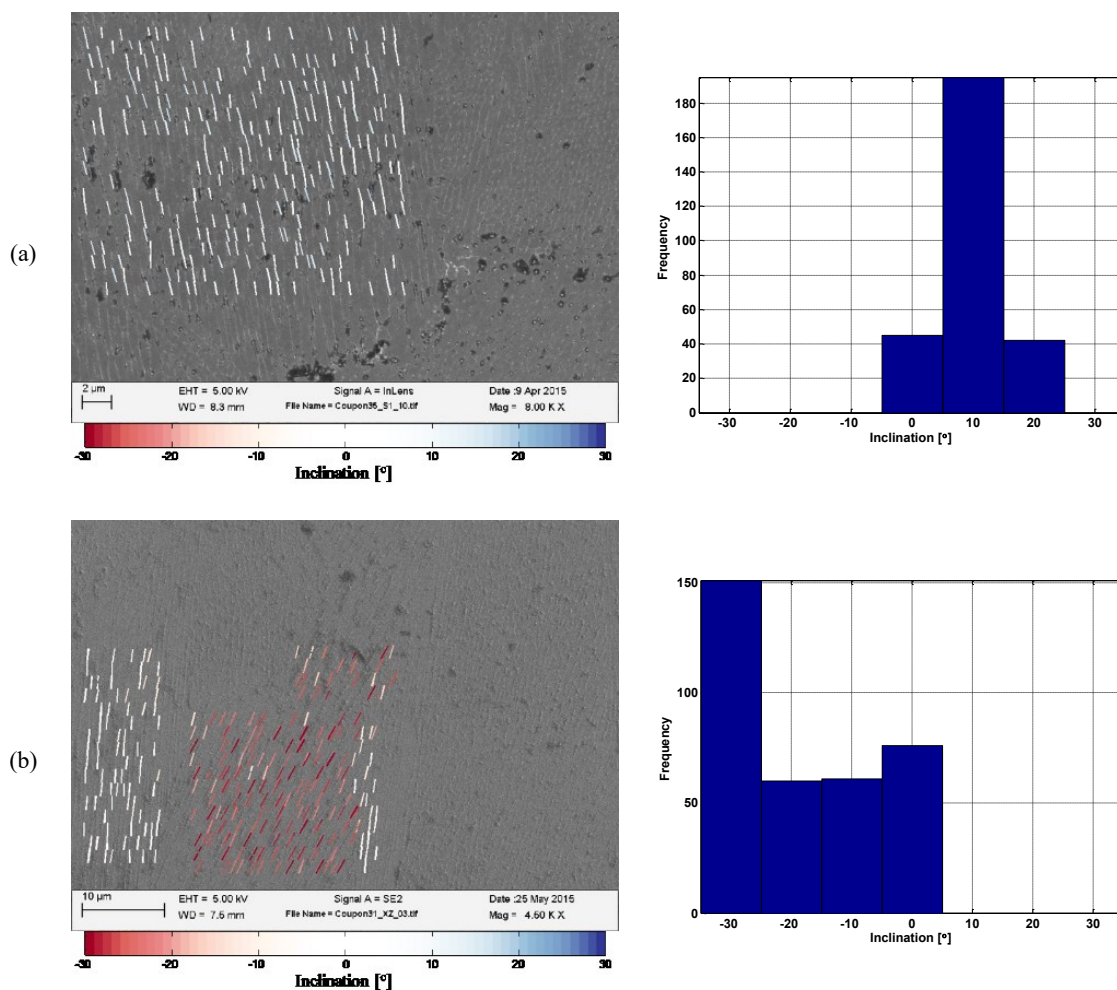


Figure 6.19 Growth directions and histograms of inclination angles for IN 625 test coupons observed from XZ faces, (a) coupon #35 (195 W, 800 mm/s, 0.1 mm, 90° rotation scan strategy) and (b) coupon #31 (195 W, 800 mm/s, 0.1 mm, 67° rotation scan strategy).

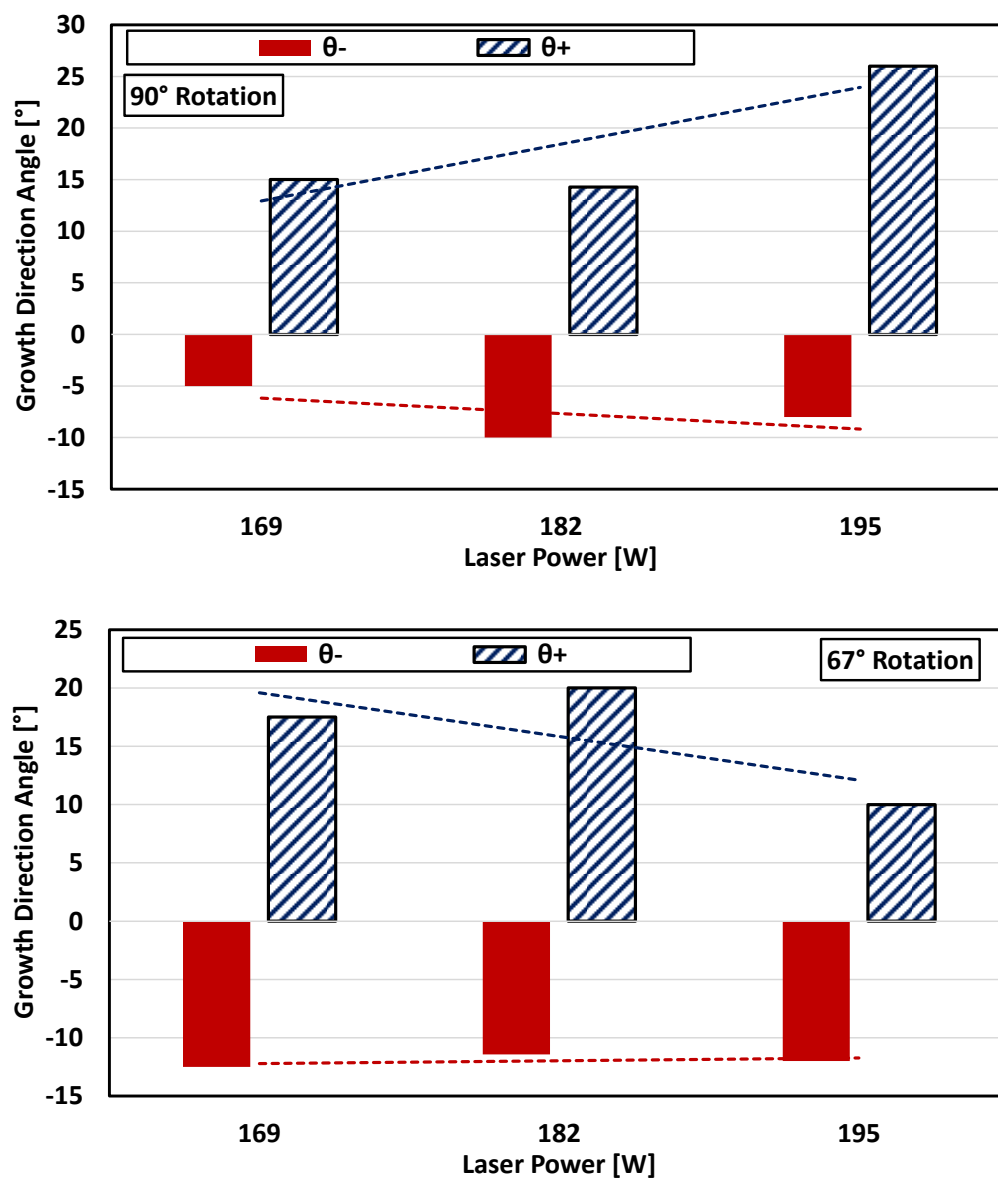


Figure 6.20 Effect of laser power on dominant positive and negative growth directions, with 90° (top) and 67° (bottom) rotation strategies.

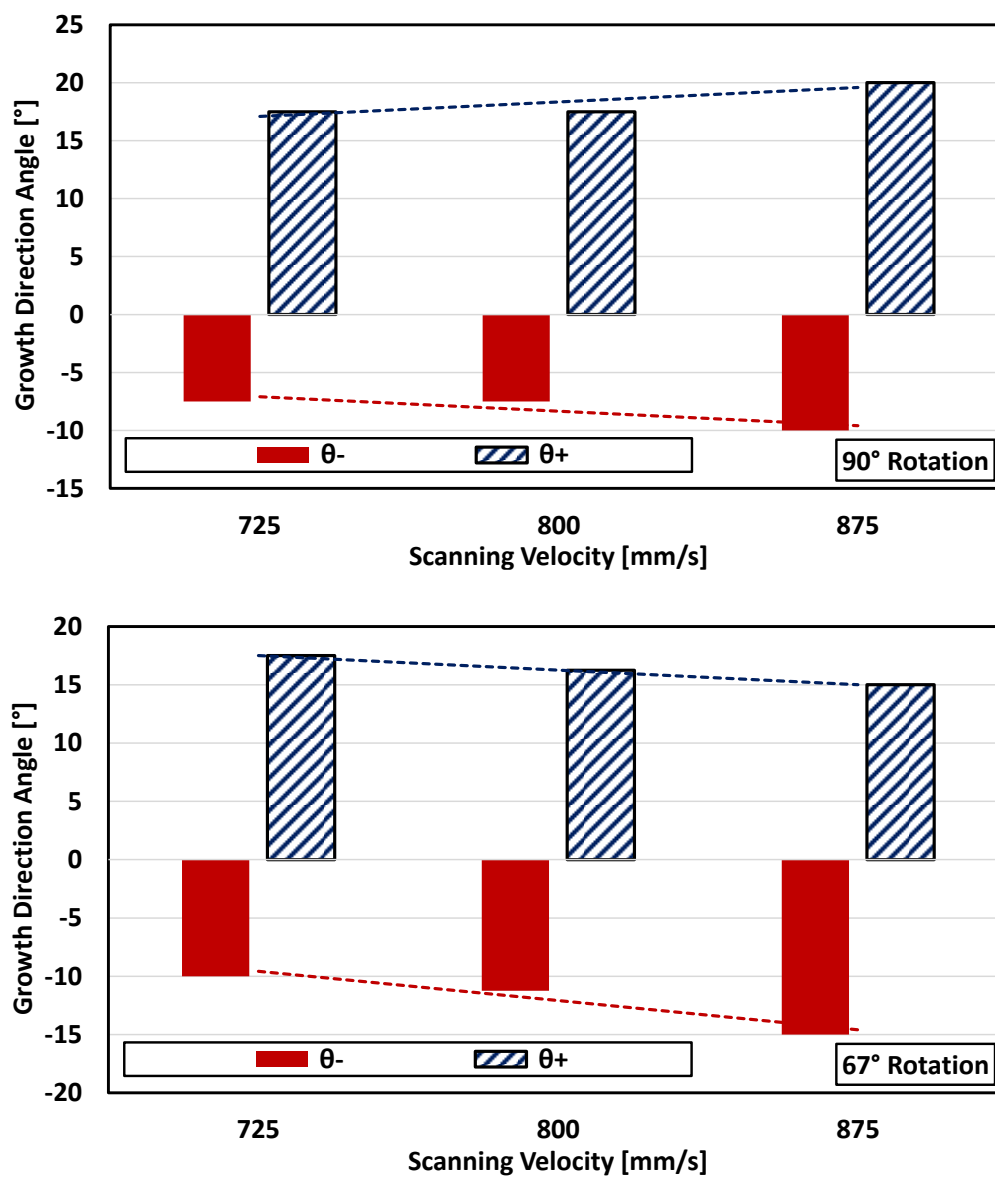


Figure 6.21 Effect of scanning speed on dominant positive and negative growth directions, with 90° (top) and 67° (bottom) rotation strategies.

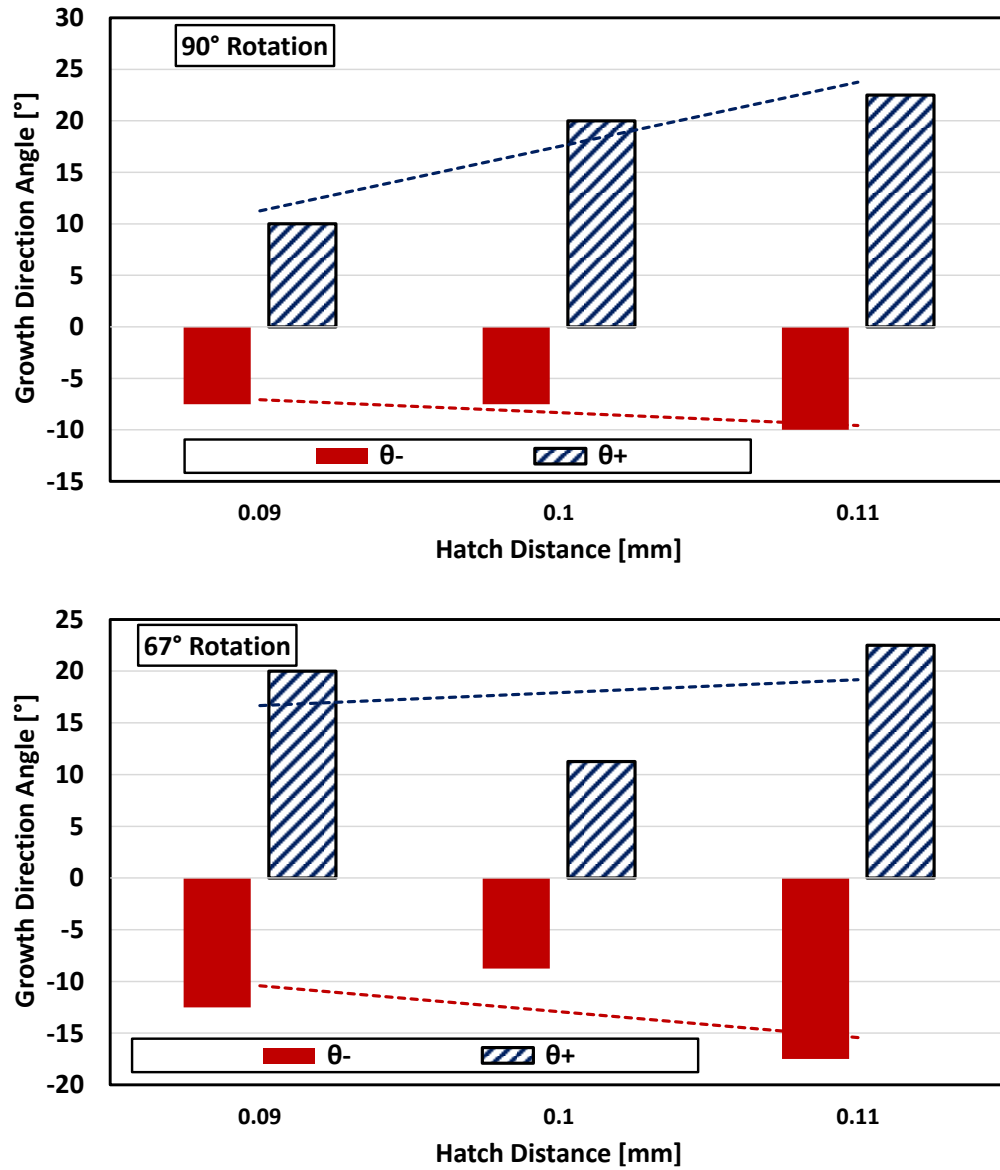


Figure 6.22 Effect of hatch distance on dominant positive and negative growth directions, with 90° (top) and 67° (bottom) rotation strategies.

Figure 6.23 shows the effect of energy intensity on the growth direction angles using the means of samples inside their respective bins. The vertical error bars represent sample standard deviations. An overall decrease in magnitude is observed with increasing energy intensity in both positive and negative angles, suggesting that as the energy intensity increases, the grains tend to grow closer to the z (build) direction. However, the effect is highly nonlinear, and a conclusion should not be drawn. Note that the 0° growth direction is considered positive in certain cases, and negative in some other cases. Since the bin sizes were 10° , each bin contained samples within the $\pm 5^\circ$ range of the bin center. Because means are considered in Figures 6.24-6.26, some of the 0° bins appear positive or negative in contrast to their names (θ^+ or θ^-).

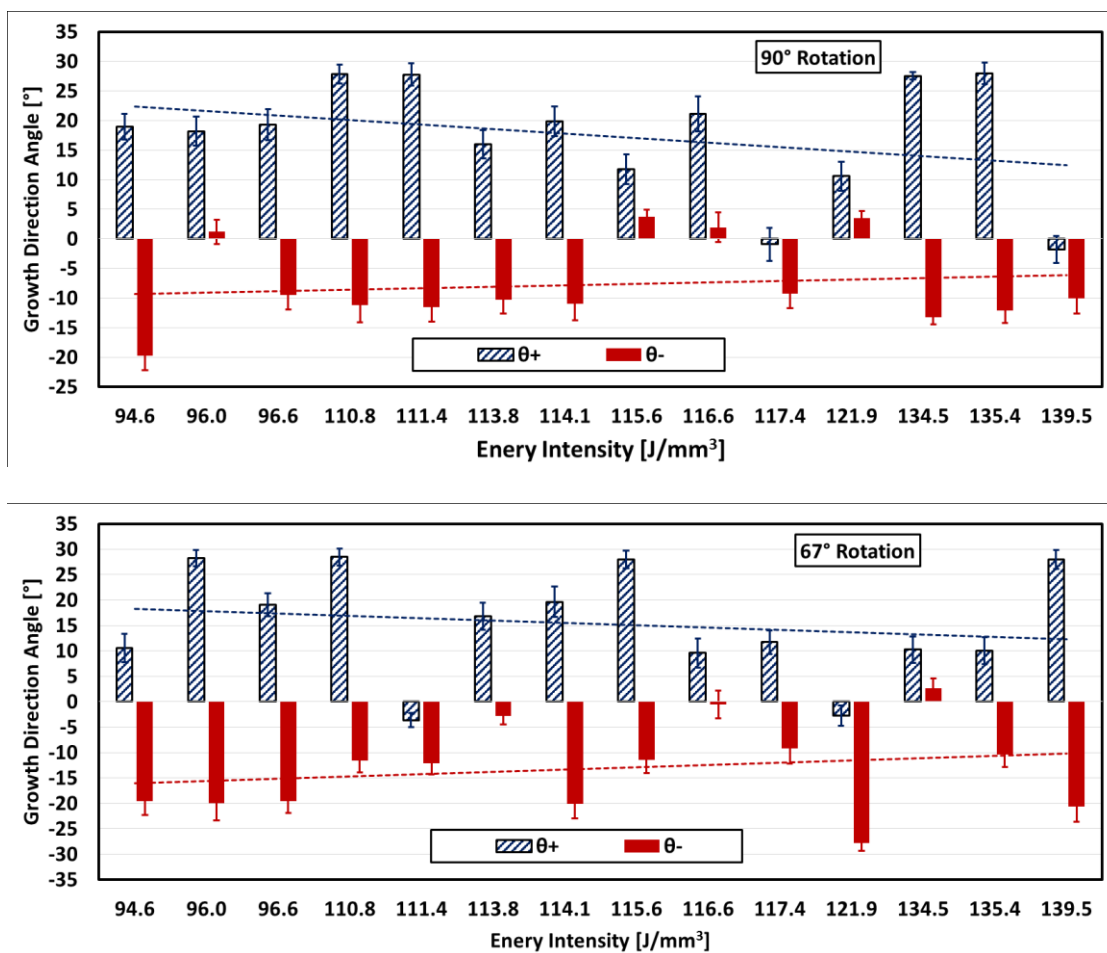


Figure 6.23 Effect of energy intensity on dominant positive and negative growth directions, for 90° (top) and 67° (bottom) rotation strategies.

Each process parameter (laser power, scanning speed and hatch distance) is further investigated in more detail by taking into account the effect of another parameter, while keeping the third one constant as shown in Figures 6.24-6.26. As in Figure 6.23, means and standard deviations of the measurements falling into dominant bins in the histograms shown in Figure A1 are utilized in these figures. Note that the figures show a nonlinear variations between different settings, therefore the trends reported here are not conclusive. Figure 6.24 shows that for 90° rotation and at the low power setting, the magnitude of θ_- increases with increasing scanning speed while θ_+ is not affected significantly. At the high power setting, both θ_- and θ_+ have nonlinear responses. For 67° rotation, magnitudes of both θ_- and θ_+ increase with increasing scanning speeds at the low power setting. At the high power setting, a decreasing trend is observed for θ_+ and a nonlinear trend is observed for θ_- .

Figure 6.25 shows very clear trends at different laser power and scanning speeds at 90° rotation. Magnitudes of both θ_+ and θ_- increase with increasing power at low and high scanning speed conditions. However, both θ_+ and θ_- magnitudes decrease with increasing power at the medium scanning speed. For 67° rotation, both θ_+ and θ_- are unaffected by laser power changes at low scanning speed. A decrease in magnitude is observed for θ_+ at medium and high speeds with increasing power. The magnitude of θ_- increases with increasing power at medium scanning speed, and decreases at high scanning speed.

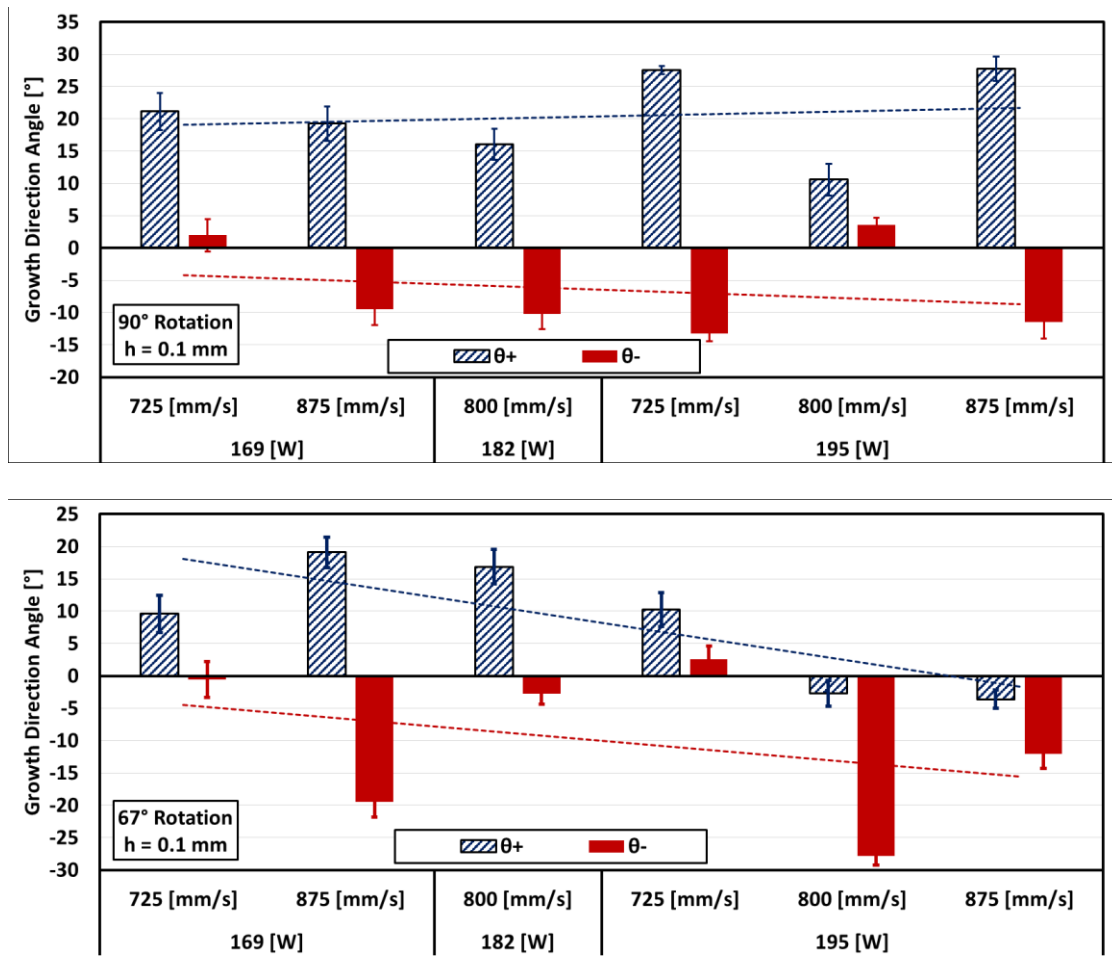


Figure 6.24 Effects of laser power and scanning speed on dominant positive and negative growth directions at constant hatch distance ($h=0.1$ mm), for 90° (top) and 67° (bottom) rotation strategies.

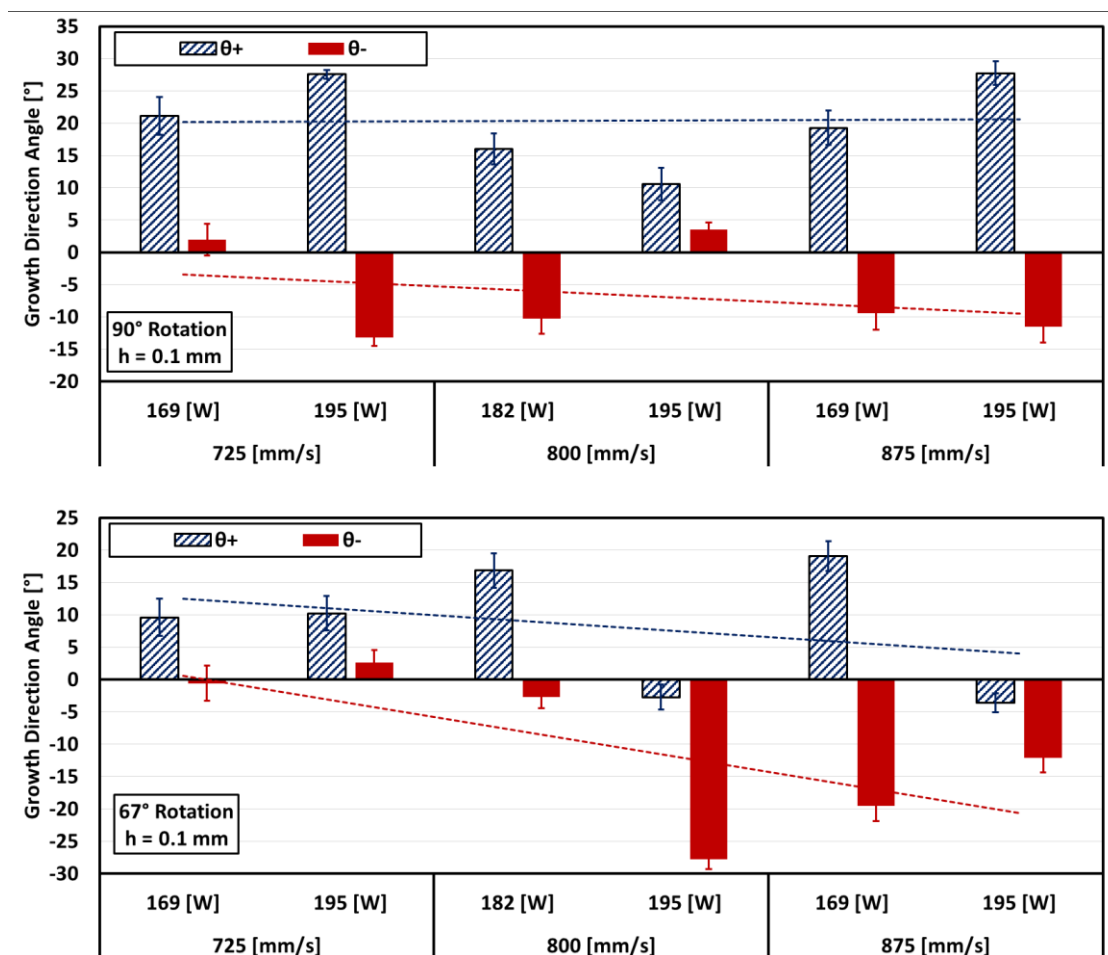


Figure 6.25 Effects of scanning speed and laser power on dominant positive and negative growth directions at constant hatch distance ($h=0.1$ mm), for 90° (top) and 67° (bottom) rotation strategies.

Figure 6.26 shows that at low hatch distance and with increasing laser power, a significant increase in the dominant positive and negative angles are observed at 90° degree rotation strategy; whereas the 67° degree rotation strategy does not affect the growth directions significantly. A decrease in positive and negative angles are seen in the 90° degree rotation strategy with increasing power. For the 90° degree rotation strategy, an increase in power yields significantly larger negative angles (in magnitude) at the medium hatch distance setting. Finally, at the high hatch distance setting, both positive and negative dominant angles increase in magnitude with increasing power for 90° degree rotation strategy. For the 67° degree rotation strategy, the positive angle is not affected with increasing power while the negative angle gets smaller in magnitude.

Figure 6.27 shows that at low hatch distance setting, the positive dominant angle increases with increasing speed for the 90° rotation strategy, while there is no significant change in the 67° rotation strategy. The negative dominant angle decreases in magnitude with increasing speed at low hatch distance setting for both 90° and 67° rotation strategies. At high hatch distance setting, the positive dominant angles decrease with increasing speed for the 90° rotation strategy. For the 90° rotation strategy, the negative dominant angle increases in magnitude with increasing speed but no significant effect was observed at the 67° rotation strategy.

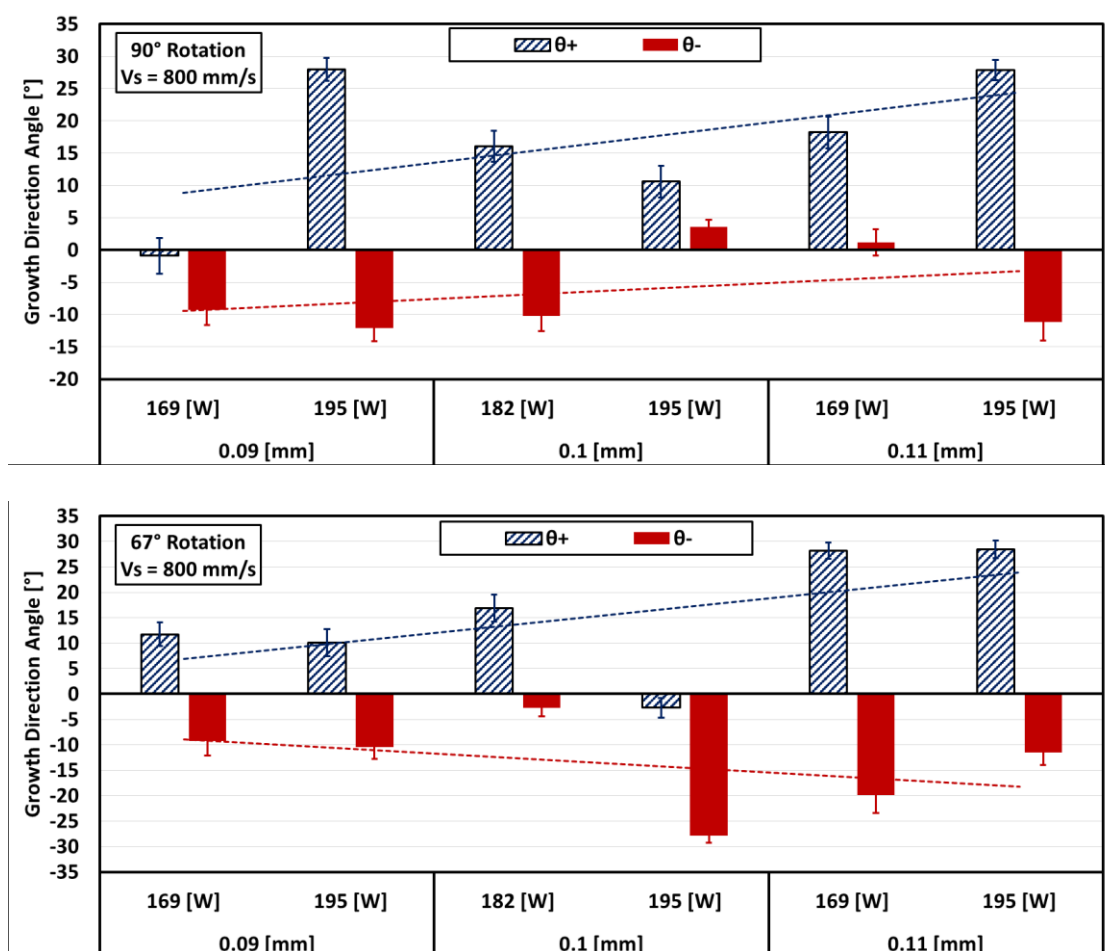


Figure 6.26 Effects of hatch distance and laser power on dominant positive and negative growth directions at constant scanning velocity ($v_s=800\text{mm/s}$), for 90° (top) and 67° (bottom) rotation strategies.

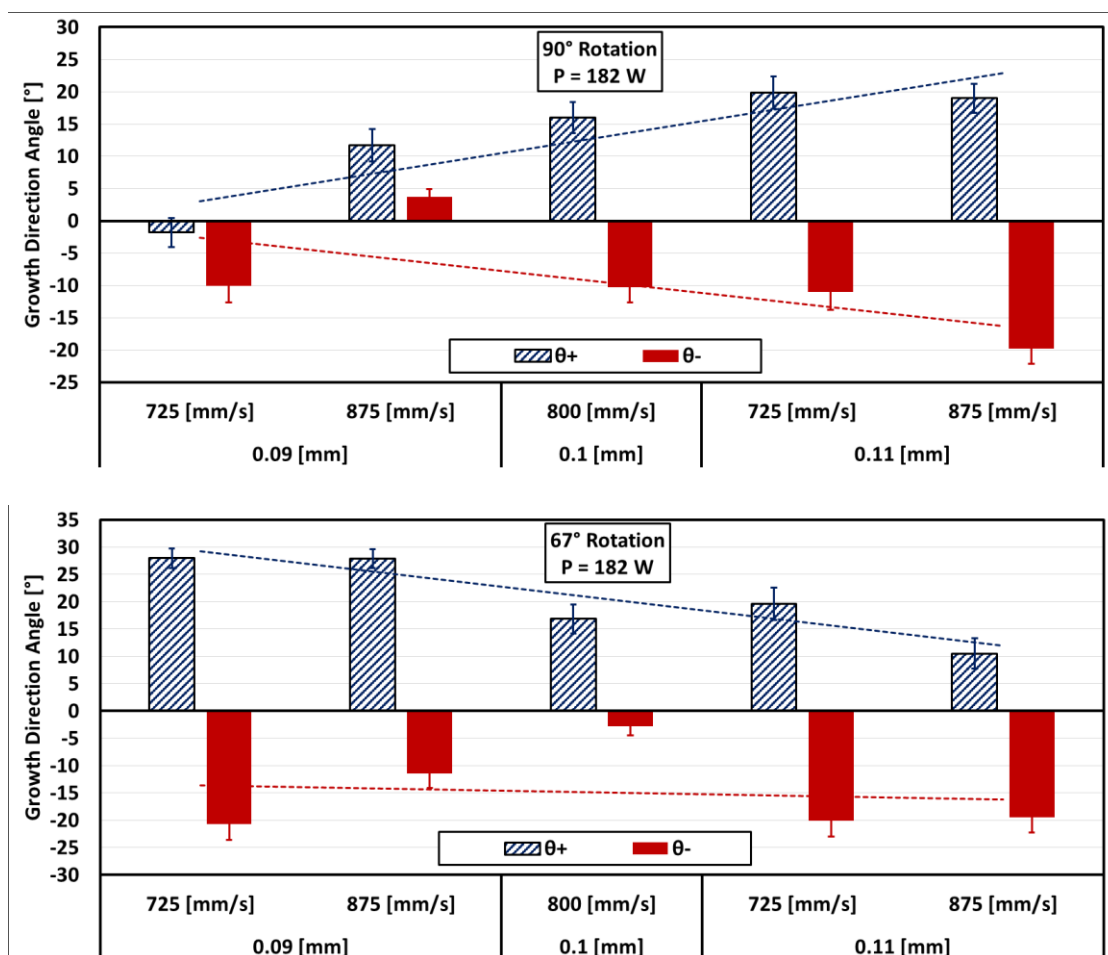


Figure 6.27 Effects of hatch distance and scanning speed on dominant positive and negative growth directions at constant laser power ($P=182\text{W}$), for 90° (top) and 67° (bottom) rotation strategies.

6.3.4 In-situ Thermal Video Analysis

In-situ monitoring of the process can be utilized to quantitatively analyze meltpool size and spattering phenomenon. Video recordings of the process can be utilized if a camera is placed in the SLM process chamber. Due to the nature of the process, i.e. a laser beam moving at very high speeds, a High Frame Rate (HFR) camera is required. An HFR thermal camera has been placed by Dr. Brandon Lane (NIST) in the processing chamber of an EOS SLM machine at the National Institute of Standards and Technology facility in Gaithersburg, MD, and the process has been recorded for the nominal processing condition. This section covers the meltpool size and spattering analyses of the process using the HFR thermal camera recording (courtesy of NIST). There are some difficulties in processing of these images. Firstly, the meltpool itself is very bright and spattering particles that occupy the same area as the meltpool in the frame (e.g. particles that are immediately above top of the pool) are not recoverable from the images. Moreover, solidified regions are highly reflective, causing noise in the measurements. Furthermore, the recording angle of the camera as well as path and altitude of flying particles, combined with lens flares create an uncertainty in the data provide additional challenges. Lastly, the temperature data may not very reliable due to local emittivity variations and camera calibration. This study does not aim to remedy all these points, but rather generate useful data from the recording under certain assumptions, as discussed in the following sections.

The thermal camera properties are shown in Table 6.5. The camera has an integration time of 0.040 ms and can record at 1800 frames per second which translates into 0.5555 ms per frame. In the instantaneous field of view (iFoV), each pixel represents is 36 μm . Thermal

video and process parameters are shown in Table 6.6. The video recording of coupon #35 (with 800 mm/s scanning velocity, 195 W laser power, 4.1 mm stripe width and 0.1 mm hatch distance) has 801 total frames. The processing occurs out of the view of the camera for 99 frames. Horizontal scanning is recorded for 602 frames with approximately 60 tracks, and a vertical scanning of the stripe boundary is recorded for 100 frames. Since each track is processed for 5.125 ms (calculated from track length divided by scanning speed), the camera records approximately 9.23 frames per track. The non-integer number means that the frequency of the process is different than what the camera records, therefore the beginning and end of each track are not necessarily recorded at the correct time with the camera. It is also important to note that some frames during processing are skipped in the recording, i.e. the recording is not continuous in certain tracks.

Moreover, as shown in Figure 6.28, the camera is placed at a 43.7° angle with the powder bed. This results in different scene sizes for x and y directions in the recording, where the size in y direction appears smaller than the actual size. In the instantaneous field of view, each pixel represents $36\ \mu\text{m}$, however, due to the recording angle, the scene size is corrected in the y direction with $dy' = \frac{dy}{\sin(43.7)} = 1.48dy = 52\ \mu\text{m}$ whereas the scene size in x direction is $dx = 0.36\ \mu\text{m}$. Figure 6.29 shows the camera signal transformation curve for different emissivity values. It is assumed that the true emissivity is between 0.2 and 0.5. For the purpose of this study, we use the value 0.2. It is important to note that for $\varepsilon=0.2$, only temperatures from $600\ ^\circ\text{C}$ to $1150\ ^\circ\text{C}$ can be reliably calculated by the camera. Temperatures outside this range should be treated with caution. A single frame from the thermal video recording is shown in Figure 6.30.

Table 6.5 Thermal camera properties.

Wavelength (filter)	1350-1600nm
Integration Time	0.040 ms
Frame Rate	1800 fps
iFoV	36 mm/pixel
Imaging window	360x128 pixels (12.96 mm x 4.61 mm)

Table 6.6 Thermal video and process parameters.

SLM parameters

$v_s = 800 \text{ mm/s}$ and stripe width (track length) = 4.1 mm

Laser scanning of a track: $4.1 \text{ mm} / 800 \frac{\text{mm}}{\text{s}} = 5.125 \text{ ms}$

Camera frame rate: 1800 fps or 0.5555 ms per frame

≈ 9.23 frames per track of laser scanning

Laser ON: ≈ 9 frames

Laser OFF (0.42 ms): 0-1 frame

Total frames: 801

Hatching: 602 frames

Vertical (track boundary): 100 frames

Out-of-frame: 99 frames

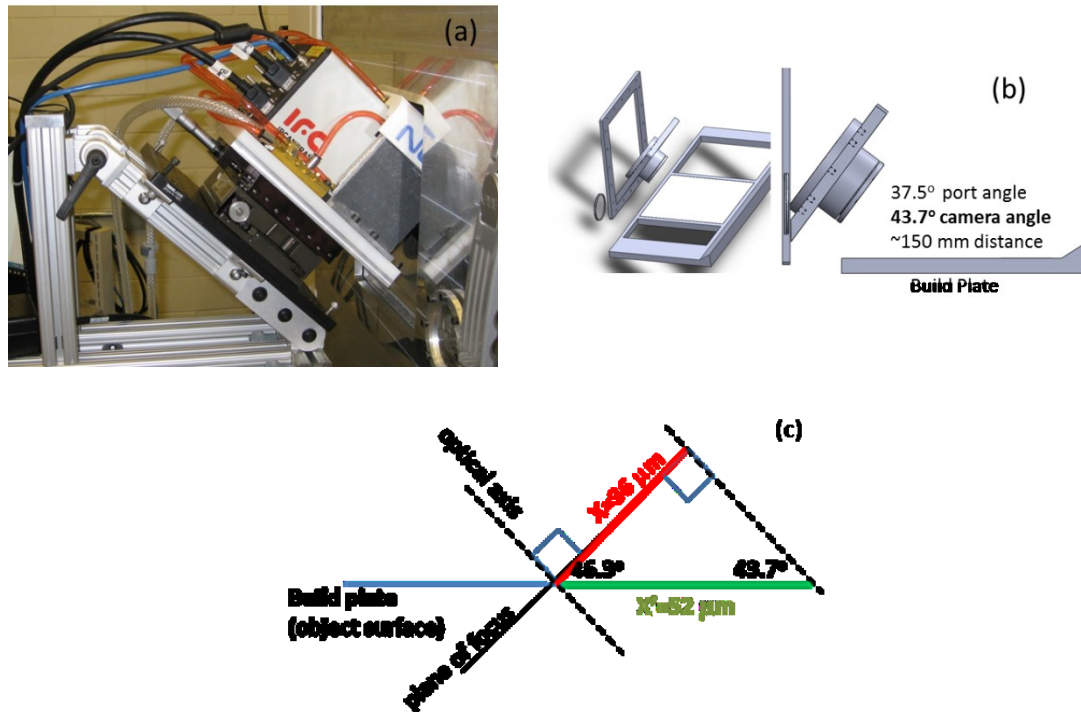


Figure 6.28 Thermal camera setup, (a) Side-view of the EOS machine, custom door, and thermal camera, (b) Solidworks model of EOS build chamber + custom viewport, (c) optical axis, plane of focus and scene size.

(Courtesy of Dr. Brandon Lane, NIST)

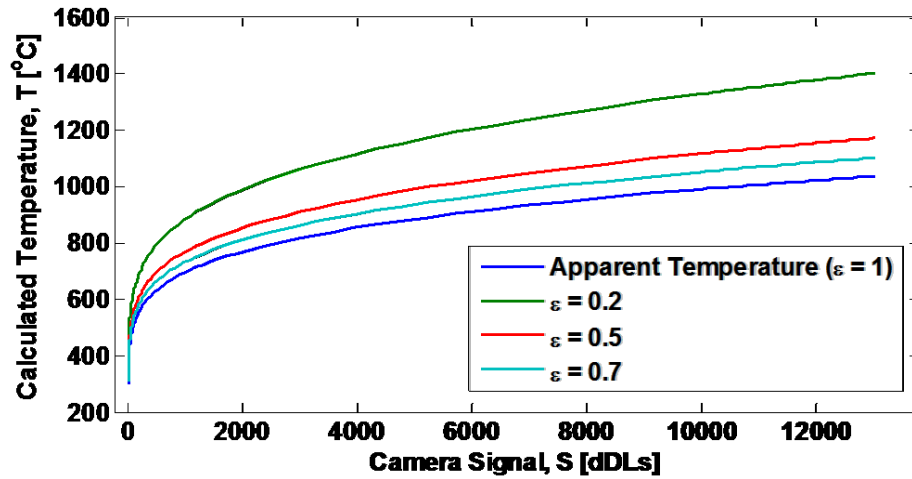


Figure 6.29 Camera signal transformation curves for different emissivity values.

(Courtesy of Dr. Brandon Lane, NIST)

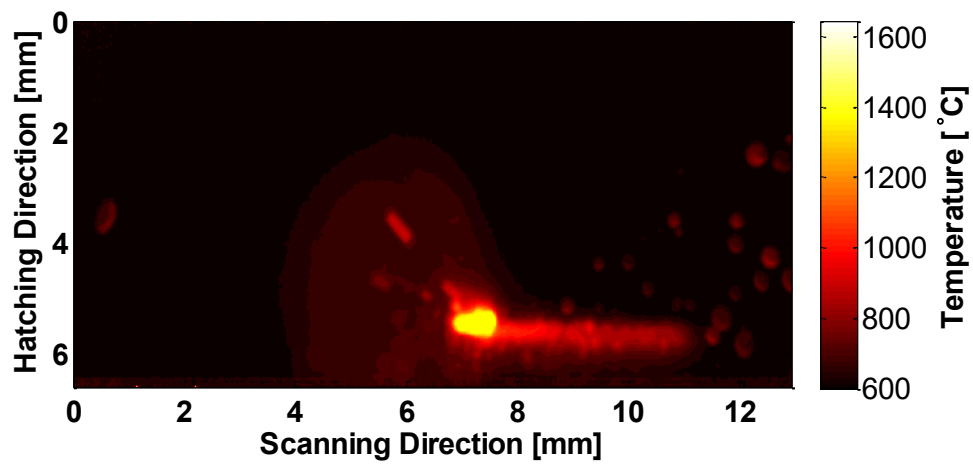


Figure 6.30 Image generated with temperature data obtained from the thermal camera.

Emissivity (ϵ) assumed to be 0.2.

6.3.4.1 Meltpool Width Measurements

It is possible to determine the sizes of meltpools from the thermal camera recording. Each frame can be processed individually such that pixels with temperatures exceeding the liquidus temperature (1350 °C for IN625) are segmented from colder pixels. Figure 6.31 shows the result of image segmentation using liquidus temperature as a threshold on single frame where the molten region is marked red, and colder region is marked blue. Afterwards, the width and length of the meltpool can be measured by simply counting the number of pixels in x and y directions, and multiplying them by their respective scene sizes. For instance, the meltpool in Figure 82 has width of $109 - 102 = 7$ pixels in the y direction, which translates to $7 \text{ px} \times 0.52 \frac{\mu\text{m}}{\text{px}} = 0.36 \mu\text{m}$. This process is done automatically using MATLAB's built in functions to create a bounding box around the meltpool such that the height of the box gives the width of the meltpool in pixels. This process is repeated for 185 different frames that belong to 20 different tracks.

During the processing of meltpool size calculations, it is observed that some of the spattering particles that are in close proximity to the meltpool affect the meltpool size calculation algorithm. For simplicity, we refer to these particles as attached particles. Figure 6.32 shows these attached particles and how they may affect the meltpool size calculation. Measurements coming from the meltpool size calculation algorithm are processed frame by frame to reduce or eliminate the errors caused by the attached spattering particles.

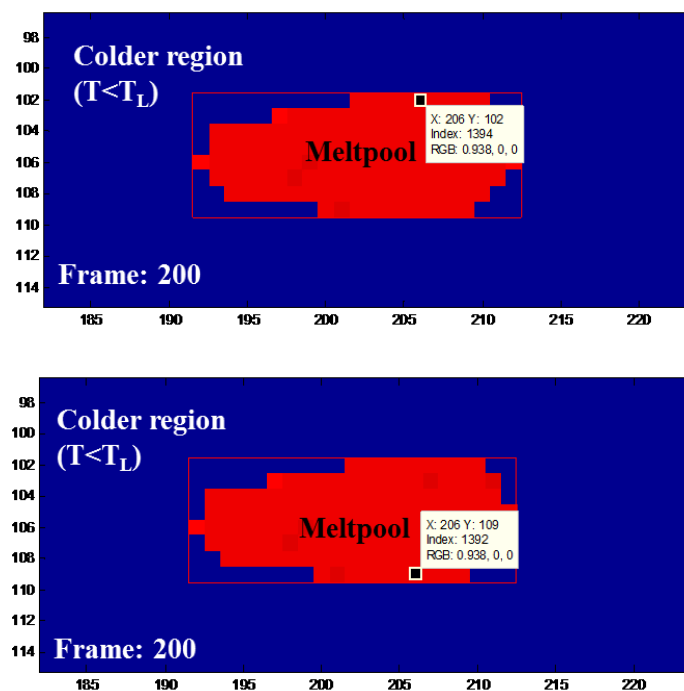


Figure 6.31 Melt pool visualization from a thermal image. Dimensions are in pixels.

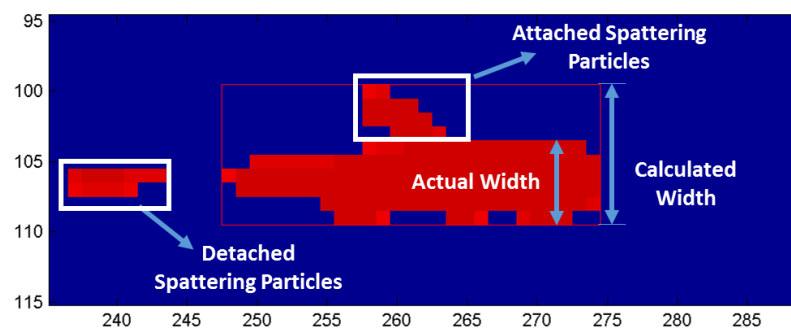


Figure 6.32 Melt pool width measurements (calculated and actual) along with attached and detached spattering particles. Dimensions are in pixels.

Furthermore, camera calibration and measurement limitations for temperatures above 1150 °C, combined with reflections from the surface of the processed area and potentially other optical phenomena result in meltpool width measurements that are considerably larger than the measurements obtained via Scanning Electron Microscopy (SEM) and Light Optical Microscopy (LOM). Table 6.7 shows the average meltpool width measurements obtained via LOM and thermal camera images for Type I and Type II meltpools. LOM meltpool width measurements for other coupons are given in Table C1 in Appendix C. Meltpool width measurements obtained via LOM are utilized in order to calculate a linear correction factor for meltpool widths obtained from thermal images. Correction factors are calculated for Type I (beginning of track, at $|x| = 0$ mm) and Type II (end of track, at $|x|=4$ mm) meltpools by dividing the LOM measured widths to thermal image measurements, as shown in Table 6.8. A linear correction function as shown in Figure 6.33 is applied on all meltpool measurements obtained via thermal imaging.

Table 6.7 Type I and Type II meltpool width measurements from thermal and optical imaging.

Coupon No.	Melt Pool Width Avg [μm]			
	Optical Imaging		Thermal Imaging	
	Type I	Type II	Type I	Type II
35	155	112	437	223

Table 6.8 Correction factor for thermal camera meltpool width measurements.

Scanning Distance $ x $ [mm]	Correction Factor	Meltpool Type
0	0.3549	Type I
4	0.5026	Type II

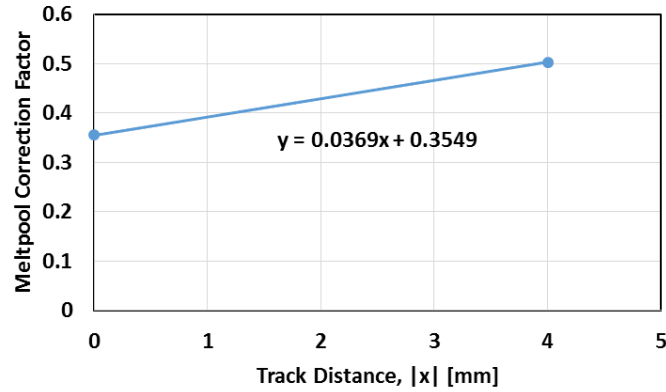


Figure 6.33 Meltpool width correction.

6.3.4.2 Results and Analysis

185 frames from the camera recording are analyzed with this method to calculate the meltpool widths. Figure 6.34 shows the results of this analysis where the values are calculated across all 185 frames and the x locations are calculated explicitly based on the number of frames recorded in that track and the scanning speed of the laser. The main conclusion that can be drawn from this analysis is that the meltpool sizes tend to decrease from the beginning of each track towards the end of each track. It is attributed to the fact that when the laser begins a track, the previous track that ended a hatch distance away from the current location is still warm, therefore the temperature at the beginning of the new track is also high, resulting in larger meltpools. Consequently, as the laser nears the end of a track, it is surrounded by a colder region, resulting in smaller meltpools. Furthermore, the increase in meltpool size between 1 mm and 3.5 mm of the track distance may be attributed to the linear correction factor. Unfortunately, it is not possible to obtain in-situ LOM measurements of the meltpool showing the meltpool width at different track distances, therefore a nonlinear correction factor cannot be calculated.

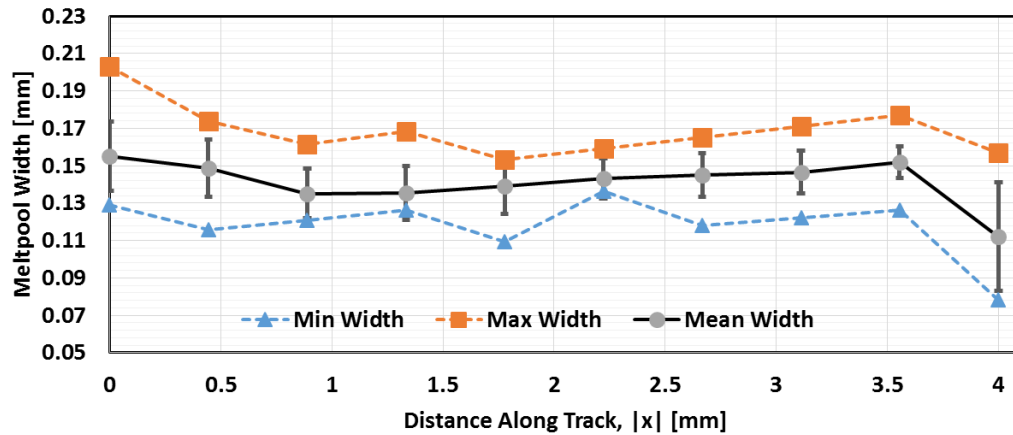


Figure 6.34 Minimum, maximum and average meltpool widths after attached particle and optical image comparison corrections. Error bars represent sample standard deviations.

6.3.5 Spattering

Spattering is a common but potentially detrimental phenomenon that is observed during SLM. When the laser beam hits an area, local evaporation of particles cause some of the surrounding hot particles to flying off and land on other areas as seen in Figure 6.35. These particles are often observed to move in opposite direction of the laser beam, and they may create significant problems during processing which may affect the quality of the end product, cause the process to fail, or even damage the equipment. For instance, if a particle lands on a solidified region, the thickness of the layer is increased by the height of the particle. This protruding particle may get caught by the re-coater blade (if exists) when the new powder layer is being placed and may result in movement of the processed part or damage the blade. Therefore it is important to quantify and analyze this phenomenon.

Future research in this subject would be to minimize spattering frequency and particle sizes by investigating the effect of process parameters to improve the process reliability.

It is possible to determine the sizes and temperatures of the spattering particles from the HFR thermal video recording. Once the temperatures and sizes of these particles are known, spattering can be represented stochastically.

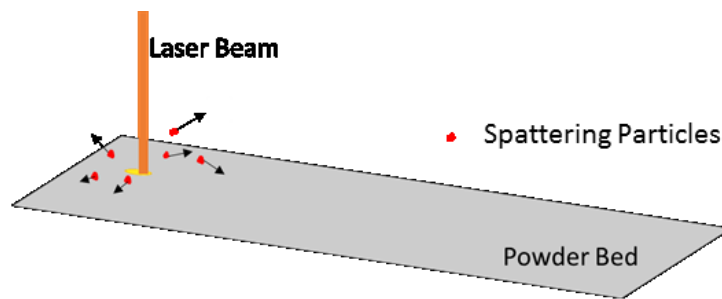


Figure 6.35 Spattering during the process.

The thermal camera provides images that have temperature information saved in brightness of pixels. Since the spattering particles are originating from the vicinity of the meltpool, they have high temperatures thus they appear as bright clusters of pixels. Figure 6.36 shows a frame from the video recorded by the thermal camera visualized in MATLAB via RGB (red, green, blue) temperature contours to allow image segmentation. Here, the original RGB image is shown on the top-left corner, and the red, green and blue channel are shown in top-right, bottom-left and bottom-right sections of the image. It is seen that the color mapping used in the segregation uses dominantly red and green channel, with green appearing at very hot areas of the image to generate the yellow color in the combined image, and the blue channel mostly contains noise.

Each frame of the thermal video recording is preprocessed in order to improve the quality of the particle count and size measurements. One of the biggest problems is the existence of the lens flare around the meltpool region. This not only creates difficulties in particle detection, but also creates spurious temperature fields. To remedy this, a lens flare filter is implemented in the region close to the meltpool. Images obtained from the red channel are first converted to grayscale images. Afterwards, thresholding based on pixel color intensity is performed to segregate the image into black and white areas such that the lens flare region as well as the meltpool inside it are grouped together, and are separated from the lower intensity regions. Then, pixels in this region are divided into multiple bins based on their intensities. Next, the median intensity of all bins that belong to the lens flare – meltpool region are calculated, and subtracted from this region. It is important to note that a tradeoff is necessary between the complete removal of the lens flare and preserving particle information, and rather conservative values are used in this study. Figure 6.37 shows the original frame on the left, and the processed frame (after segregation and median subtraction) on the right. An improvement to this methodology may be to implement the procedure iteratively with localized refinement, each time removing more (and smaller) regions of the lens flare as the region converges to the meltpool itself, however it is not implemented in this study.

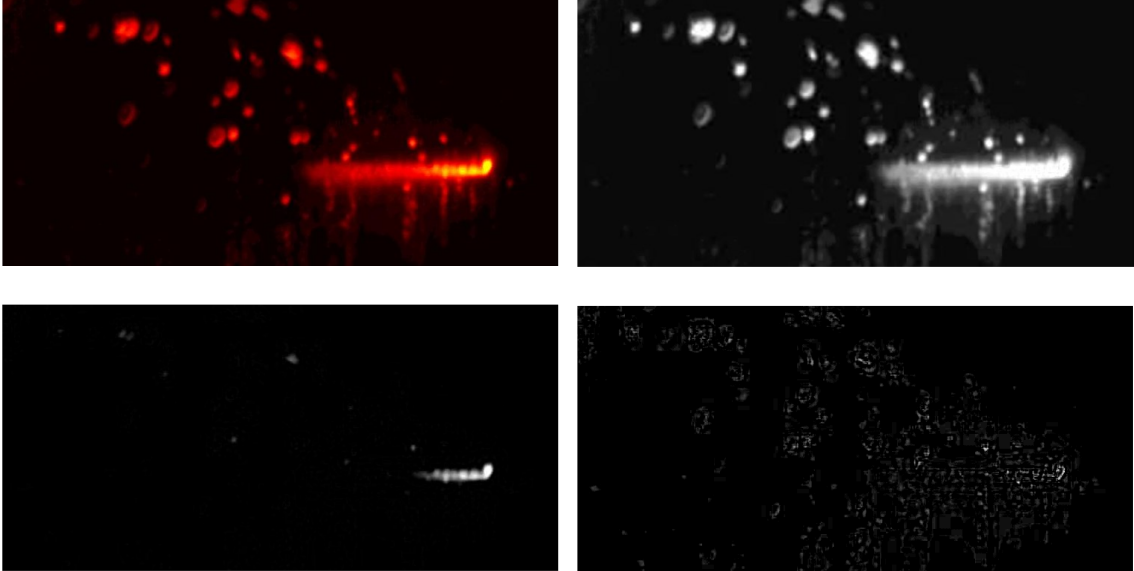


Figure 6.36 An image captured from the thermal camera plotted in MATLAB showing combined RGB (top-left), red (top-right), green (bottom-left) and blue (bottom-right) channels. Temperature information is not shown here.

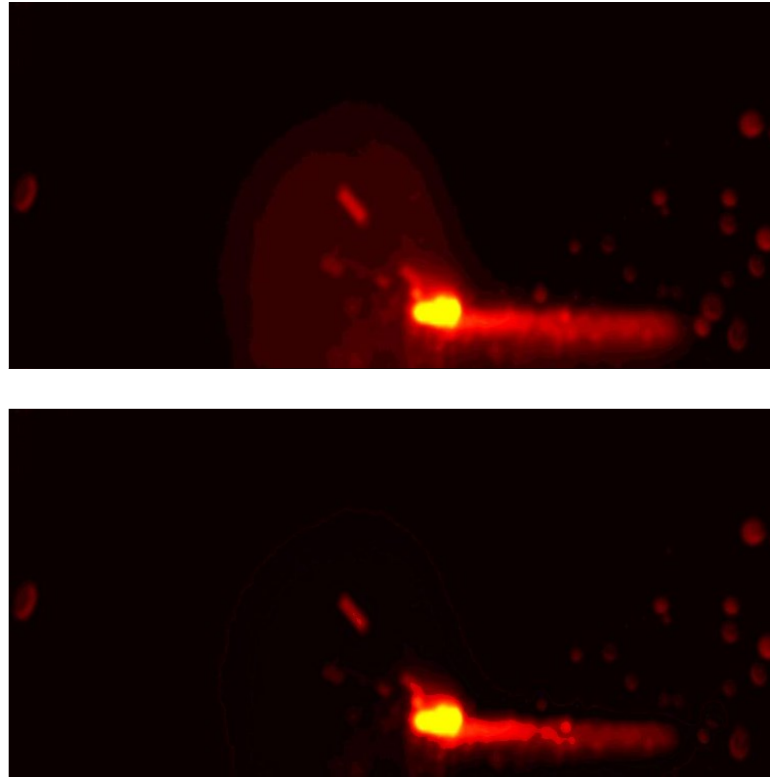


Figure 6.37 Lens flare removal around the meltpool region with the original frame (top) and the processed frame (bottom).

Furthermore, through a series of image processing steps, all particles are identified in each frame of the video and their sizes are calculated in terms of pixels. During the image processing, particles are not tracked individually, i.e. at any given frame, all particles are assumed to be “new” particles. Consequently, particle trajectory tracking is not performed in this study, mainly due to the restrictions discussed in the previous section. Furthermore, since the depth (out-of-plane) information is not available through the thermal camera images, particle trajectories in the build direction are unknown. This follows from the fact that a particle gets dimmer as it cools down, and within each particle the area at a certain temperature is not constant over time. Thus, performing size tracking that could also be

correlated with the distance from the lens is not possible. As the next step in particle detection, another intensity based thresholding is employed to reveal the pixels at a certain temperature range, followed by median filtering to reduce noise. The resulting image is then processed to count the number of pixels in each particle that represent the area of each particle. These areas, in units of pixels, are then converted to millimeters using the scene sizes calculated for the camera, disregarding the size changes caused by their location in the direction towards the camera. Figure 6.38 shows the preprocessed (after lens-flare removal) frame on the left, and the processed (with detected particles) frame on the right where centroids of detected particles are marked blue. Figure 6.39 summarizes the processing steps for spattering calculation. This process is repeated for each frame in the thermal video, and detected particles are recorded. The ratio of total area of spattering particles to the total processing area ($6\text{ mm} \times 4.1\text{ mm} = 24.6\text{ mm}^2$), denoted by percentage spatter (%S) is reported for each of the processed frames.

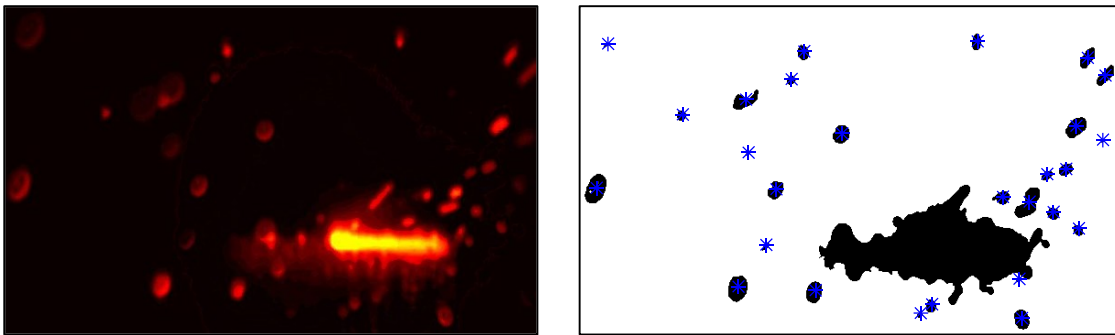


Figure 6.38 Preprocessed thermal camera image (left), detected particles (right).

Centroids or spattering particles are marked blue.

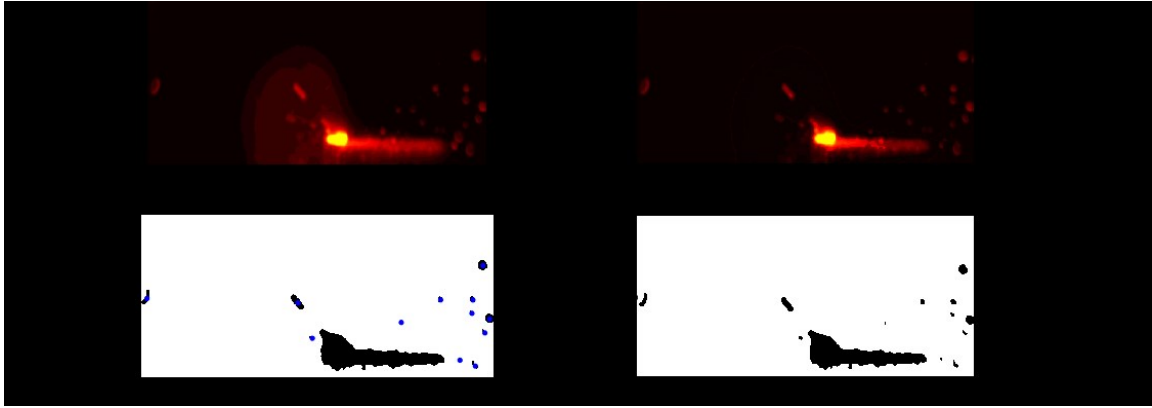


Figure 6.39 Processing steps for spattering particle detection.

6.3.5.1 Results and Analysis

Figure 6.40 shows thermal images from a single track. Note that only a 6 mm x 3 mm region is shown in these images in order to visualize the meltpool region better. Measured meltpool width (MP_w), frame number (F), calculated relative track distance (x_r) and spattering percentage (%S) are shown in each of the frame. Here, x_r is calculated by assuming the first frame of each track is at $x_r = 0$ mm, and each frame increases this distance with respect to the recording rate and laser speed ($0.5555 \text{ ms/frame} \times 800 \text{ mm/s} = 0.4444 \text{ mm/frame}$), rather than measuring the coordinates of the meltpool at each frame. Figures D1-D20 in Appendix D show the thermal images from all 20 tracks that were processed. Please note that the meltpool width measurements on these images do not account for the optical microscopy corrections.

6.3.6 Heating and Cooling Rates

As discussed previously, it is known that the rapid heating and cooling seen in the SLM causes a significantly different microstructure than traditionally processed IN625 alloy parts. The thermal camera images can be utilized to quantify these heating and cooling rates. By sampling the temperature data at certain points, the rate of cooling and heating can be estimated.

At this point, it is important to note that due to the asynchrony between the frequency of track processing and the recording rate of the camera, the x-coordinates of meltpools do not align across tracks. Theoretically, there can be up to $\frac{4.1mm}{10} = 40 \mu m$ difference in meltpool x-coordinates between different tracks, considering that each track takes at most 10 frames to be processed. This causes an inconsistency in temperature measurements between tracks, when analyzed individually. To alleviate this, the temperature histories for certain tracks are shifted temporally (± 1 frame) as a post processing operation in an attempt to create an agreement with the rest of the tracks. Furthermore, multiple tracks are used in the analysis and an average temperature history is constructed. Out of the 20 tracks analyzed, 10 of them have a positive scanning direction (laser moves in the +x direction) while the other 10 have a negative scanning direction. These two groups of tracks are analyzed separately. At each frame from the thermal camera data, the centroid of the meltpool is calculated. Each track's center in y-coordinate is identified using the mean of meltpool centroids that are observed in that track. These y-coordinates are used in the following analysis. Temperature measurements at various x-coordinates (the beginning, middle, and end of the track) are recorded during the timeframe of the processing of each

track (up to a maximum of 10 frames), at the respective track centers in y-coordinates. It is important to note that spattering particles, if positioned on top of the sampling points, can affect the result of this analysis. However, they are not filtered out in this study due to the associated challenges.

Figure 6.41 shows the minimum, maximum and mean temperatures observed at three different x locations: the beginning, middle and the end of the track, for the tracks with positive scanning directions. It is seen that the temperatures are very high at the beginning of the track when the processing starts, because the meltpool is located in this region. As the time passes, this point cools down. In contrast, the end of the track starts off with a low temperature, and heats up when the laser reaches and melts the region. As expected, the middle point of the track heats up as the laser approaches, and cools down as it departs. Figure 6.42 shows the temperatures for the tracks with negative scanning directions which indicates similar results. Figures 6.41-6.42 reveal similar heating and cooling profiles due to the nature of the process. The differences between them can be related to conductivity due to the layout of neighboring solid / powder regions, local differences in emittivity and powder geometry as well as spattering particles that overlap the sampling points. Furthermore, it is possible to obtain the rate of cooling and heating from these figures. Heating rates in Figure 6.41 are roughly 600 °C/ms and heating rates in Figure 6.42 are roughly 1000 °C/ms. Cooling rates are approximately 150 °C/ms in both figures. These observations are in agreement with the literature (Li et al., 2015; Vilaro et al., 2012). In comparison, the welding process has a much slower cooling rate of 0.550 °C/ms (DuPont, 1996).

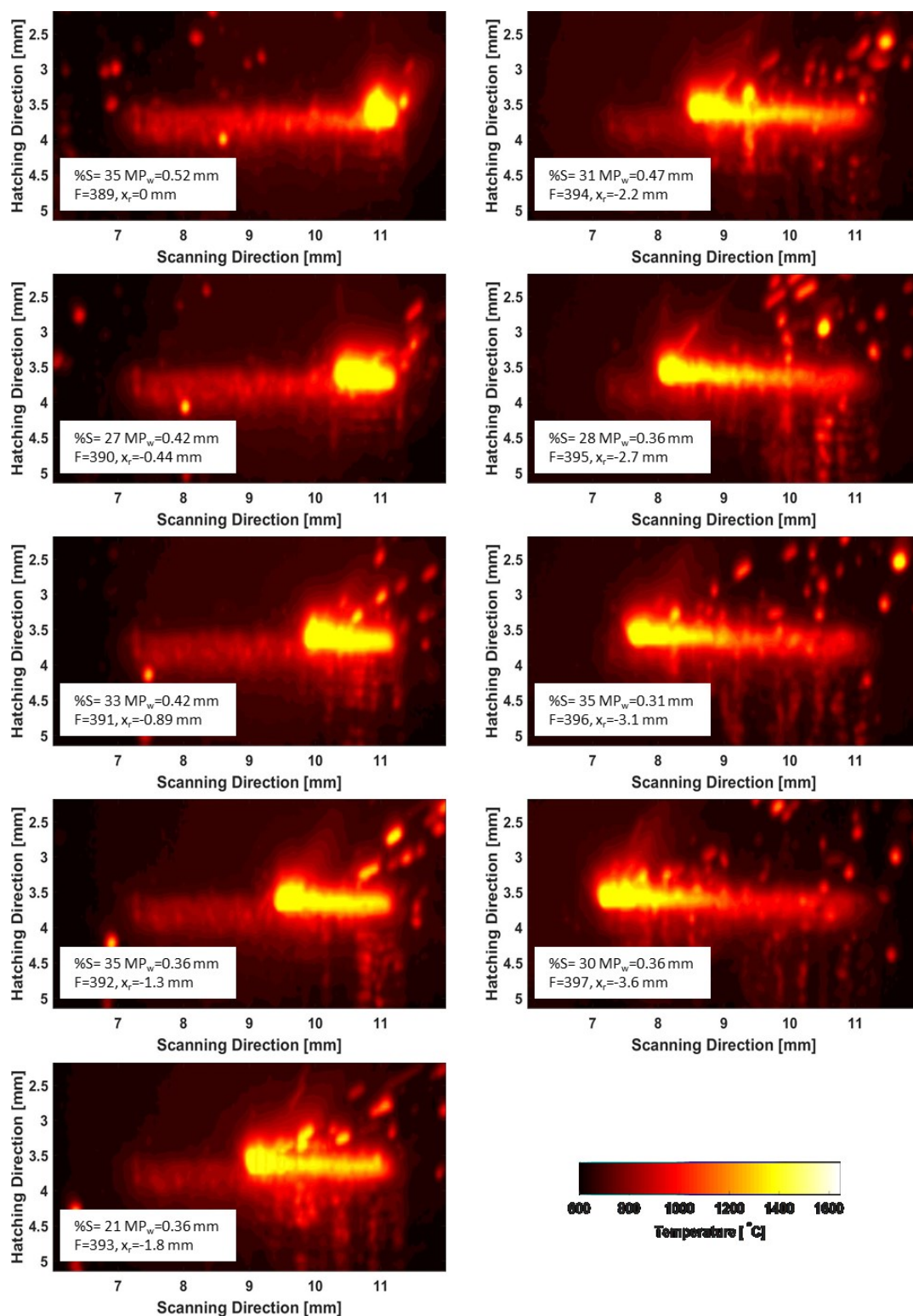


Figure 6.40 Frames from the thermal camera video showing the processing of a single track.

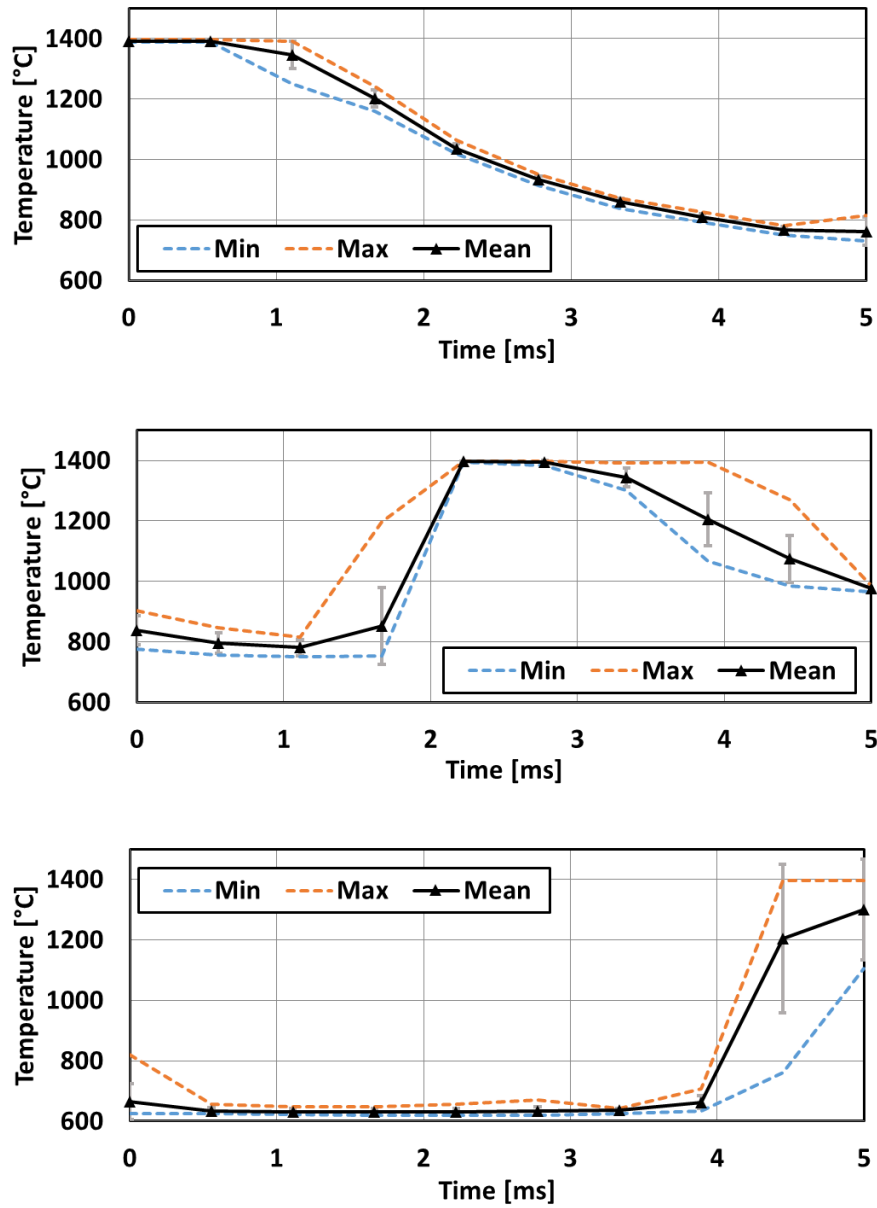


Figure 6.41 Minimum, maximum and average temperature histories grouped by the x coordinates: At the beginning of the track (top), middle of the track (middle) and end of the track (bottom) across multiple tracks. Error bars represent sample standard deviations.

Only the tracks with positive scanning direction (+x) are shown.

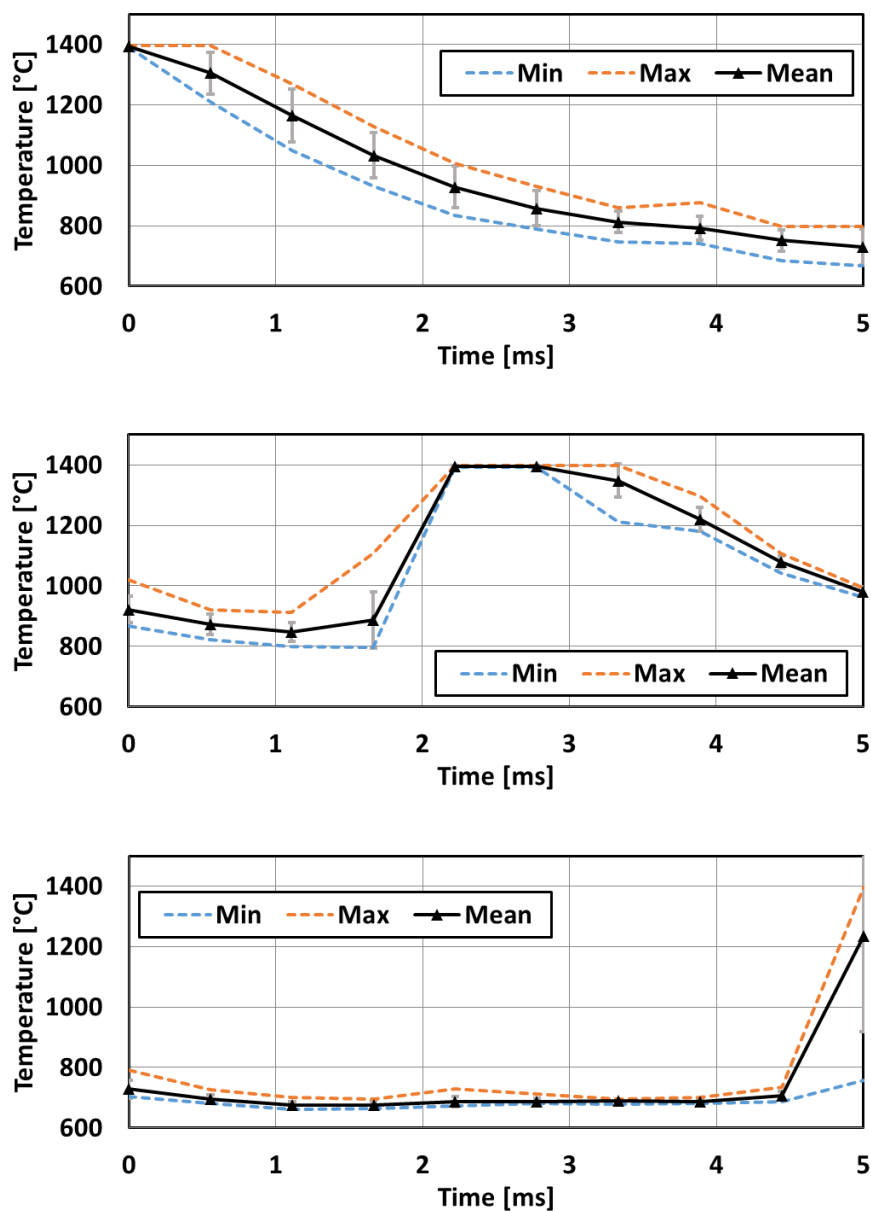


Figure 6.42 Minimum, maximum and average temperature histories grouped by the x coordinates: At the beginning of the track (top), middle of the track (middle) and end of the track (bottom) across multiple tracks. Error bars represent sample standard deviations.

Only the tracks with negative scanning direction (-x) are shown.

CHAPTER 7: MICROSTRUCTURAL MODELING OF SLM PROCESS

7.1 Introduction

Computational modeling of the IN625 SLM process can reveal information that is hard to obtain or unobtainable by experiments. For instance, a 3D thermal field that is not visible by the thermal camera can be obtained by solving the 3D heat transfer problem. Furthermore, microstructural modeling can be used to predict the quality and mechanical properties of the product. In this chapter, a nonlinear 3D Finite Element Method based MATLAB program is written to simulate the SLM process with different process parameters such as laser power, and scanning speed. The program is further improved by utilizing an in-situ thermal camera recording to predict spattering which is in turn included as a stochastic heat loss. Then, a phase field method based post processing is applied on the thermal solution to predict the resulting microstructure as a preliminary result.

7.2 3D Thermal Modeling with Finite Element Method

The 3D heat convection-diffusion equation is used to solve the transient heat transfer problem. Heat conduction in 3D is governed by the diffusion equation:

$$\rho C_p \frac{\partial T}{\partial t} = \frac{\partial}{\partial x} \left(k \frac{\partial T}{\partial x} \right) + \frac{\partial}{\partial y} \left(k \frac{\partial T}{\partial y} \right) + \frac{\partial}{\partial z} \left(k \frac{\partial T}{\partial z} \right) + q \quad (7.1)$$

where ρ is the density [kg/m³], C_p is the isobaric specific heat [J/kg K], T is the temperature [K], k is the thermal conductivity [W/m K] and q is the volumetric heat source [J/m³].

Convective effects are ignored due to the time scale of the SLM process.

Table 7.1 gives a short summary of different Finite Element formulations addressing material nonlinearities in steady state and transient solutions. Here, \mathbf{C} is the global heat capacity matrix, \mathbf{K} is the global heat conduction matrix, \mathbf{T} is the global temperature vector and \mathbf{q} is the global heat source vector that are used in the Finite Element scheme. Note that temperature-dependent material properties require \mathbf{C} and \mathbf{K} matrices to be a function of \mathbf{T} , which makes the problem nonlinear. There may be other nonlinearities that may require different formulations than those shown in Table 7.1. Details of transient formulations are covered in the following sections where a 3D FEM based thermal model of the SLM process has been constructed using MATLAB, following the derivations in (Felippa, 2014; Kwon and Bang, 2000; Huebner, 2001; Hughes, 1987). Nonlinearities can be accounted for with relatively simple modifications to the equation at the cost of computational time. We start with the linear formulation, and gradually move towards the nonlinear formulation.

Table 7.1 Finite Element formulations for steady state, transient, linear and nonlinear solution to the diffusion equation.

Steady State Solution	Linear Formulation	$\mathbf{KT} = \mathbf{q}$	For constant material properties
	Nonlinear Formulation	$\mathbf{K}(T)\mathbf{T} = \mathbf{q}$	For temperature-dependent material properties
Transient Solution	Linear Formulation	$\mathbf{C}\dot{\mathbf{T}} + \mathbf{KT} = \mathbf{q}$	For constant material properties
	Nonlinear Formulation	$\mathbf{C}(T)\dot{\mathbf{T}} + \mathbf{K}(T)\mathbf{T} = \mathbf{q}$	For temperature-dependent material properties

7.2.1 Linear 3D FEM Formulation

When the nonlinearities such as temperature-dependent material properties are ignored, the linear formulation can be used to obtain a solution to the diffusion equation. The FE formulation of the heat diffusion is given by:

$$\mathbf{C}\dot{\mathbf{T}} + \mathbf{K}\mathbf{T} = \mathbf{q} \quad (7.2)$$

where, as discussed previously, \mathbf{C} is the global heat capacity matrix, \mathbf{K} is the global heat conduction matrix, \mathbf{T} is the global temperature vector and \mathbf{q} is the global heat source vector. Global matrices and vectors are assembled from element matrices and vectors, based on the element connectivity in the mesh. The element \mathbf{C}^e and \mathbf{K}^e matrices and vectors are given by:

$$\mathbf{C}^e = \int_{\Omega^e} \rho C_p \mathbf{N}^T \mathbf{N} d\Omega^e \quad (7.3)$$

$$\mathbf{K}^e = \int_{\Omega^e} k \mathbf{B}^T \mathbf{B} d\Omega^e \quad (7.4)$$

$$\mathbf{q}^e = \int_{\Omega^e} \mathbf{q} \mathbf{N}^T d\Omega^e \quad (7.5)$$

In this formulation, \mathbf{N} is the element shape function vector of the element and \mathbf{B} is the Cartesian – natural coordinate derivative matrix of the element. Note that the superscript e is dropped for simplicity from these matrices and element-wise constants ρ , C_p and k .

The spatial integrals in Equation (7.3)-(7.5) can be calculated numerically using Gaussian quadrature. In an n -point Gaussian quadrature in 1D, the integral in Eq. (7.4) approximated by:

$$\mathbf{K}^e = \int_{\Omega} k \mathbf{B}^T \mathbf{B} d\Omega \approx \sum_{i=1}^n w_i \mathbf{F}(\xi_i) \quad (7.6)$$

with

$$\mathbf{F}(\xi_i) = k \mathbf{B}^T \mathbf{B} \mathbf{J} \quad (7.7)$$

where ξ_i are the quadrature points, w_i are the weights corresponding to ξ_i , $J = \det(\mathbf{J})$ and \mathbf{J} is the Jacobian matrix of the element. For dimensions higher than 1, the Gaussian quadrature rules are used on each dimension separately, and the number of integration points are selected based on the order of the interpolating polynomials on the element. $2 \times 2 \times 2$ rule is required to for the quadrature to be exact in 3D 8-node hexahedron elements. The points and weights are calculated from Legendre polynomials, following the formulation in (Hughes, 1987). Isoparametric 8-node hexahedral elements are used in the current simulations due to their simple geometry, formulation and accuracy. Higher order elements are not considered because a linear representation of the temperature over the element is considered sufficient for this study. Note that isoparametric hexahedral elements can have various shapes, i.e. they are not limited to cubes or cuboids. A representative image of an 8-node hex element is shown in Figure 7.1.

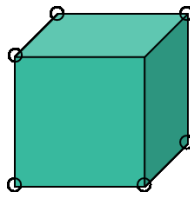


Figure 7.1 Isoparametric 8-node hexahedral element.

The Jacobian matrix of the 3D element is given by:

$$\mathbf{J} = \frac{\delta(x, y)}{\delta(\xi, \eta)} = \begin{bmatrix} \frac{\delta x}{\delta \xi} & \frac{\delta y}{\delta \xi} & \frac{\delta z}{\delta \xi} \\ \frac{\delta x}{\delta \eta} & \frac{\delta y}{\delta \eta} & \frac{\delta z}{\delta \eta} \\ \frac{\delta x}{\delta \zeta} & \frac{\delta y}{\delta \zeta} & \frac{\delta z}{\delta \zeta} \end{bmatrix} = \begin{bmatrix} J_{11} & J_{12} & J_{13} \\ J_{21} & J_{22} & J_{23} \\ J_{31} & J_{32} & J_{33} \end{bmatrix} \quad (7.8)$$

The element shape function vector \mathbf{N} can be written in natural coordinates, ξ, η, ζ for each node i as (Felippa, 2013):

$$N_i = \frac{1}{8} (1 + \xi \xi_i) (1 + \eta \eta_i) (1 + \zeta \zeta_i) \quad (7.9)$$

where ξ_i, η_i and ζ_i are the coordinates of the i^{th} node, which are given in Table 7.2.

Table 7.2 Natural coordinates of the nodes of a 8-node hexahedron element.

(Felippa, 2013)

Node	ξ	η	ζ
1	-1	-1	-1
2	+1	-1	-1
3	+1	+1	-1
4	-1	+1	-1
5	-1	-1	+1
6	+1	-1	+1
7	+1	+1	+1
8	-1	+1	+1

The Cartesian derivatives of the shape function vector are then calculated using the chain rule:

$$\begin{aligned}\frac{\delta \mathbf{N}}{\delta x} &= \frac{\delta \mathbf{N}}{\delta \xi} \frac{\delta \xi}{\delta x} + \frac{\delta \mathbf{N}}{\delta \eta} \frac{\delta \eta}{\delta x} + \frac{\delta \mathbf{N}}{\delta \zeta} \frac{\delta \zeta}{\delta x} \\ \frac{\delta \mathbf{N}}{\delta y} &= \frac{\delta \mathbf{N}}{\delta \xi} \frac{\delta \xi}{\delta y} + \frac{\delta \mathbf{N}}{\delta \eta} \frac{\delta \eta}{\delta y} + \frac{\delta \mathbf{N}}{\delta \zeta} \frac{\delta \zeta}{\delta y} \\ \frac{\delta \mathbf{N}}{\delta z} &= \frac{\delta \mathbf{N}}{\delta \xi} \frac{\delta \xi}{\delta z} + \frac{\delta \mathbf{N}}{\delta \eta} \frac{\delta \eta}{\delta z} + \frac{\delta \mathbf{N}}{\delta \zeta} \frac{\delta \zeta}{\delta z}\end{aligned}\tag{7.10}$$

The \mathbf{B} matrix is then calculated from:

$$\mathbf{B} = \begin{bmatrix} \frac{\delta \mathbf{N}}{\delta x} & \frac{\delta \mathbf{N}}{\delta y} & \frac{\delta \mathbf{N}}{\delta z} \end{bmatrix}^T = \begin{bmatrix} J_{11}^{-1} \frac{\delta \mathbf{N}}{\delta \xi} + J_{12}^{-1} \frac{\delta \mathbf{N}}{\delta \eta} + J_{13}^{-1} \frac{\delta \mathbf{N}}{\delta \zeta} \\ J_{21}^{-1} \frac{\delta \mathbf{N}}{\delta \xi} + J_{22}^{-1} \frac{\delta \mathbf{N}}{\delta \eta} + J_{23}^{-1} \frac{\delta \mathbf{N}}{\delta \zeta} \\ J_{31}^{-1} \frac{\delta \mathbf{N}}{\delta \xi} + J_{32}^{-1} \frac{\delta \mathbf{N}}{\delta \eta} + J_{33}^{-1} \frac{\delta \mathbf{N}}{\delta \zeta} \end{bmatrix}\tag{7.11}$$

A similar procedure is used to calculate the \mathbf{C} matrix and \mathbf{q} vector. Once the element level matrices are calculated, they are assembled into global matrices.

7.2.2 Heat Source Implementation

During the SLM process, a laser beam travels across the powder bed, melting and occasionally evaporating the material on its path. In this FE implementation, the laser beam is modeled as an internal heat source that acts on the elements that fall within the beam's radius. At each time step, elements that fall within the beam's diameter (based on the location of their nodes) are determined, and the heat flux is applied internally.

Elements that are under the beam at each time step, i.e. the “captured” elements are calculated by checking whether they intersect with the beam. In node based capturing, an

element is captured if any node of that element is within the beam. Similarly, in centroid based capturing, the element is captured if its centroid is within the beam. The heat source is applied only to the captured elements. Figure 7.2 shows a circular beam on a finite element mesh, where node based capturing is utilized, and captured elements are colored in yellow.

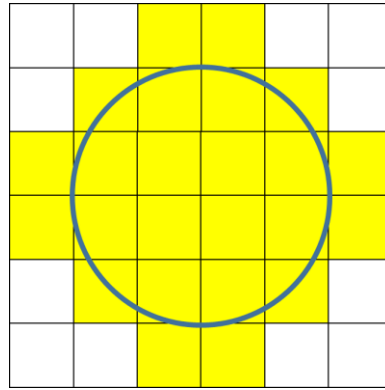


Figure 7.2 Node based element capturing under a circular beam. Captured elements are shown in yellow.

The laser beam profile can be represented in various shapes, such as uniform, or Gaussian. The uniform beam profile causes the area under the beam to receive a uniform heat flux. The heat flux generated by a Gaussian beam on a point with reflectivity R is given by:

$$q = (1 - R) \frac{2P}{\pi w_o^2} e^{-2(r^2/w_o^2)} \quad (7.12)$$

where P is the power, w_o is the waist size and r is the distance between the point and the beam center.

Furthermore, captured elements should receive a heat flux proportional to their areas, and in case of non-uniform beam shapes, their locations with respect to the beam center should affect the heat flux as well. In order to achieve this, Monte-Carlo sampling is utilized to accurately distribute the laser beam power to the elements under the beam. The circular beam area is sampled by m points distributed uniformly and elements that fall inside the beam are heated based on the number and intensity of points that fall within their area. Therefore, the beam can be approximated as:

$$P = \frac{1}{m} \sum_m q_m \quad (7.13)$$

If the uniform beam shape is used, this procedure results in each element being heated up proportionally to its area. If the Gaussian beam profile is used, the sampled (lumped) beam intensity on the points can account for the nonlinear change of flux with distance from the beam center. Figure 7.3 shows a representative Gaussian beam intensity as it hits the surface, and Figure 7.4 shows a representation of the sampled beam.

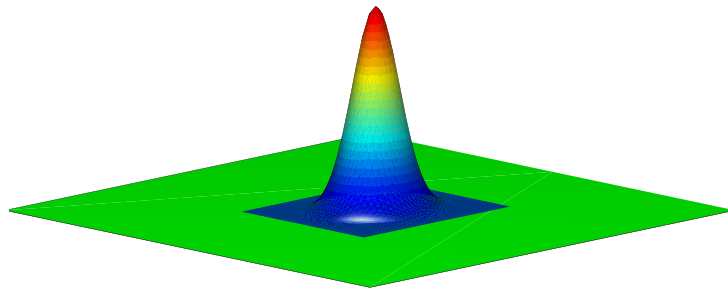


Figure 7.3 Gaussian beam intensity on the surface.

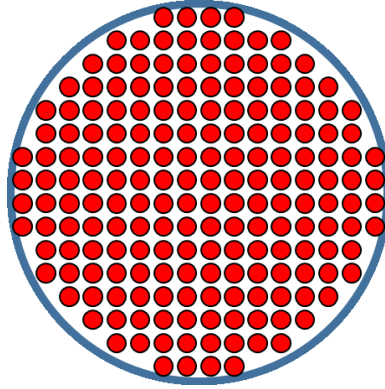


Figure 7.4 Representation of the beam area (contoured) sampled with points.

The power absorbed by point p under the laser beam, denoted q_p , is calculated as:

$$q_p = (1 - R)P\beta_p \quad (7.14)$$

where x_p and y_p are the coordinates of point p under the beam, x_{lc} and y_{lc} , Here, β_p is a function of the coordinates of point p , and it is defined as

$$\beta_p = \begin{cases} \frac{2}{\pi w_0^2} e^{-2[(x_p - x_{lc})^2 + (y_p - y_{lc})^2]/w_0^2}, & \text{Gaussian} \\ 1 & \text{Uniform} \end{cases} \quad (7.15)$$

Let n be the number of sampling points that fall within the element. Then, the total power input to the element, q^e when the beam is estimated by m points ($m \geq n$) is given by:

$$q^e = \sum_{p=1}^m q_p = (1 - R)P \frac{1}{m} \sum_{p=1}^n \beta_p \quad (7.16)$$

Movement of the laser beam also needs to be implemented in the simulation. The laser moves at a predetermined velocity, and therefore the coordinates of its center at each time step is known. Consequently, the laser beam center coordinates are replaced by $x_{lc} = x_{lc}(t)$ and $y_{lc} = y_{lc}(t)$. Furthermore, element capturing procedure is repeated at each time step as the beam moves. Note that node based element capturing yields more accurate heat distribution when combined with Monte-Carlo sampling, therefore we prefer node based

capturing over centroid based capturing in this study. Figure 7.5 shows the application of Monte-Carlo sampling with node based capturing on the FE mesh, where heated elements are shown in blue. The number of points should be increased with finer mesh size. Overall, this approach provides a dynamic, accurate and computationally efficient distribution of the laser beam power over the elements that can be used with different beam profiles. The model can further be improved by utilizing a non-uniform sampling that would better suit the beam profile.

After the amount of total power acting on each element is determined, the heat source is implemented in the FE model as a volumetric internal heat on the first layer of elements using Eq. (7.5). Figure 7.6 shows the elements at the top where the laser beam is applied as an internal heat, and the unaffected elements below. Due to the fact that the heat is applied only to the elements at the top regardless of their size, the temperature solution depends on the height of these elements. If elements with smaller height are chosen, the applied laser power is unchanged but since the mass of the element are lower, their temperatures will rise more. Similarly, if taller elements are chosen, they will reach smaller temperatures due to their increased mass. This may seem like a drawback at first, but it has a meaningful physical interpretation when element heights are chosen to be equal to the layer size to represent a layer.

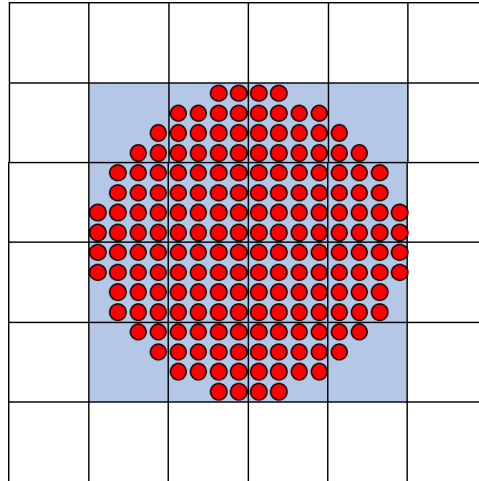


Figure 7.5 Power distribution on node-captured elements with Monte-Carlo sampling of the laser beam.

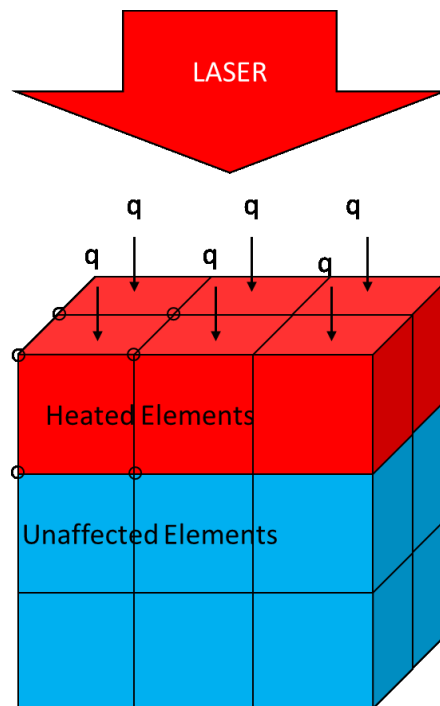


Figure 7.6 The affected (heated) and unaffected elements under the beam. Only the elements in the top are affected.

7.2.3 Nonlinearities

During the SLM process, as the material heats up, melts, and solidifies, its thermal properties change with temperature. To accurately model the process, temperature-dependent material properties must be accounted for, which makes the problem nonlinear. The global capacitance and conductance matrices must be updated to account for these changes. Therefore, Eq. (7.2) becomes

$$\mathbf{C}(T)\dot{\mathbf{T}} + \mathbf{K}(T)\mathbf{T} = \mathbf{q} \quad (7.17)$$

where $\mathbf{C}(T)$ and $\mathbf{K}(T)$ represent the temperature-dependent global capacitance and conductance matrices, respectively. Eq. (7.17) also allows the model to account for the latent heat during melting and solidification. Furthermore, this formulation allows powder to solid (varying packing density) conversion during the simulation.

7.2.3.1 Temperature-dependent Material Properties

It is known that IN625 nickel based alloy's specific heat, and thermal conductivity increases with temperature. The bulk material properties and SLM process parameters for IN625 are given in Table 7.3. The specific heat and conductivity values are linearly dependent on temperature in the solid region ($T \leq T_S$). In the solidus-liquidus region ($T_S < T < T_L$), C_p and k are interpolated linearly between the liquid and the solid values (with the added effect of phase change on C_p as described in the next section). In the $T \geq T_L$ region, the liquid properties are used without temperature dependence. Note that temperature-dependent density is not utilized to conserve the mass and energy in the system, as volume changes are ignored. This is further explained in Section 7.2.3.3.

Table 7.3 Bulk Material Properties for IN 625.

(Yadroitsev et al., 2013)

Parameter	Value
Liquidus Temperature, T_L [K]	1623
Solidus Temperature, T_S [K]	1563
Density, ρ [kg/m ³]	8440
Latent Heat of Fusion, L_f [kJ/kg]	227
Specific Heat, C_p [J/kg K] ($T \leq T_S$)	$338.98 + 0.2437 \times T$
Specific Heat, $C_{p,L}$ [J/kg K] ($T \geq T_L$)	735
Thermal conductivity, k [W/mK] ($T \leq T_S$)	$5.331 + 0.015 \times T$
Thermal conductivity, k [W/mK] ($T \geq T_L$)	30.05
Reflectivity, R	0.7

7.2.3.2 Phase Change

Phase changes between solid and liquid (melting / solidification) are handled by the equivalent specific heat formulation, which modifies the specific heat of the material at different temperature zones to imitate melting and solidification. It is given by:

$$C_{eq}(T) = \begin{cases} C_p(T), & T \leq T_S \\ C_p(T) + \frac{L_f}{T_L - T_S}, & T_S < T < T_L \\ C_{p,L}, & T \geq T_L \end{cases} \quad (7.18)$$

where $C_{p,L}$ is the specific heat of the material in liquid phase, L_f is the latent heat of fusion of the material, T_S is the solidus temperature, and T_L is the liquidus temperature.

7.2.3.3 Powder to Solid Conversion

It is known that during the SLM process, the powder bed is not fully dense, since the powder is not compressed after it is placed. This loose powder packing entails the existence of air gaps in between the particles that reduce the overall thermal conductivity, and the density of the region. To compensate for the porosity (how loosely the powder is packed compared to a bulk material) of the powder, the density and conductivity of the material can be modified such that

$$\rho_{powder} = (1 - \tau)\rho_{bulk} \quad (7.19)$$

$$k_{powder} = (1 - \tau)k_{bulk} \quad (7.20)$$

where τ is the porosity of the powder material.

Eqs. (7.19) and (7.20) can be easily implemented in the linear model (ignoring temperature-dependent material properties, and solid-liquid phase changes) such that the **K** and **C** matrices are calculated accordingly. However, the implementation of these equations in a linear model would mean that after the powder exceeds the liquidus temperature, it solidifies back to a loosely packed powder geometry. This is clearly not the case in the SLM process, therefore it needs to be accounted for.

To model the powder-liquid-solid change, it is assumed that an element loses its “powder property” once it reaches the liquidus temperature, T_L . As soon as the temperature T_L is reached, the element can no longer go back to the powder state. This can easily be implemented in the simulation such that elements in powder state use temperature-dependent powder properties whereas elements that have lost the powder state use solid

properties. However, the implementation of Eq. (7.19) in this manner is problematic, as it going from a powder to bulk material causes an increase in the density, which in turn means an increase in the mass of the system since the volume of the FE problem domain is kept constant in the current implementation.

One solution to this problem would be to utilize a larger geometry (and mesh) for powder areas (more height) proportional to the packing density, and adaptively reducing geometry as the region melts and solidifies. One may even couple the heat diffusion problem with thermal expansion and stress-strain equations to create a full-fledged model of the SLM process. However, this approach would require higher order interface elements to connect the solid/liquid elements to powder elements. Furthermore, it would be computationally prohibitive, and is not the scope of this study.

A basic solution would be to simply assume that the volume of the powder after melting and solidification does not change in the simulation itself (albeit changing in reality in conjunction with thermal expansion, and filling the air-gaps between powder particles due to expansion and liquid motion); meaning that the density of the powder is equal to the density of the bulk material given that the volume change does not affect calculations. If the problem geometry remains unchanged at constant volume, then the mass can only be conserved if the density is constant. In fact, considering heat source is constant with depth and the conductivity reduction is already accounted for in Eq. (7.20), this is a valid approximation.

Consequently, only Eq. (7.20) is utilized in the FE simulations, and Eq. (7.19) is not utilized because powder is assumed to have the same density as the bulk material.

7.2.4 Time Integration

Time integration is necessary in order to obtain a transient solution to the problem. Equation (7.17) can be discretized in time in the following way:

$$\mathbf{C}(T) \left(\frac{\mathbf{T}^{t+\Delta t} - \mathbf{T}^t}{\Delta t} \right) + \mathbf{K}(T)(\theta \mathbf{T}^{t+\Delta t} + (1 - \theta) \mathbf{T}^t) = \mathbf{f}(T) \quad (7.21)$$

where θ is the time parameter. $\theta=0$ yields the explicit method, $\theta=0.5$ yields the Crank-Nicolson type semi-implicit method and $\theta=1$ yields the implicit method. The explicit scheme requires time step to be chosen with respect to the Courant–Friedrichs–Lewy (CFL) condition for convergence. The implicit scheme allows the use of larger time steps, but adds to the computational time required to find the solution. An implicit time integration scheme is required along with a direct sub-iteration to determine the nonlinear \mathbf{K} and \mathbf{M} matrices during each time step.

7.2.5 Verification and Convergence

Verification of the FE program must be performed to ensure that it is accurately representing the solution of the model. One way to perform verification is to compare the energy conservation with an analytical solution. We consider applying a certain amount of heat for a limited time to the mesh and comparing the steady state solution to the equation for the linear problem, given by:

$$Q = \int_{t_i}^{t_f} P dt = m C_p \Delta T \quad (7.22)$$

where Q is the heat, P is laser power, t_i and t_f are the initial and final time in which the heat source is being applied, m is the mass of the whole geometry, C_p is the isobaric specific heat and ΔT is the temperature difference between initial temperature and final (steady state) temperature. A verification study in our case can utilize a stationary or moving heat source. These test results will be identical as long as Monte Carlo sampling points fall within the mesh and the same amount of heat is applied to the surface. A stationary heat source is used for simplicity. A cube with 1 mm^3 volume discretized with 1000 elements is considered. The heat source is a laser beam with 0.5 mm radius, with 195 W power, centered on the top surface of the cube. The heating time is set to 0.01 ms. The material properties follows IN625 properties at room temperature, with reflectivity 0.7, specific heat 0.412 J/gK and total mass $0.00844 \text{ g/mm}^3 \times 1 \text{ mm}^3 = 0.00844 \text{ g}$. Heat conductivity can be set to high values to speed up convergence to steady state solution for energy verification purposes. Adiabatic boundary conditions are used with a uniform initial temperature of 353K across all the elements in the cube. The steady state temperature obtained from the FE solution is 521.234951 K. The expected steady state temperature T_{SS} can be calculated using Eq. (7.22) as:

$$T_{SS} = 353 \text{ K} + \frac{58.5 \text{ W} \times 0.01 \text{ s}}{0.00844 \text{ g} \times 0.412 \text{ J/gK}} = 521.2349 \text{ K} \quad (7.23)$$

which is in close agreement with the FE solution. Therefore, we can conclude that the energy verification is successful.

Next, we consider mesh convergence. Mesh size can affect the solution and as a rule of thumb, a smaller mesh size should be utilized in locations with high gradients in the solution. The overall mesh size used in the problem should be reduced until the reduction has little to no effect on the solution. Furthermore, the laser beam (with 100 μm radius in actual simulations) should be discretized into multiple elements to allow a smooth movement and accurate distribution of power on the surface while taking Monte Carlo sampling into consideration. For this reason, we should choose to utilize elements smaller than 30 μm in the simulations. It is important to note that due to computational limitations, it is not possible to reduce the mesh size much more than the current size.

Furthermore, it is imperative to select the time step so that the solution is correct. The implicit scheme is unconditionally stable, which allows larger time steps than an explicit scheme. Moreover, since there is no convection, the Peclet number (ratio of advective transport rate to diffusive transport rate) and Reynolds number (ratio of inertial forces to viscous forces) are zero. Therefore the numerical stability of the solution is not affected by the time step size. However, there is still another factor to consider to allow an accurate representation of the temperature field. The time step should be small enough so that the laser beam does not skip over any elements during the processing. If an element is skipped and consequently the laser power is applied on other elements over a longer time period (rather than a smooth transition), the skipped elements will be much colder and the overexposed elements will be much hotter than expected temperatures. Therefore, the time step should be calculated taking the element size into account, such that:

$$dt \geq \frac{dx}{v_s} = \frac{0.03 \text{ mm}}{800 \text{ mm/s}} = 3.75 \times 10^{-5} \text{ s} \quad (7.24)$$

where dt is the time step size, dx is the smallest element dimension on the scanning axis, and v_s is the scanning velocity of the laser. Furthermore an even smaller time step of $dt = 5 \times 10^{-6} \text{ s}$ is chosen in order to represent the discrete Monte Carlo sampling and circular shape of the beam better.

7.2.6 Problem Geometry and Process Parameters

The problem geometry is 4 mm long, 0.5 mm wide and 0.22 mm tall, as shown in Figure 7.7. Considering each SLM layer is $s=0.02 \text{ mm}$, this model accounts for 11 layers, with the 11th (top) layer being the powder layer. The lower 10 layers are assumed to be solid with bulk material properties. The bottom layer is assumed to be in contact with the base plate, which is kept at a constant temperature of 80°C (353 K). The mesh consists of 27588 isoparametric linear hexahedron elements, and is obtained with the Gmsh software by Geuzaine & Remacle (Geuzaine and Remacle, 2009). The mesh is imported to MATLAB using the load_gmsh4 software by Almeida & Lorphevre (Almeida and Lorphevre, 2007). Process parameters used in the simulations are given in Table 7.4 where the energy intensity values are calculated from $E = P/(v_s \times h \times s)$.

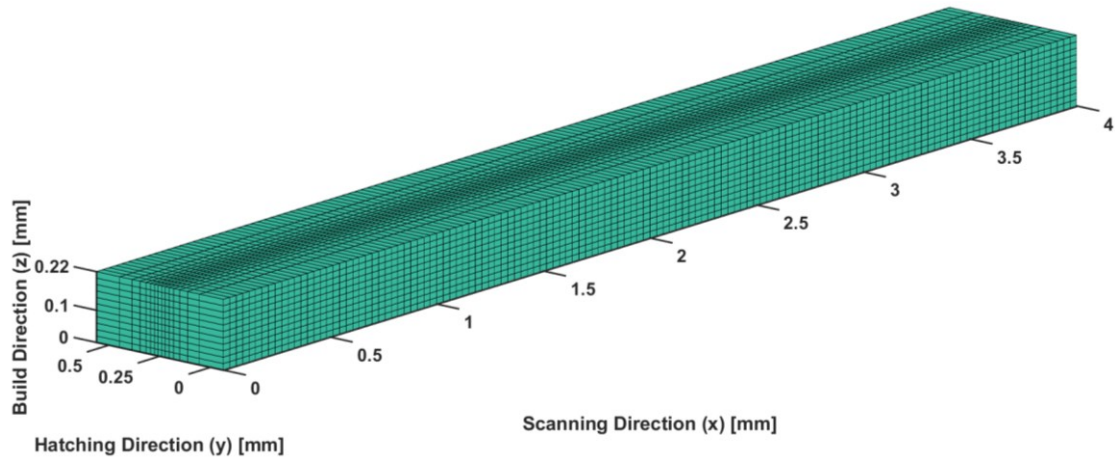


Figure 7.7 Problem geometry with hexahedra mesh.

Table 7.4 SLM Process parameters used in the simulation.

(Special Metals, 2015).

	Low Energy Intensity $E=96.6 \text{ J/mm}^3$	Medium Energy Intensity $E=113.8 \text{ J/mm}^3$	High Energy Intensity $E=134.5 \text{ J/mm}^3$
Hatch distance, h [mm]	0.1	0.1	0.1
Spot size diameter, d [μm]	100	100	100
Powder bed thickness, s [μm]	20	20	20
Laser power, P [W]	169	195	195
Scanning speed, v_s [mm/s]	875	800	725
Track length [mm]	3.6	3.6	3.6
Beam type	Uniform	Uniform	Uniform

7.2.7 Experimental Validation

The FE simulation was run with the medium intensity parameters for validation. The track was processed with a Gaussian laser beam with 0.1 mm radius, with 195 W power, and 800 mm/s scanning speed. Temperature-dependent IN625 material parameters are used, and the nonlinear transient solution is obtained.

To validate the FE solution with experiments, thermal camera images discussed in Chapter 6 are utilized. A comparison can be made between the cooling rates observed from the thermal images in Chapter 6 and the FE solution. Figure 7.8 shows the FE solution along with the thermal camera cutoff temperatures. Cooling rates are observed with the thermal camera measurements. It is seen that the average cooling rate is about 700 K/ms, which is higher than those observed in the thermal camera images. It is important to note here that the thermal camera has a measurement ceiling after which all temperature measurements are truncated. This causes a discrepancy in the peak temperatures of the measurements and the FE solution. Furthermore, continuous processing of the powder bed causes an overall increase in the temperature in the piece, which is further amplified by the processing of adjacent tracks. Thermal camera measurements indicate that tracks cool down towards approximately 1000K during processing. The current FE model considers a single track simulation at 353 K initial temperature, and since only a single layer is considered, there is no significant heat buildup and the beginning of the track cools down to approximately 500K at the end of the simulation. A higher initial temperature that represents the gradual heat buildup in the piece can be utilized to obtain a better match between measurements and simulation results.

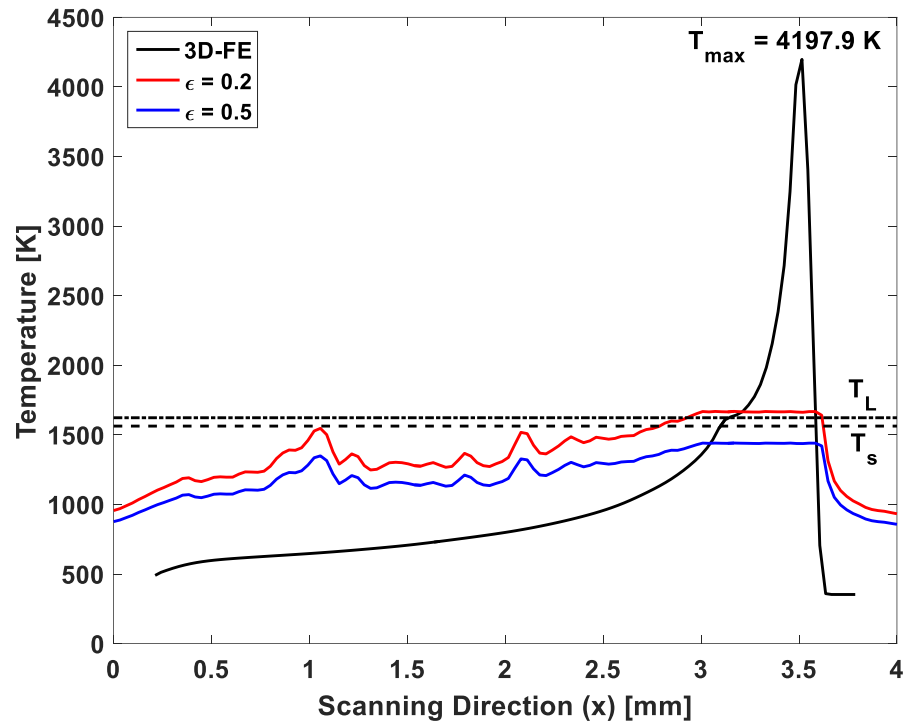


Figure 7.8 Comparison of thermal camera and FE results on a single track with medium energy intensity ($P=195 \text{ W}$, $h=0.1 \text{ mm}$, $v_s=800 \text{ mm/s}$). Liquidus and solidus temperatures are marked with dashed lines.

7.2.8 Single-track Simulation Results

Results of the single track simulations are shown in Figures 7.9-7.11 where temperatures are plotted on the FE mesh at the last time step of the simulation. The temperature scale is limited to $T \leq T_L$ in order to allow a better visualization of the lower temperature ranges. The results show that heat diffusion occurs towards the sides and the bottom of the meltpool. The meltpool has a shape similar to that is observed from the thermal images in Chapter 6. These results are obtained at low, medium and high energy intensities at 96.6 J/mm³, 113.8 J/mm³ and 134.5 J/mm³, respectively.

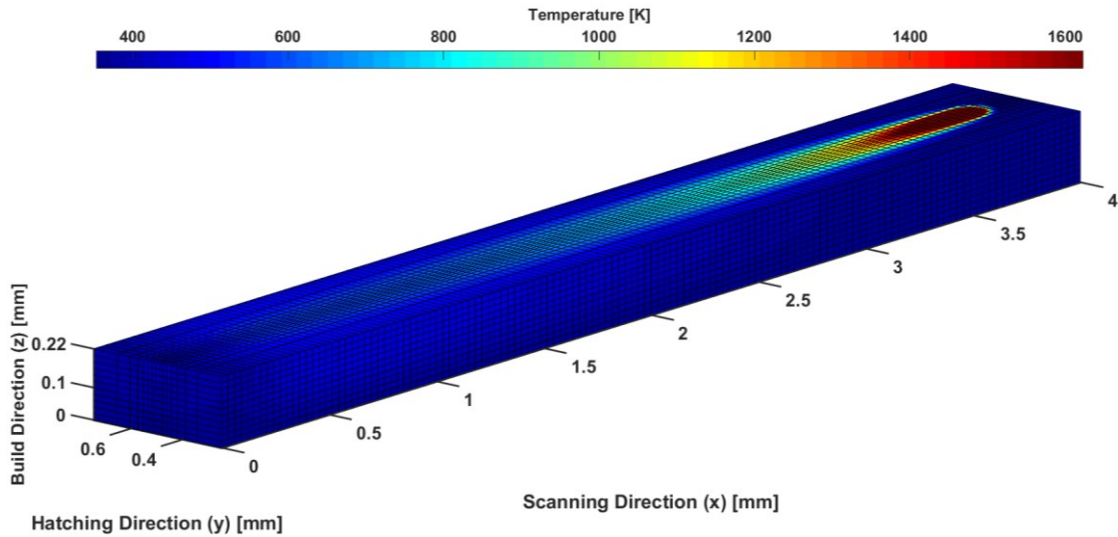


Figure 7.9 FE solution for the high energy intensity ($P=195$ W, $h=0.1$ mm, $v_s=725$ mm/s) case. Temperatures are limited to $T \leq T_L$.

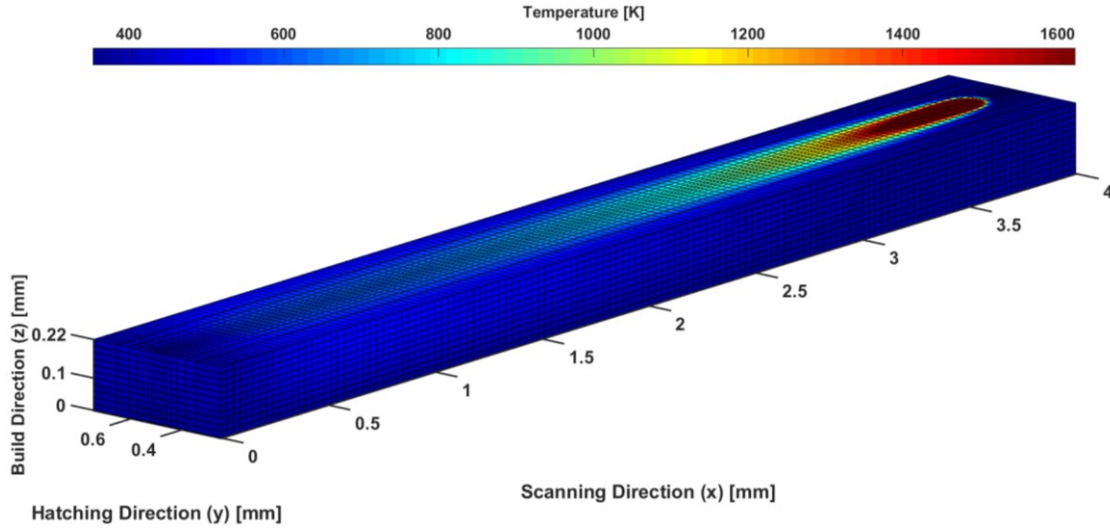


Figure 7.10 FE solution for the medium energy intensity ($P=195$ W, $h=0.1$ mm, $v_s=800$ mm/s) case. Temperatures are limited to $T \leq T_L$.

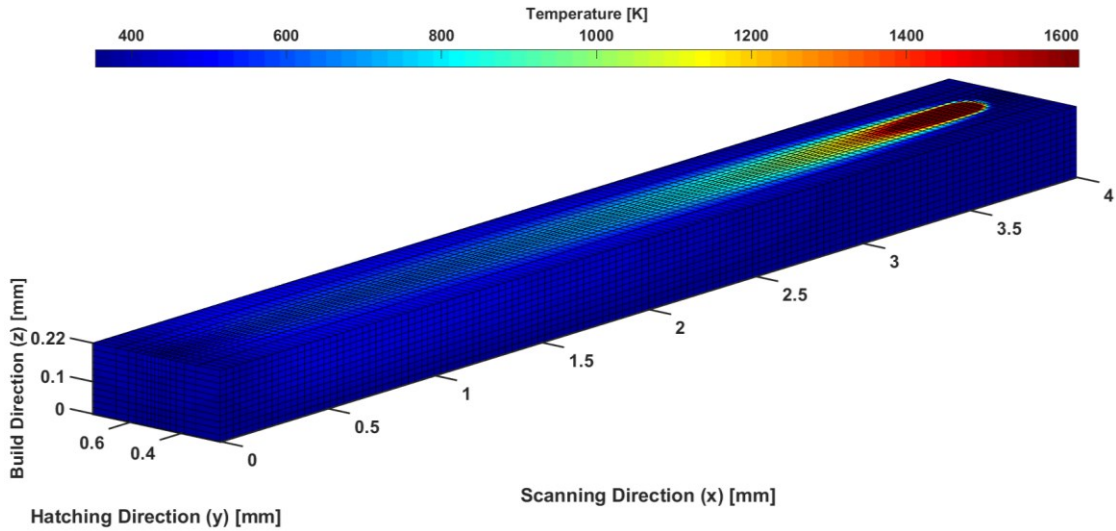


Figure 7.11 FE solution for the low energy intensity ($P=169$ W, $h=0.1$ mm, $v_s=875$ mm/s) case. Temperatures are limited to $T \leq T_L$.

To be able to compare these results, temperatures from 6 different points were extracted from all three simulations. These points are on the top and bottom of the top layer ($z = 0.22$ at the surface and $z = 0.20$), at the center of the track ($y = 0.25$) and at 3 different x locations along the track ($x = 1$, $x = 2$ and $x = 3$). The points on the surface, denoted p_1 , p_2 and p_3 , are illustrated in Figure 7.12. The remaining points, p_4 , p_5 and p_6 , are directly below the first three points and inside the geometry at a depth of $20\text{ }\mu\text{m}$. The results are shown in Figures 7.13-7.15 for high, medium and low intensity cases, respectively. As expected, it is seen that the peak temperatures drop as the energy intensity is lowered. Another observation is that the FE simulations predict peak temperatures that are above the melting temperature at the bottom of the top layer, suggesting meltpool depths greater than the layer thickness.

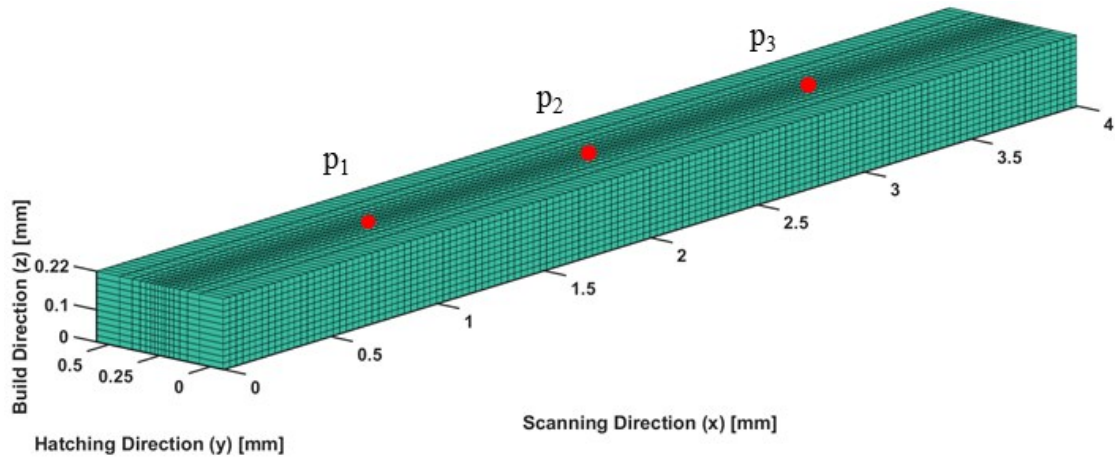


Figure 7.12 Temperature extraction points.

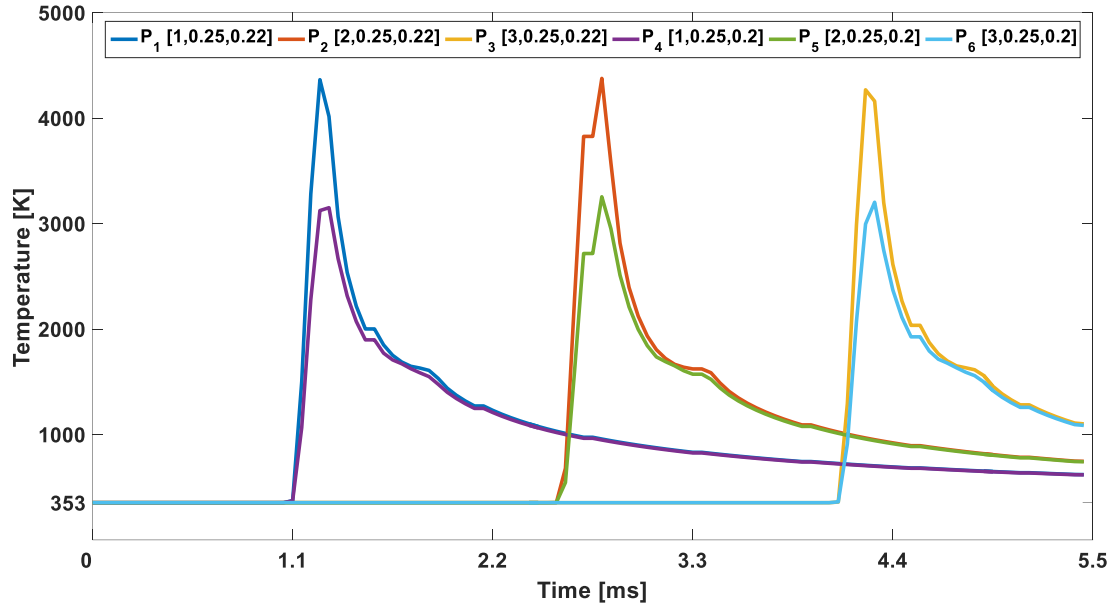


Figure 7.13 Temperature histories at six points for the high energy intensity ($P=195$ W, $h=0.1$ mm, $v_s=725$ mm/s) case.

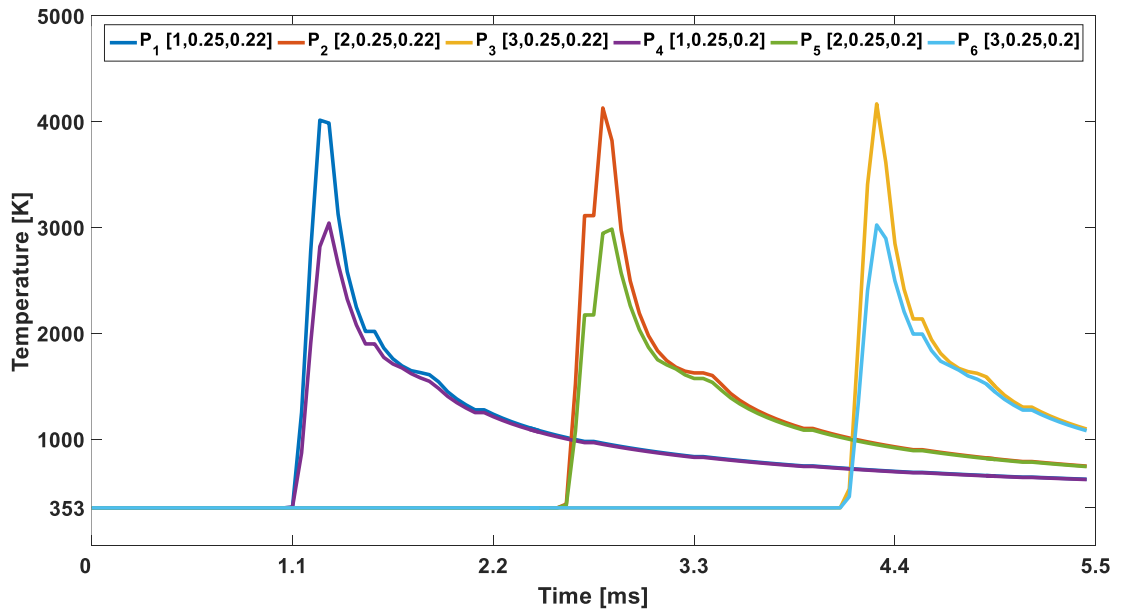


Figure 7.14 Temperature histories at six points for the medium energy intensity ($P=195$ W, $h=0.1$ mm, $v_s=800$ mm/s) case.

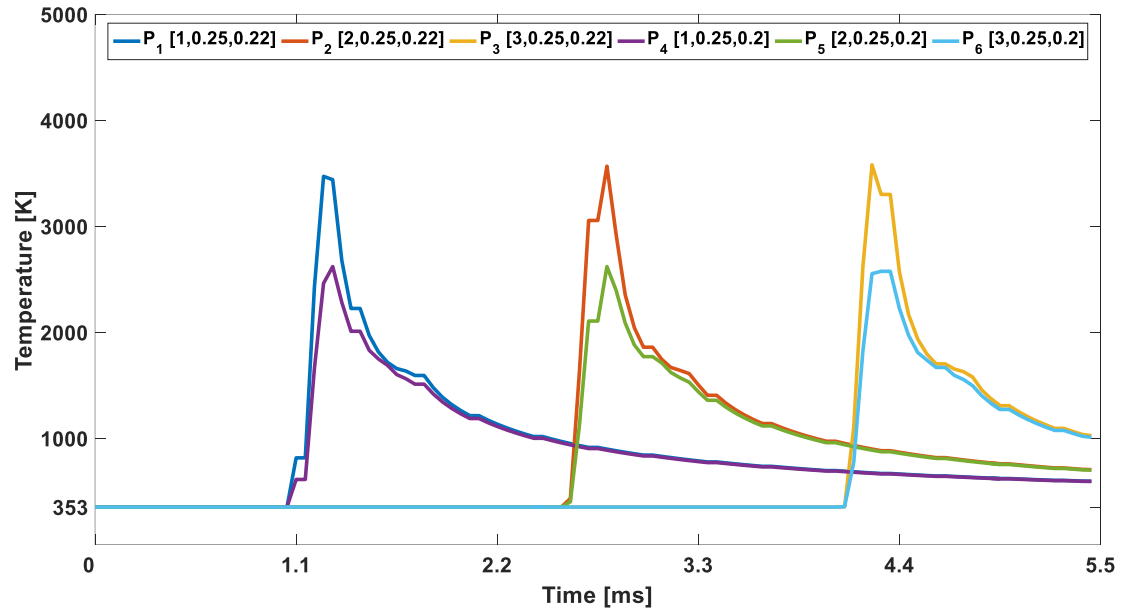


Figure 7.15 Temperature histories at six points for the low energy intensity ($P=169$ W, $h=0.1$ mm, $v_s=875$ mm/s) case.

7.2.9 Multi-track Simulations

Aside from the single track simulations shown in the previous section, multi-track simulations were designed and run with 2 tracks. Multi-track simulations can reveal the larger Type-I meltpools discussed in Chapter 6, arising from the remaining heat in the workpiece from the previous track when the laser starts processing a new track.

7.2.9.1 Problem Geometry and Process Parameters

The problem geometry is 5 mm long, 1 mm wide and 0.1 mm tall, as shown in Figure 7.16. Note that the height of the problem geometry is reduced from 0.22 mm to 0.1 mm due to computational limitations. The mesh is designed to accommodate 2 scanning tracks with a hatch distance of 0.1 mm in the y direction. Considering each SLM layer is 0.02 mm, this model accounts for 5 layers, with the 5th (top) layer being the powder layer. The lower 4 layers are assumed to be solid. The bottom layer is assumed to be touching the base plate, which is kept at a constant temperature of 80°C (353 K). The mesh consists of 21450 isoparametric linear hexahedron elements, and is obtained with the Gmsh software. Similar to the single track experiments, the mesh is designed such that the center of the mesh in y direction is more refined to allow a better and more accurate representation of the laser beam and resulting meltpools. The smallest elements in the central region of the mesh (between $y=0.3$ mm and $y=0.7$ mm) have dimensions $30\ \mu m \times 25\ \mu m \times 20\ \mu m$ which provides a sufficient resolution for the laser beam, while the largest elements on the near $y=0$ mm and $y=1$ mm have dimensions $30\ \mu m \times 100\ \mu m \times 20\ \mu m$.

The scanning starts on the top surface ($z=0.1$ mm) at $(x, y)=(0.5, 0.45)$ mm, and the first track ends at $(x, y)=(0.5, 4.6)$ mm after 4.1 mm of scanning. At the end of the track, the laser is turned off for 0.042 ms. The laser then starts processing the second track, with a hatch distance of $h=0.1$ mm, beginning at $(x, y)=(4.6, 0.55)$ mm and ending at $(x, y)=(0.5, 0.55)$ mm. Process parameters used in the simulation are given in Table 7.5.

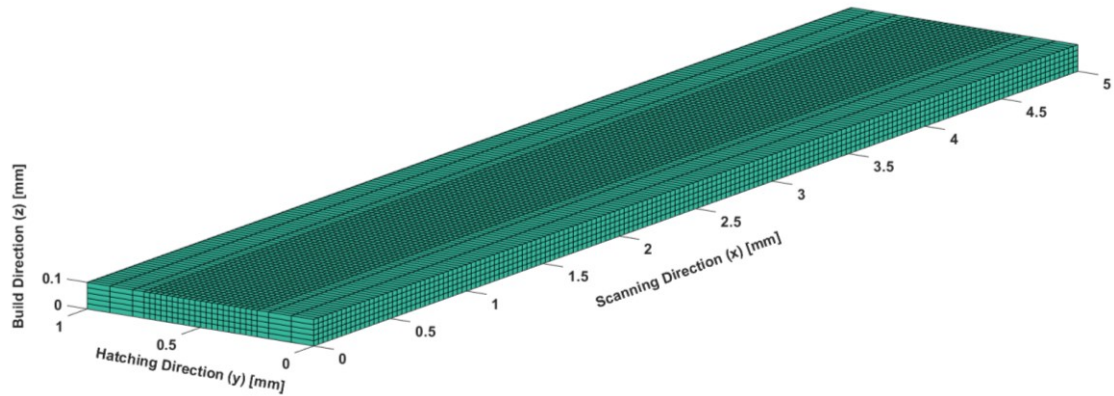


Figure 7.16 Multi-track simulation geometry with hexahedra mesh.

Table 7.5 SLM process parameters used in the simulation.

	Low Energy Intensity	Medium Energy Intensity	High Energy Intensity
Hatch distance, h [mm]	0.1	0.1	0.1
Spot size diameter, d [μm]	100	100	100
Powder bed thickness, s [μm]	20	20	20
Laser power, P [W]	169	195	195
Scanning speed, v_s [mm/s]	875	800	725
Track length [mm]	4.1	4.1	4.1
Beam type	Gaussian	Gaussian	Gaussian

7.2.9.2 Multi-track Simulation Results

Meltpool width measurements can be compared between the FE solution and thermal camera images corrected with optical images. Based on the previous discussion in Chapter 6, the mean width of the meltpool varies between 155 μm and 111 μm based on the location on the track for the default parameters used in processing Coupon #35. As a reminder, the difference between the meltpool width measurements (specifically the Type-I and Type-II meltpools) were attributed to the following fact: When the laser starts processing a new track, the remaining heat from the processing of the previous track causes the meltpool to be wider initially, and this effect decays towards the end of the track causing the meltpool to shrink.

Meltpool widths extracted from the low, medium and high energy intensity FE simulation results are shown in Figure 7.17. As expected, higher energy intensities result in wider meltpools. Furthermore, Type-I and Type-II meltpools are observed for all cases at around 5 ms and 11 ms marks. Note that the gap between first and second tracks in Figure 7.17 results from the lack of heating when the laser is turned off, causing the meltpool size to decrease. The medium intensity FE simulation estimates the maximum meltpool width to be 130 μm , while the minimum meltpool width after reaching steady state is about 116 μm . Overall, the results are in good agreement with the measurements in Chapter 6.

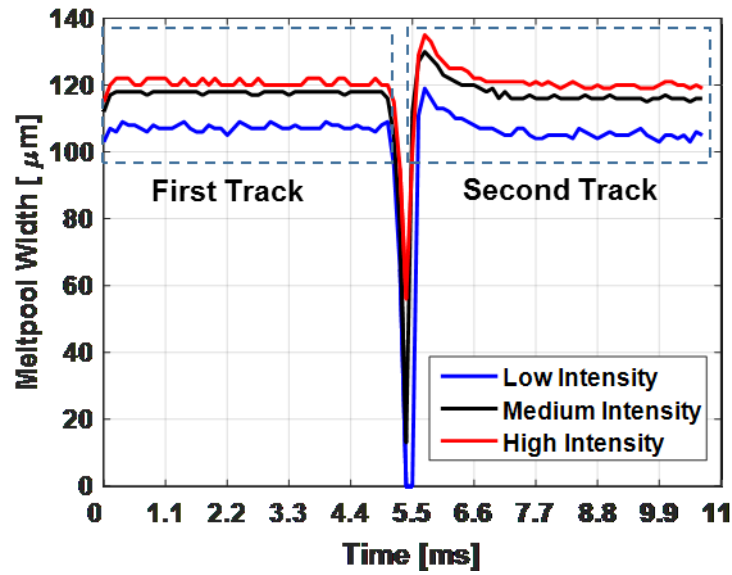


Figure 7.17 Meltpool width calculated from low, medium and high energy intensity FE simulation results showing two tracks of processing.

Furthermore, temperatures were extracted at 6 points from each simulation. These points lie on the top surface of the powderbed ($z=0.1$ mm), and on the track centers ($y=0.45$ mm and $y=0.55$ mm) at three different x locations along the track ($x=1$ mm, $x=2.5$ mm and $x=4$ mm). Note that P_1 , P_2 and P_3 belong to track 1 whereas P_4 , P_5 and P_6 belong to track 2. The temperature history is tracked from the beginning of the simulation until the end of the simulation, upon the completion of the scanning of 2nd track. The results are given in Figures 7.18-7.20. As expected, the high energy intensity simulation shown in Figure 7.18 reaches higher peak temperatures than the medium and low energy intensity simulations. Furthermore, it is observed that when the laser beam passes a point, the temperature of the point in the previous track (on the same x coordinate) also rises. However, the temperature rise is not sufficient to cause melting which coincides with the fact that these points are $h=0.1$ mm apart and the meltpool half-widths are less than 0.1 mm. The difference in peak

temperatures are caused by the remaining temperature fields on the workpiece as well as the temporal and spatial sampling of the simulations.

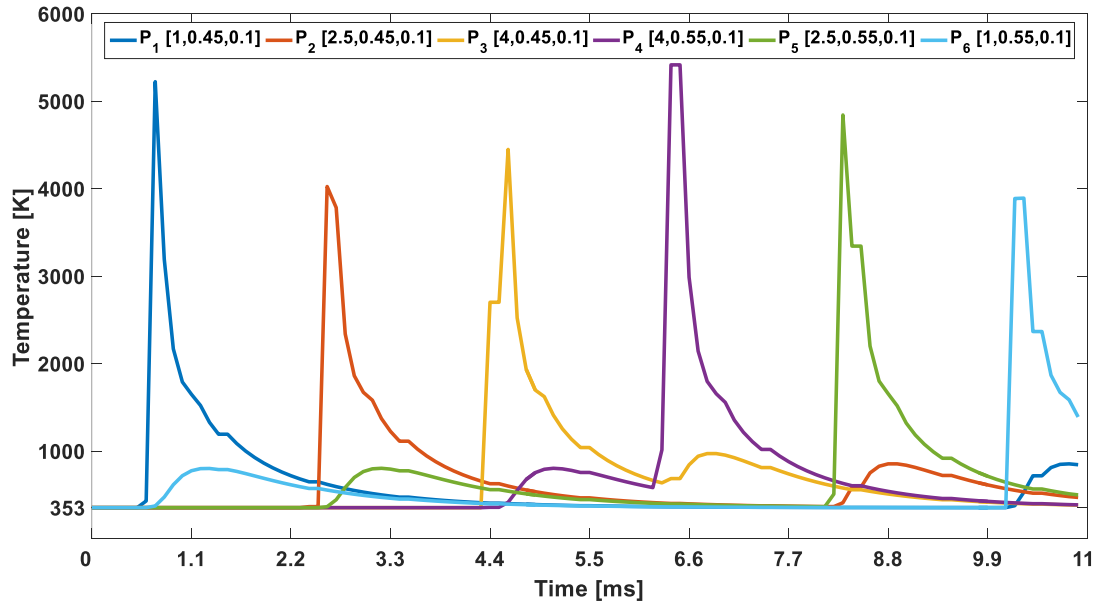


Figure 7.18 Temperature histories at six points along the scanning direction for the high energy intensity ($P=195$ W, $h=0.1$ mm, $v_s=725$ mm/s) case.

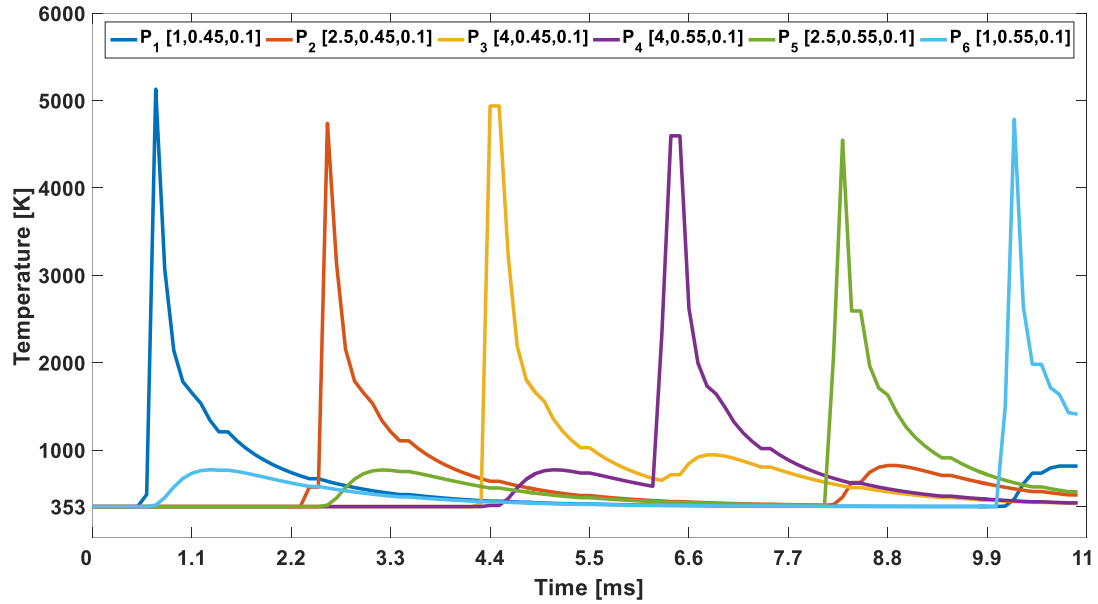


Figure 7.19 Temperature histories at six points along the scanning direction for the medium energy intensity ($P=195$ W, $h=0.1$ mm, $v_s=800$ mm/s) case.

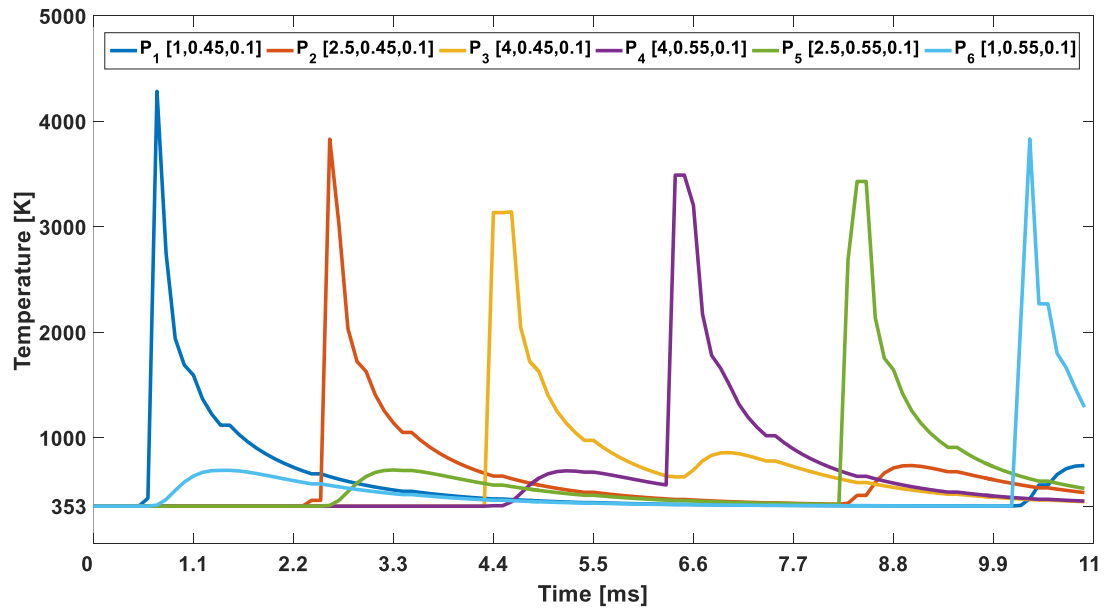


Figure 7.20 Temperature histories at six points along the scanning direction for the low energy intensity ($P=169$ W, $h=0.1$ mm, $v_s=875$ mm/s) case.

7.3 Microstructure Prediction

7.3.1 Thermal Gradients

As discussed previously, columnar grains observed from the SEM images of the SLM process IN625 samples are indicative of diffusion based growth. In the case of SLM, thermal gradients play a major role in solidification. As solidification happens, local fluctuations in energy cause certain sites to solidify faster than others. As the grain grows, the latent heat of freezing causes the temperatures to rise at the solidification front, which causes the surrounding areas to heat up. If the temperature rise reaches the melting temperature, solidification can no longer continue. Therefore, the local temperature field is critical in determining the direction in which the grains grow towards. Furthermore, as a solidified grain grows through the liquid, it experiences different temperature fields which may inhibit or accelerate its growth. Any information on the thermal gradients in the melt pool can therefore help predict the solidification direction. The 3D FEM simulation results in thermal field and gradients can be utilized to obtain this information.

The temperature field of the FE solution is sampled at various points, and thermal gradients at each point are calculated based on central differences. Figure 7.21 shows the thermal gradients observed on the XY (top) surface of the powder bed, at the end of the simulation with default processing condition ($P=195$ W, $h=0.1$ mm, $v_s=800$ mm/s). Negative gradient vectors are shown with red arrows, and the length of the arrows indicate their magnitude.

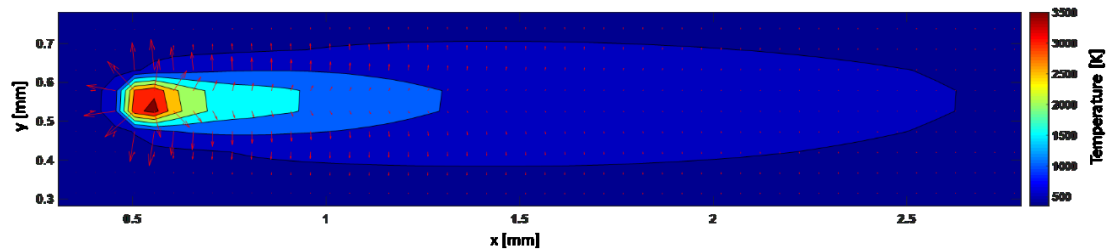


Figure 7.21 Contour plot of the temperature field and the negative thermal gradients on sampled points at the end of the medium energy intensity ($P=195$ W, $h=0.1$ mm, $v_s=800$ mm/s) simulation.

Figure 7.22 shows the negative thermal gradients of the 3D FE solution from the YZ view and Figure 7.23 shows the negative thermal gradients from the XZ view. Both views depict strong gradient vectors in the Z direction, caused by heating of the laser at the top and cooling of the base plate. The YZ view shows some heat diffusion in the Y direction, which indicate that the meltpool region also cools down towards the cooler regions on the sides of the track. This lateral cooling is further affected by the neighboring material; solidified regions transfer the heat more effectively than powder regions. Other than the strong gradients in the Z direction in the XZ view in Figure 7.23, lateral cooling is also observed especially at the end of the track after $x=4.5$ mm where the laser is turned off for a period of time (0.042 ms) followed by the initiation of the scanning of the subsequent track, as the simulation models two tracks. Both figures reveal the nature of solidification in SLM process as it is these thermal gradients that shape the microstructure during solidification.

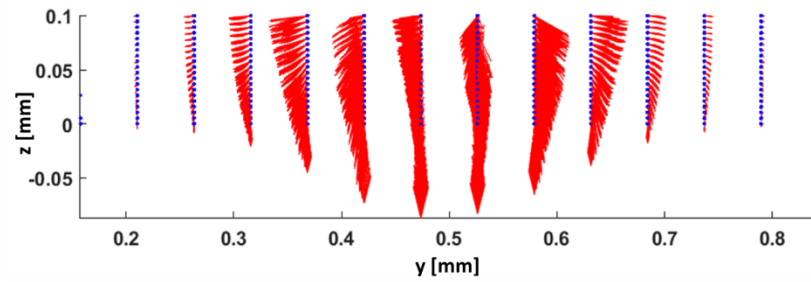


Figure 7.22 YZ view of the negative thermal gradients extracted from the FE solution ($P=195$ W, $h=0.1$ mm, $v_s=800$ mm/s) sampled at various points (shown as blue). Note that the thermal gradients are summed over time.

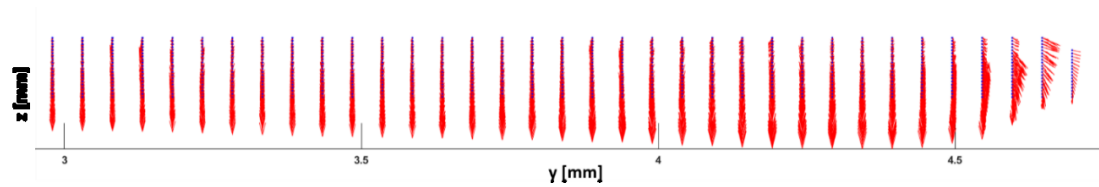


Figure 7.23 YZ view of the negative thermal gradients extracted from the medium energy intensity FE solution ($P=195$ W, $h=0.1$ mm, $v_s=800$ mm/s) sampled at various points (shown as blue). Note that the thermal gradients are summed over time.

Furthermore, for all three simulations, temperature fields are sampled on the scanning area of the second track ($0.5 \text{ mm} \leq y \leq 0.6 \text{ mm}$), $10 \text{ }\mu\text{m}$ below the top surface ($z = 0.09 \text{ mm}$) coinciding with the half-thickness of the top layer, with $50 \text{ }\mu\text{m}$ distance between the sampling points in X and Y directions. Histograms of the angles between the build direction and X and Y directions of the negative thermal gradients are obtained and are given in Figures 7.24 and 7.25.

Angles in XZ planes given in Figure 7.24 show that majority of the heat diffusion aligns directly with the build direction, with a slight tilt towards the scanning direction indicated by the positive angles. The negative angles in XZ planes are in the opposite of the scanning direction, and result from the area near the beginning of the second track ($x = 4.6 \text{ mm}$). It is observed that as the scanning speed decreases, the 0° angles are tilted towards 10° , in the direction of scanning.

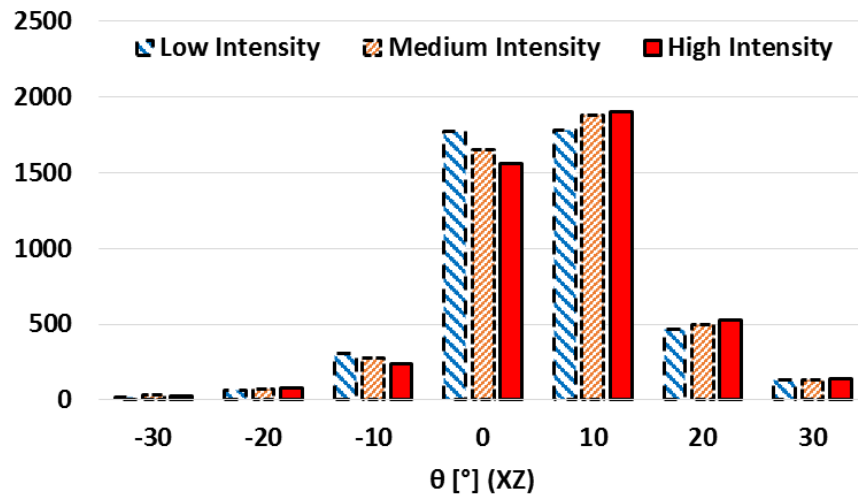


Figure 7.24 Gradient directions in the XZ plane obtained from FE solutions.

The majority of the YZ plane angles shown in Figure 7.25 are also aligned with the Z axis, with some heat diffusion occurring in the hatching direction Y. Here, negative angles indicate the direction towards the next hatch, while the positive angles indicate the direction towards the previous hatch. The frequency of 0° angle gradients is observed to decline with decreasing energy intensity, and in the low intensity case the vectors lean towards the -10° direction slightly more than the other cases.

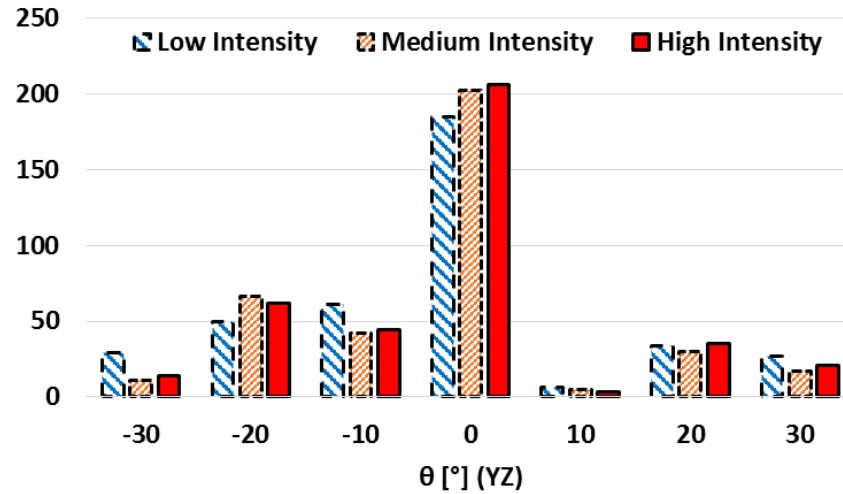


Figure 7.25 Gradient directions in the YZ plane obtained from FE solutions.

Overall, these angles indicate the growth direction of columnar grains affected by the heat diffusion with respect to the build direction. It is important to note that while these angles largely coincide with the direction angles observed in Chapter 6, however, a direct comparison should not be made between them.

7.3.2 Phase Field Method

The phase field method is a computational method that is used in modeling of solidification and microstructure. A brief introduction to the phase field method was given in Chapter 1. This study focuses on applying the basic 2D phase field method algorithm that can achieve dendritic growth as proposed by Kobayashi (Kobayashi, 1993) to the results of 3D FEM simulations as a post-processing step in an attempt to capture the effects of different process parameters on the resultant microstructure of the IN625 material.

It is important to note some of the deficiencies of the method. As stated by Voorhees (Voorhees, 2015), one deficiency of the phase field method lies in where it provides the biggest advantage against other methods. In reality, the thickness of the interface must be very small, and in the computational domain it must be resolved accurately for the calculations to be correct. However, such a high resolution is computationally prohibitive, and interface thicknesses much larger than the reality are used in computational domains. Karma&Rappel (Karma and Rappel, 1998) addresses this by allowing very small interface thicknesses that are smaller than the reciprocal of the mean curvature of the interface. Furthermore, certain properties of the system, such as diffusivity, are often interpolated at the diffuse interfaces using the order parameter, which makes the actual solution dependent on the interpolation itself, rather than the physical phenomena taking place at the interface. Since utilizing physical interface sizes is not possible in the computational domain, spurious terms appear due to the interpolations, such as diffusion happening at the interface as it grows. Moreover, due to the large size of the interface, solute trapping becomes an

issue, and anti-trapping terms are included to compensate for this in the calculation of the concentration diffusion equations (Ebrahimi, 2010).

Nevertheless, phase field method is a very popular method in computational modeling of solidification. It is utilized to explore a comparison between high and medium energy intensity cases.

7.3.2.1 Implementation of the Model

The phase field method utilizes the temperature fields obtained from the FE simulations. Because the implemented phase field algorithm is 2D, the temperature field needs to be extracted at desired cross-sections from the 3D FE model over a period of time steps. Once the temperatures are known, the phase field can be initialized with liquid and solid phases. During the phase field simulation, the temperature field is updated using the solution of the FE model. The phase field method requires higher spatial and temporal resolution, therefore the temperature field obtained from the FE simulation is interpolated linearly, both spatially and temporally.

The Type-II meltpool location (at the beginning of second track) is chosen as a suitable location to investigate solidification. Temperatures are extracted from the YZ cross-section at $x=0.4576$ at the corresponding the time step. The laser beam is centered on $y=0.55$ mm during the scanning of the second track. Meltpool widths were observed to be between 120-140 μm for the Type-II meltpool region.

Equations 1.30-1.32 are solved using a Forward-Time Central-Space (FTCS) Finite Difference (FD) scheme. The Fortran implementation by Kiran (Kiran, 2010) is utilized to create a MATLAB code for the phase field method, following the paper by Kobayashi (Kobayashi, 1993). Model parameters are given in Table 7.6, some of which are suggested by Kobayashi (Kobayashi, 1993). The value of K is chosen such that the latent heat buildup yields a dendritic structure and the value of j is chosen to eliminate preferred directions.

Table 7.6 Parameters used in the phase field simulations.

μ	K	δ	α	γ	$\bar{\varepsilon}$	τ	j
1	2.4	0.01	0.9	10	0.01	0.0003	0

The problem domain is described as follows. It is assumed that the meltpool is symmetric about the x-axis, which allows only half of the meltpool to be considered rather than the full meltpool region. In reality, one side of the meltpool is solidified material (due to the processing of the previous track) while the other side is still powder, which affects the cooling rates (due to different thermal conductivity) and nucleation sites (existing grains on the solidified structure versus the microstructure of the powder). In these simulations, the problem considers that the meltpool is surrounded with the previously processed (solidified) region rather than powder material.

Phase field method is run between the FE time steps where the initial melting is observed in the selected cross section and where the maximum temperature drops below 70% of the melting temperature (T_L). For this purpose, 200 FE time steps are utilized that are sampled every 20 steps. The time step size for FE simulation was given as $dt = 5e - 6$ s. This time period is further divided into 10000 time steps for the phase field simulation. The time step size for the evolution of the phase field method is chosen internally to be $dt = 2e - 4$, making it effectively $dt = 1e - 7$ s. The spatial is 621 by 411, with 0.1 μ m spatial step size in both directions. Symmetry boundary conditions are used on the top and right edges of the geometry.

The initial phase field is shown in Figure 7.26 in terms of the order parameter p . In order to obtain comparable results between simulations, the meltpool region is assumed to be an ellipsoid, consistent across simulations. Furthermore, the perimeter of the ellipsoid is superimposed with a sine wave function to act as nucleation sites.

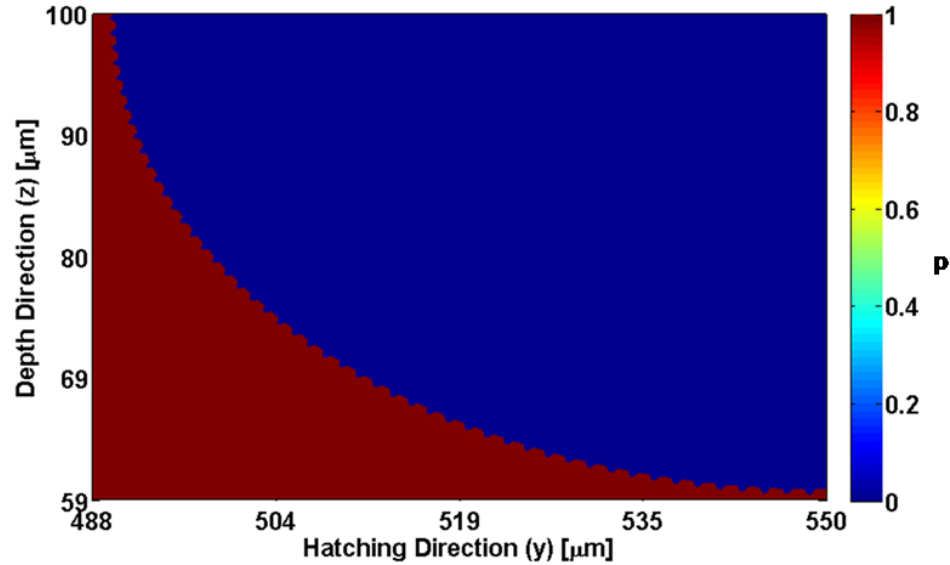


Figure 7.26 Initial phase field. The red region ($p=1$) is solid while the blue region ($p=0$) is liquid.

7.3.2.2 Results and Discussion

Results of the medium and high energy intensity simulations are shown in Figures 7.27 and 7.28, respectively. Both results look very similar, and a quantitative comparison is not possible to be made based on the results. The initialization of the order parameter p results in some solid regions to have lower temperatures than others, which amplifies their growth rate. Note that the heating occurs from the top-right corner of the problem domain, which

corresponds to the center of the laser beam. As the laser beam moves away, the area cools down, initiating solidification. Dendrites are formed according to the temperature field, and the directions indicate the preferred growth direction is towards the y -axis and z -axis, as observed from the SEM images. The release of latent heat during the growth keeps dendrite arms away from each other. Note that the implemented model considers only the solid and liquid phases of the metal.

As future research, additional phases (such as the Ni_3Nb γ'') may be implemented in a binary fashion, and when combined with material diffusion, it can greatly improve the results. Furthermore, the result of the simulation is very sensitive to the parameters shown in Table 7.6, and the problem domain. Rather than forced dendritic growth through the initial conditions, random noise can be added to the system to alter the order parameter.

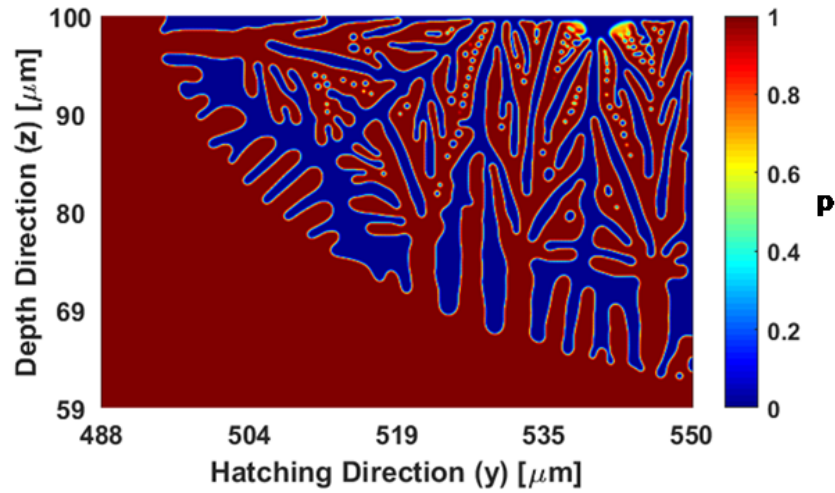


Figure 7.27 Microstructure at the end of the phase field simulation that utilizes the temperature field from the high energy intensity ($P=195$ W, $h=0.1$ mm, $v_s=725$ mm/s) FE simulation.

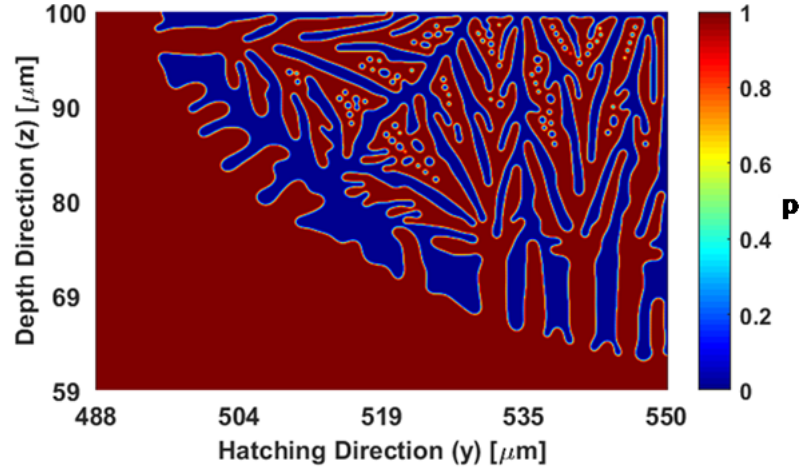


Figure 7.28 Microstructure at the end of the phase field simulation that utilizes the temperature field from the medium energy intensity ($P=195$ W, $h=0.1$ mm, $v_s=800$ mm/s) FE simulation.

CHAPTER 8: CONTRIBUTIONS AND FUTURE WORK

This dissertation focuses on understanding the effects of machining and Selective Laser Melting (SLM) on the surface integrity of certain titanium and nickel based alloys. Chapter 1 contains background information, literature review, methods and formulations that are used in the dissertation. In Chapter 2, machining induced microstructural changes in IN100 nickel-based alloy and Ti-6Al-4V titanium alloy samples are investigated. Hardness measurements are taken from the samples, and Scanning Electron Microscopy (SEM) images obtained from the electropolished or etched surfaces of the samples are analyzed with image processing to determine the average grain sizes and volume fractions of different phases. In Chapter 3, 3D Finite Element Method based process simulations are utilized for machining of IN100 nickel-based and Ti-6Al-4V titanium alloys. Temperatures, strain, and strain-rate fields are predicted. Microstructure with grain sizes resulting from dynamic recrystallization is predicted by employing the Johnson-Mehl-Avrami-Kolmogorov (JMAK) model. In Chapter 4, machine learning based predictive modeling of microhardness and grain size is performed. Non-linear and Random Forests regression models are created to capture the relationships between temperature, machining parameters, hardness and grain sizes. In Chapter 5, multi-objective machining parameter optimization is performed to maximize the productivity, minimize the machining temperature and minimize the grain size alterations in the workpiece, using Genetic Algorithms. Grain size measurements from SEM images and temperature fields from FE simulations are fitted to regression models which are then utilized as objective functions. Furthermore, parameters for the existing JMAK equation based microstructural model are identified using an optimization scheme based on grain size prediction results extracted

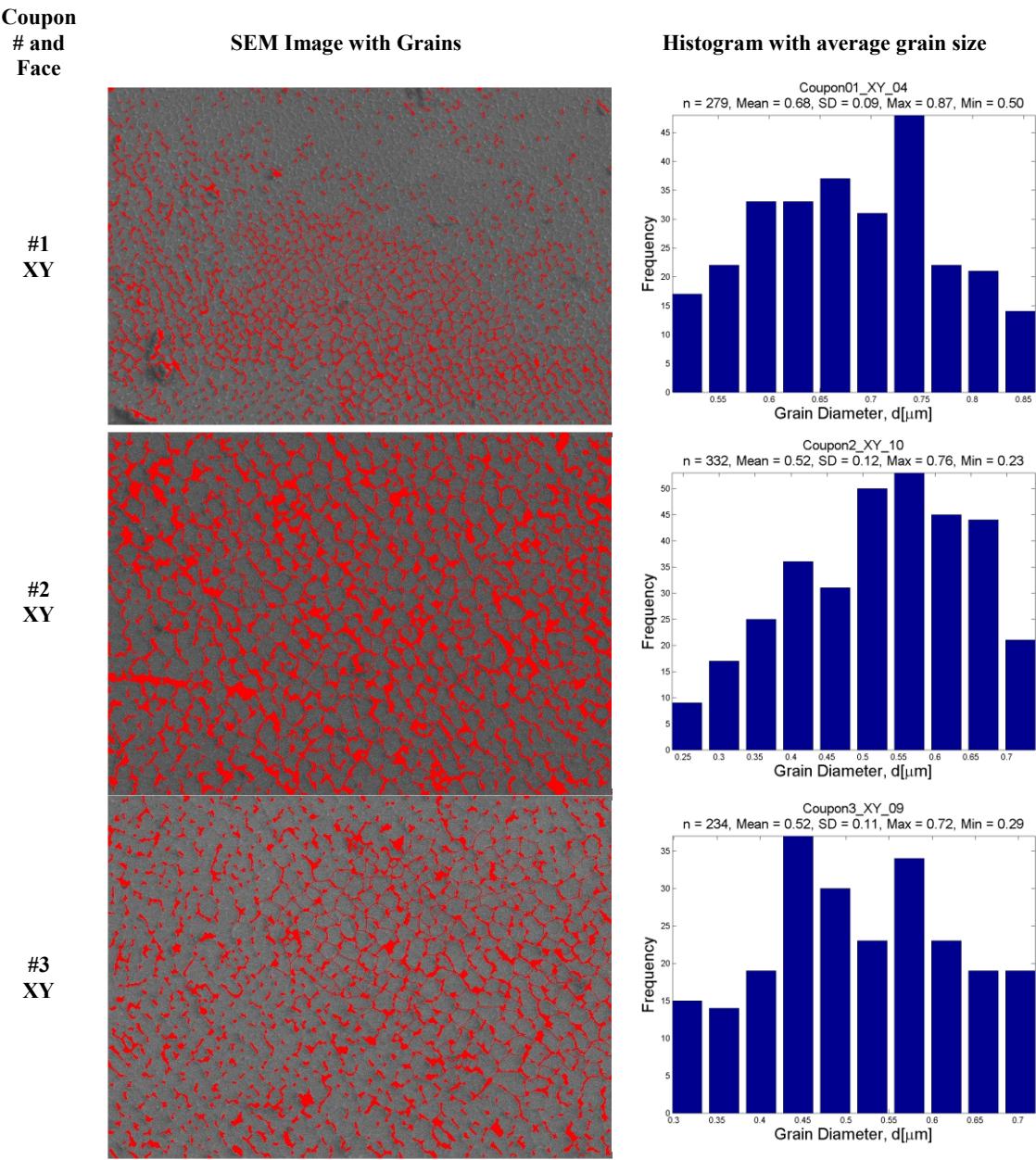
from FE simulations and compared against measured grain sizes. In Chapter 6, microstructure in SLM processing of IN625 nickel alloy is investigated. Processed coupons are analyzed with SEM and image processing to reveal grain sizes and growth directions. Using an in-situ thermal camera recording, the spattering phenomenon is quantified, meltpool sizes are identified and heating/cooling rates are determined. Finally, in Chapter 7, computational modeling of the SLM process is performed with in-house developed 3D FEM for thermal field solution and 2D Phase Field method for localized solidification investigation.

The experimental and computational work presented in this dissertation is multidisciplinary in nature, spanning computational science, materials science, statistics, industrial and manufacturing engineering areas. Therefore, many opportunities for improvement exist as future research. More detailed and different experiments can be done to learn more about the underlying physics and the effects of these processes on surface integrity and microstructural changes. For instance, using the SLM processed coupons, hardness measurements can be taken to reveal the effect of processing parameters on the mechanical properties of the part, or X-Ray Diffraction analysis can be performed to reveal the crystal orientations. Capabilities of the computational models can also be enhanced. Machining simulations can also be improved to account for static and meta-dynamic recrystallization, as well as grain growth. In SLM modeling, spattering can be implemented physically, or stochastically with the use of in-situ thermal recordings. More advanced phase field models can be utilized to predict the solidification microstructure globally and

more accurately, and perform optimization of the microstructure in critical (stress-bearing) locations of the part.

APPENDIX A: MICROSTRUCTURAL ANALYSIS - GRAIN SIZE MEASUREMENTS

Figure A.1 Grain size analysis of SLM processed IN625 coupons.

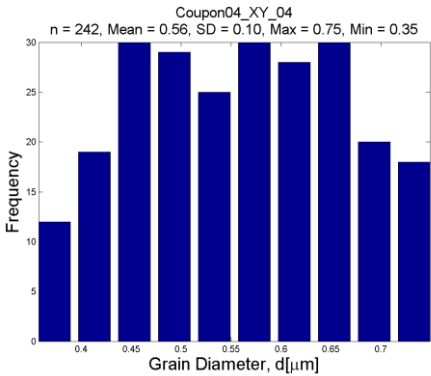
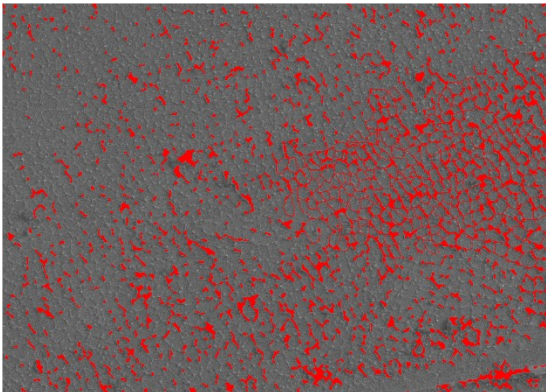


Coupon
and
Face

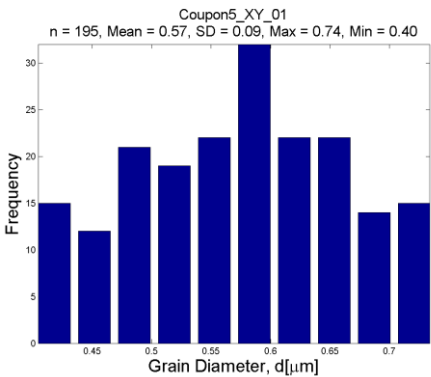
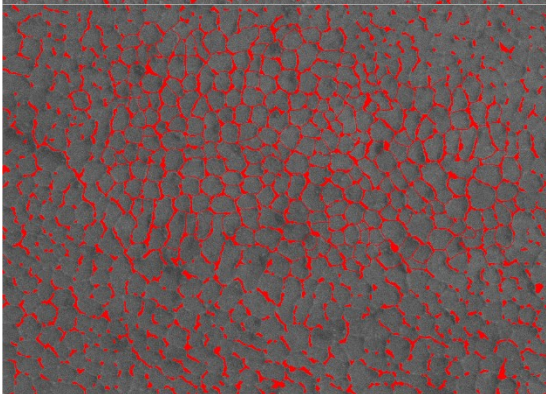
SEM Image with Grains

Histogram with average grain size

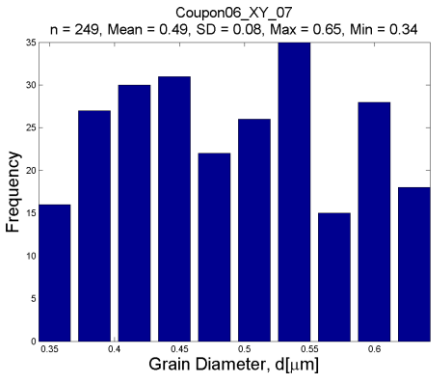
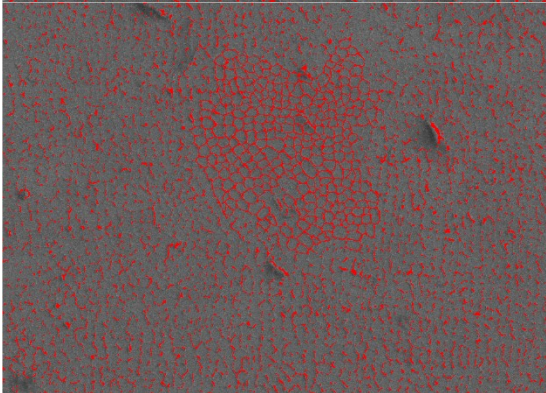
#4
XY



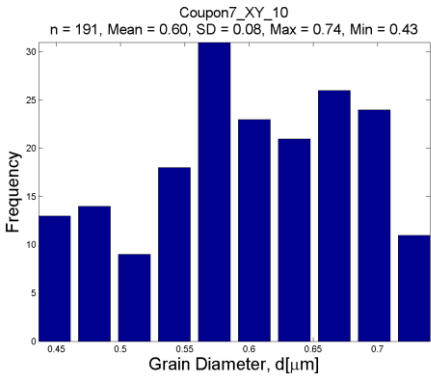
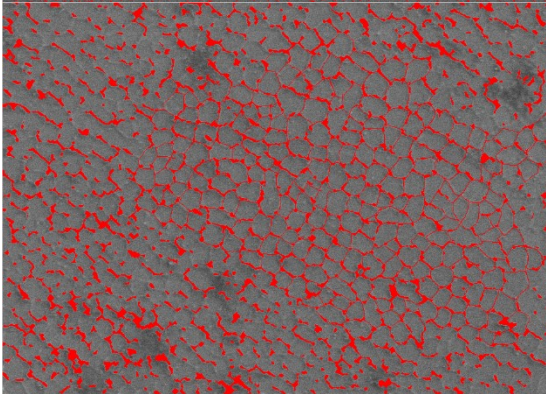
#5
XY



#6
XY



#7
XY

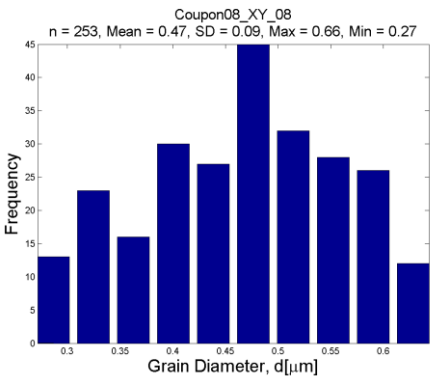
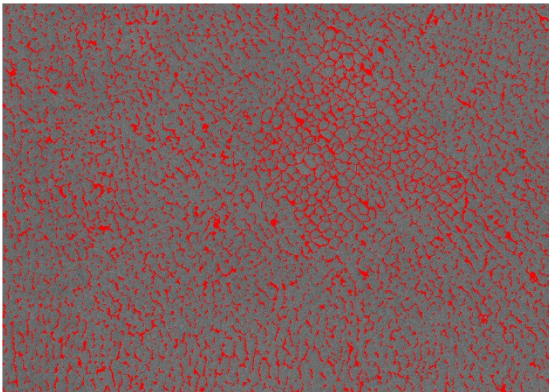


Coupon
and
Face

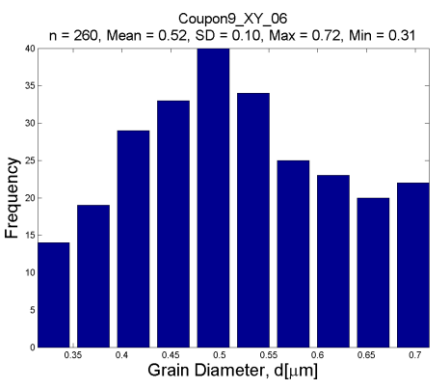
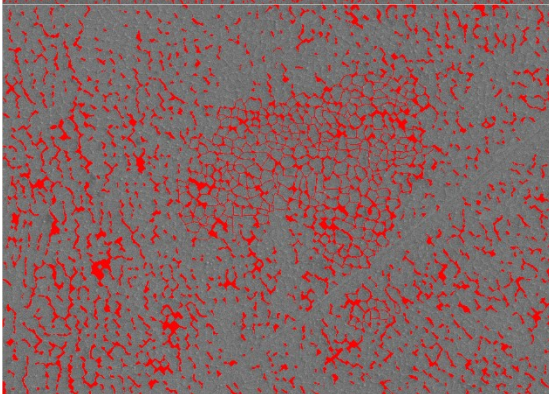
SEM Image with Grains

Histogram with average grain size

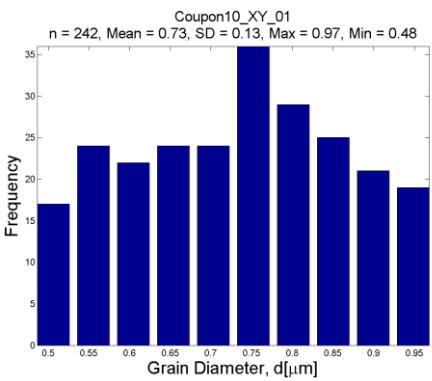
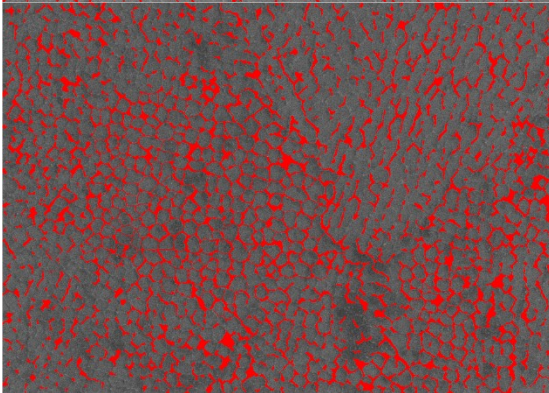
#8
XY



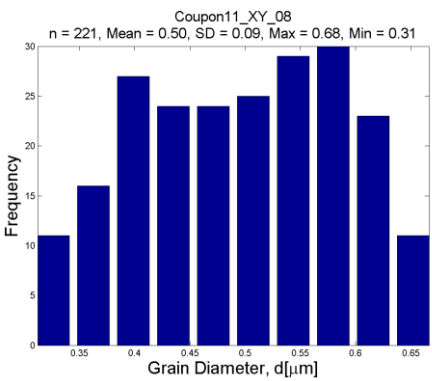
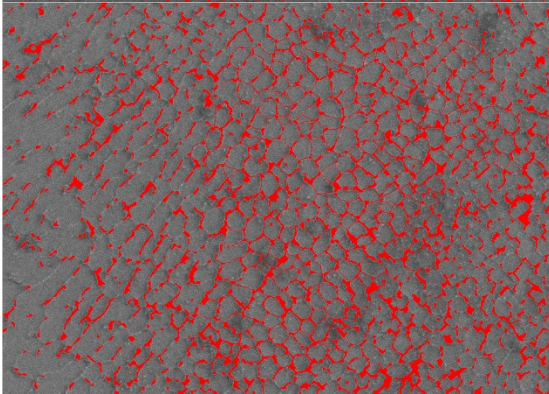
#9
XY



#10
XY



#11
XY

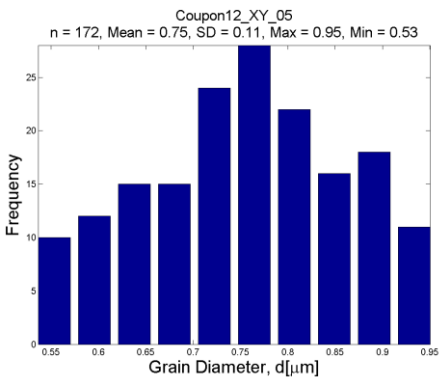
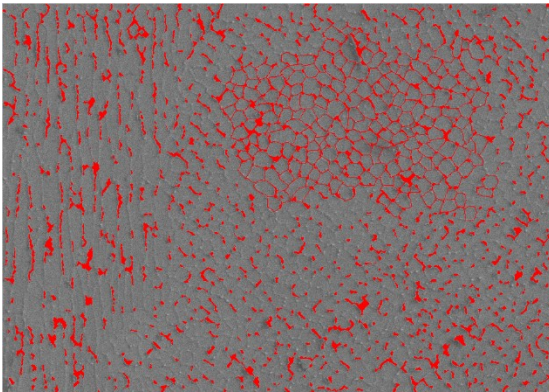


Coupon
and
Face

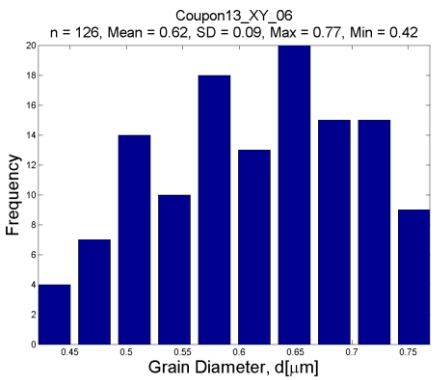
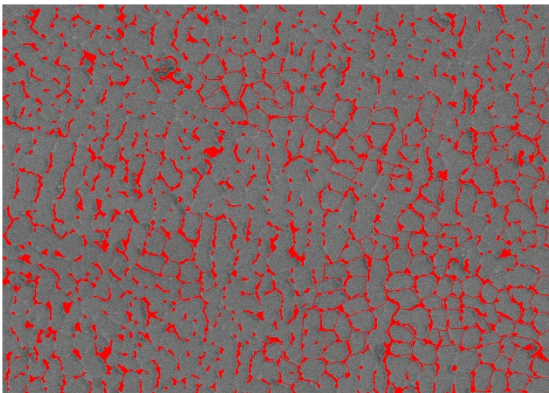
SEM Image with Grains

Histogram with average grain size

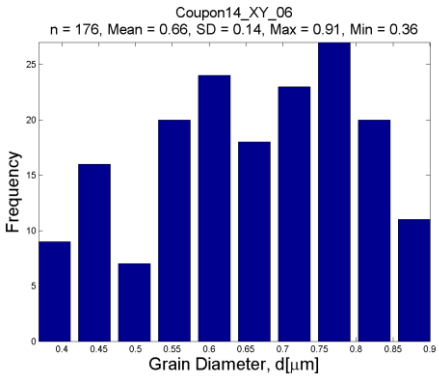
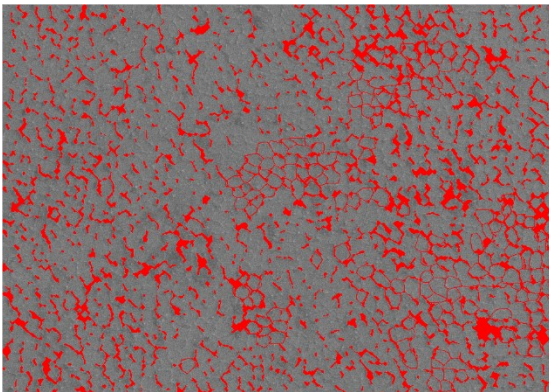
#12
XY



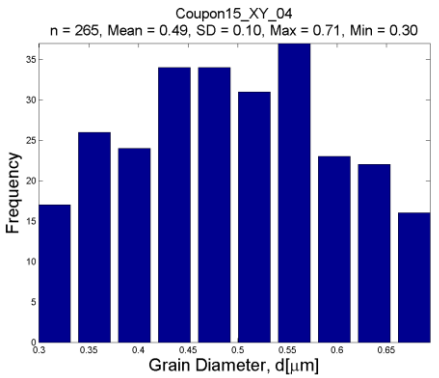
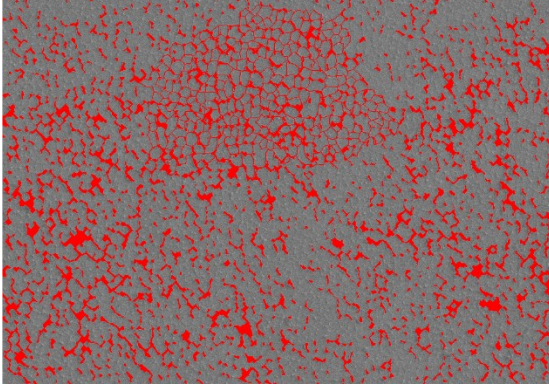
#13
XY



#14
XY



#15
XY

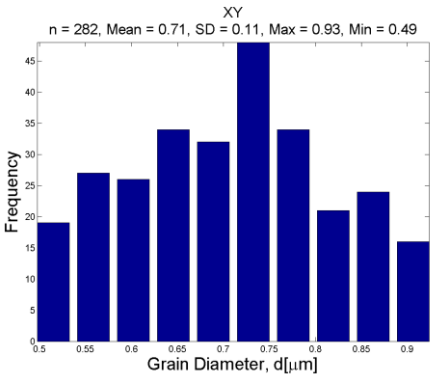
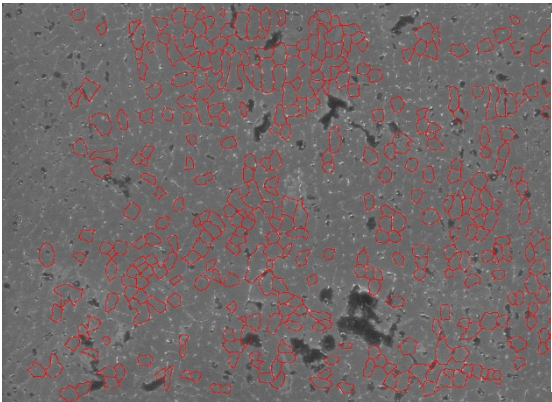


Coupon
and
Face

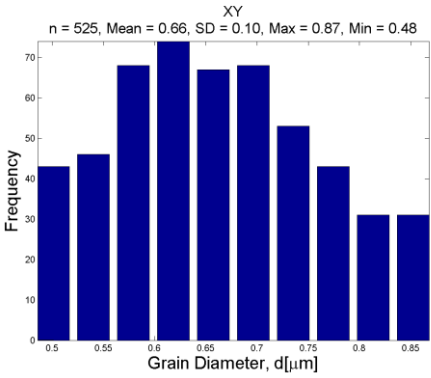
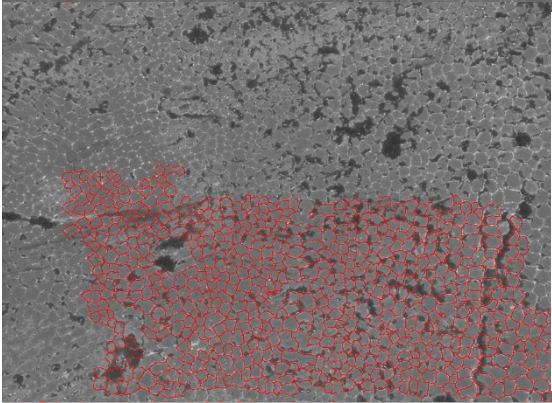
SEM Image with Grains

Histogram with average grain size

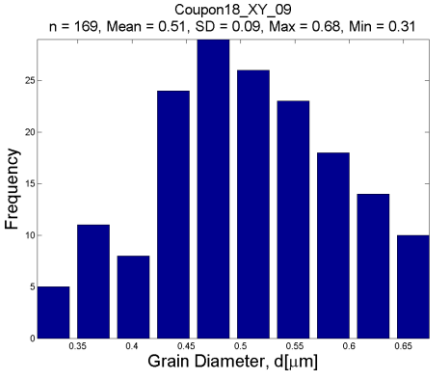
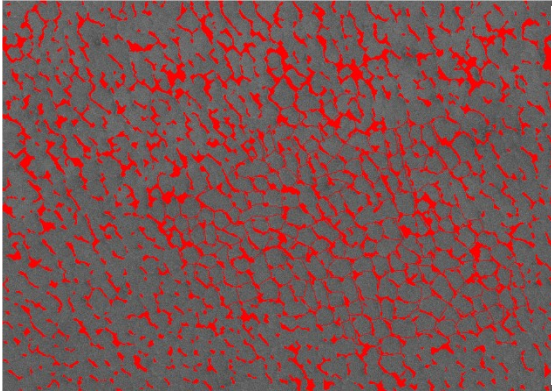
#16
XY



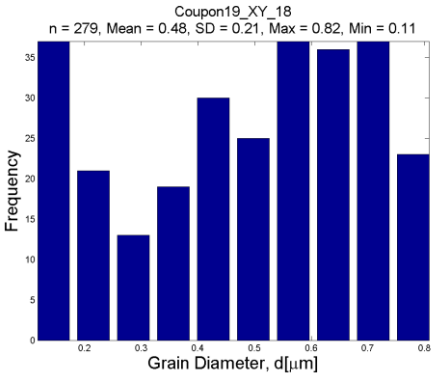
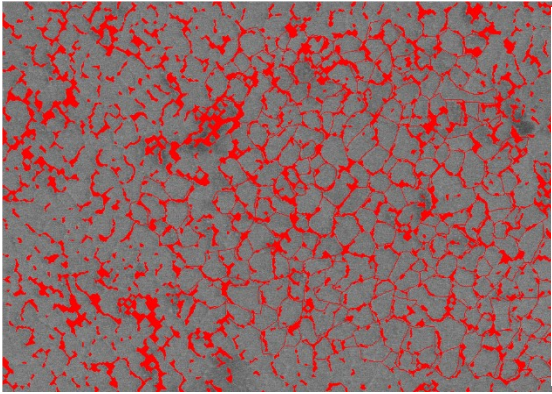
#17
XY



#18
XY



#19
XY

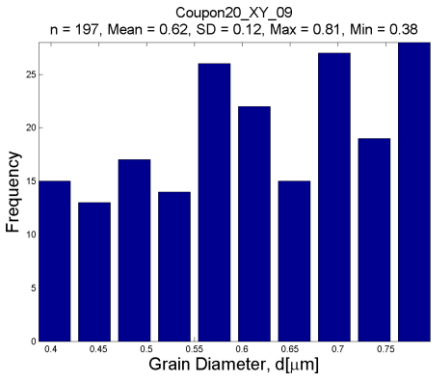
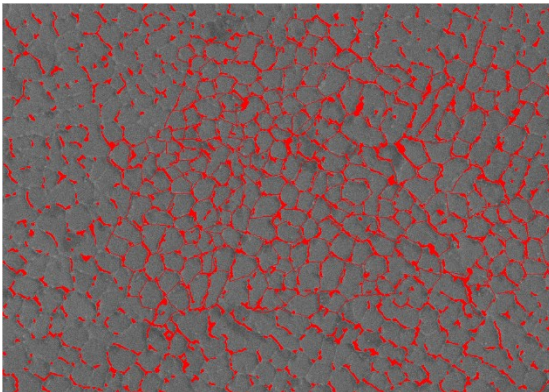


Coupon
and
Face

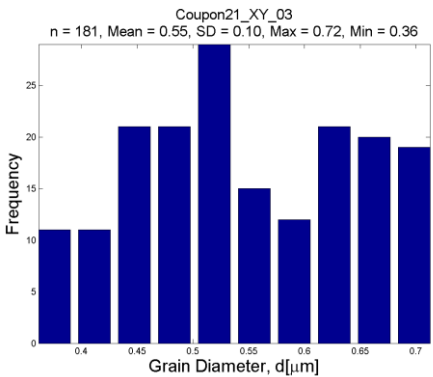
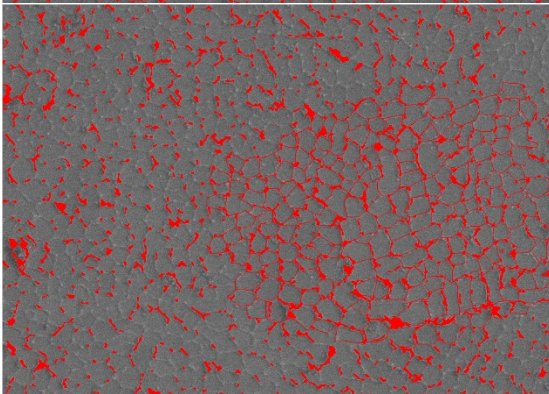
SEM Image with Grains

Histogram with average grain size

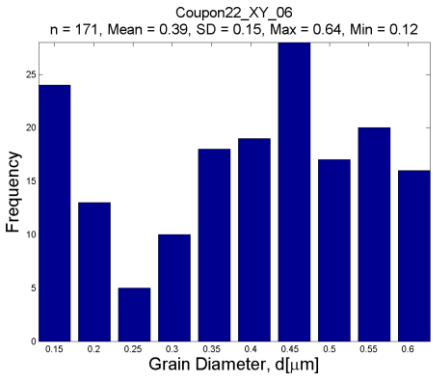
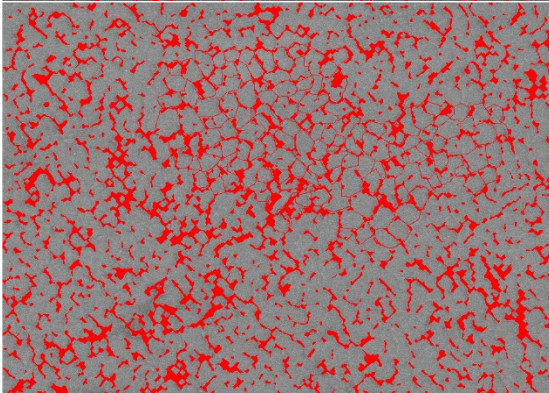
#20
XY



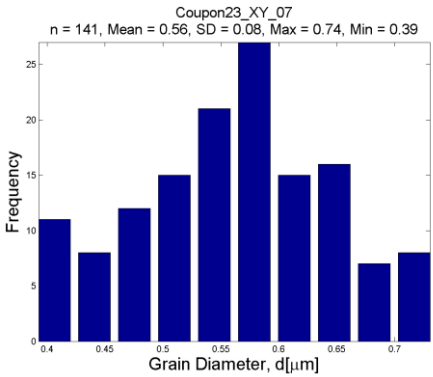
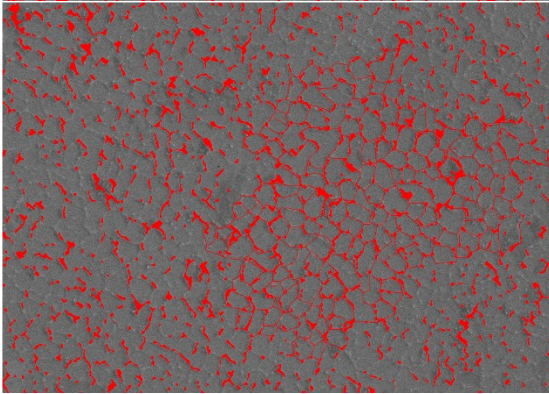
#21
XY



#22
XY



#23
XY

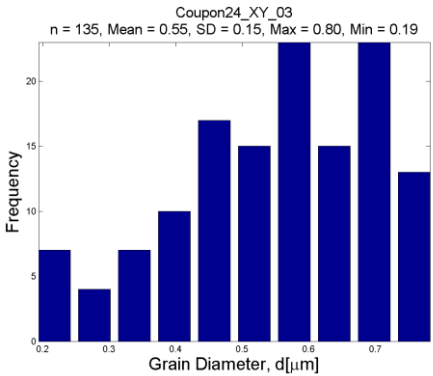
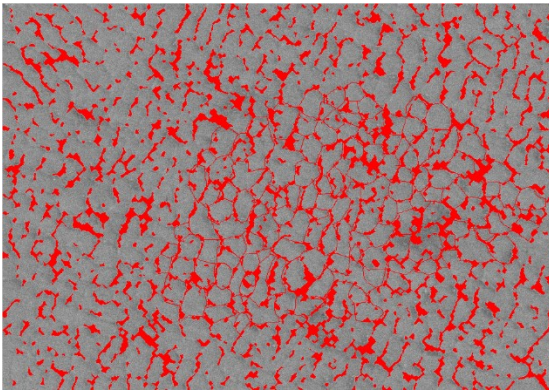


Coupon
and
Face

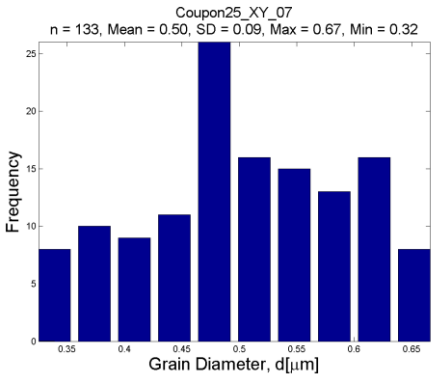
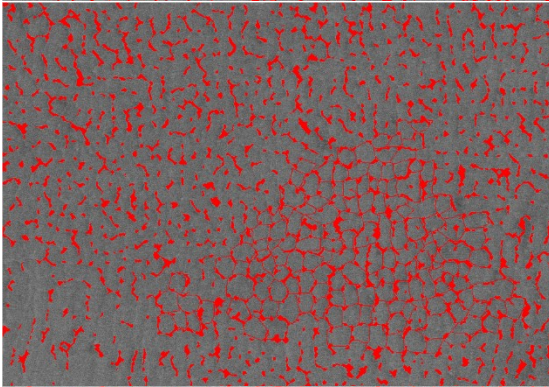
SEM Image with Grains

Histogram with average grain size

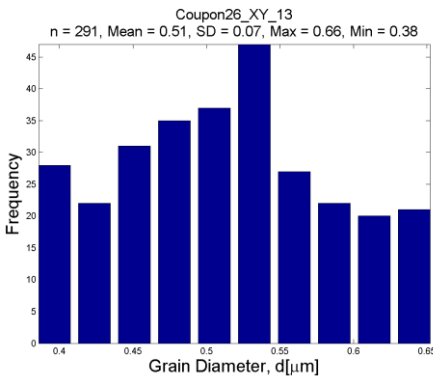
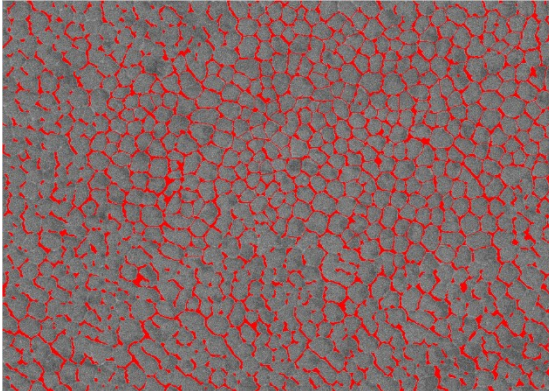
#24
XY



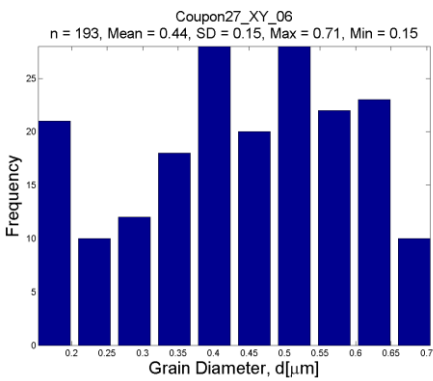
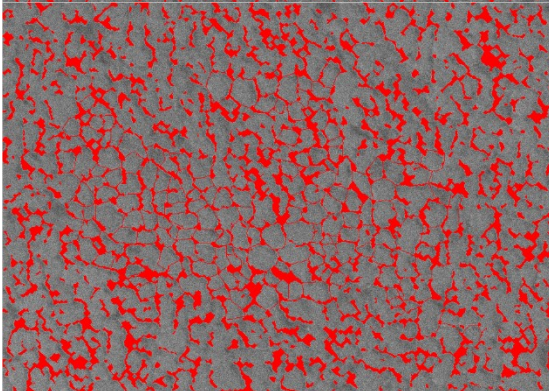
#25
XY



#26
XY



#27
XY

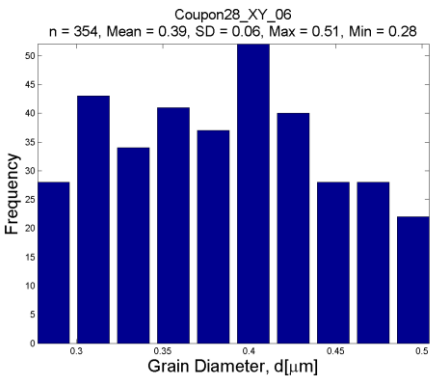
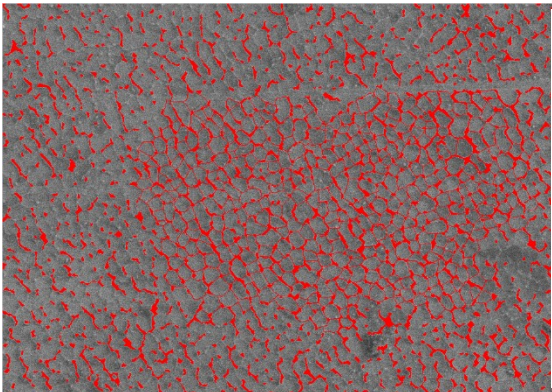


Coupon
and
Face

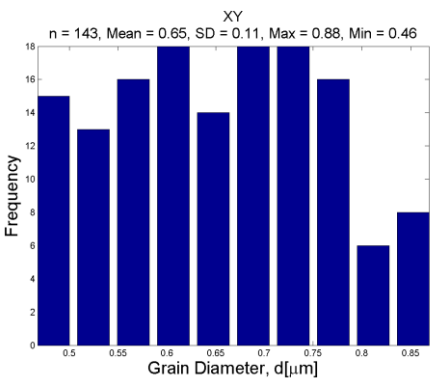
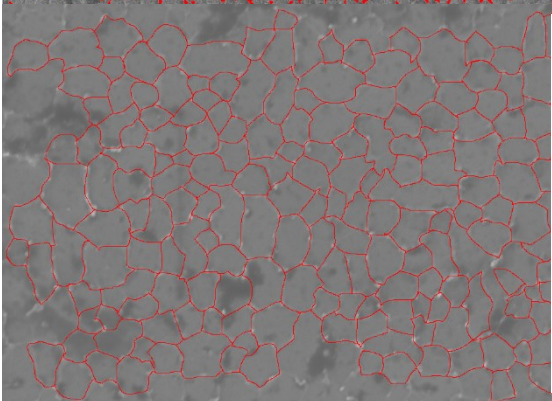
SEM Image with Grains

Histogram with average grain size

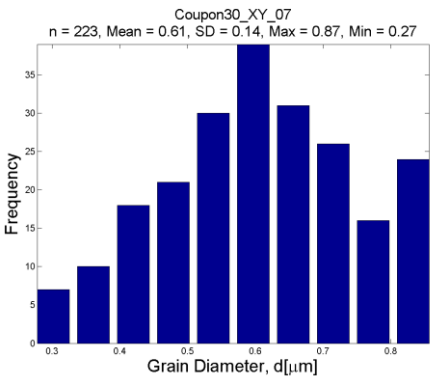
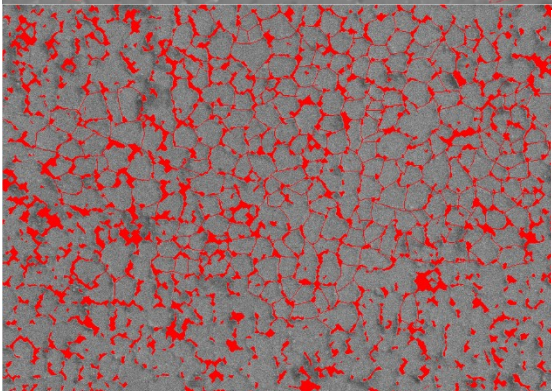
#28
XY



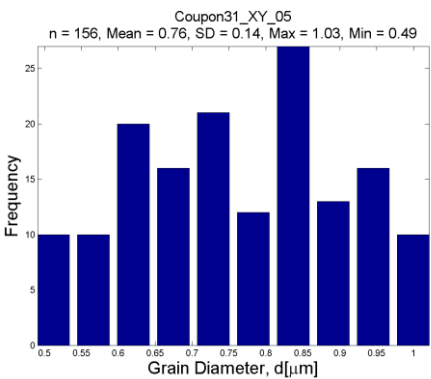
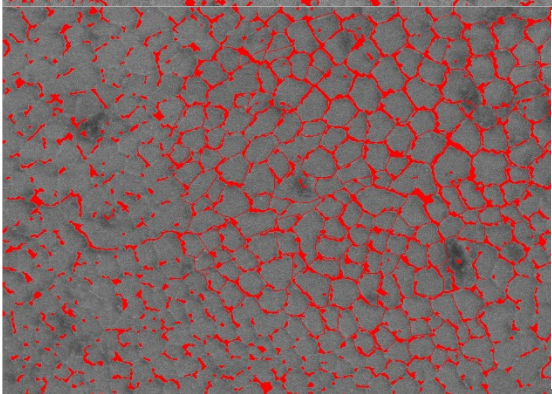
#29
XY



#30
XY

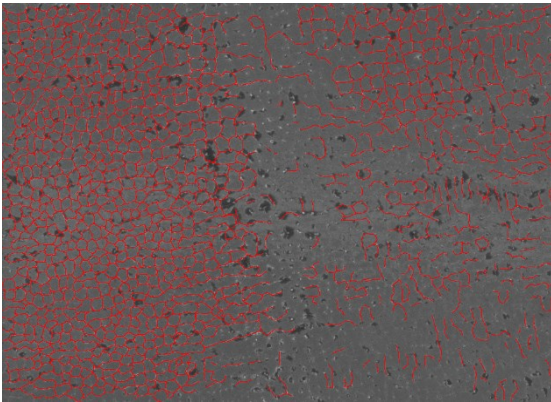


#31
XY



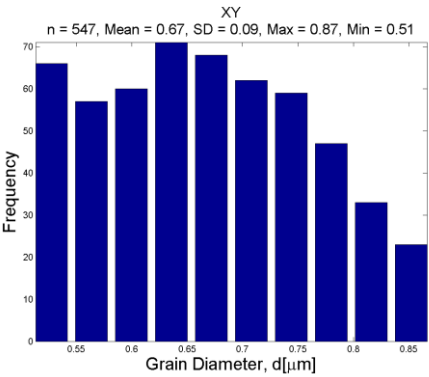
Coupon
and
Face

SEM Image with Grains



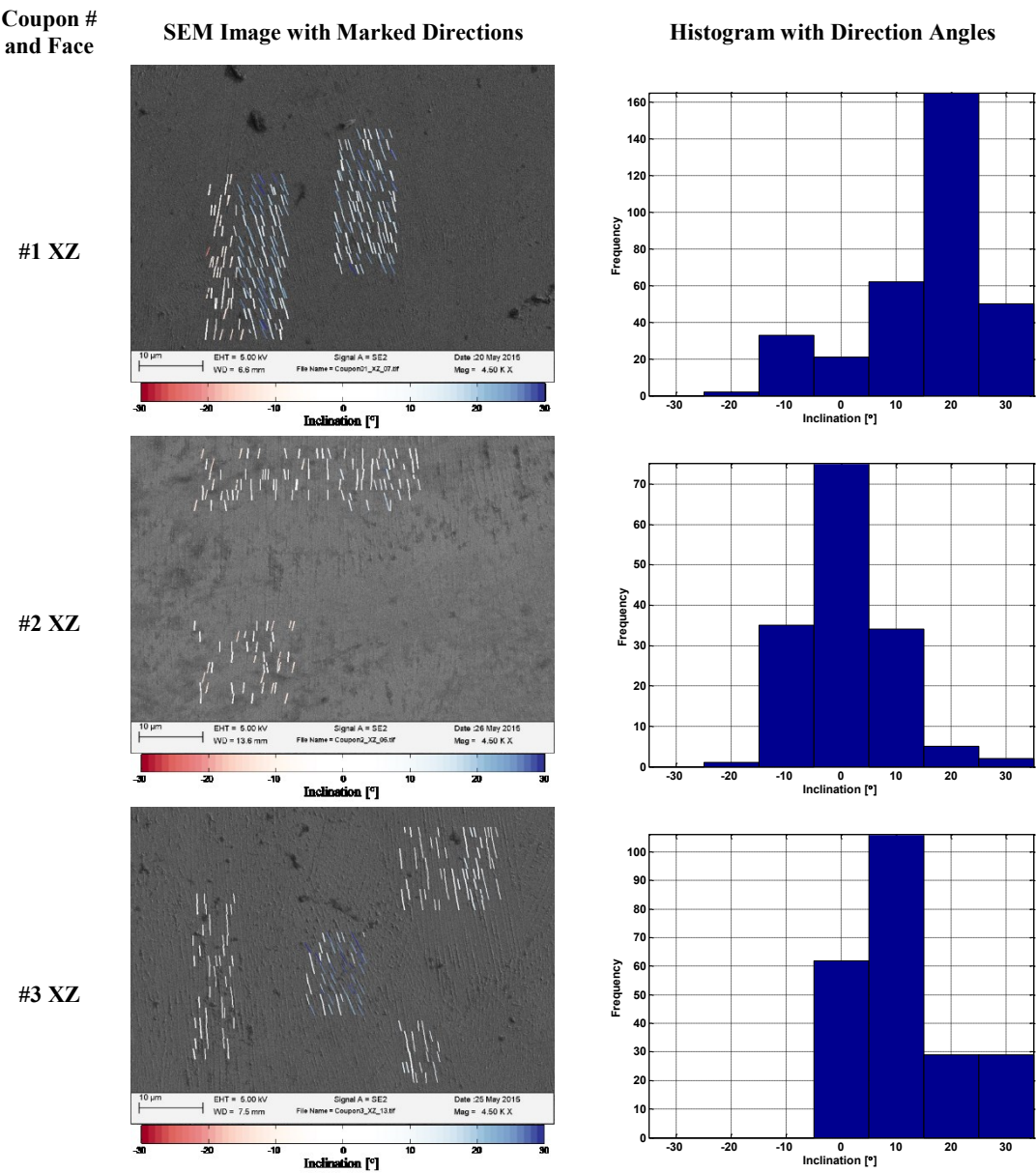
#35
XY

Histogram with average grain size



APPENDIX B: MICROSTRUCTURAL ANALYSIS - GRAIN GROWTH
DIRECTION MEASUREMENTS

Figure B.1 Growth directions and histograms of inclination angles for all IN 625 test coupons.

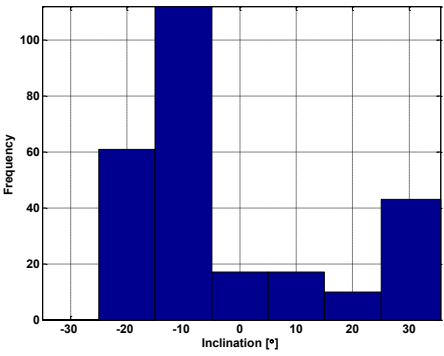
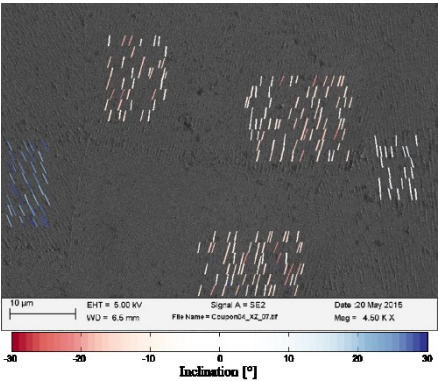


Coupon #
and Face

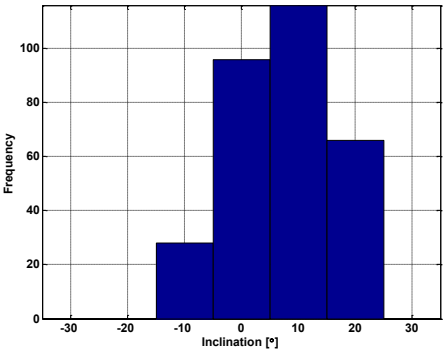
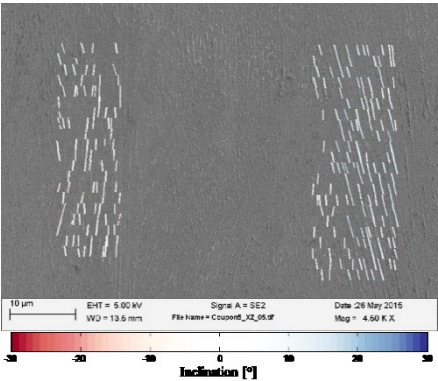
SEM Image with Marked Directions

Histogram with Direction Angles

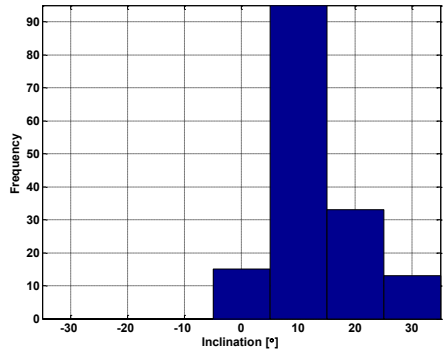
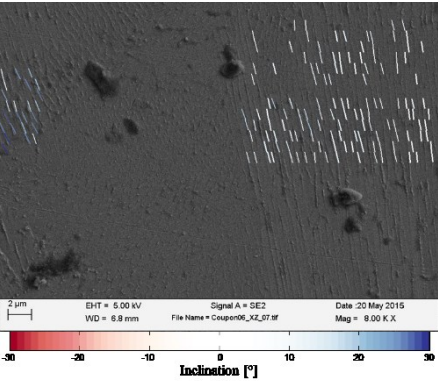
#4 XZ



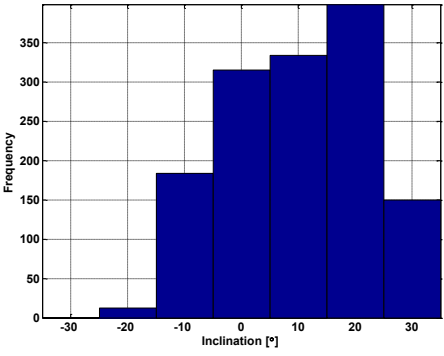
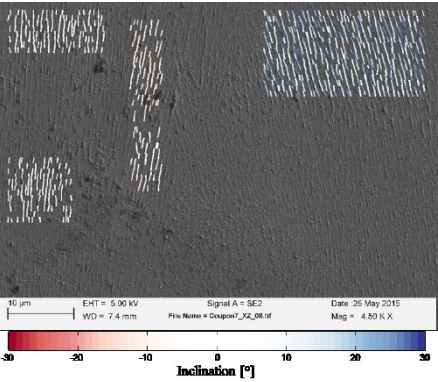
#5 XZ



#6 XZ



#7 XZ

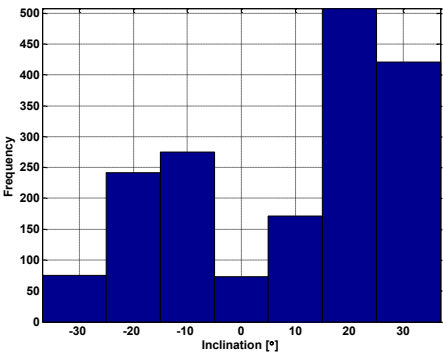
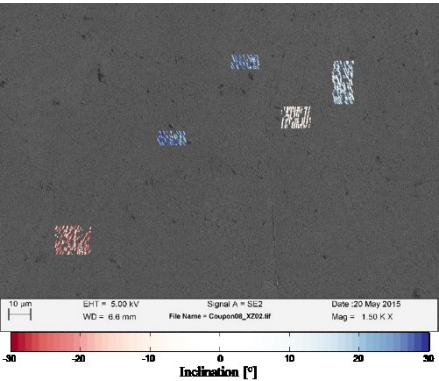


Coupon #
and Face

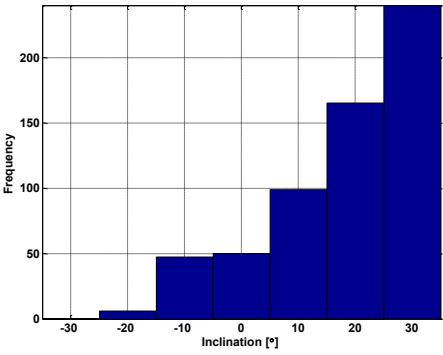
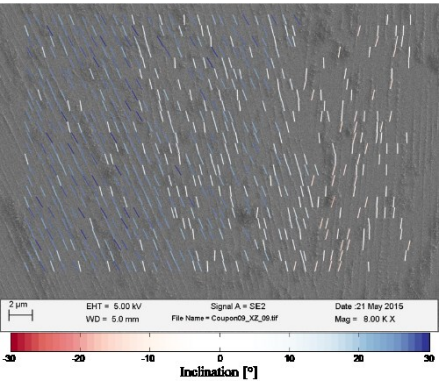
SEM Image with Marked Directions

Histogram with Direction Angles

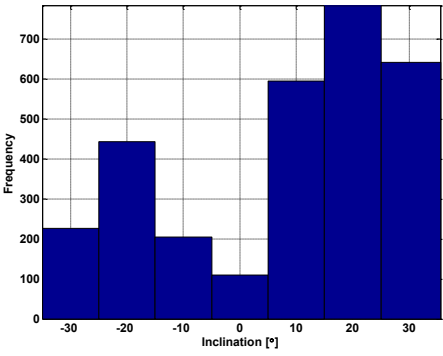
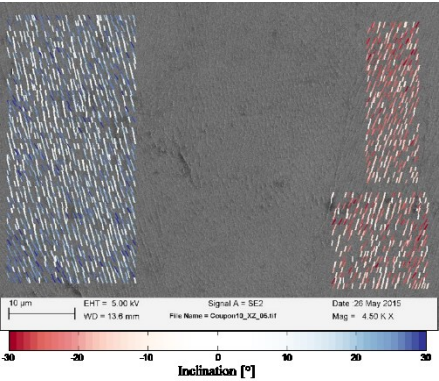
#8 XZ



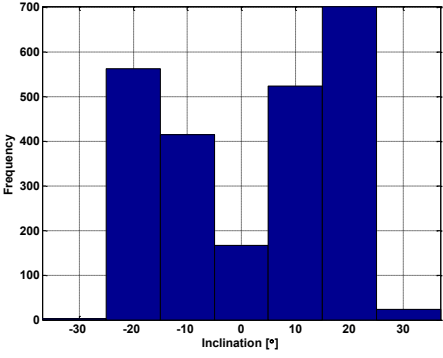
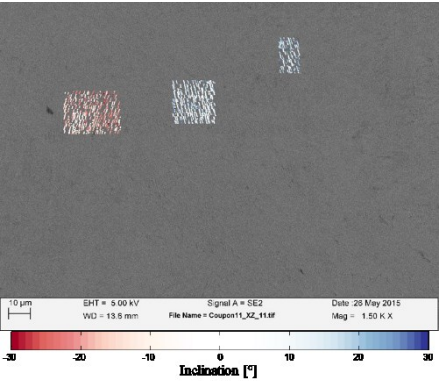
#9 XZ



#10 XZ



#11 XZ

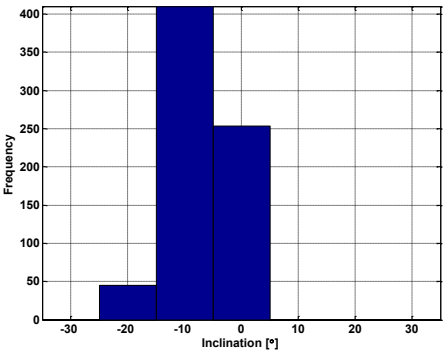
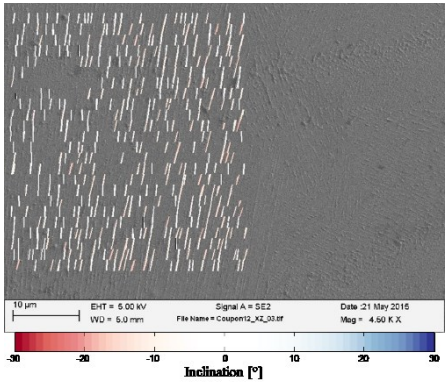


Coupon #
and Face

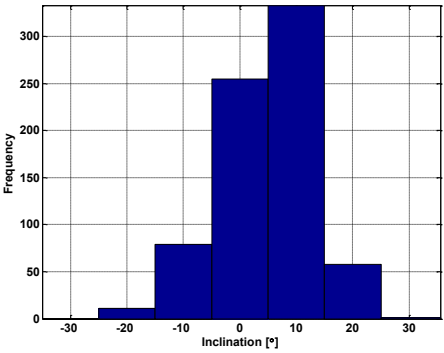
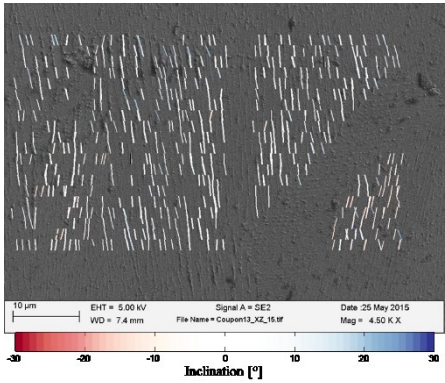
SEM Image with Marked Directions

Histogram with Direction Angles

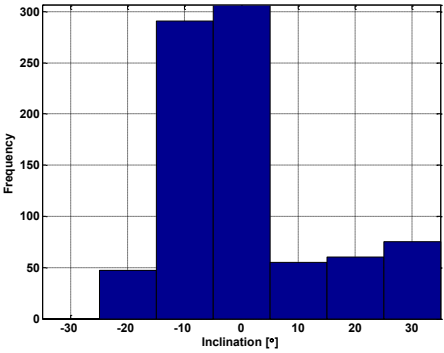
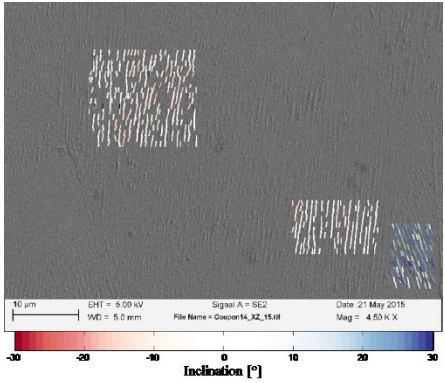
#12 XZ



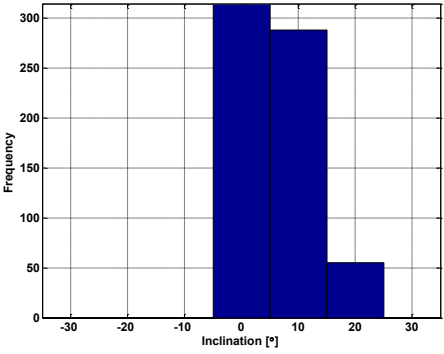
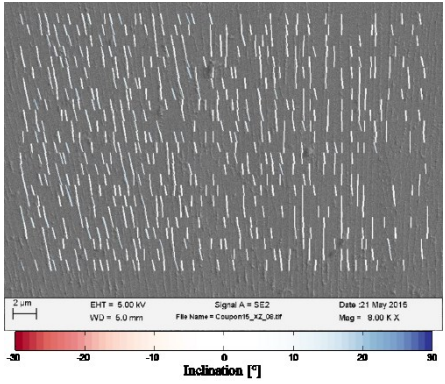
#13 XZ



#14 XZ



#15 XZ

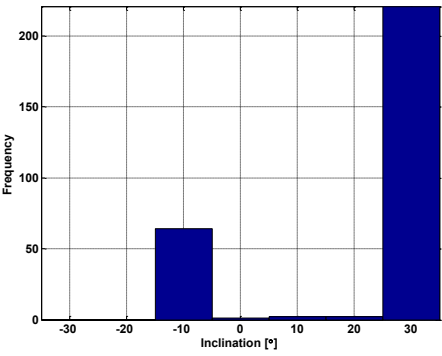
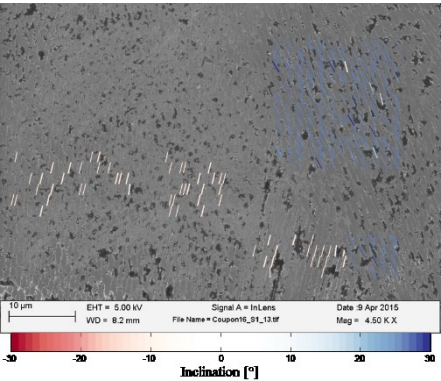


Coupon #
and Face

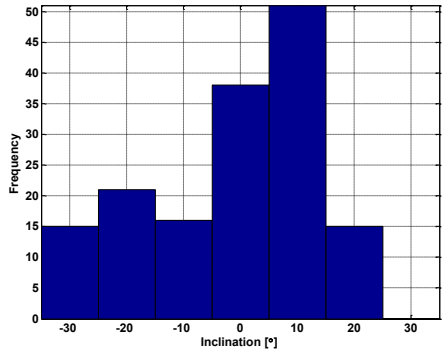
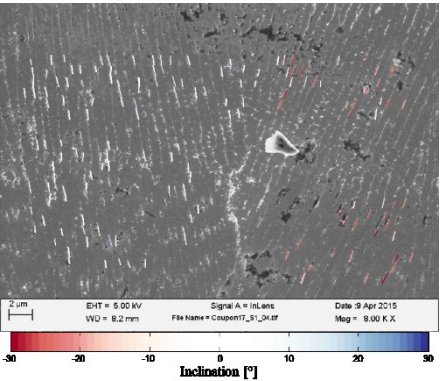
SEM Image with Marked Directions

Histogram with Direction Angles

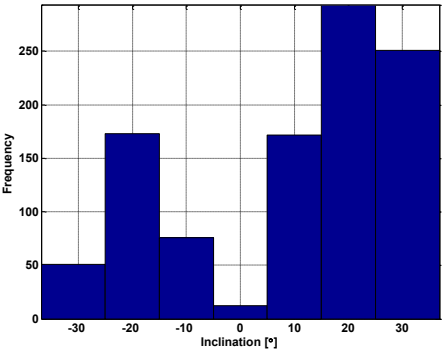
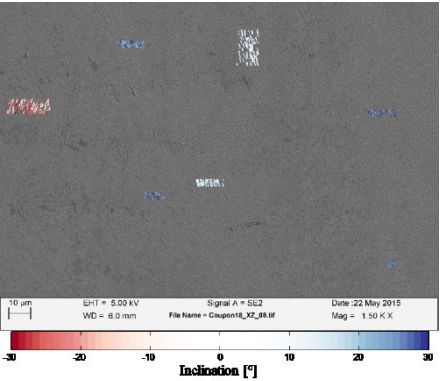
#16 XZ



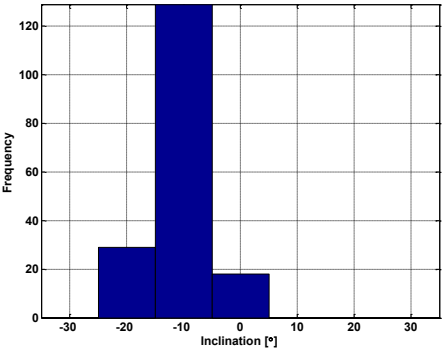
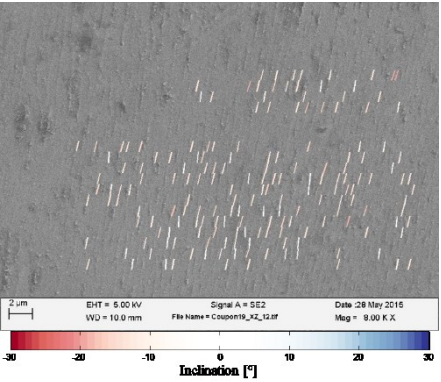
#17 XZ



#18 XZ



#19 XZ

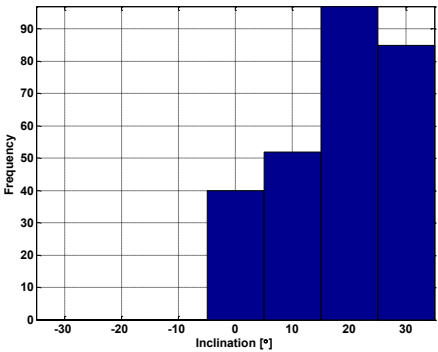
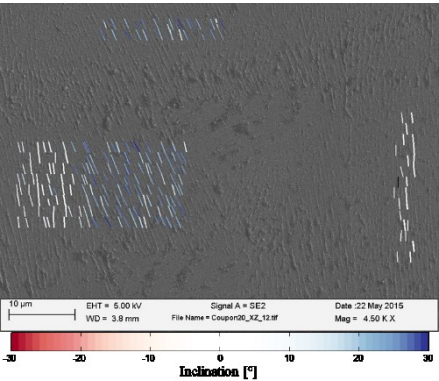


Coupon #
and Face

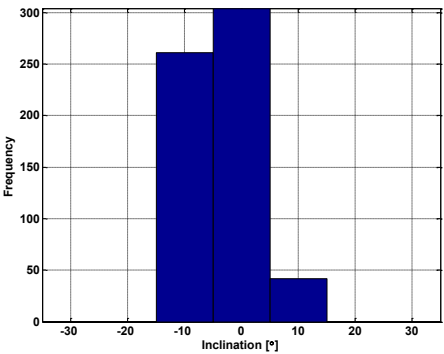
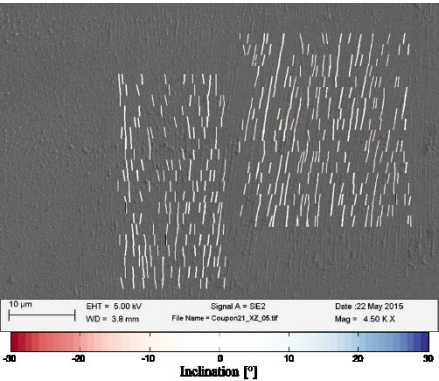
SEM Image with Marked Directions

Histogram with Direction Angles

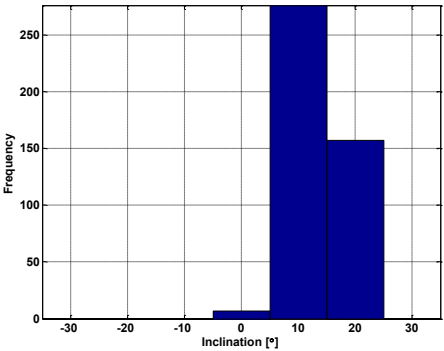
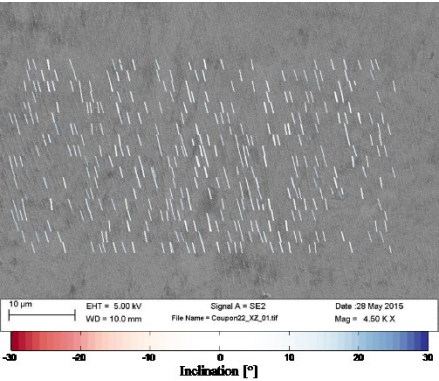
#20 XZ



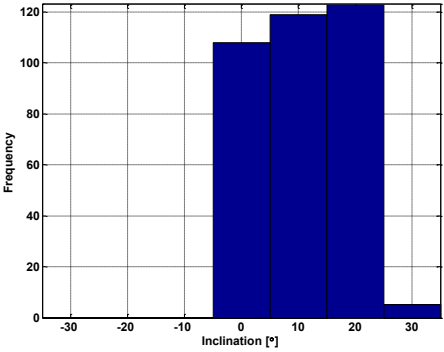
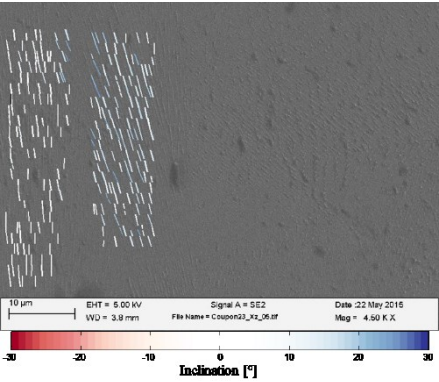
#21 XZ



#22 XZ



#23 XZ

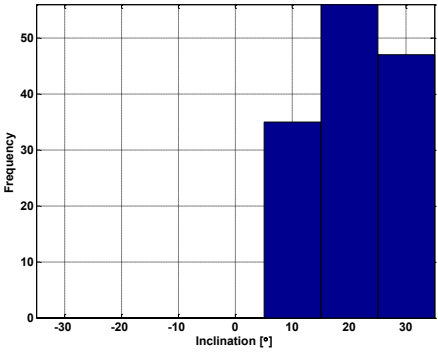
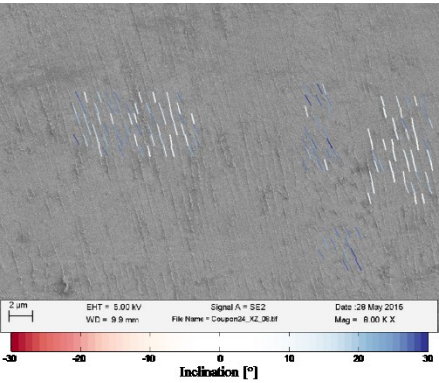


Coupon #
and Face

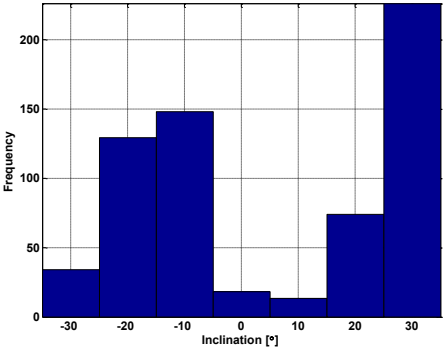
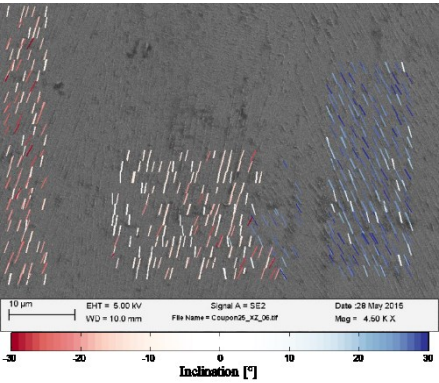
SEM Image with Marked Directions

Histogram with Direction Angles

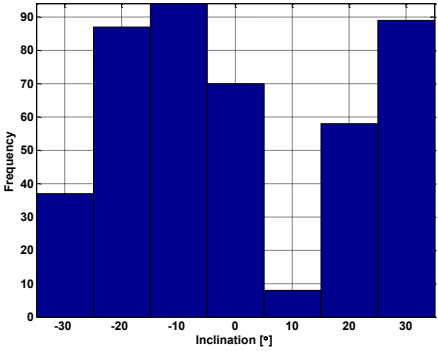
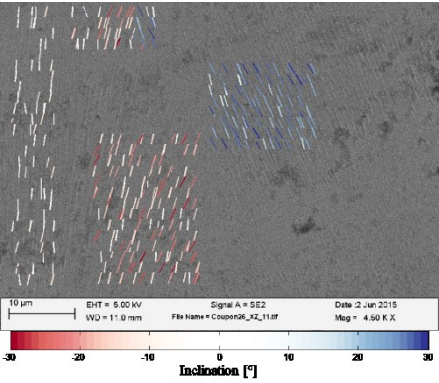
#24 XZ



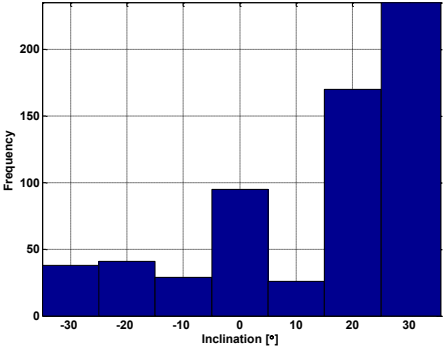
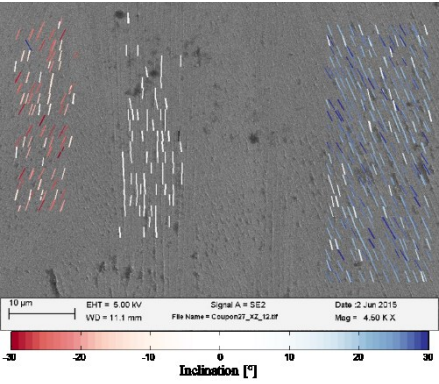
#25 XZ



#26 XZ



#27 XZ

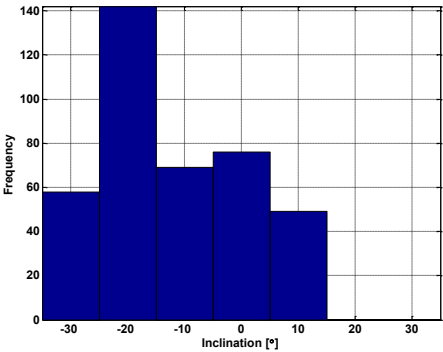
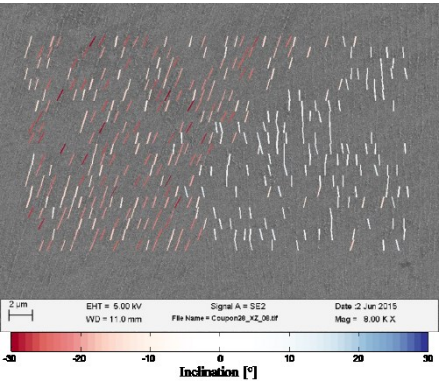


Coupon #
and Face

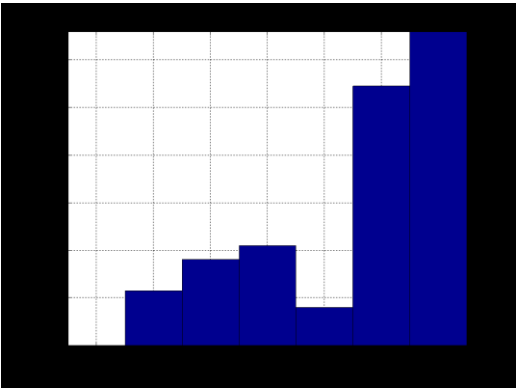
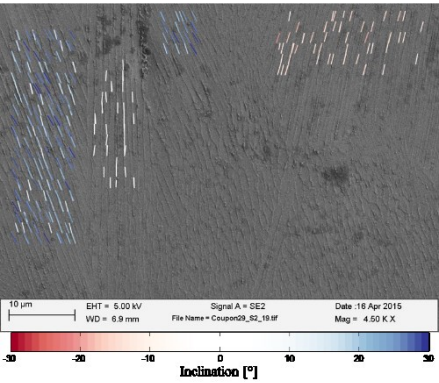
SEM Image with Marked Directions

Histogram with Direction Angles

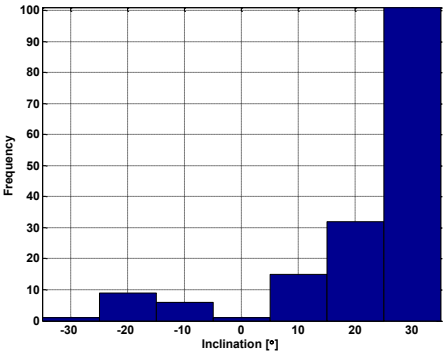
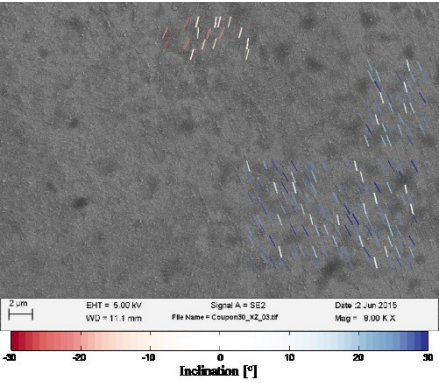
#28 XZ



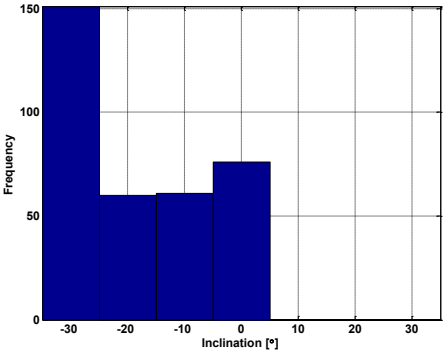
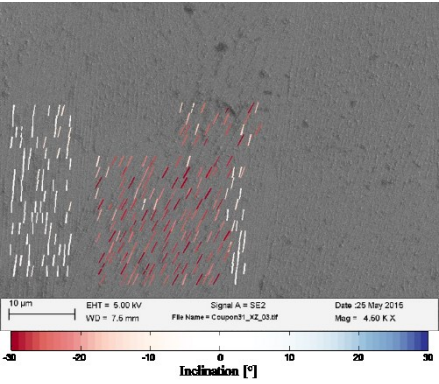
#29 YZ



#30 XZ



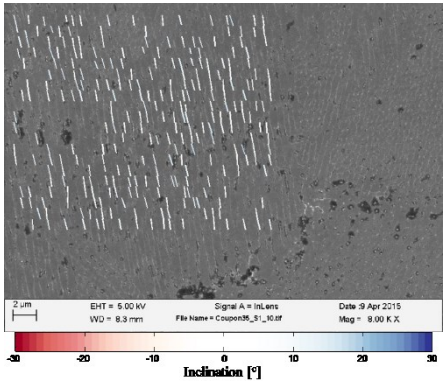
#31 XZ



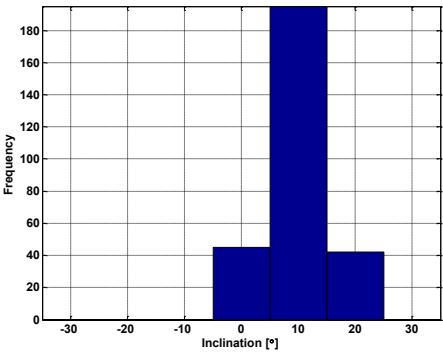
Coupon #
and Face

SEM Image with Marked Directions

#35 XZ



Histogram with Direction Angles



APPENDIX C: OPTICAL IMAGE ANALYSIS

Table C.1 Meltpool width measurements with optical microscopy.

Coupon #	Laser Power P [W]	Scanning Velocity v_s [mm/s]	Hatch Distance h [mm]	Type I Width [μm]	Type II Width [μm]	Average Width [μm]
1	169	875	0.1	134	92	113
4	195	875	0.1	170	111	135
6	182	875	0.09	149	101	128
8	182	725	0.11	153	107	130
9	195	800	0.11	143	109	128
12	182	725	0.09	134	113	126
14	182	800	0.1	132	109	121
15	182	800	0.1	128	105	119
16	195	725	0.1	152	114	133
17	182	800	0.1	143	112	127
18	182	875	0.11	134	110	126
20	169	725	0.1	159	106	136
21	169	800	0.09	154	107	131
23	169	800	0.11	150	96	120
29	195	800	0.09	149	103	128
35	195	800	0.1	155	112	128

APPENDIX D: THERMAL IMAGE ANALYSIS

Figure D.1 Thermal images for track #1.

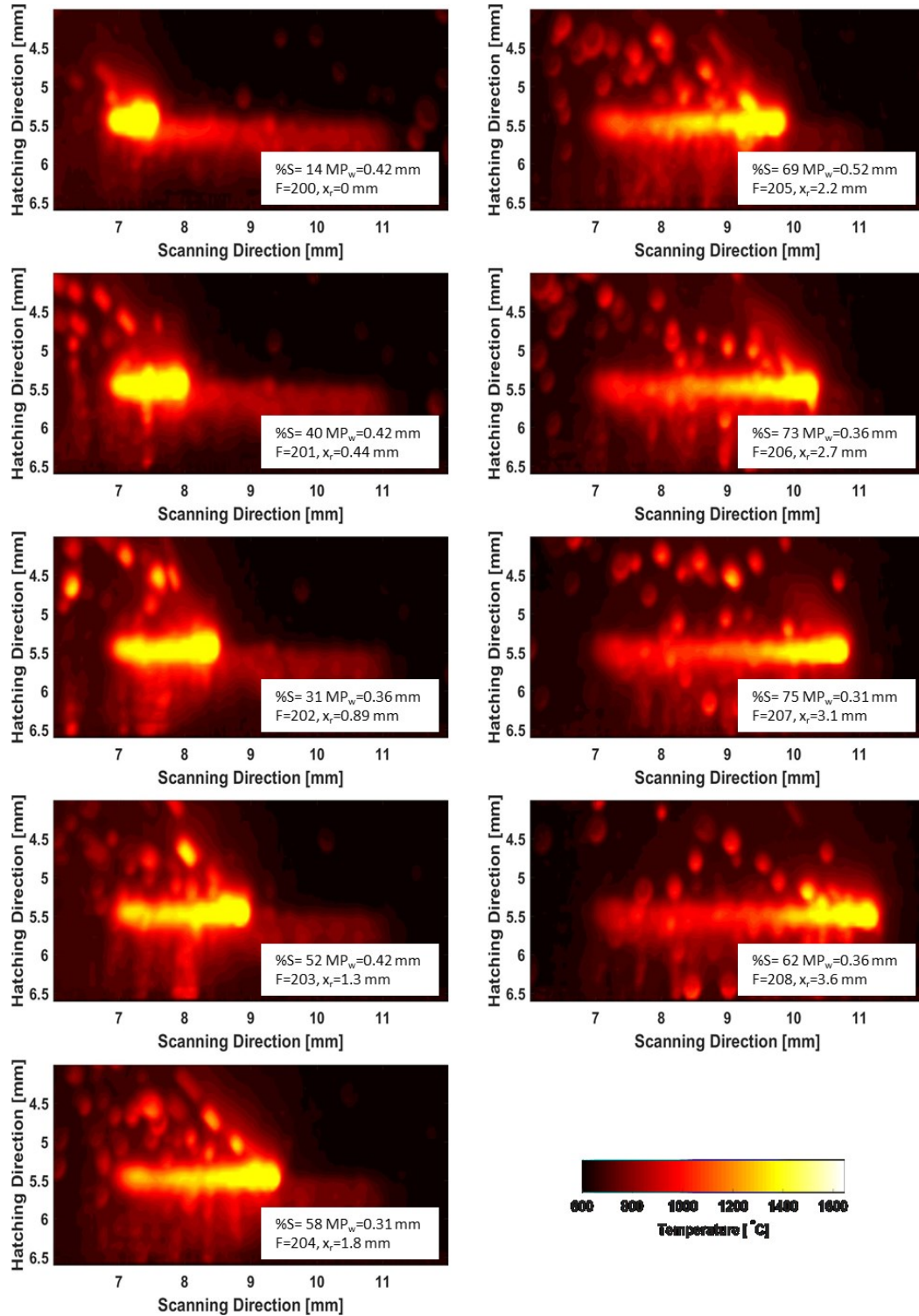


Figure D.2 Thermal images for track #2.

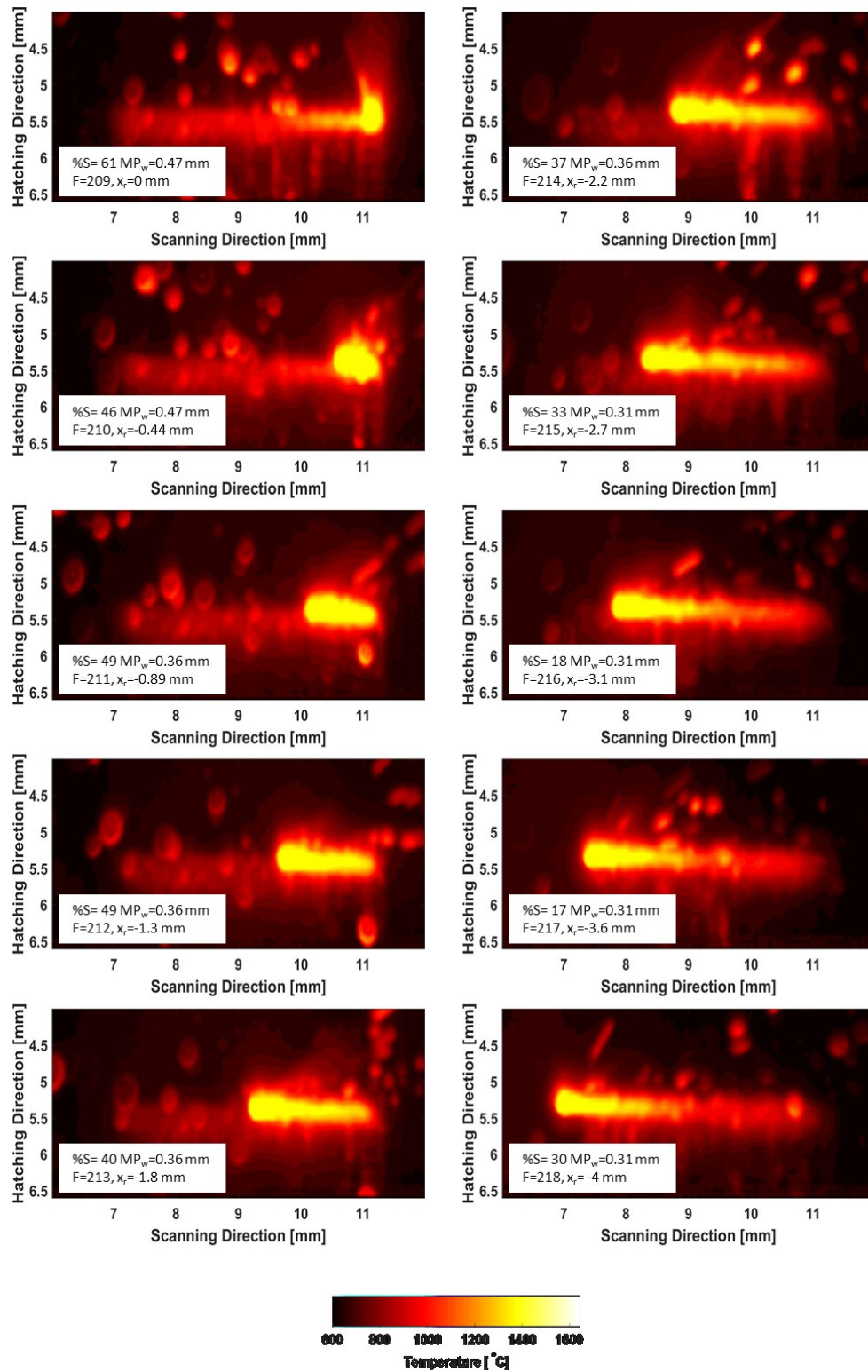


Figure D.3 Thermal images for track #3.

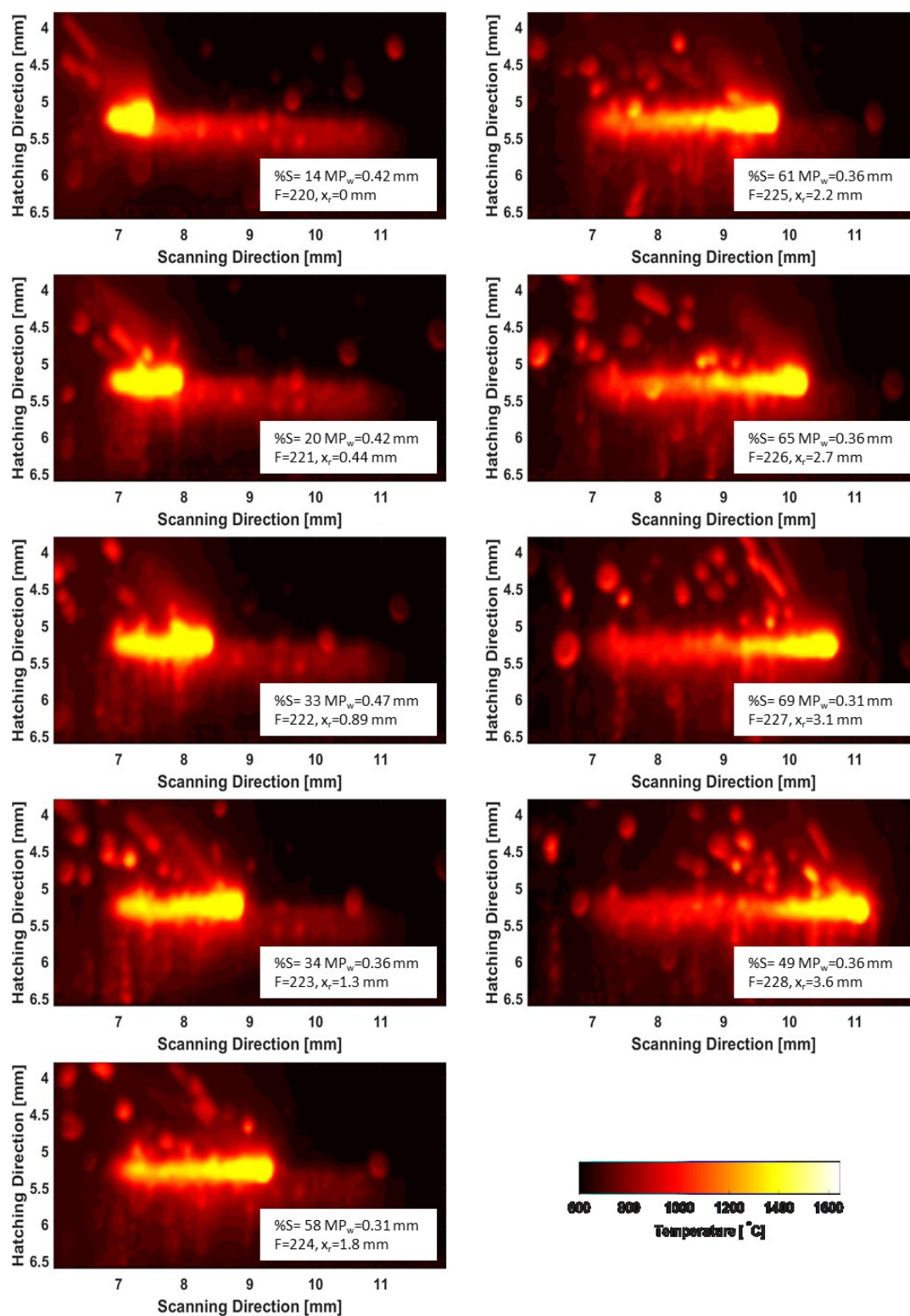


Figure D.4 Thermal images for track #4.

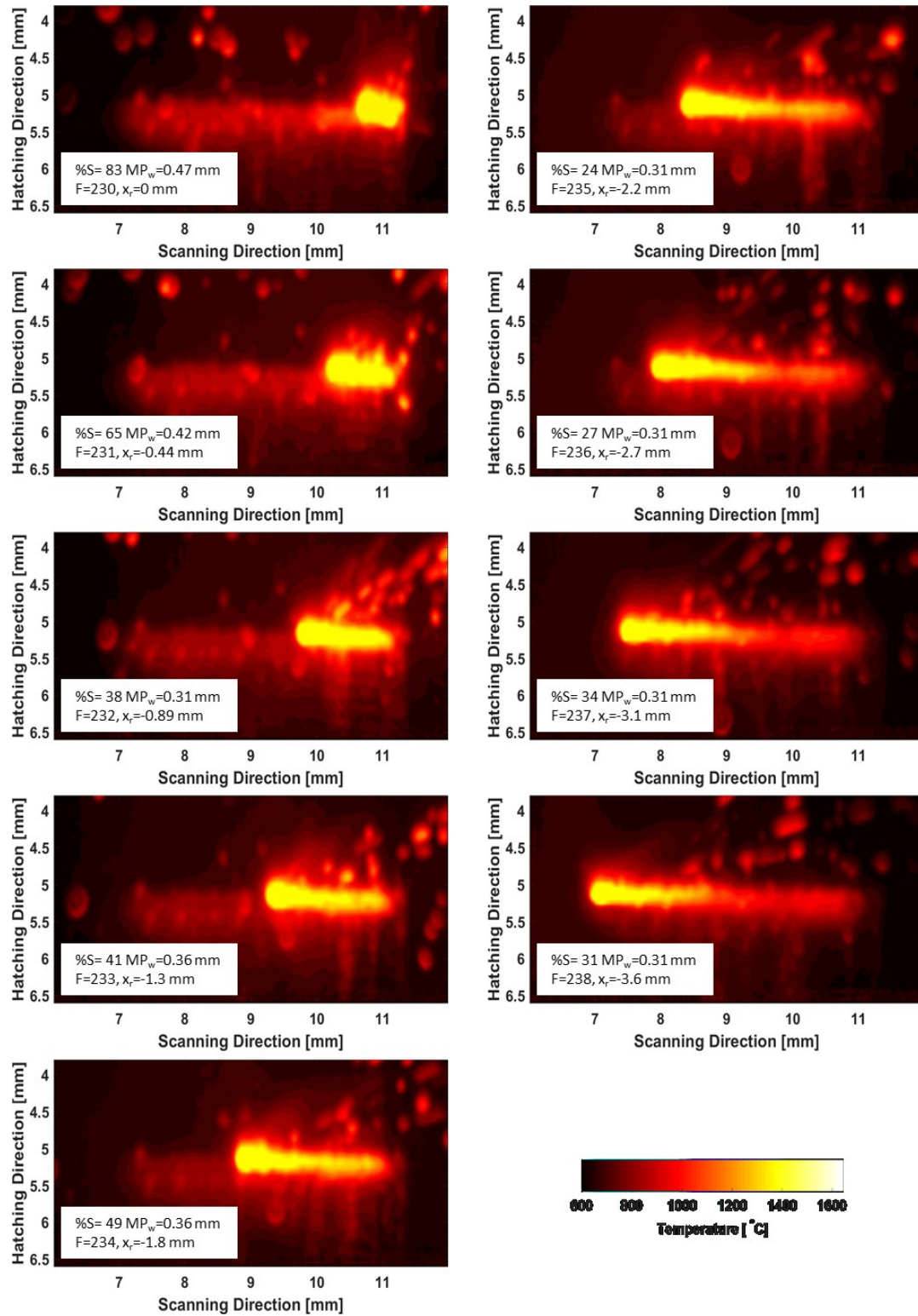


Figure D.5 Thermal images for track #5.

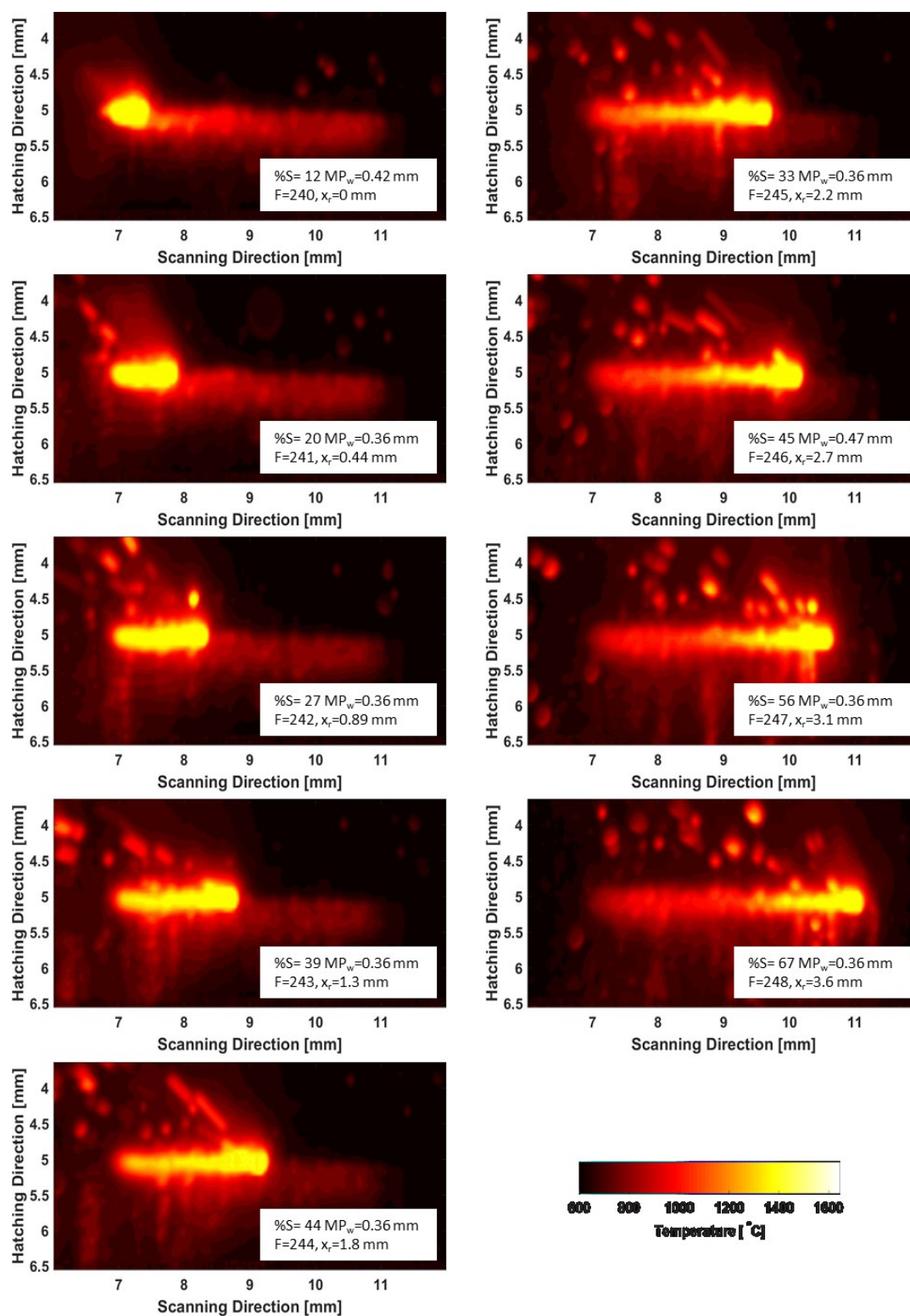


Figure D.6 Thermal images for track #6.

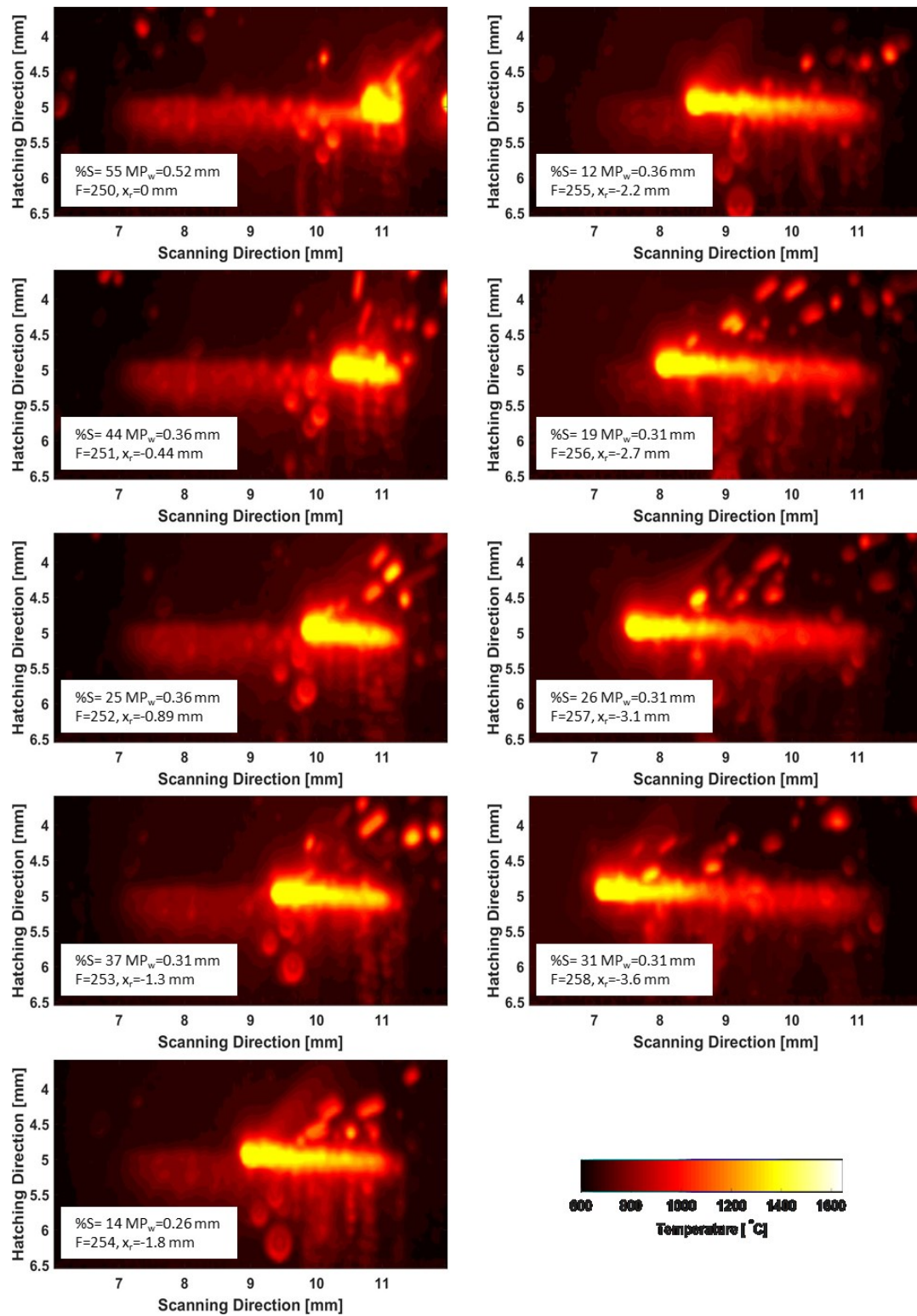


Figure D.7 Thermal images for track #7.

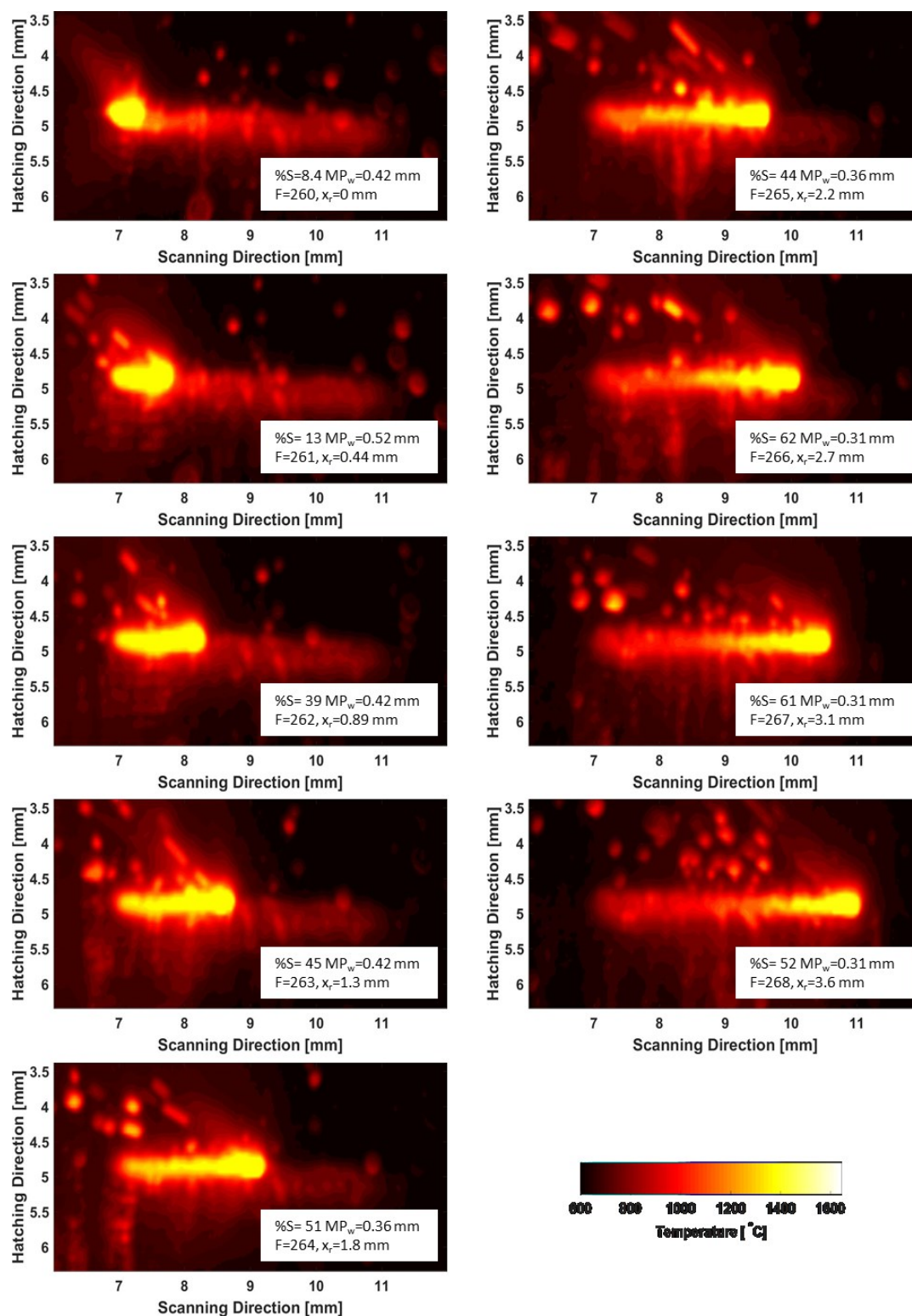


Figure D.8 Thermal images for track #8.

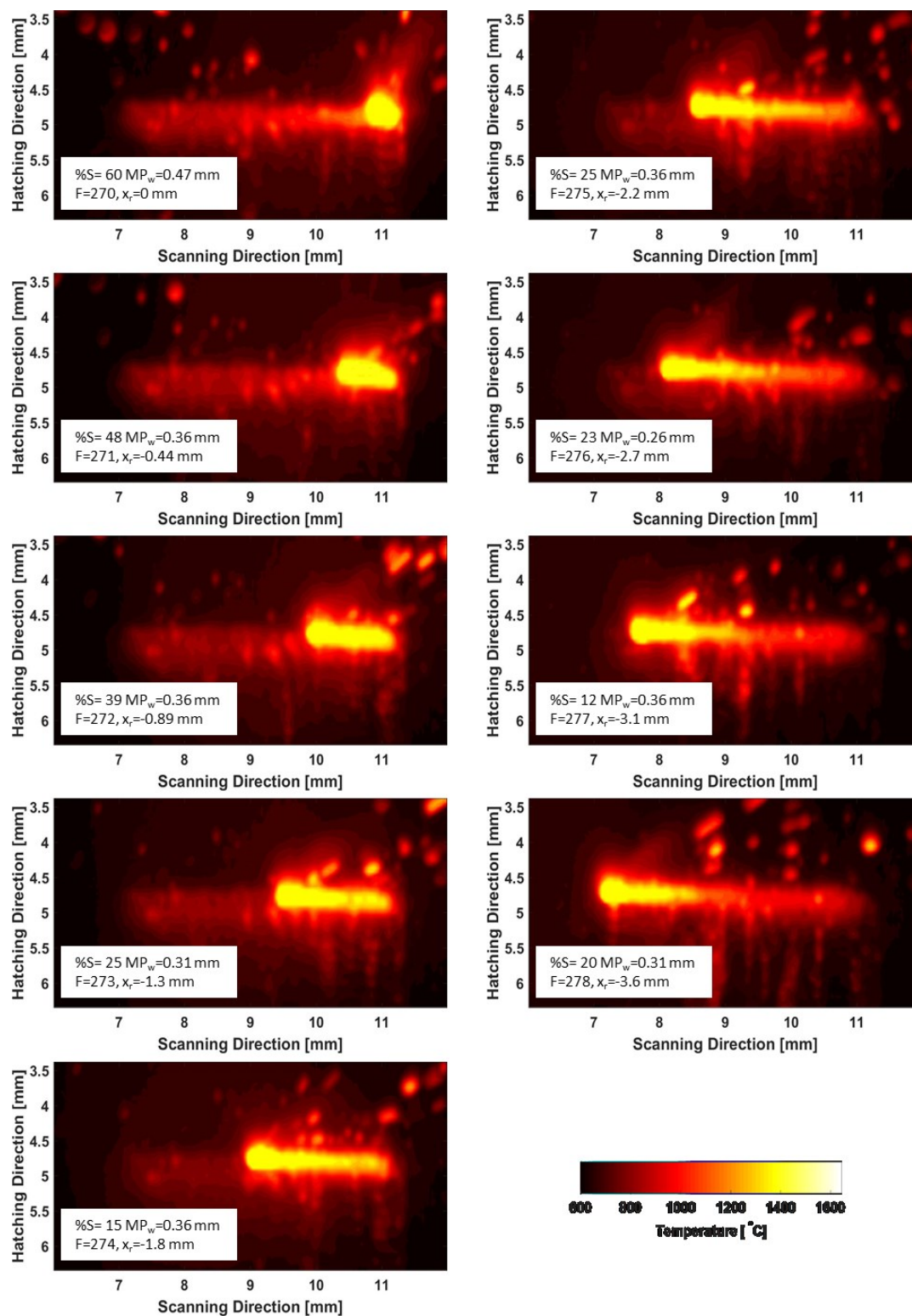


Figure D.9 Thermal images for track #9.

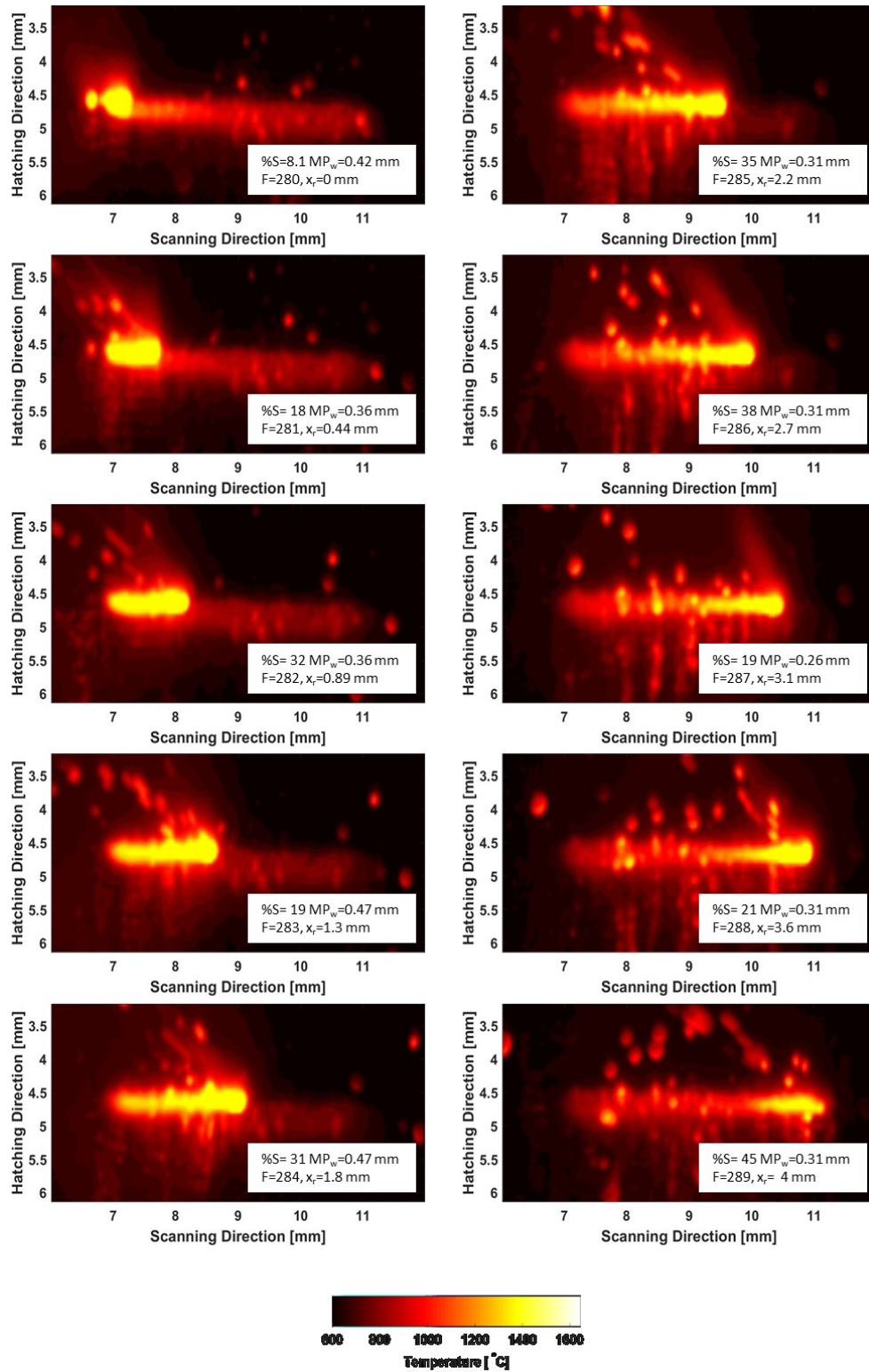


Figure D.10 Thermal images for track #10.

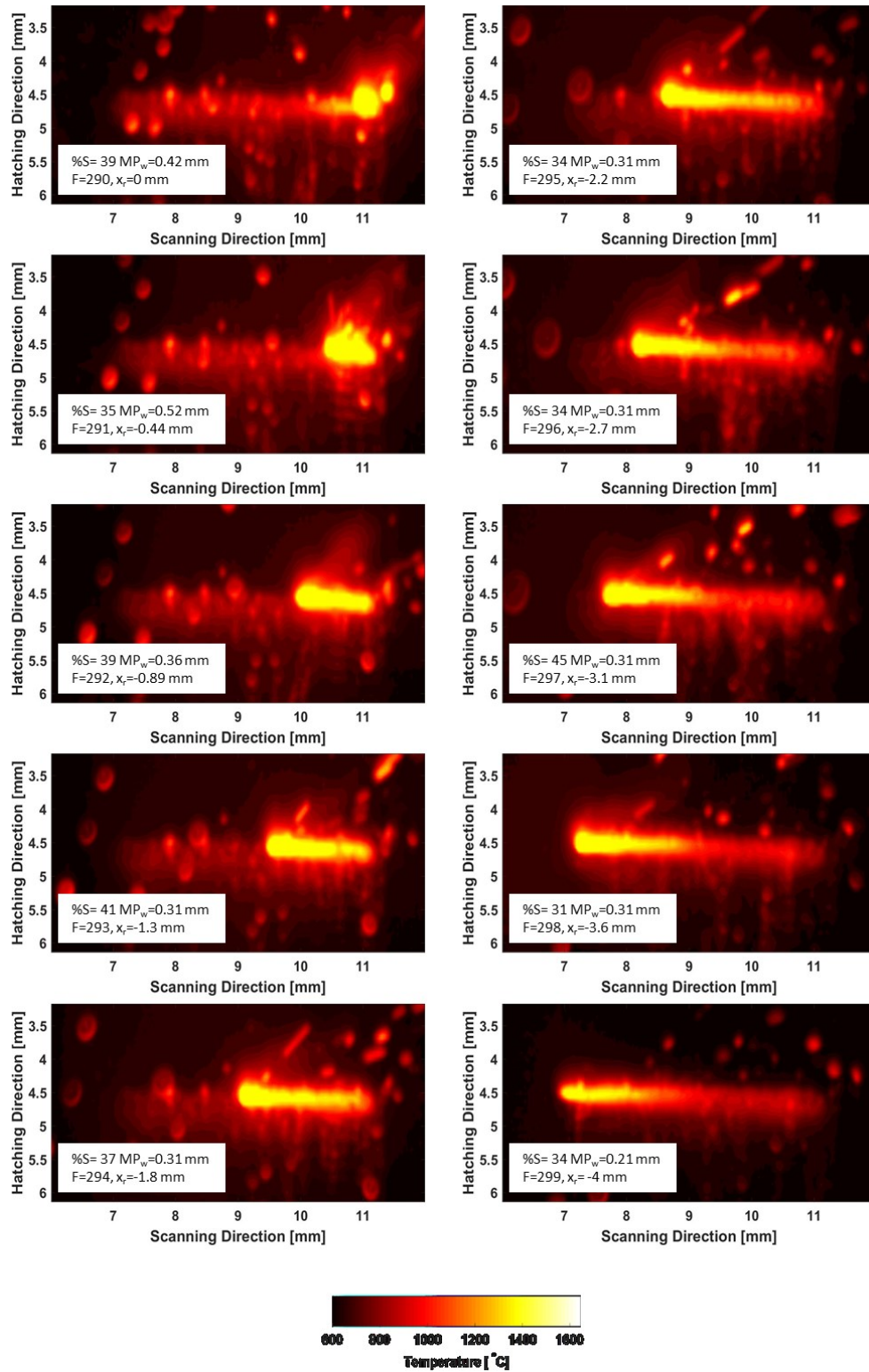


Figure D.11 Thermal images for track #11.

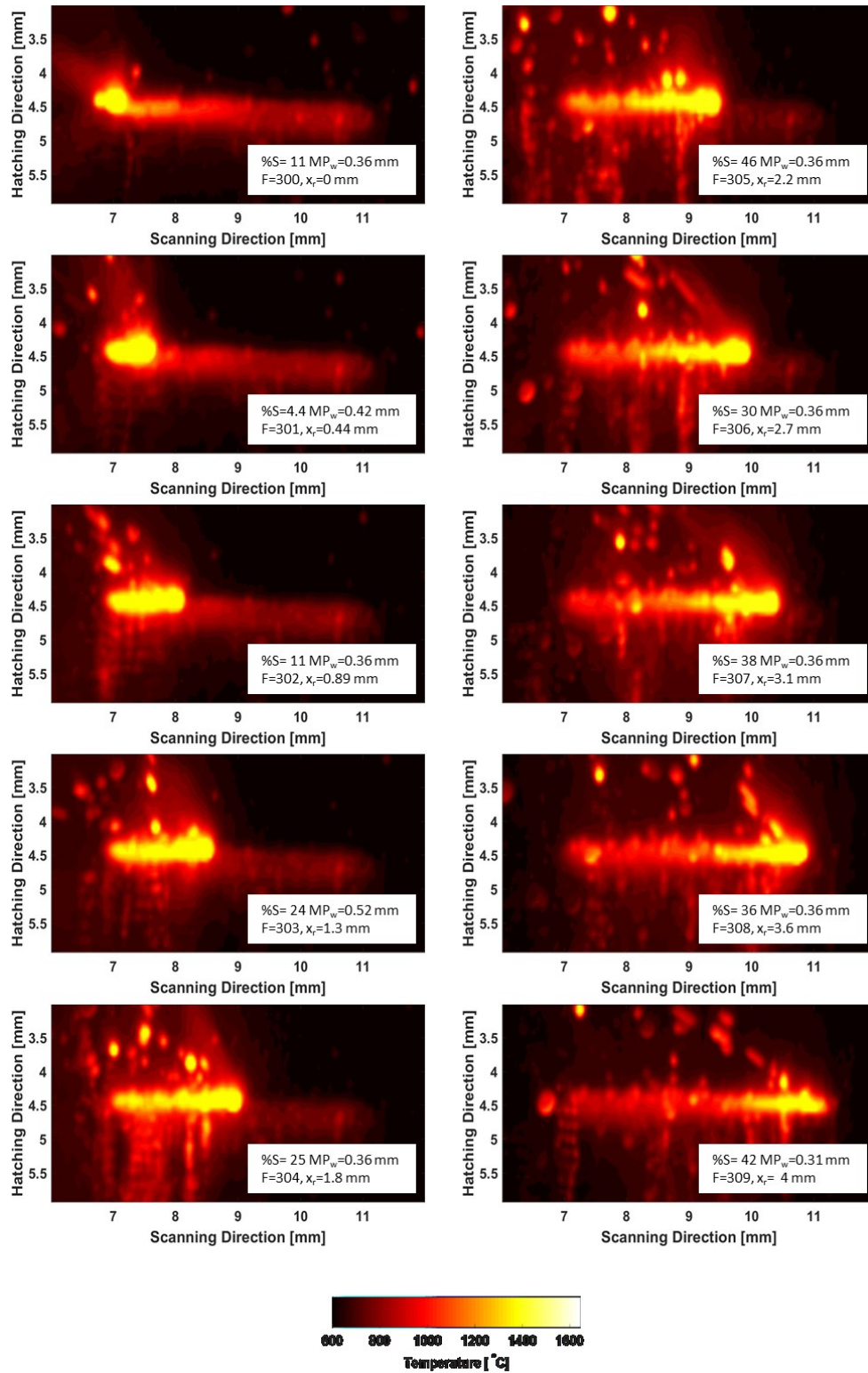


Figure D.12 Thermal images for track #12.

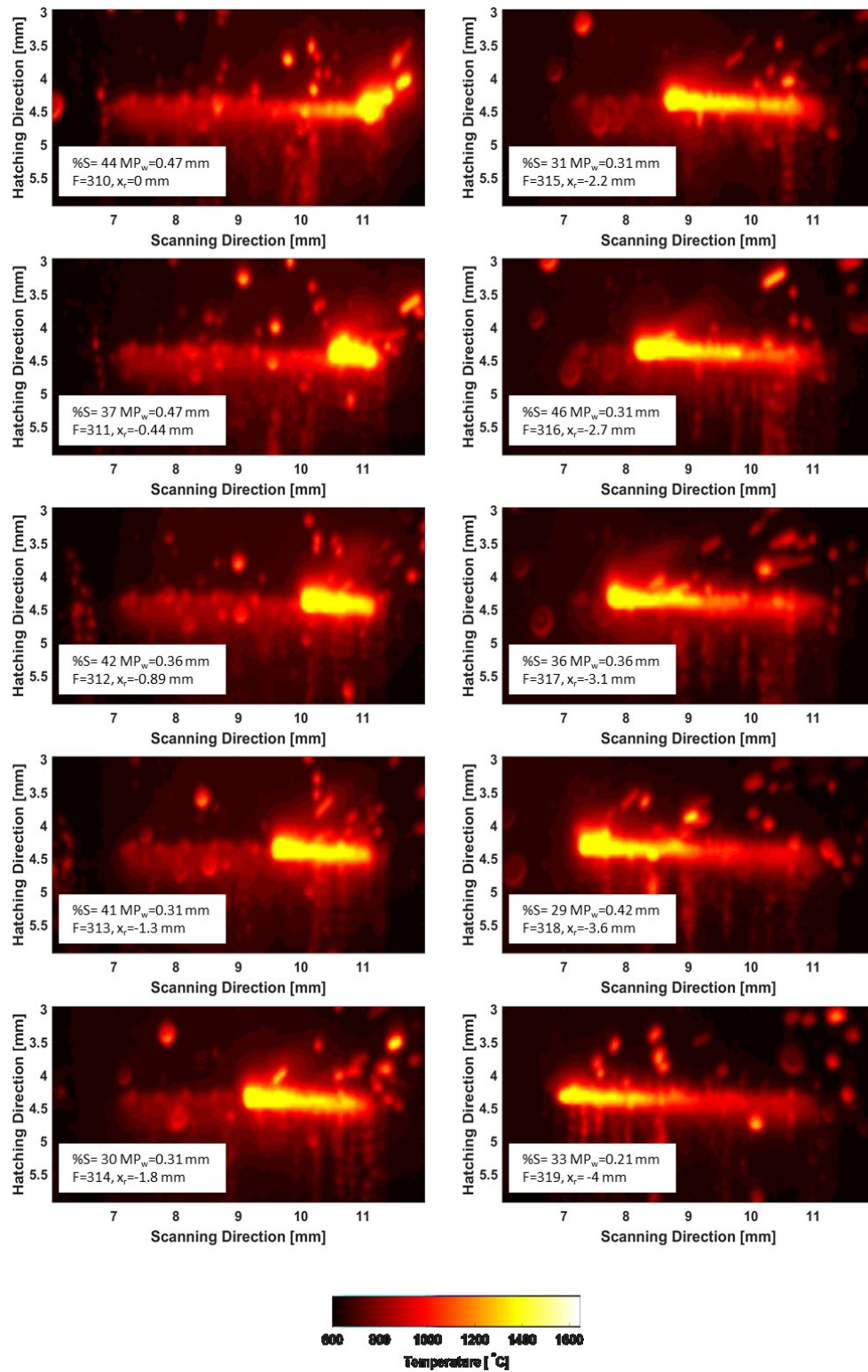


Figure D.13 Thermal images for track #13.

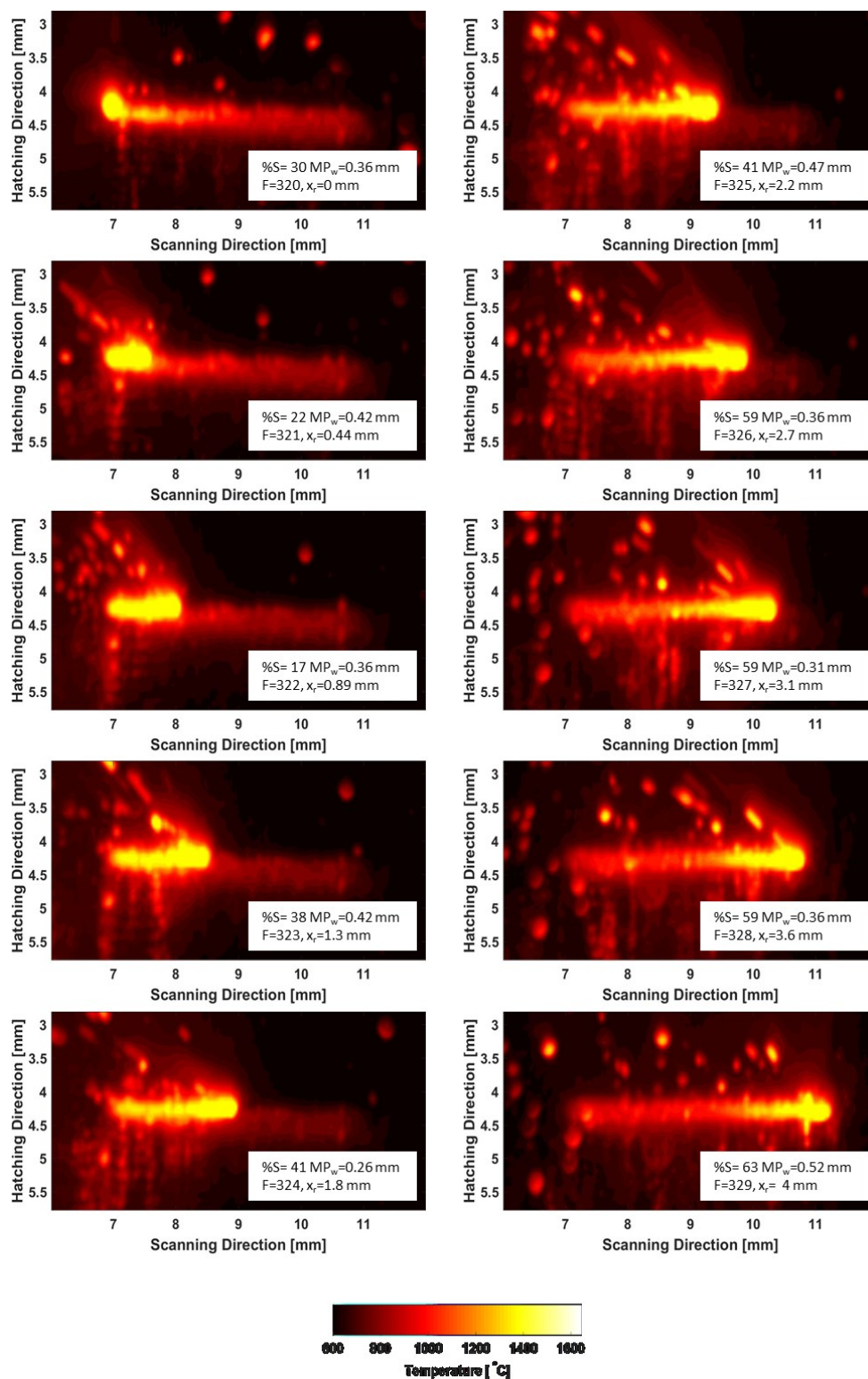


Figure D.14 Thermal images for track #14.

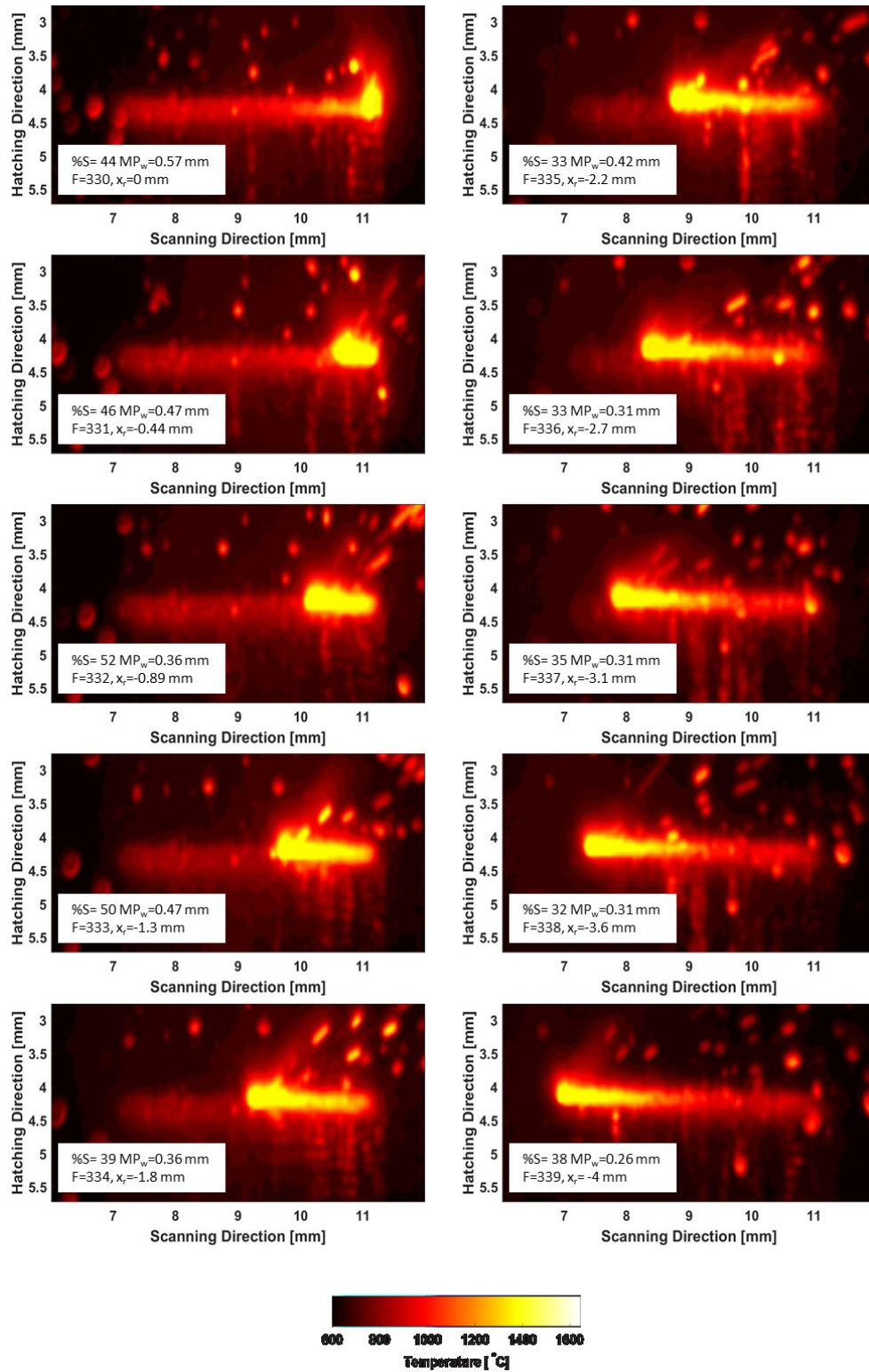


Figure D.15 Thermal images for track #15.

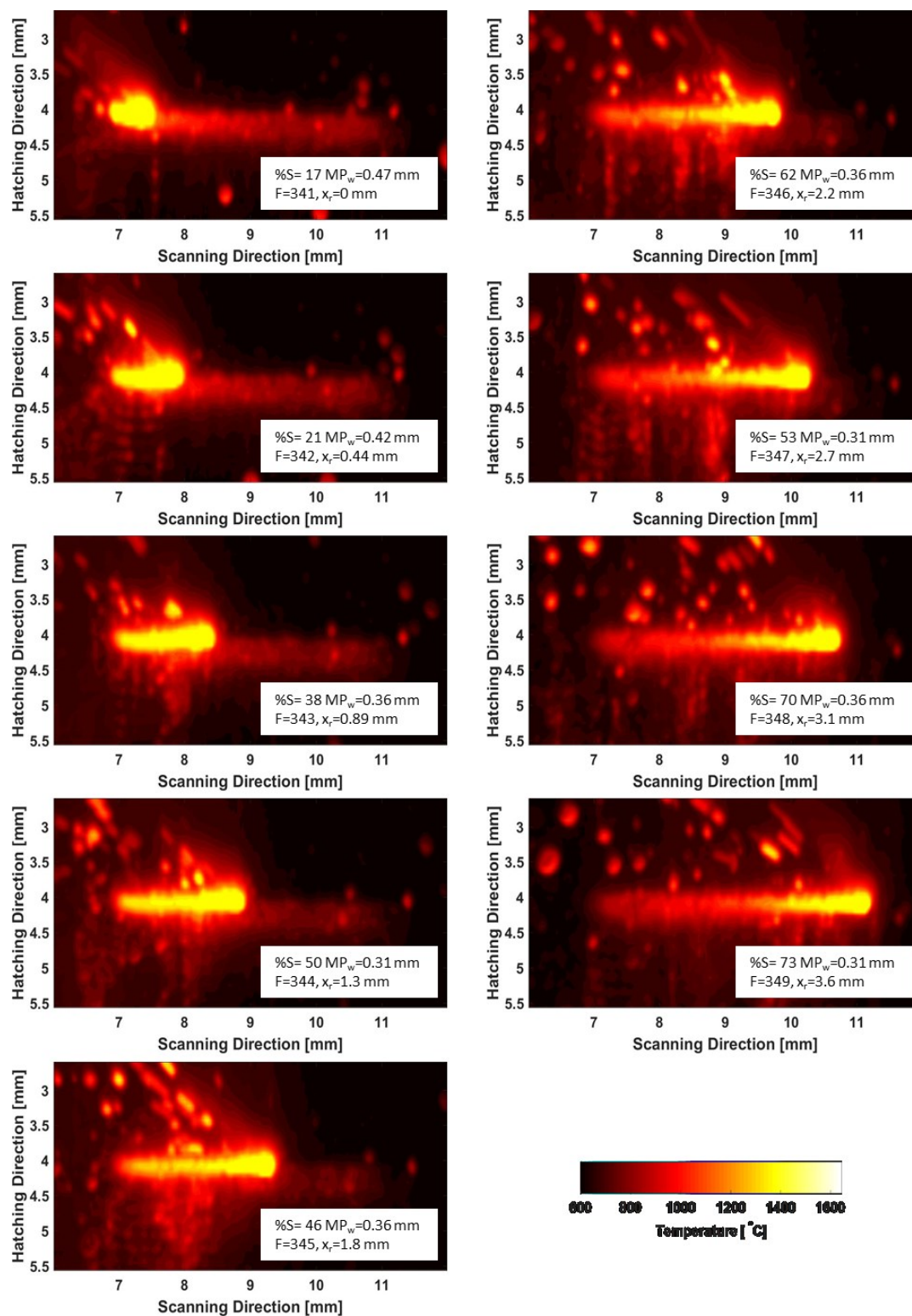


Figure D.16 Thermal images for track #16.

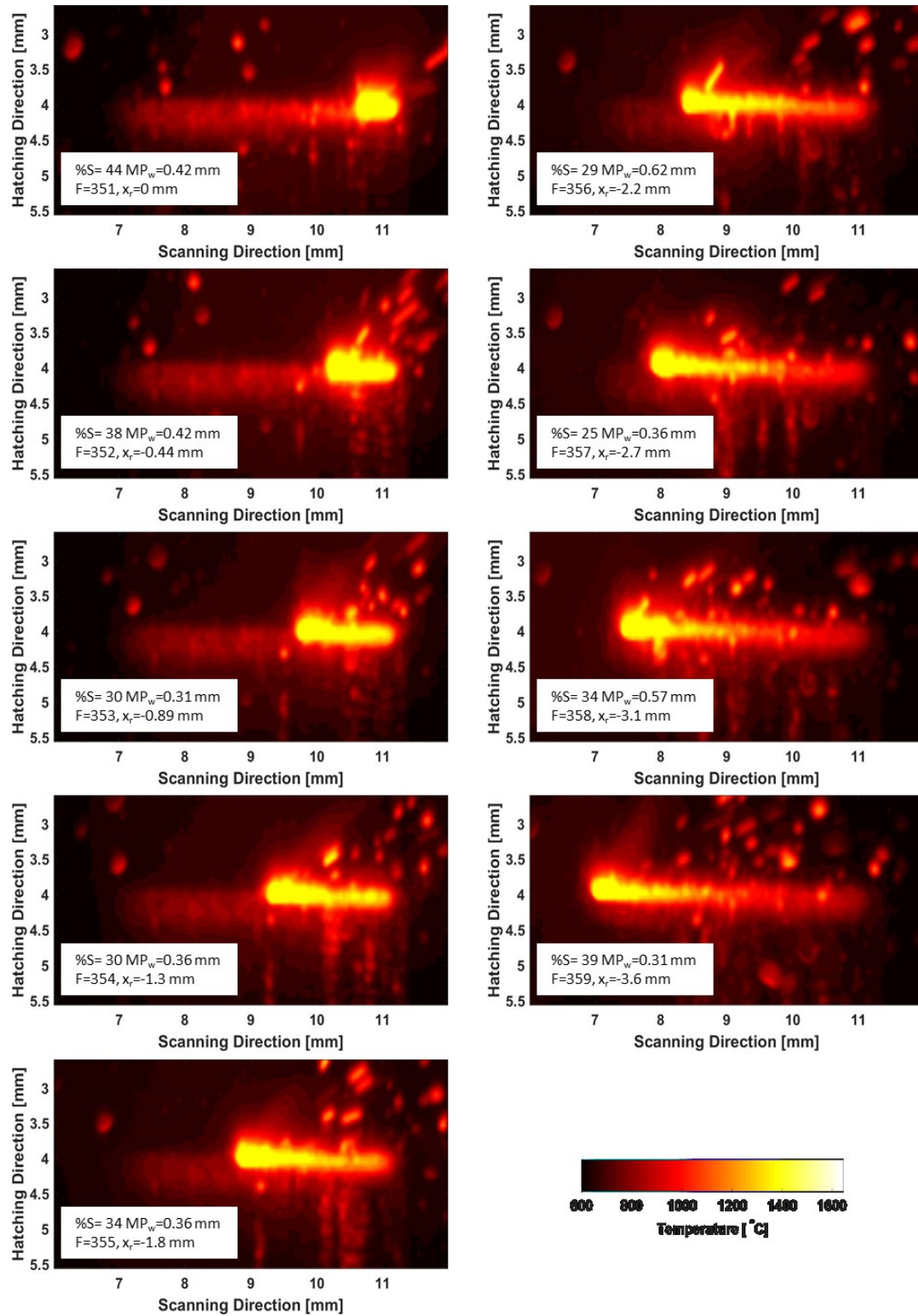


Figure D.17 Thermal images for track #17.

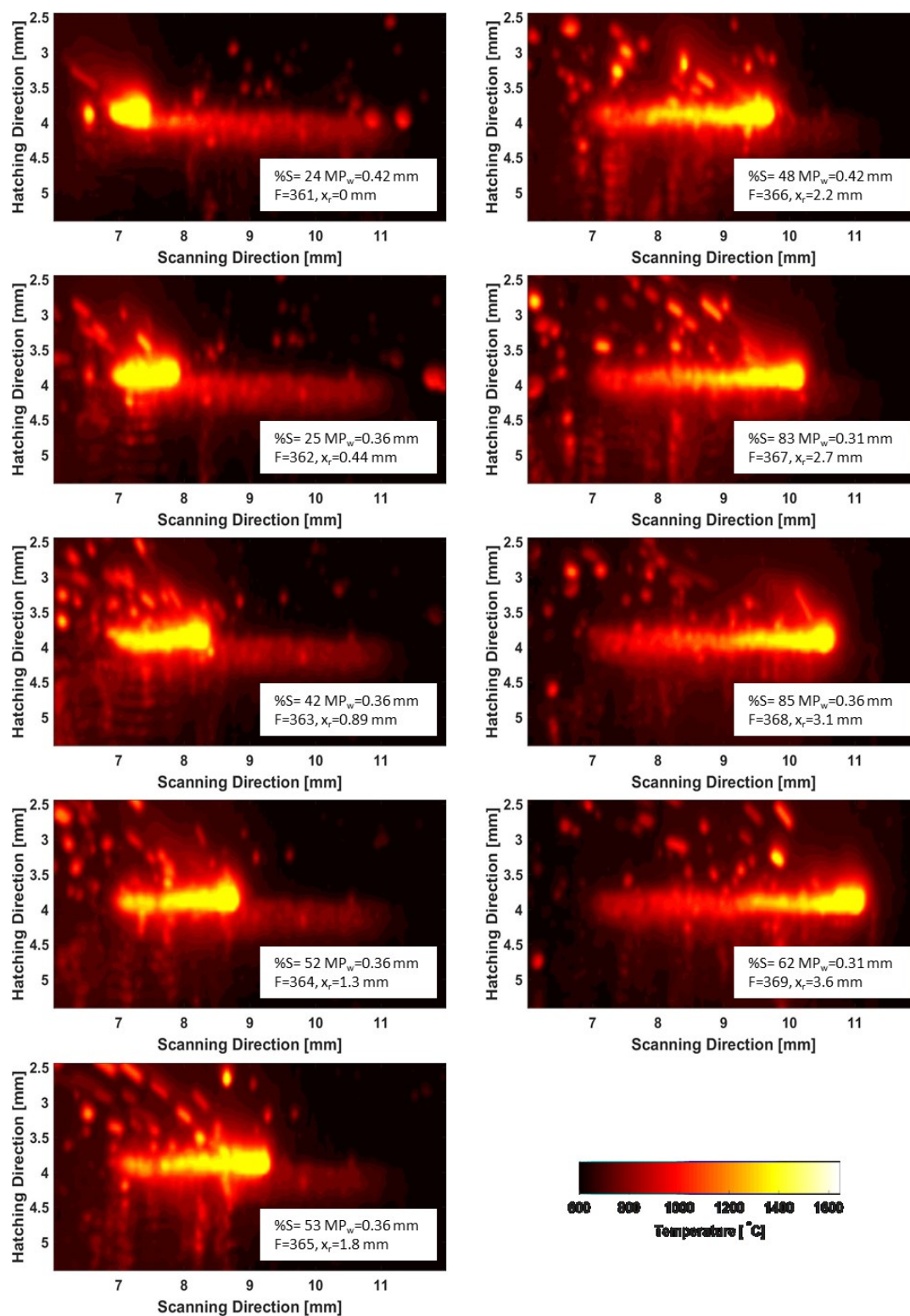


Figure D.18 Thermal images for track #18.

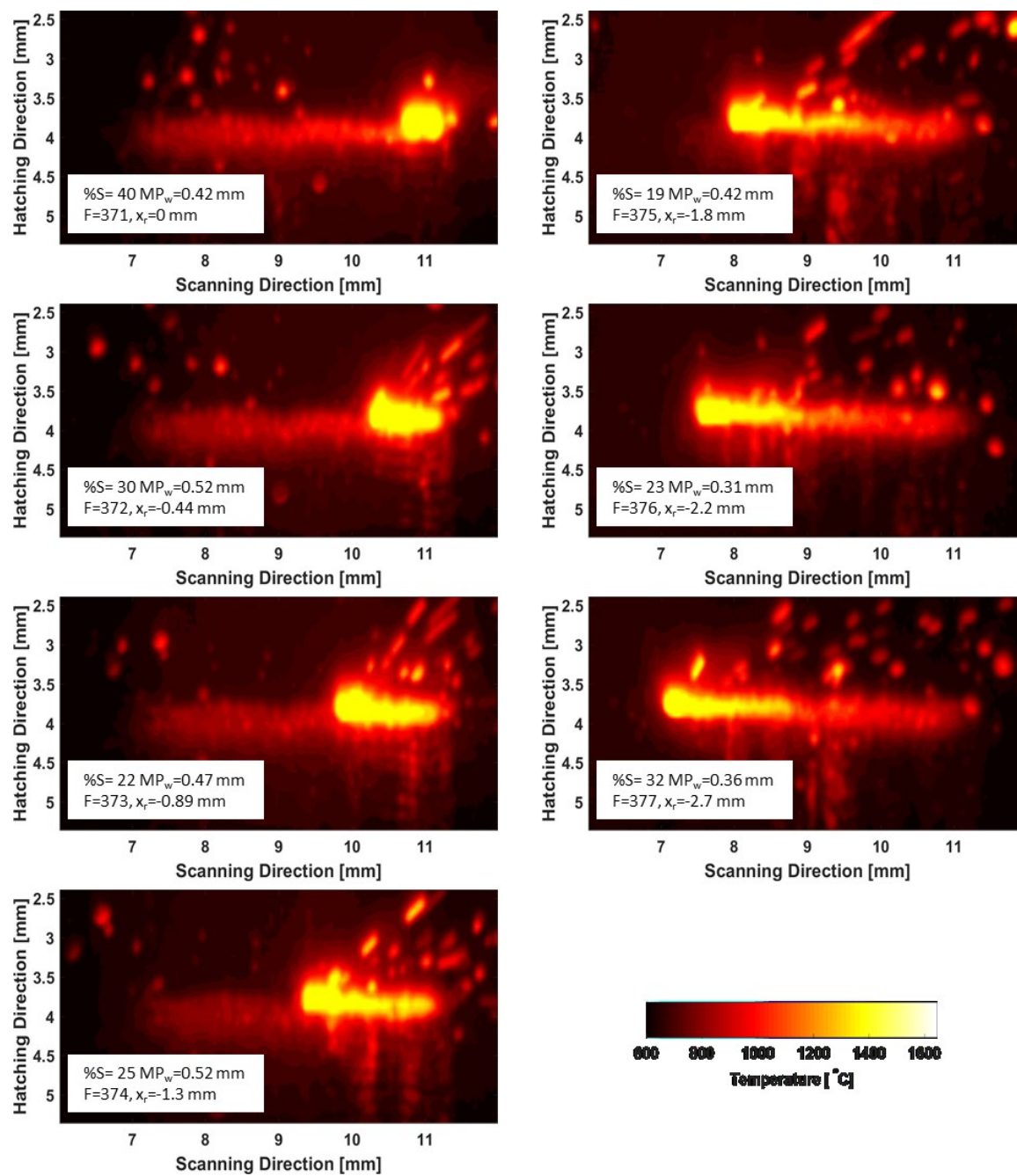


Figure D.19 Thermal images for track #19.

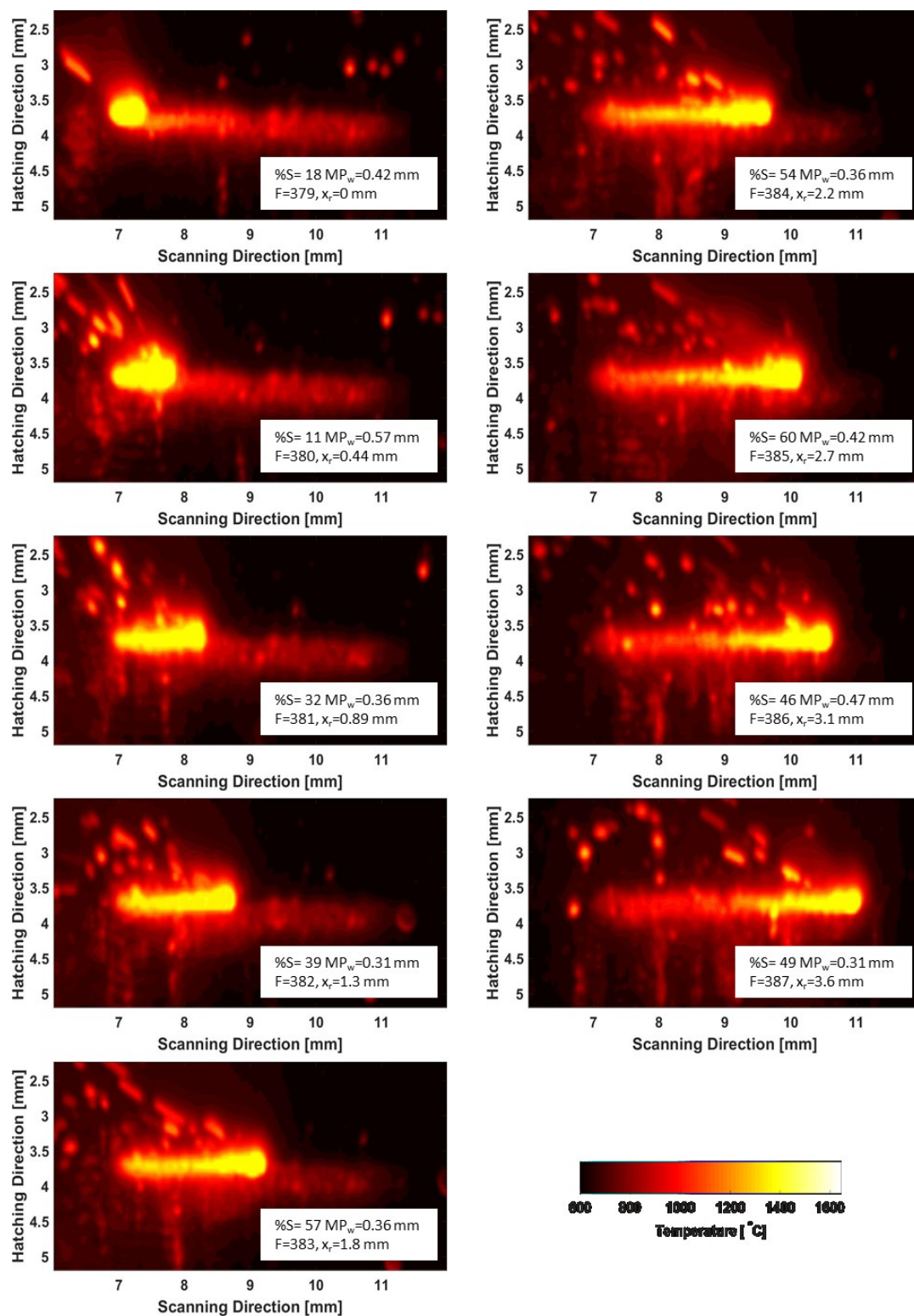
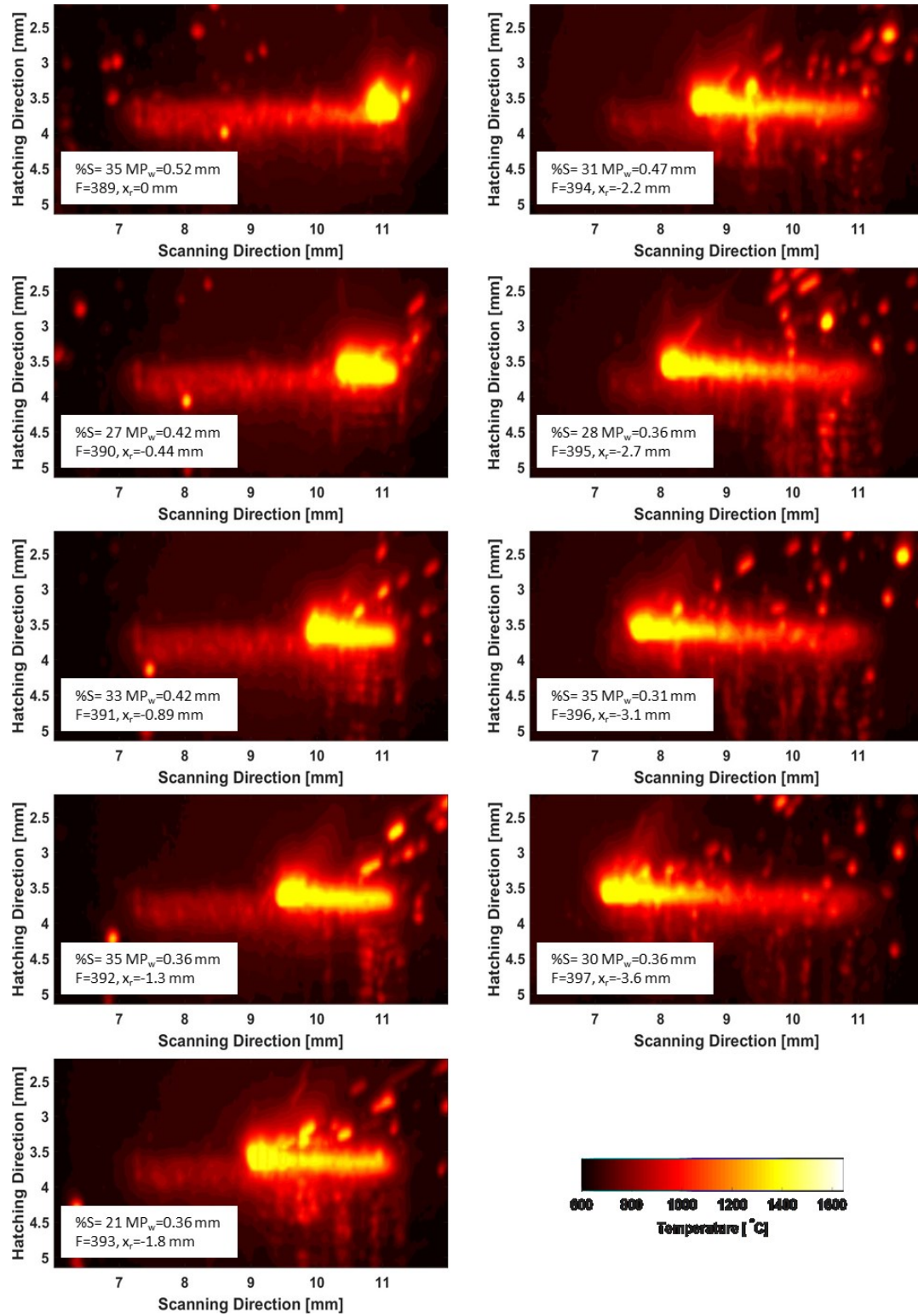


Figure D.20 Thermal images for track #20



REFERENCES

- Almeida, J. M. d. & Lorphevre, R. 2007. load_gmsh2.
- Amato, K. N., Gaytan, S. M., Murr, L. E., Martinez, E., Shindo, P. W., Hernandez, J., Collins, S. & Medina, F. 2012. Microstructures and mechanical behavior of Inconel 718 fabricated by selective laser melting. *Acta Materialia*, 60, 2229-2239.
- Anam, M. A., Dilip, J. J. S., Pal, D. & Stucker, B. 2014. Effect of Scan Pattern on the Microstructural Evolution of Inconel 625 during Selective Laser Melting. *SFF Symposium*.
- Anam, M. A., Pal, D. & Stucker, B. Modeling and Experimental validation of Nickel-based super alloy (Inconel 625) made using Selective Laser Melting. Proc. 24th Annual Int. Solid Freeform Fabrication Symp.—An Additive Manufacturing Conf., Austin, TX, USA, 2013a. 463-473.
- Anam, M. A., Pal, D. & Stucker, B. 2013b. Modeling and Experimental validation of Nickel-based super alloy (Inconel 625) made using Selective Laser Melting. *SFF Symposium*.
- Arieli, A. & Rosen, A. 1977. Superplastic deformation of Ti-6Al-4V alloy. *Metallurgical Transactions A*, 8, 1591-1596.
- Arisoy, Y. M. & Özel, T. 2014. Machine Learning Based Predictive Modeling of Machining Induced Microhardness and Grain Size in Ti-6Al-4V Alloy. *Materials and Manufacturing Processes*, 30, 425-433.
- Arisoy, Y. M. & Özel, T. 2015. Prediction of machining induced microstructure in Ti-6Al-4V alloy using 3-D FE-based simulations: Effects of tool micro-geometry,

- coating and cutting conditions. *Journal of Materials Processing Technology*, 220, 1-26.
- Arisoy, Y. M., Özel, T., Guo, C., Davut, K. & Kaftanoglu, B. 2015. Modeling of Microstructural Changes due to Machining Process on Nickel Superalloy Surfaces. *8th International Conference and Exhibition on Design and Production of Machines and Dies/Molds*.
- Arrazola, P. J., Garay, A., Iriarte, L. M., Armendia, M., Marya, S. & Le Maître, F. 2009. Machinability of titanium alloys (Ti6Al4V and Ti555.3). *Journal of Materials Processing Technology*, 209, 2223-2230.
- Axinte, D. A., Andrews, P., Li, W., Gindy, N., Withers, P. J. & Childs, T. H. C. 2006. Turning of advanced Ni based alloys obtained via powder metallurgy route. *CIRP Annals - Manufacturing Technology*, 55, 117-120.
- Banabic, D. 2007. *Advanced Methods in Material Forming*, Springer Berlin Heidelberg.
- Breiman, L. 2001. Random Forests. *Machine Learning*, 45, 5-32.
- Buffa, G., Ducato, A., Fratini, L. & Micari, F. Advanced FEM Modeling of Friction Stir Welding of Ti6Al4V: Microstructural Evolutions. *Proceedings of NAMRI/SME*, 2013.
- Calamaz, M., Coupard, D. & Girot, F. 2008. A new material model for 2D numerical simulation of serrated chip formation when machining titanium alloy Ti-6Al-4V. *International Journal of Machine Tools and Manufacture*, 48, 275-288.
- Carpenter. 2000. *Titanium Alloy Ti 6Al-4V Technical Datasheet* [Online]. Available: <http://cartech.ides.com/datasheet.aspx?i=101&E=269> [Accessed 2/9/2015 2015].

- Chakraborti, N. 2013. Promise of multiobjective genetic algorithms in coating performance formulation. *Surface Engineering*, 30, 79-82.
- Chakraborti, N. 2014. Critical Assessment 3: The unique contributions of multi-objective evolutionary and genetic algorithms in materials research. *Materials Science and Technology*, 30, 1259-1262.
- Chakraborti, N., Das, S., Jayakanth, R., Pekoz, R. & Erkoç, Ş. 2007. Genetic Algorithms Applied to Li⁺ Ions Contained in Carbon Nanotubes: An Investigation Using Particle Swarm Optimization and Differential Evolution Along with Molecular Dynamics. *Materials and Manufacturing Processes*, 22, 562-569.
- Che-Haron, C. H. & Jawaid, A. 2005. The effect of machining on surface integrity of titanium alloy Ti-6% Al-4% V. *Journal of Materials Processing Technology*, 166, 188-192.
- Chun, Y. B., Semiatin, S. L. & Hwang, S. K. 2006. Monte Carlo modeling of microstructure evolution during the static recrystallization of cold-rolled, commercial-purity titanium. *Acta Materialia*, 54, 3673-3689.
- Criales, L. E., Arisoy, Y. M. & Özel, T. A Sensitivity Analysis Study on The Material Properties and Process Parameters for Selective Laser Melting of Inconel 625. Proceedings of 2015 ASME International Conference on Manufacturing Science and Engineering, June 8-12 2015 Charlotte, North Carolina, USA.
- Datta, S. & Chattopadhyay, P. P. 2013. Soft computing techniques in advancement of structural metals. *International Materials Reviews*, 58, 475-504.
- Deb, K. 2001. *Multi-Objective Optimization Using Evolutionary Algorithms*, John Wiley & Sons, Inc.

- Ding, R., Guo, Z. X. & Wilson, A. 2002. Microstructural evolution of a Ti–6Al–4V alloy during thermomechanical processing. *Materials Science and Engineering: A*, 327, 233-245.
- DuPont, J. N. 1996. Solidification of an alloy 625 weld overlay. *Metallurgical and Materials Transactions A*, 27, 3612-3620.
- DuPont, J. N., Narwocki, J. G. & Griffith, M. L. 2001. Solidification Modeling and Microstructural Characterization of Alloy IN718 Deposited by Laser Engineered Net Shaping. *SFF Symposium*.
- Eberhart, R. C. & Kennedy, J. A new optimizer using particle swarm theory. Proceedings of the sixth international symposium on micro machine and human science, 1995. New York, NY, 39-43.
- Ebrahimi, Z. 2010. *Micromechanical Phase-Field Model and Simulation of Eutectic Growth with Misfit Stresses*. PhD, RWTH Aachen.
- Fan, X. G. & Yang, H. 2011. Internal-state-variable based self-consistent constitutive modeling for hot working of two-phase titanium alloys coupling microstructure evolution. *International Journal of Plasticity*, 27, 1833-1852.
- Felippa, C. A. 2013. *Advanced Finite Element Methods: Chapter 11 - Hexahedron Elements* [Online]. Available: <http://www.colorado.edu/engineering/CAS/courses.d/AFEM.d/> [Accessed August 22 2015].
- Felippa, C. A. 2014. *Introduction to Finite Elements. Chapter 24: Implementation of iso-P Triangular Elements* [Online]. Available: <http://www.colorado.edu/engineering/cas/courses.d/IFEM.d/> [Accessed 2/9/2015].

- Follansbee, P. S. & Kocks, U. F. 1988. A constitutive description of the deformation of copper based on the use of the mechanical threshold stress as an internal state variable. *Acta Metallurgica*, 36, 81-93.
- Geuzaine, C. & Remacle, J. F. 2009. Gmsh: A 3-D finite element mesh generator with built-in pre-and post-processing facilities. *International Journal for Numerical Methods in Engineering*, 79, 1309-1331.
- Gong, H., Rafi, K., Starr, T. & Stucker, B. 2013. The Effects of Processing Parameters on Defect Regularity in Ti-6Al-4V Parts Fabricated By Selective Laser Melting and Electron Beam Melting. *SFF Symposium*.
- Huebner, K. H. 2001. *The Finite Element Method for Engineers*, John Wiley & Sons.
- Hughes, T. 1987. The finite element method: linear static and dynamic finite element analysis.
- Jia, Q. & Gu, D. 2014. Selective laser melting additive manufacturing of Inconel 718 superalloy parts: Densification, microstructure and properties. *Journal of Alloys and Compounds*, 585, 713-721.
- Jovanović, M. T., Tadić, S., Zec, S., Mišković, Z. & Bobić, I. 2006. The effect of annealing temperatures and cooling rates on microstructure and mechanical properties of investment cast Ti-6Al-4V alloy. *Materials & Design*, 27, 192-199.
- Karma, A. & Rappel, W.-J. 1998. Quantitative phase-field modeling of dendritic growth in two and three dimensions. *Physical Review E*, 57, 4323-4349.
- Kikuchi, S., Ando, S., Futami, S., Kitamura, T. & Koiwa, M. 1990. Superplastic deformation and microstructure evolution in PM IN-100 superalloy. *Journal of Materials Science*, 25, 4712-4716.

- Kiran, A. 2010. *Phase-Field Simulation of Microstructure Evolution (implementation in Fortran)* [Online]. Available: <http://www.apoorvakiran.com/downloads.html> [Accessed 2015].
- Kobayashi, R. 1993. Modeling and numerical simulations of dendritic crystal growth. *Physica D: Nonlinear Phenomena*, 63, 410-423.
- Kocks, U. F. 1976. Laws for Work-Hardening and Low-Temperature Creep. *Journal of Engineering Materials and Technology*, 98, 76-85.
- Krauss, H., Zeugner, T. & Zaeh, M. F. 2014. Layerwise Monitoring of the Selective Laser Melting Process by Thermography. *Physics Procedia*, 56, 64-71.
- Kundin, J., Mushongera, L. & Emmerich, H. 2015. Phase-field modeling of microstructure formation during rapid solidification in Inconel 718 superalloy. *Acta Materialia*, 95, 343-356.
- Kwon, Y. W. & Bang, H. 2000. *The finite element method using MATLAB*, CRC press.
- Lee, W.-S. & Lin, C.-F. 1998. Plastic deformation and fracture behaviour of Ti-6Al-4V alloy loaded with high strain rate under various temperatures. *Materials Science and Engineering: A*, 241, 48-59.
- Li, S., Wei, Q., Shi, Y., Zhu, Z. & Zhang, D. 2015. Microstructure Characteristics of Inconel 625 Superalloy Manufactured by Selective Laser Melting. *Journal of Materials Science & Technology*.
- M'Saoubi, R., Axinte, D., Herbert, C., Hardy, M. & Salmon, P. 2014. Surface integrity of nickel-based alloys subjected to severe plastic deformation by abusive drilling. *CIRP Annals - Manufacturing Technology*, 63, 61-64.

- Mecking, H. & Kocks, U. F. 1981. Kinetics of flow and strain-hardening. *Acta Metallurgica*, 29, 1865-1875.
- Milligan, W. W., Orth, E. L., Schirra, J. J. & Savage, M. F. 2004. Effects of Microstructure on the High Temperature Constitutive Behavior of IN100. *Superalloys*.
- Mitchell, M. 1996. *An introduction to genetic algorithms*, MIT Press.
- Moussaoui, K., Mousseigne, M., Senatore, J., Chieragatti, R. & Monies, F. 2013. Influence of milling on surface integrity of Ti6Al4V—study of the metallurgical characteristics: microstructure and microhardness. *The International Journal of Advanced Manufacturing Technology*, 67, 1477-1489.
- Murr, L. E., Gaytan, S. M., Ramirez, D. A., Martinez, E., Hernandez, J., Amato, K. N., Shindo, P. W., Medina, F. R. & Wicker, R. B. 2012. Metal Fabrication by Additive Manufacturing Using Laser and Electron Beam Melting Technologies. *Journal of Materials Science & Technology*, 28, 1-14.
- Nalla, R. K., Altenberger, I., Noster, U., Liu, G. Y., Scholtes, B. & Ritchie, R. O. 2003. On the influence of mechanical surface treatments—deep rolling and laser shock peening—on the fatigue behavior of Ti–6Al–4V at ambient and elevated temperatures. *Materials Science and Engineering: A*, 355, 216-230.
- National Institute of Standards and Technology. 2015. Box-Behnken designs. Available: <http://www.itl.nist.gov/div898/handbook/pri/section3/pri3362.htm> [Accessed 2015].
- Nie, P., Ojo, O. A. & Li, Z. 2014. Numerical modeling of microstructure evolution during laser additive manufacturing of a nickel-based superalloy. *Acta Materialia*, 77, 85-95.

- Özel, T. & Arisoy, Y. M. 2014. Experimental and Numerical Investigations on Machining Induced Surface Integrity in Inconel-100 Nickel-Base Alloy. *Procedia CIRP*, 13, 302-307.
- Ozel, T., Arisoy, Y. M. & Ulutan, D. 2013. Prediction of Machining Induced Microhardness using Finite Element Simulations and Machine Learning in Titanium Alloys. *7th International Conference and Exhibition on Design and Production of Machines and Dies/Molds*.
- Özel, T. & Ulutan, D. 2012. Prediction of machining induced residual stresses in turning of titanium and nickel based alloys with experiments and finite element simulations. *CIRP Annals - Manufacturing Technology*, 61, 547-550.
- Park, C. H., Ko, Y. G., Park, J.-W. & Lee, C. S. 2008. Enhanced superplasticity utilizing dynamic globularization of Ti-6Al-4V alloy. *Materials Science and Engineering: A*, 496, 150-158.
- Pu, Z., Umbrello, D., Dillon Jr, O. W., Lu, T., Puleo, D. A. & Jawahir, I. S. 2014. Finite element modeling of microstructural changes in dry and cryogenic machining of AZ31B magnesium alloy. *Journal of Manufacturing Processes*, 16, 335-343.
- Quan, G. Z., Wu, D. S., Luo, G. C., Xia, Y. F., Zhou, J., Liu, Q. & Gao, L. 2014. Dynamic recrystallization kinetics in alpha phase of as-cast Ti-6Al-2Zr-1Mo-1V alloy during compression at different temperatures and strain rates. *Materials Science and Engineering a-Structural Materials Properties Microstructure and Processing*, 589, 23-33.

- Ranganath, S., Guo, C. & Hegde, P. 2009. A finite element modeling approach to predicting white layer formation in nickel superalloys. *CIRP Annals - Manufacturing Technology*, 58, 77-80.
- Rotella, G., Dillon Jr, O. W., Umbrello, D., Settineri, L. & Jawahir, I. S. 2013. Finite element modeling of microstructural changes in turning of AA7075-T651 Alloy. *Journal of Manufacturing Processes*, 15, 87-95.
- Rotella, G., Dillon, O. W., Jr., Umbrello, D., Settineri, L. & Jawahir, I. S. 2014. The effects of cooling conditions on surface integrity in machining of Ti6Al4V alloy. *The International Journal of Advanced Manufacturing Technology*, 71, 47-55.
- Rotella, G. & Umbrello, D. 2014. Finite element modeling of microstructural changes in dry and cryogenic cutting of Ti6Al4V alloy. *CIRP Annals - Manufacturing Technology*, 63, 69-72.
- Seshacharyulu, T., Medeiros, S. C., Frazier, W. G. & Prasad, Y. V. R. K. 2000. Hot working of commercial Ti6Al4V with an equiaxed alpha beta microstructure materials modeling considerations. *Materials Science and Engineering A*, 284, 184-194.
- Seshacharyulu, T., Medeiros, S. C., Frazier, W. G. & Prasad, Y. V. R. K. 2002. Microstructural mechanisms during hot working of commercial grade Ti-6Al-4V with lamellar starting structure. *Materials Science and Engineering: A*, 325, 112-125.
- SFTC. *DEFORM User's Manual* [Online]. Scientific Forming Technologies Corporation. Available: <http://www.deform.com/>.

- Shafaat, M. A., Omidvar, H. & Fallah, B. 2011. Prediction of hot compression flow curves of Ti-6Al-4V alloy in $\alpha+\beta$ phase region. *Materials & Design*, 32, 4689-4695.
- Shen, G. 2005. Microstructure modeling in superalloy forging. In: G., A. T. N. G. S. (ed.) *Cold and Hot Forging: Fundamentals and Applications*. ASM International.
- Shen, G., Semiatin, S. L. & Sivpuri, R. 1995. Modeling Microstructural Development during the Forging of Waspaloy.
- Sima, M. & Özel, T. 2010. Modified material constitutive models for serrated chip formation simulations and experimental validation in machining of titanium alloy Ti-6Al-4V. *International Journal of Machine Tools and Manufacture*, 50, 943-960.
- Smith, G. & Patel, S. 2005. The role of niobium in wrought precipitation-hardened nickel-base alloys. *Superalloys 718, 625, 706 and Various Derivatives*.
- Special Metals. 2015. *Inconel alloy 625* [Online]. Available: <http://www.specialmetals.com/documents/Inconel%20alloy%20625.pdf>.
- Sun, Z. C., Yang, H., Han, G. J. & Fan, X. G. 2010. A numerical model based on internal-state-variable method for the microstructure evolution during hot-working process of TA15 titanium alloy. *Materials Science and Engineering: A*, 527, 3464-3471.
- Ulutun, D. & Ozel, T. 2011. Machining induced surface integrity in titanium and nickel alloys: A review. *International Journal of Machine Tools and Manufacture*, 51, 250-280.
- Ulutun, D. & Özel, T. 2013a. Determination of Constitutive Material Model Parameters in FE-Based Machining Simulations of Ti-6Al-4V and IN-100 Alloys: An Inverse Methodology. *Proceedings of NAMRI/SME*, 41.

- Ulutan, D. & Özel, T. 2013b. Determination of tool friction in presence of flank wear and stress distribution based validation using finite element simulations in machining of titanium and nickel based alloys. *Journal of Materials Processing Technology*, 213, 2217-2237.
- Ulutan, D. & Özel, T. 2013c. Multiobjective Optimization of Experimental and Simulated Residual Stresses in Turning of Nickel-Alloy IN100. *Materials and Manufacturing Processes*, 28, 835-841.
- Umbrello, D. & Filice, L. 2009. Improving surface integrity in orthogonal machining of hardened AISI 52100 steel by modeling white and dark layers formation. *CIRP Annals - Manufacturing Technology*, 58, 73-76.
- Vilaro, T., Colin, C., Bartout, J. D., Nazé, L. & Sennour, M. 2012. Microstructural and mechanical approaches of the selective laser melting process applied to a nickel-base superalloy. *Materials Science and Engineering: A*, 534, 446-451.
- Vo, P., Jahazi, M. & Yue, S. 2008. Recrystallization during Thermomechanical Processing of IMI834. *Metallurgical and Materials Transactions A*, 39, 2965-2980.
- Voorhees, P. W. 2015. The workshop on Semiconductors, Electronic Materials, Thin Films and Photonic Materials. Tel Aviv University.
- Wang, Z., Guan, K., Gao, M., Li, X., Chen, X. & Zeng, X. 2012. The microstructure and mechanical properties of deposited-IN718 by selective laser melting. *Journal of Alloys and Compounds*, 513, 518-523.
- Wusatowska-Sarnek, A. M., Blackburn, M. J. & Aindow, M. 2003a. Techniques for microstructural characterization of powder-processed nickel-based superalloys. *Materials Science and Engineering: A*, 360, 390-395.

- Wusatowska-Sarnek, A. M., Ghosh, G., Olson, G. B., Blackburn, M. J. & Aindow, M. 2003b. Characterization of the microstructure and phase equilibria calculations for the powder metallurgy superalloy IN100.
- Y. M. Arısoy, C. G., B. Kaftanoğlu, T. Özel 2016. Investigations on Microstructural Changes in Machining of Inconel 100 alloy using Face Turning Experiments and 3D Finite Element Simulations. *International Journal of Mechanical Sciences*.
- Yadroitsev, I., Krakhmalev, P., Yadroitsava, I., Johansson, S. & Smurov, I. 2013. Energy input effect on morphology and microstructure of selective laser melting single track from metallic powder. *Journal of Materials Processing Technology*, 213, 606-613.
- Yazdipour, N., Davies, C. H. J. & Hodgson, P. D. 2008. Microstructural modeling of dynamic recrystallization using irregular cellular automata. *Computational Materials Science*, 44, 566-576.
- Yi, Y.-p., Fu, X., Cui, J.-d. & Chen, H. 2008. Prediction of grain size for large-sized aluminium alloy 7050 forging during hot forming. *Journal of Central South University of Technology*, 15, 1-5.